

Oxidation characteristics, acid neutralization, secondary minerals, and trace elements associated with
pyrrhotite oxidation in historical waste rock

by

Lianna Jane DeGeer Smith

A thesis

presented to the University of Waterloo

in fulfillment of the

thesis requirement for the degree of

Doctor of Philosophy

in

Earth Sciences

Waterloo, Ontario, Canada, 2022

© Lianna Jane DeGeer Smith

Examining Committee Membership

The following served on the Examining Committee for this thesis. The decision of the Examining Committee is by majority vote.

External Examiner: Dr. Michael Parsons
Adjunct Professor

Supervisor: Dr. David Blowes
Professor

Internal Members: Dr. Carol Ptacek
Professor

Dr. Dogan Paktunc
Adjunct Professor

Internal-external Member: Dr. Vassili Karanassios
Professor

Other Members: Dr. Richard Amos
Associate Professor

Author's Declaration

This thesis consists of material all of which I authored or co-authored: see Statement of Contributions included in this thesis. This is a true copy of the thesis, including any required final revisions, as accepted by my examiners.

I understand that my thesis may be made electronically available to the public.

Statement of Contributions

This thesis consists of a series of manuscripts that have been either published or prepared for submission to peer-reviewed journals. As the first author of each paper, I was primarily responsible for designing and conducting the experiments, collecting the samples that form the primary suite of samples for this research, analyzing and interpreting data, and writing manuscripts. Contributions for each chapter are summarized below:

Chapter 1: This chapter was written solely by Lianna Smith.

Chapter 2: Lianna Smith conceptualized the study with input from David Blowes. Lianna Smith conducted all data collection and data analyses under the supervision of David Blowes. Dogan Paktunc provided supervision and feedback for mineralogical characterization and XANES analyses. Lianna Smith wrote the manuscript, with review by David Blowes and Dogan Paktunc. Chapter 2 is modified from: Smith, L.J.D., Paktunc, D., Blowes, D.W. 2021. Trace elements in sulfides and release to porewater from sulfide oxidation in a historical waste-rock pile, Ontario, Canada. *Appl. Geochem.* 126, 14899. <https://doi.org/10.1016/j.apgeochem.2021.104899>.

Chapter 3: Lianna Smith and David Blowes conceptualized the study. Lianna Smith prepared the samples, collected the XANES data and interpreted the results. Dogan Paktunc provided feedback on the interpretations and conceptualized and calculated the uncertainty related to bond lengths as a proxy for distortion. Lianna Smith wrote the manuscript, with review by David Blowes and Dogan Paktunc.

Ch 4: Lianna Smith conceptualized the study with input from David Blowes. This study used samples collected for this thesis and archived samples for Ca-isotope analyses. Ca-isotope analyses were conducted by Chris Holmden at the University of Saskatchewan. Archived cation samples were obtained from the Diavik Waste Rock Research Project and the research program at Detour Lake Mine. The cation, anion and field parameters collected as part of the Diavik Waste Rock Research Program, the research program conducted at the Detour Lake Mine, and samples collected for this thesis were used for data analysis and PHREEQC modelling. Lianna Smith conducted the PHREEQC modelling on the datasets, conceptualized and performed the calculations, and analyzed all data. Lianna Smith wrote the manuscript, with feedback from Richard Amos and David Blowes.

Ch 5: Lianna Smith and Dogan Paktunc conceptualized this study with input from David Blowes. Lianna Smith prepared the samples and analyzed the data. MLA was conducted by David Grant at Memorial University. Dogan Paktunc provided feedback on the MLA results, and conceptualized the calculations of modal abundances of chalcopyrite, pentlandite and sphalerite from four-acid digestion concentrations. Derek Smith and Dogan Paktunc reviewed the XRD patterns for the presence of jarosite. Lianna Smith wrote the manuscript, with review by David Blowes and Dogan Paktunc.

Chapter 6: This chapter was written solely by Lianna Smith.

Abstract

The Detour Lake Mine is an open pit, greenstone-hosted gold mine in Ontario, Canada. Mining produced waste-rock piles that were constructed from 1983 – 1999. Redevelopment and expansion of the open pit required the excavation and relocation of the waste-rock piles, providing an opportunity to collect samples of waste rock that had been weathering *in situ* for 30 years. Samples of this weathered waste rock and extracted porewater were analyzed for solid-phase and aqueous geochemistry, characteristics of sulfide-mineral oxidation, stable calcium isotopes ($^{40/44}\text{Ca}$), and secondary minerals.

Characterization of weathered waste rock suggest the waste rock was potentially acid generating or of uncertain acid-generating potential and had depleted neutralization potential compared to unweathered samples. Porewater was circumneutral with measurable alkalinity. Mineralogical observations identified pyrrhotite as the sulfide mineral with greatest abundance and oxidation characteristics. Pyrite was present in abundances of approximately half that of pyrrhotite; chalcopyrite was present in lesser amounts and trace amounts of sphalerite and pentlandite were identified. Pyrrhotite was typically strongly altered, with intensity ranging from thick rims surrounding intact-cores to complete replacement by iron-(oxyhydr)oxides. Pyrrhotite, pyrite, chalcopyrite and pentlandite contained trace elements; no sphalerite grains were encountered during the measurements. Of the trace elements measured, Ni occurred in the highest concentrations in pyrrhotite, pyrite, and alteration rims associated with these sulfide minerals. Nickel concentrations in the associated porewater were elevated and sorption sites were calculated to be saturated, suggesting the oxidation of sulfide minerals released Ni that accumulated in porewater, with some attenuation by sorption to iron-(oxyhydr)oxide phases. Synchrotron studies identified Ni in alteration rims associated with an oxidizing pyrrhotite grain, in addition to phases consisting of mixed oxidation states of Fe and S.

An additional synchrotron study focused on iron speciation at 1 μm intervals across transects of three partially oxidized pyrrhotite grains to better understand how pyrrhotite oxidation proceeds. Grains were selected from an unweathered sample, a sample of intermediate weathering characteristics, and a sample with more advanced weathering characteristics. Analysis of the spectral features suggests that at the 1 μm scale oxidation products were mixtures of Fe-(oxyhydr)oxides, Fe-(hydroxy)sulfates, and Fe-depleted sulfides. Measurements on visually unoxidized pyrrhotite grains in the samples suggested variable bonding arrangements of Fe among the grains studied, either due to

the mineral structure or early-stage oxidation that were not apparent in other features of the spectra. The pyrrhotite standard and some ferrous iron [Fe^{2+}] standards had discordant spectral features; ratios of ferric iron [Fe^{3+}] to [$\text{Fe}^{2+} + \text{Fe}^{3+}$] calculated for the transect spots exhibited a clustering at a Fe^{3+} component of 0.2. Together, these results suggested oxidation from Fe^{2+} to Fe^{3+} may retain characteristics of the Fe^{2+} pre-edge spectral feature until a threshold component of Fe^{3+} is exceeded.

Existing datasets of porewater and solids chemistry were evaluated from Detour Lake Mine and Diavik Diamond Mine to attempt to discriminate the contributions of carbonate minerals and non-carbonate minerals to acid neutralization based on Ca concentrations. Diavik waste rock had low concentrations of calcite and Ca-bearing minerals, and periods with no measurable alkalinity in the drainage water, in contrast to Ca-rich Detour waste rock and porewater samples with measurable alkalinity. The porewater from both Diavik and Detour had higher molar proportions of Ca to major cations than the solids, indicating preferential release during weathering and/or preferential retention in the aqueous phase. The formation of the secondary Ca-bearing phase gypsum, but not Mg- or K-bearing phases, affected the molar proportions of Ca in porewater. Calculations based on measured alkalinity and concentrations of calculated dissolved inorganic carbon provided a lower bound for concentrations of dissolved Ca derived from carbonate-mineral dissolution. Results were consistent with expectations based on Diavik and Detour lithology and measured porewater alkalinity trends.

A small number of samples were analyzed for stable Ca isotopes. This is the first study believed to apply stable Ca-isotopes to mine-waste systems. No trends were discernable between the Ca-isotope values and alkalinity or ratios of major cations, but the dataset was small. Two-component mixing using assumed carbonate and non-carbonate endmembers appeared to over-ascribe Ca to carbonate minerals in the Diavik samples, indicating endmembers may not have been representative, and/or another mechanism was affecting porewater values. Mixing calculations could not be completed on the Detour samples because Ca-isotope values of the endmembers were lower than the porewater values, suggesting a confounding mechanism, likely gypsum precipitation/dissolution, affected the Ca-isotope ratios. Calculated fractionation factors were consistent with previously reported fractionation factors for gypsum.

Secondary minerals associated with sulfide-mineral oxidation were characterized by automated quantitative mineralogy (mineral liberation analysis, MLA). Grain sizes, modal abundances and mineral habits of gypsum produced by MLA suggested geochemical conditions were spatially and

temporally variable in the historical waste-rock pile. The secondary mineral jarosite was inferred to be present by MLA and by X-ray diffraction analysis, though porewater was calculated to be undersaturated with respect to this phase. Calculated mineral associations and grain habits produced by MLA suggested that jarosite formed in microenvironments associated with oxidizing sulfide minerals. MLA calculates elemental concentrations based on idealized mineral formulae in the database, and comparisons to results from four-acid digestions of solid samples revealed that the MLA results under-represented concentrations of some trace elements by an order of magnitude. Modal abundances provided by MLA and concentrations of trace elements measured by electron-probe microanalysis were used to calculate concentrations of trace elements in sulfide minerals and their alteration rims. Combining these techniques resulted in an increase of up to 170% (relative percent difference) of some trace elements compared to MLA, but concentrations remained lower than the four-acid digestion results. The discrepancy may be (i) an artefact of the MLA resolution, which may not capture mineral grains $< 1.5 \mu\text{m}$; (ii) the MLA sample size, which considers a much small number of particles compared to four-acid digestion; and/or (iii) the incorporation of trace elements as impurities in silicate minerals, which are digested by the four-acid method.

This research provided new insights into the complex processes of pyrrhotite oxidation that affect solid phase and aqueous phase geochemistry of mine-waste systems. Results of this research illustrate that integrating standard and novel bulk and microanalytical techniques will contribute to more robust predictive models of mine-drainage chemistry and, therefore, reduced environmental risk from mine drainage.

Acknowledgements

Funding for this research was provided by the Ontario Research Fund, Natural Sciences and Engineering Research Council of Canada (NSERC) through a Collaborative Research and Development Grant (Award CRDPJ 485334-15) awarded to D. Blowes and Detour Gold Corporation (now Agnico Eagle Mines Ltd.), and in-kind contributions from Agnico Eagle Mines Ltd. This research used resources of the Advanced Photon Source, a U.S. Department of Energy (DOE) Office of Science User Facility operated for the DOE Office of Science by Argonne National Laboratory under Contract No. DE-AC02-06CH11357. Research described in this thesis was performed at the Canadian Light Source, which is supported by the Canada Foundation for Innovation, Natural Science and Engineering Research Council of Canada (NSERC), the University of Saskatchewan, the Government of Saskatchewan, Western Economic Diversification Canada, the National Research Council of Canada, and the Canadian Institute of Health Research.

It is difficult to express how much I appreciate the patience, guidance, and technical knowledge provided by my supervisor, Dr. David Blowes, throughout my graduate student career. My sincerest thanks.

Thank you to Dr. Carol Ptacek for introducing me to the University of Waterloo, and always providing constructive advice and feedback.

I am grateful to Dr. Richard Amos and Dr. Dogan Paktunc for providing access to facilities and equipment at Carleton University and CanmetMINING, and for invaluable discussions, guidance and reviews.

I sincerely appreciate Dr. Michael Parsons and Dr. Vassili Karanassios for providing their time to review my thesis, providing insightful feedback, and participating in my thesis defense.

I wouldn't have been able to pursue this PhD without the support of Gord Macdonald of Diavik Diamond Mines. Thank you to Dave and Gord for the latitude to work at various latitudes.

I am very privileged to have worked with the dedicated, smart and genuinely nice people, past and current, in the research group and university, without whom this research would not have been possible: Zhongwen Bao, Jane Eagling, Krista Elena, David Hilger, Steve Holland, Ismail Hussain,

Julia Jamieson-Hanes, Lisa Kester, Corina McDonald, Brayden McNeill, Stephen Marshall, Eva Pakostova, Roberta Parigi, Jen Parks, Mark Steinepreis, Emily Saurette, Harish Veeramani, Alana Wang, and the co-op students, technicians, graduate students and post-docs I didn't meet, but who helped with my sample preparation, laboratory analyses, and administrative tasks. Thank you to the students and technicians who collected data for the Diavik Waste Rock Research Project and the samples at Detour Lake Mine. Special thank yous to Jeff Bain for your indispensable knowledge and always being willing to help, Mike Moncur for proving it could be done, David Wilson for your ongoing support, and Laura Groza and Joy Hu for your reliable analyses.

My immense gratitude to Sue Fisher.

Derek Smith at CanmetMINING was generous with his time, helping me with the SEM, XRD and sample preparation. Glenn Poirier at the University of Ottawa guided me on the electron probe. David Grant at Memorial University conducted the MLA analyses and Chris Holmden at the University of Saskatchewan analyzed the calcium isotope samples. Thank you to Jason Arnott and Sheila Thayer at Carleton University. I am grateful to Yongeng Hu, Tony Lanzirotti, Matt Newville, and Qunfeng Xiao for your technical expertise.

I am honoured to have had the support of old and new friends, colleagues, and communities around the world. Special mentions to Chantal, Erin, Helen, James, Katherine, Linda, Luke, Lyndon, Mika, Nat, Paul, Steve, CBS, DDMI, Fulton, Glen Park, ISM, ISK, Rosslyn, Urdaneta TLL, YK.

I am deeply grateful to my family for their unconditional love, support, and encouragement:

To my parents, Bill and Mary, and my sister, Colleen for instilling that I can do anything.

To Julia and Lara, who have no memory of me not as a student, and who are now old enough to recognize that graduating from “grade 33” is both funny and an accomplishment. You can do anything.

Finally, to Brian Post for providing me with your unwavering support as the grade levels ticked up.

Dedication

To my dad.

For my sake, let's hope this isn't your namesake.

Table of Contents

Examining Committee Membership.....	ii
Author’s Declaration	iii
Statement of Contributions.....	iv
Abstract	vi
Acknowledgements	ix
Dedication	xi
List of Figures	xvi
List of Tables.....	xxvi
Chapter 1 Introduction.....	1
1.1 Pyrrhotite oxidation in mining waste rock	1
1.1.1 Acid neutralization	2
1.1.2 Secondary minerals associated with pyrrhotite oxidation	5
1.1.3 Trace elements associated with pyrrhotite oxidation	6
1.2 Detour Lake Mine	7
1.3 Thesis structure.....	8
Chapter 2 Trace elements in sulfides and release to porewater from sulfide oxidation in a historical waste-rock pile, Ontario, Canada	10
2.1 Summary	10
2.2 Introduction	10
2.3 Experimental section	12
2.3.1 Site description	12
2.3.2 Sample collection and analyses	12
2.4 Results and discussion.....	15

2.4.1 Acid-base accounting	15
2.4.2 Mineralogical observations of sulfide oxidation characteristics	18
2.4.3 Microanalysis of sulfide minerals.....	19
2.5 Conclusions	28
Chapter 3 Fe K-edge XANES across oxidizing pyrrhotite grains from natural samples of mining waste rock.....	30
3.1 Summary	30
3.2 Introduction	30
3.3 Experimental section	32
3.3.1 Sample description	32
3.3.2 Standards	32
3.3.3 Fe K-edge data collection and analysis	33
3.4 Results and discussion.....	35
3.4.1 Standards	35
3.4.2 Transects across altered pyrrhotite grains	42
3.5 Conclusions	48
Chapter 4 Major ion chemistry and calcium isotopic composition of waste rock and porewater in calcite-dominant and calcite-depleted systems.....	51
4.1 Summary	51
4.2 Introduction	52
4.3 Experimental section	55
4.3.1 Site descriptions.....	55
4.3.2 Existing datasets	56
4.3.3 Solid samples: additional analyses	60

4.3.4 Solid samples: treatments for calcium-isotope analyses	60
4.3.5 Isotope analysis	61
4.4 Results and discussion.....	62
4.4.1 Major cations	62
4.4.2 Secondary minerals	64
4.4.3 Alkalinity.....	66
4.4.4 Calcium derived from carbonate-mineral dissolution: lower-bound calculations.....	67
4.4.5 $\delta^{44/40}\text{Ca}$ values of porewater	73
4.4.6 Porewater $\delta^{44/40}\text{Ca}$ values and ion ratios.....	73
4.4.7 Apportioning calcium to carbonate and silicate fractions using $\delta^{44/40}\text{Ca}$ values	75
4.5 Conclusions	81
Chapter 5 Secondary mineral formation and trace-element reservoirs in weathered waste rock:	
Integration of quantitative mineralogy and conventional mineralogical techniques.....	82
5.1 Summary	82
5.2 Introduction	82
5.3 Experimental section	84
5.4 Results and discussion.....	87
5.4.1 Modal mineralogy	87
5.4.2 Secondary sulfate minerals.....	89
5.4.3 Trace elements reservoirs	97
5.5 Conclusions	103
Chapter 6 Conclusions and contributions to science	
6.1 Summary of results.....	107
6.2 Contributions to science	109

References	112
Appendices	138
Appendix A Supplementary Material for Chapter 2	139
Appendix B Supplementary Material for Chapter 3.....	148
Appendix C Supplementary Material for Chapter 4.....	164
Appendix D Supplementary Material for Chapter 5	174

List of Figures

- Figure 2-1: (a) Site location of the Detour Lake Mine and (b) lithological distribution, historical pit outline and current pit outline (modified from BBA and SGS, 2014). 12
- Figure 2-2: Waste-rock samples collected from profile locations illustrating visual oxidation characteristics. Samples collected from top (beneath cover), middle and bottom at six locations across a transect approximately 150 m long. White notebook in photos measures 24×18 cm. 16
- Figure 2-3: (a) alkalinity (open squares) and porewater pH (solid grey circles) vs. the log of the saturation index (SI) of calcite, (b) porewater pH (solid grey circles) and concentration of SO_4 (solid black upward triangles) vs. $\log[\text{SI}]$ of calcite; (c) alkalinity (open squares) and porewater pH (solid grey circles) vs. $\log[\text{SI}]$ of amorphous $\text{Al}(\text{OH})_3$; (d) dissolved concentration of Al (solid black downward triangles) and pH (solid grey circles) vs. $\log[\text{SI}]$ of amorphous $\text{Al}(\text{OH})_3$. Vertical dashed lined in (a) and (b) at $\log[\text{SI}] = 0$ indicates saturation..... 18
- Figure 2-4: Sulfide oxidation characteristics in the historical samples with varying degrees of oxidation. Pyrrhotite grains in (a – d) in reflected light and pyrite grains in (e – f) as backscattered electron images. (a) completely altered pyrrhotite; (b) strongly altered with remnant pyrrhotite cores; (c) slightly to moderately altered pyrrhotite; (d) mostly intact pyrrhotite grain with minor alteration rim; (e) pyrite oxidation propagating along fractures; (f) pyrite grain with minor etch pits. 19
- Figure 2-5: Rows 1 – 3 are SEM/EDX mapping of selected weathered sulfide grains, illustrating elevated cobalt (Co), nickel (Ni) and copper (Cu) concentrations in the unaltered cores and alteration rims. Row 1: two altered pyrrhotite grains (upper left and lower right) and smaller chalcopyrite flecks (evident in Cu map, with gypsum evident in the sulfur (S) plot (absent in the iron (Fe) map; see Figure A-4). Row 2: moderately altered pyrrhotite grain. Row 3: moderately to strongly altered pyrrhotite (upper left) and a separate alteration rim (right). The dark center of the alteration rim evident in the third row suggests a sulfide grain was plucked during slide preparation. Row 4: μXRF mapping (at beamline 13-ID-E) of the same grain as in Row 3. The μXRF maps are rotated approximately 35° clockwise from the SEM/EDX maps. Scale bars represent $60 \mu\text{m}$. .. 21

- Figure 2-6: Nickel (Ni) and cobalt (Co) concentrations in historical and freshly blasted samples in (a) pyrrhotite grains and (b) pyrrhotite alteration rims, and (c) pyrite grains and (d) pyrite alteration rims. Co with ND measurements plotted at 1.5 ppm, half the LOD. Samples plotted by porewater pH: black filled circles = 8.1; grey filled circles = 7.8; black open circles = 7.4; grey open = 7.0; × = freshly blasted sample. 23
- Figure 2-7: (a) Saturation indices in log scale ($\log[\text{SI}]$) of goethite versus Ni:Fe molar ratios in pyrrhotite (“po”; circles), alteration rims (“rims”; triangles) and porewater (blue squares). (b) S:Fe molar ratios versus Ni:Fe molar ratios in alteration rims. Samples plotted by porewater pH: solid black symbols = 8.1; solid grey symbols = 7.8; open black symbols = 7.4; open grey symbols = 7.0; × = freshly blasted sample. Solid blue squares in (a) indicate porewater samples with corresponding EPMA measurements. Symbols plotted in (a) at median values and bars indicate 25th and 75th percentiles. 25
- Figure 2-8: Saturation indices in log scale ($\log[\text{SI}]$) of goethite versus Ni:Fe molar ratios in pyrrhotite (circles) and alteration rims (triangles) measured by EPMA, and PHREEQC-calculated molar ratios of Ni:Fe for Ni sorbed on alteration rims as ferrihydrite (green triangles). Samples plotted by porewater pH: solid black symbols = 8.1; solid grey symbols = 7.8; open black symbols = 7.4; open grey symbols = 7.0. Symbols for pyrrhotite and alteration rims are plotted as the median, and bars denote 25th and 75th percentiles..... 25
- Figure 2-9: Row 1: μXRF element maps of target pyrrhotite grain. Colour scale represents relative abundance by element, with red as highest concentration and blue as lowest. Row 2: XANES spectra for target spots identified in the element maps. Row 3: linear combination fitting (LCF) residual. Blue lines in Fe LCF residual indicate fit with only Fe-(oxyhydr)oxides and black line indicates fit that includes schwertmannite. Vertical dotted lines indicate K-edge energies. Standard spectra are provided in Figure A-6 and measured spectra plotted with LCF fits are presented in Figure A-7. 28
- Figure 3-1: Pre-edge peaks (baseline-subtracted) for Fe^{2+} and Fe^{3+} standards. Blue curves represent measured spectra, black dotted curves represent deconvoluted spectra. Vertical grey bars illustrate centroid energy (of main peaks). Fit statistics provided in Figure B-3. 39
- Figure 3-2: Calculated pre-edge centroid intensity (main peaks) vs. average standard deviations of the Fe-O bond lengths for Fe^{3+} minerals (circle symbols). Dashed line represents regression

line for Fe^{3+} minerals with equation: $[\text{centroid intensity}] = 0.037 + (1.19 \times [\text{standard deviation of Fe-O bond length}])$ with $R^2 = 0.84$. Included for information: Fe^{2+} minerals (square symbols) and $\text{FeSO}_4 \cdot 7\text{H}_2\text{O}^*$ (triangle symbol); $\text{FeSO}_4 \cdot 7\text{H}_2\text{O}^*$ plotted with the calculated pre-edge centroid intensity of the standard used in this study, at the bond length uncertainty of melanterite because of the poor-quality spectra of melanterite obtained in this study. References from which bond length uncertainty was calculated are provided in Table 3-2.....	41
Figure 3-3: Pre-edge centroid energy vs. (main peak) intensity of standards and transect spots for (a) grain 117, (b) grain 3M, (c) grain 4T, and (d) transect spots from all three grains.	42
Figure 3-4: XANES features at transect spots across partially oxidized pyrrhotite grains 117, 3M and 4T. μXRF maps of Fe in grain in (a) and reflected light images in (b) for each grain. ...	47
Figure 3-5: Pre-edge centroid energies vs. ratios of ferric iron to ferrous iron plus ferric iron ($\text{Fe}^{3+}/\Sigma\text{Fe}$) calculated from LCF fits of the pre-edge region (open circles), and the full spectrum (solid circles) for (a) grain 117, (b) grain 3M, (c) grain 4T and (d) the combined dataset. Pre-edge centroid intensities vs $\text{Fe}^{3+}/\Sigma\text{Fe}$ calculated from LCF fits of the pre-edge region (open squares), and the full spectrum (solid squares) for (e) grain 117, (f) grain 3M, (g) grain 4T, and (h) the combined dataset. Horizontal dashed line in all plots at $\text{Fe}^{3+}/\Sigma\text{Fe} = 0.2$	49
Figure 4-1: Locations of the Diavik Diamond Mine and the Detour Lake Mine.	56
Figure 4-2: Ternary plots for (a) Diavik and (b) Detour showing molar proportions of calcium (Ca), magnesium (Mg) and sodium plus potassium (Na + K). Molar proportions of calcium to the sum of major cations ($\text{Ca}/\Sigma\text{cations}$) vs. pH for (c) Diavik and (d) Detour. $\text{Ca}/\Sigma\text{cations}$ vs. measured alkalinity for (e) Diavik and (f) Detour. Note different y-axes scales in (e) and (f). Diavik waste rock (solid dark-grey diamonds), porewater (open light-grey diamonds), Detour waste rock (solid dark-grey circles) and porewater (open light-grey circles). Porewater samples analyzed for calcium isotopes are illustrated with blue outlines. Detour waste-rock samples with extracted porewater analyzed for calcium isotopes are illustrated with solid blue symbols. Note the x-axes in (c) – (f) in reverse order to correspond to Ca-axes of ternary diagrams.	63

Figure 4-3: Relationship between calcium concentrations as molar proportion ($\text{Ca}/\sum\text{cations}$) and the calculated saturation indices ($\log \text{SI}$) of the Diavik porewater dataset of (a) calcite, (b) gypsum and (c) jarosite; and for the Detour porewater dataset of (d) calcite, (e) gypsum, and (f) jarosite. Open grey symbols identify porewater values and open blue symbols identify samples analyzed for Ca isotopes. Data points at or above dashed horizontal line at $\log \text{SI} = 0$ are calculated to be (super)saturated with respect to the mineral phase. Samples with no measurable alkalinity are plotted at $\log \text{SI calcite} = -6$ for display. 65

Figure 4-4: Measured alkalinity, PHREEQC-calculated alkalinity, and PHREEQC-calculated dissolved inorganic carbon (DIC) concentrations for (a – c) the Diavik porewater dataset; and (d – f) the Detour porewater dataset. Open grey symbols indicate porewater samples, open blue symbols indicate samples analyzed for Ca-isotope values. Horizontal dashed line at $\text{pH} = 4.5$ and $\text{pH} = 6.3$ in all plots. Vertical dashed line in (b) at alkalinity concentration of 0 mmol L^{-1} as CaCO_3 67

Figure 4-5: (a) Diavik and (b) Detour datasets of Ca-molar proportion of cations ($\text{Ca}/\sum\text{cations}$) vs. the calculated proportion of dissolved Ca in porewater contributed by calcite dissolution ($\text{Ca}_{\text{cal-diss}}/\text{Ca}_{\text{pw}}$), and the calculated proportion of Ca from calcite in the total concentration of Ca ($\text{Ca}_{\text{cal-minl}}/\text{Ca}_{\text{sol}}$) in solid samples. (c) Diavik (e) Diavik dataset of pH vs. ($\text{Ca}_{\text{cal-diss}}/\text{Ca}_{\text{pw}}$). (e) Diavik and (f) Detour datasets of dissolved inorganic carbon (DIC) vs. $\text{Ca}_{\text{minl-diss}}/\text{Ca}_{\text{pw}}$. $\text{Ca}_{\text{minl-diss}}/\text{Ca}_{\text{pw}}$ indicates ratio calculated assuming calcite dissolution or dolomite dissolution. (g) Diavik and (h) Detour dataset of the calculated proportion of Ca from calcite or dolomite in the total concentration of Ca ($\text{Ca}_{\text{minl}}/\text{Ca}_{\text{sol}}$) in solid samples. Axes denoted $\text{Ca}_{\text{minl}}/\text{Ca}_{\text{sol}}$ indicates the ratio of carbonate calculated as $[\text{mol calcite}] [\text{kg waste rock}]^{-1}$, or as $[\text{mol dolomite}] [\text{kg waste rock}]^{-1}$ to the concentration of Ca as $[\text{mol Ca}] [\text{kg waste rock}]^{-1}$. Horizontal dashed line in (a) and (e) at a molar ratio of 1. Vertical dashed lines in (c) and (d) at $\text{pH} 4.5$ and 6.3 . Dotted lines in (e) and (f) are the regression lines for $\text{Ca}_{\text{cal-diss}}/\text{Ca}_{\text{pw}}$ vs. DIC for the various systems. Dashed horizontal lines at 1 indicate all Ca measured is attributable to carbonate-mineral presence (for solid samples), or dissolution (for aqueous samples) for this calculation approach. 72

Figure 4-6: Molar ratios of calcium (Ca) to (a) sodium (Na); (b) potassium (K); (c) magnesium (Mg); and sulfate (SO ₄).	74
Figure 4-7: $\delta^{44/40}\text{Ca}$ values as a function of (a) calculated molar proportion of calcium [Ca] in porewater attributed to alkalinity, based on calcite dissolution ($\text{Ca}_{\text{cal-diss}}/\text{Ca}_{\text{pw}}$) in log scale; (b) calcium concentrations as molar proportion ($\text{Ca}/\sum\text{cations}$); (c) calculated dissolved inorganic carbon (DIC) in mmol L^{-1} ; (d) Ca concentration; (e) log saturation index (log SI) of calcite; and (f) log SI of gypsum. For display purposes, samples with no measurable alkalinity are plotted at vertical grey dashed lines in (a) at 0.01 proportion Ca from alkalinity, in (c) at DIC concentration of 0.01 mmol L^{-1} , and in (e) at log SI of -6.5 . Vertical black dashed lines in (e) and (f) at log SI = 0 (saturation). Dotted lines in (b) and (c) are regression lines with R^2 of 0.62 and 0.94 ($P < 0.005$), respectively. Legend the same as in Figure 4-6.	76
Figure 5-1: (a) Site location of Detour Lake Mine and (b) local geology with original pit and expansion pit outline (modified from BBA and SGS, 2014).	84
Figure 5-2: Calculated mineral associations for altered Fe-sulfides, Ca-Fe-sulfate and yavapaiite (jarosite). Minerals with $<0.01 \text{ wt } \%$ modal abundance not included in the calculations.	91
Figure 5-3: MLA-produced grain images. (a) Typical gypsum habit in sample 2M with smallest d50; (b) typical gypsum habit in sample 4Mb with second smallest d50; (c) typical occurrence of Ca-Fe-sulfate in various grains and samples; (d) distributions and associations of jarosite in various grains and samples.....	92
Figure 5-4: Distribution of d50 values of (a) altered Fe-sulfides; (b) yavapaiite (jarosite); (c) Ca-Fe-sulfate; (d) gypsum. Top boxes (green fill) in each frame are data from historical samples, bottom boxes (blue fill) are from freshly blasted samples. Boxes represent 25 th and 75 th percentiles, with median line; whiskers represent 5th and 95th percentile.	95
Figure 5-5: Concentrations of trace elements provided by MLA compared to concentrations measured by four-acid digestion, and calculated concentrations using median and 75 th percentile concentrations measured by electron-probe micro analysis (EPMA) and applied to the MLA-provided modal mineralogies for pyrrhotite, pyrite, chalcopyrite, pentlandite and	

altered Fe-sulfides. Sphalerite excluded because MLA modal abundance considered an estimate and no sphalerite grains encountered during EPMA analysis. Recall that freshly blasted samples 117 and 119 had mafic to ultramafic lithologies, whereas the other freshly blasted samples had felsic lithologies. All concentrations in ppm of waste-rock fraction < 425 μm , i.e., $[\text{mg trace element}] [\text{kg} < 425 \mu\text{m fraction of waste rock}]^{-1}$ 105

Figure A-1: Ratios of neutralization potential (NP) to acid-generating potential (AP) (NP:AP) of samples from historical waste rock (samples) and freshly blasted waste rock (triangles). Lines at 1:1, 1.5:1 and 2:1 represent designations of acid-generating potential. Samples with NP:AP < 1:1 are typically designated “potentially acid generating”. Samples with 1:1 < NP:AP < 2:1 are typically designated “of uncertain acid-generating potential”. Samples with NP:AP > 2:1 are typically designated “non-acid generating.”. Detour Lake Mine designates samples with NP:AP > 1.5:1 as “non-acid generating”.	139
Figure A-2: Porewater concentrations of major ions and key trace elements.	140
Figure A-3: Saturation indices (SI) of key secondary phases calculated by PHREEQC.	141
Figure A-4: SEM/EDX maps of two altered pyrrhotite grains (upper left and lower right in each frame), and gypsum grains or coatings evident in the Sulfur and Calcium maps. Scale bar represents 60 μm	141
Figure A-5: Concentrations of trace metals measured by EPMA in pyrrhotite (“po”, filled grey circles), and pyrite (“py”, open grey circles), and measured in porewater (blue circles). Filled blue circles represent porewater samples with corresponding EPMA measurements of po and py, open blue circles represent porewater samples with no corresponding EPMA measurements. Grey circles plotted at “N/A fresh” on the x-axis represent EPMA measurements on po and py in the freshly blasted sample most similar to the historical samples. Dotted line in the As and Se plots identify the method detection limits for the aqueous samples.	142
Figure A-6: Standard spectra for (a) iron-XANES, (b) sulfur-XANES, and (c) nickel-XANES.	143
Figure A-7: Measured spectra of iron (Fe; blue lines); sulfur (S; yellow lines); and nickel (Ni, green lines) and linear combination fitting results (dotted lines).	144

Figure B-1: Diffractograms from reference materials collected with a Rigaku MiniFlex II Desktop X-ray diffractometer. (a) jarosite, (b) hematite, (c) goethite, (d) ferrihydrite, (e) schwertmannite, (f) marcasite, (g) magnetite. Data was collected over $3 - 80 2\theta^\circ$ with a step size of 0.05° and scan speed of $4.00^\circ \text{ min}^{-1}$. A copper anode tube X-ray source was used with a voltage of 30 kV and current of 15 mA. All materials were positively identified using the PDF4+ database and JADE Pro software (Materials Data, Inc., USA) Diffractograms from ferrihydrite and schwertmannite samples showed no evidence of crystalline transformation products and contained broad peaks aligned with PDF4+ database patterns 01-072-7673 and 00-047-1775, respectively. The marcasite sample was identified to contain a mixture of szomolnokite [$\text{FeSO}_4 \cdot \text{H}_2\text{O}$; 04-008-9680] and marcasite [04-008-8452]. Jarosite [04-015-8168], hematite [01-087-1166], goethite [04-015-2899], and magnetite [04-012-7038] were positively identified. The diffractogram from magnetite contained seven unidentified peaks at d-spacings of 6.96, 5.51, 3.50, 2.76, and 2.34 Å..... 150

Figure B-2: Normalized standard spectra for (a) pyrrhotite standard (dark line) and sample spots from sample 117, 3M and 4T used as sample-specific standards in linear combination fitting; labels denote sample (117, 3M, 4T) and separate grains in each sample (a – g); and (b) standard spectra. Dotted line in (b) indicates standard spectra collected in transmission mode, demonstrating over-absorption occurred for spectra collected in fluorescence mode, with the exception of $\text{FeSO}_4 \cdot 7\text{H}_2\text{O}$ 151

Figure B-3: (a) Baseline-subtracted pre-edge spectra (blue line), with deconvolution fit (dotted black line) for standard spectra collected in fluorescence mode. Vertical grey lines denote centroid energy of full pre-edge feature. Horizontal dashed lines represent the baseline. (b) Residual and fit parameters for pre-edge deconvolution using a baseline spline function and pseudo-Voigt components with a fixed 0.4 Gaussian fraction. 152

Figure B-4: (a) Baseline-subtracted pre-edge spectra (blue line), with deconvolution fit (dotted black line) for pyrrhotite spectra collected in fluorescence mode. Vertical grey lines denote centroid energy of full pre-edge feature. Horizontal dashed lines represent the baseline. (b) Residual and fit parameters for pre-edge deconvolution using a baseline spline function and pseudo-Voigt components with a fixed 0.4 Gaussian fraction. 153

Figure B-5: Successive melanterite spectra illustrating oxidation and dehydration during data collection.....	154
Figure B-6: Transects across pyrrhotite grains (a) 117, (b) 3M and (c) 4T. E0 energy values denoted by filled triangle symbols, white line energy values denoted by open triangles. Numbers indicate transect spot number.....	155
Figure B-7: Linear combination fitting results for transect spots across grain 117. Energy range of fit 7070 – 7220 eV.....	156
Figure B-8: Linear combination fitting results for transect spots across grain 3M. Energy range of fit 7070 – 7220 eV.....	157
Figure B-9: Linear combination fitting results for transect spots across grain 4T. Energy range of fit 7070 – 7220 eV.....	158
Figure B-10: Linear combination fitting results of the pre-edge region for transect spots across grain 117. Energy range of fit 7104 – 7119 eV.....	159
Figure B-11: Linear combination fitting results of the pre-edge region for transect spots across grain 3M. Energy range of fit 7104 – 7119 eV.....	160
Figure B-12: Linear combination fitting results of the pre-edge region for transect spots across grain 4T. Energy range of fit 7104 – 7119 eV.	161
Figure C-1: Ternary diagrams by waste-rock system for (a) Diavik waste rock and porewater and (b) Detour waste rock and porewater. Higher metasediment systems in the Diavik waste rock contain higher sulfur concentrations.....	165
Figure C-2: Ratios of K/Na and Mg/Na vs. Ca/Na for Diavik and Detour datasets. Open light-grey symbols indicate porewater samples, solid dark grey symbols indicate solid samples, blue open symbols indicate porewater samples analyzed for Ca-isotope values and solid blue symbols indicate solid samples analyzed for Ca-isotope values. Lines plotted at 1:1. Diavik solid samples were not exposed to ambient conditions prior to analysis and have no observable trend. Detour solid samples were recovered from <i>in situ</i> waste-rock pile and the distributions indicate increasing K/Na and Mg/Na ratios with increasing Ca/Na ratios, suggesting ongoing weathering.....	166

- Figure C-3: Time series for Diavik porewater samples collected from 2 m scale experiments and a 15 m scale experiment. Alkalinity and calcium (Ca) concentrations from experiments from 2007 to 2011 previously reported by Bailey (2013), Bailey et al. (2016) and Hannam (2012). Calculated saturation indices from 2007 – 2011 also reported but re-calculated for this study; re-calculated saturation indices (as log SI calcite and log SI gypsum) presented here. All data from 2012 to 2016 inclusive have not been previously published. Calcite saturation indices for samples with alkalinity = 0 mmol L⁻¹ as CaCO₃ are plotted at log SI calcite = -6. 167
- Figure C-4: Time series for Detour porewater samples collected from soil-water soliton samplers (SWSS) installed in WRS#4. Data previously reported by McNeill (2016). Concentrations of alkalinity and calcium (Ca) converted to mmol L⁻¹ for this study. Saturation indices of calcite and gypsum calculated for this study. 168
- Figure C-5: Calculated saturation indices of gypsum for (a) full Diavik porewater dataset (b) Diavik porewater samples with no measurable alkalinity; (c) Diavik porewater samples with measurable alkalinity. Samples with no measurable alkalinity had slightly higher proportion of samples calculated to be saturated with respect to gypsum (n = 18 of 401 samples), compared to samples with measurable alkalinity (n = 9 of 392 samples) 169
- Figure C-6: Diavik porewater datasets illustrating relationships between (a) and (b) calculated carbonate contributions and calculated dissolved inorganic carbon (DIC) (log scale for y-axis in (a), linear scale in (b)); pH and calculated DIC (log scale for x-axis in (c), linear scale in (d)); (e) pH and PHREEQC-calculated alkalinity; (f) pH and measured alkalinity, with inset illustrating samples with low measured alkalinity concentrations and pH > 5. Open grey symbols indicate porewater samples, open blue symbols indicate porewater samples analyzed for Ca-isotopes; open black symbols indicate porewater samples with pH < 4.5, but with measured alkalinity concentrations..... 170
- Figure C-7: Calculated regression curves for each of the five Diavik systems that comprise the full Diavik porewater dataset. (a) all five systems; (b) Systems 1UE and 1UW with lower sulfur component (note the change in scale from (a)); and (c) Systems 3UE , 3UW and CB with higher sulfur component (note the change in scale from (a)). Yellow series 3UE with grey label in (a) and (c) for clarity. 171

Figure D-1: Mineral associations with gypsum. Minerals with < 0.01 wt% modal abundances not included in association calculations. Y-axes scale (calculated association ratio) to 250.	175
Figure D-2: Mineral associations with Ca-Fe-sulfate. Minerals with < 0.01 wt% modal abundances not included in association calculations. Y-axes scale (calculated association ratio) to 250.	176
Figure D-3: Mineral associations with jarosite. Minerals with < 0.01 wt% modal abundances not included in association calculations. Y-axes scale (calculated association ratio) to 250.	177
Figure D-4: Mineral associations with altered Fe-sulfide. Minerals with < 0.01 wt% modal abundances not included in association calculations. Y-axes scale (calculated association ratio) to 250.....	178
Figure D-5: Mineral associations with pyrrhotite. Minerals with < 0.01 wt% modal abundances not included in association calculations. Y-axes scale (calculated association ratio) to 250.	179
Figure D-6: Sulfide mineral liberation calculated by mineral liberation analysis (MLA).	180

List of Tables

Table 2-1: Summary of nickel (Ni) and cobalt (Co) concentrations in pyrrhotite grains. Historical samples are identified by their porewater pH values. Non-detect (ND) values of Co were assigned 1.5 ppm and half the limit of detection (LOD) for mean calculations of concentrations and Ni:Co. A single Ni measurement in sample with pH 7.0 was < LOD and assigned a value of 54, half the LOD. Concentrations > LOD but < MDL are considered estimates and are in provided in parentheses for median and mean values. Ranges for Ni:Co ratios present the ratios calculated with Co concentrations > LOD, values in parentheses indicated the maximum Ni:Co when 1.5 ppm was assigned to Co concentrations < LOD, and the number of measurements with Co < LOD are noted.....	22
Table 2-2: Linear combination fitting results for Fe-, S- and Ni-XANES analyses at target spots illustrated in Figure 2-9. Standard spectra and sensitivity analyses are presented in Table A-1 through Table A-3.....	27
Table 3-1: E0, white line and pre-edge centroid (PEC) characteristics for standards in fluorescence mode.....	40
Table 3-2: Summary of Fe-O bond lengths and calculated standard deviations for Fe-O octahedra...	41
Table 3-3: Linear and second order regressions for pre-edge centroid energies and ratios of ferric iron to ferrous iron plus ferric iron ($\text{Fe}^{3+}/\Sigma\text{Fe}$) calculated from linear combination fitting (LCF) best fits of the full energy XANES spectra (7070 – 7220 eV) , and separately the pre-edge energy range of the XANES spectra (7104 – 7119 eV) P < 0.001 for all regressions. C [eV] denotes centroid energy.	50
Table 4-1: Measured values of pH, alkalinity and dissolved calcium [Ca], and calculated saturation indices of calcite and gypsum for the porewater samples analyzed for Ca isotopes in this study. Data with * denotes data reported or presented in referenced study; reference with † indicates data presented in the supplementary material. Data with no symbols indicate this study is the first to present the value.	58
Table 4-2: Standard reference material from the National Institute of Standards and Technology measured during sample analyses.....	61
Table 4-3: Descriptions of solid samples and measured values of $\delta^{44/40}\text{Ca}$	78

Table 4-4: Two-component mixing results for the Diavik samples. The $\delta^{44/40}\text{Ca}$ value (-3.84 ‰) from four-acid digestion sample T1-pl-4a was used as the silicate value and the $\delta^{44/40}\text{Ca}$ value (-0.92 ‰) from the acetic leach sample T1-aa was used as the carbonate value. Calculated silicate and carbonate components from $\text{Ca}_{\text{al-diss}}/\text{Ca}_{\text{pw}}$ are summarized for comparison.....	80
Table 4-5: Fractionation factors ($\Delta^{44/40}\text{Ca}$) for the three Detour samples with measured values of for porewater, acetic acid leached solids and four-acid digested solids.	80
Table 4-6: Apportioned calcium (Ca) to soluble mineral phases in acetic acid leach based on magnesium [Mg], sulfur [S] and Ca concentrations.	80
Table 5-1: MLA-derived modal mineralogy for key minerals in wt%. “Qtz-plg-mix” denotes a mixture of quartz and plagioclase and was not included in the database for all MLA analyses. Gypsum was not included for sample 119. MLA-labeled mineral yavapaiite has been interpreted to occur in the samples as jarosite (See Section 3.2.1.3). Bulk chemical compositions for major elements are provided in Appendix D. Freshly-blasted samples 117 and 119 exhibited mafic to ultramafic lithology, whereas the remaining freshly blasted samples exhibited felsic lithology.	88
Table 5-2: Carbon [C] and sulfur [S] concentrations calculated by mineral liberation analyzer (MLA) and measured by induction furnace (IF). “n.a.” denotes not analyzed.	89
Table 5-3: MLA- calculated assay based on assigned mineral formulae vs. trace elements measured by four-acid digestion. Concentration of the trace elements zinc [Zn], selenium [Se], copper [Cu], cobalt [Co], nickel [Ni], and arsenic [As]. The detection limit for Se was 2.2 ppm. “n.a.” denotes the sample was not analyzed by four-acid digestion. All concentrations in ppm.	103
Table 5-4: Abundances of sphalerite, chalcopyrite and pentlandite based on zinc, copper and nickel concentrations, respectively, measured by four-acid digestion. “n.a.” denotes the sample was not analyzed by four-acid digestion.....	104
Table 5-5: Concentrations of selenium [Se], cobalt [Co] and arsenic [As] measured by electron-probe microanalysis (EPMA) applied to modal abundances of pentlandite and chalcopyrite calculated by four-acid digestion (4AD) concentrations. Includes contributions from	

pyrite, pyrrhotite and altered Fe-sulfide calculated based on MLA modal abundance.
 “n.a.” denotes sample not analyzed by four-acid digestion. All concentrations in ppm of waste-rock fraction < 425 μm , i.e., $[\text{mg trace element}] [\text{kg} < 425 \mu\text{m fraction of waste rock}]^{-1}$ 106

Table A-1: Sensitivity analyses for linear combination fitting (LCF) for X-ray absorption near edge spectra of iron (Fe-XANES). The % improvement in fit statistics compares the LCF combination in the previous column for the measured spot. “N.I.” in schwertmannite row indicates “not included” 145

Table A-2: Sensitivity analyses for linear combination fitting (LCF) for X-ray absorption near edge spectra of sulfur (S-XANES). The % improvement in fit statistics compares the LCF combination in the previous column for the measured spot. Grey font represents insufficient improvement in fit statistic to include phases < 5%. 146

Table A-3: Sensitivity analyses for linear combination fitting (LCF) for X-ray absorption near edge spectra of nickel (Ni-XANES). The % improvement in fit statistics compares the LCF combination in the previous column for the measured spot. Grey font represents insufficient improvement in fit statistic to include to include phases < 5%. 147

Table B-1: Pre-edge centroid energies and intensities for standard spectra collected in fluorescence mode and transmission mode 162

Table B-2: References for data used to calculate standard deviation of Fe-S/O bond distances 163

Table C-1: Electron probe microanalysis (EPMA) results for carbonate grains in weathered and fresh waste-rock samples from Detour Lake Mine. Reported as atomic proportion based on three oxygen molecules 172

Table C-2: Linear regressions for the calculated minimum proportion of calcium derived from calcite and dolomite dissolution ($\text{Ca}_{\text{cal-diss}}/\text{Ca}_{\text{pw}}$ or $\text{Ca}_{\text{dol-diss}}/\text{Ca}_{\text{pw}}$, respectively) to the calculated dissolved inorganic carbon (DIC) concentrations for each of the Diavik waste-rock systems, and the Detour waste rock systems. 173

Table D-1: Trace sulfide modal mineralogies calculated from four-acid digestion concentrations. Calculation verifications using MLA-provided pyrrhotite, pyrite, gypsum and jarosite modal mineralogies compared to sulfur [S] concentrations measured by induction

furnace [IF]. All concentrations in wt%. Modal mineralogies <0.01 wt %, presented in italics, are considered estimates but were maintained at MLA-reported values for calculations. Jarosite* indicates modal mineralogies taken from the yavapaiite modal mineralogies, with the jarosite mineral formula applied. “n.a.” denotes “not analyzed”.

..... 181

Table D-1: MLA-calculated assay for carbon [C], sulfur [S], and the major cations associated with silicate minerals in the samples in this study: calcium [Ca], sodium [Na], potassium [K], iron [Fe], magnesium [Mg], silicon [Si], and aluminum [Al]. 184

Table D-2: Whole rock analysis [WRA] of the major cations associated with silicate minerals in the samples in this study: calcium [Ca], sodium [Na], potassium [K], iron [Fe], magnesium [Mg], silicon [Si], and aluminum [Al]. WRA results converted from reported as oxides (wt%) to elemental concentrations for direct comparison to MLA-calculated assay. “n.a.” denotes not analyzed. 185

Table D-3: Results of whole rock analysis by lithium metaborate fusion with ICP-finish. Conducted by SGS (Burnaby, Canada), method code ICP95A. 186

Table D-4: Results of four-acid digestion conducted at AGAT Laboratories (Mississauga, ON), with analysis by ICP-MS and ICP-OES at the University of Waterloo. 187

Table D-5: Trace-element concentrations in MLA mineral formulae, and calculated trace element concentrations from EPMA measurements (as median values) applied to MLA mineral abundance. Median EPMA concentrations from sample 117 was applied to MLA samples 117 and 119; EPMA concentrations from 090 was applied to 090, 223, 224 and 25-26; and the median EPMA concentrations from all historical samples analyzed by EPMA (2M, 3B, 4T, 5M) were applied to the historical samples 2M, 3B, 3M, 3T, 4Mb, 4T, 5B, 5M and 5T analyzed by MLA. All concentrations in ppm of waste-rock fraction < 425 µm– i.e., [mg trace element] [kg < 425 µm fraction of waste rock]⁻¹. Sphalerite concentrations are considered estimates because sphalerite modal abundances were < 0.01 wt% in all samples. Cells with “-” indicate measurements were non-detect. * denotes sphalerite abundances considered estimates. 188

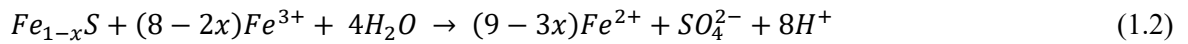
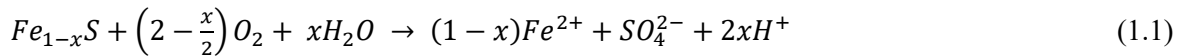
Chapter 1

Introduction

1.1 Pyrrhotite oxidation in mining waste rock

Waste rock produced during mining is commonly stored subaerially in large, heterogeneous waste-rock piles. Coupled physical and biogeochemical processes influence the weathering of sulfide minerals within the waste rock. Microbially-mediated oxidation of the sulfide minerals releases acidity [H^+], sulfate [SO_4], iron [Fe], and any trace-element components of the sulfide minerals (Nordstrom, 1982; Nordstrom and Southam, 1997; Blowes et al., 2003; Schippers 2004; Lindsay et al., 2015). The release of oxidation products to drainage water can be persistent and deleterious to the receiving environment (Nordstrom et al., 2000; Moncur et al., 2005; Byrne et al., 2010; Luís, et al., 2013; Bird, 2016; Cánovas et al., 2021; Moreno-González et al., 2022).

Pyrite [FeS_2] and pyrrhotite [$Fe_{1-x}S$] are the two most common sulfide minerals in mining waste rock. The oxidation of pyrite and pyrrhotite can proceed by a number of microbially-mediated and/or mineral-catalyzed pathways (Blowes et al., 2003). Pyrite and pyrrhotite oxidation by atmospheric oxygen [O_2] can be described by a simplified series of reactions (Nordstrom, 1982; Jambor, 2003; Nordstrom et al., 2015). Pyrrhotite can be oxidized by oxygen [O_2] (Equation 1.1), or ferric iron [Fe^{3+}] (Equation 1.2). At $pH < 3$ and in the presence of O_2 , the ferrous iron [Fe^{2+}] produced in Equation 1.1 can oxidize to Fe^{3+} (Equation 1.3) and perpetuate the reaction in Equation 1.2. At $pH > 3$, Fe^{3+} precipitates as Fe^{3+} -oxyhydroxide (e.g., ferrihydrite [nominally $5Fe_2O_3 \cdot 9H_2O$], represented as $Fe(OH)_3$), releasing additional H^+ (Equation 1.4).



Reactions described by Equations 1.1 and 1.2 may not proceed to completion, producing intermediate products of polysulfides [S_n^{2-}], elemental sulfur [S^0], Fe-depleted phases, Fe-(oxyhydr)oxides, Fe-hydroxysulfates, and possibly excess negative charge (Steger, 1982; Mycroft et al., 1995; Becker et al., 1997; McGregor et al., 1998; Thomas et al., 1998, 2001; Janzen et al., 2000;

Moncur et al., 2009; Harries et al., 2013; Langman et al., 2015; Nordstrom et al., 2015; Steinepreis, 2017; Smith et al., 2021; Bao et al., 2022). The production of intermediate products during oxidation and the higher rate of oxidation of pyrrhotite compared to pyrite have been attributed to the influence of crystal structure and vacancies (Pratt et al., 1994; Becker et al., 1997; Janzen et al., 2000; Jambor, 2003; Belzile et al., 2004; Harries et al., 2013). Pyrrhotite has a NiAs crystal structure (Carpenter and Desborough, 1964; Morimoto et al., 1970; Becker et al., 1997; Jin et al., 2021). Depending on stoichiometry, pyrrhotite can form in monoclinic or hexagonal crystal systems; more Fe-deficient structures are monoclinic and less Fe-deficient structures are hexagonal (Fleet, 1970; Belzile et al., 2004). The non-stoichiometry arises from ordered Fe vacancies (Tokonami et al., 1972; Pierce and Buseck, 1994; Jin et al., 2021), and these vacancies cause strong ferromagnetic behaviour in monoclinic pyrrhotite (Wang and Salverson, 2005). Ferric iron provides thermodynamic stability to the lattice (Tokonami et al., 1972; Pratt et al., 1994; Becker et al., 1997) and may facilitate rapid electron exchange with Fe^{2+} within the bulk solid (Pratt et al., 1994).

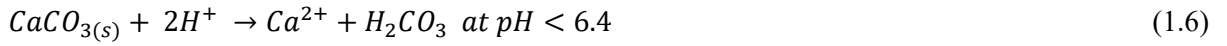
The oxidation model suggests sulfide oxidation is diffusion-limited at the grain scale, with the O_2 or Fe^{3+} oxidant diffusing to the pyrrhotite grain edge where oxidation occurs (Mycroft et al., 1995; Pratt and Nesbitt, 1997). As oxidation proceeds and reaction rims thicken, the rate of sulfide oxidation is affected; this process has been described conceptually and mathematically by the shrinking core model (Levenspiel, 1972; Cathles, 1979; Davis et al., 1986; Wunderly et al., 1996; Mayer et al., 2002, 2003;).

Pyrrhotite and pyrrhotite oxidation products include species containing either or both of Fe^{2+} and Fe^{3+} . Iron oxidation states, bonding arrangements and coordination geometry have been identified by pre-edge features of spectra collected by synchrotron X-ray absorption spectroscopy, particularly X-ray absorption near edge spectra (XANES) at the Fe K-edge (White and McKinsty, 1966; Srivastava and Nigam, 1973; Shulman et al., 1976; Waychunas et al., 1983; Dräger et al., 1988). Studies on silicate glasses, natural minerals, mechanical mixtures of minerals, and soil samples successfully estimated Fe^{2+} and Fe^{3+} contributions from the pre-edge spectral features (Wilke et al., 2001; Berry et al., 2003; Farges et al., 2004; Prietzel et al., 2007; Cottrell et al., 2009; Fiege et al., 2017). No studies of the pre-edge features of Fe K-edge XANES spectra of oxidizing or partially-oxidized sulfide grains have been identified.

1.1.1 Acid neutralization

Acidity produced by pyrrhotite oxidation (Equations 1.1, 1.2 and 1.4) can be neutralized by carbonate-, (hydr)oxide-, and silicate-mineral dissolution, though the dissolution of these minerals occurs at different rates (Jambor, 2003). Calcite [CaCO_3] is typically the most important mineral to

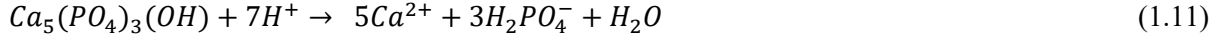
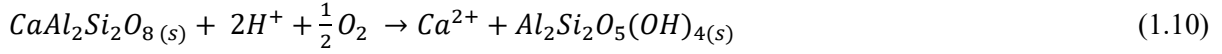
provide neutralization in mine-waste systems because it has a high solubility and rapid dissolution kinetics in acidic solutions at ambient temperatures (Plummer et al., 1978; Plummer and Busenberg, 1982; Sjöberg and Rickard, 1984), and is common in crustal rocks and ore deposits (White et al., 1999, 2005; Seal and Hammarstrom, 2003). Dolomite [$\text{CaMg}(\text{CO}_3)_2$] is also considered fast dissolving and important in neutralizing H^+ produced by sulfide oxidation (Paktunc 1999; Jambor, 2003). Based on solution pH and dictated by carbonate equilibria, the dissolution of calcite neutralizes one or two moles of H^+ produced by sulfide oxidation (as sulfuric acid [H_2SO_4]). Calcite dissolution releases one mole of Ca (as aqueous species Ca^{2+}), regardless of carbonate species produced (Equations 1.5 and 1.6).



Carbonic acid, [H_2CO_3] produced in the reaction described by Equation 1.6, is in equilibrium with dissolved CO_2 [$\text{CO}_{2(aq)}$], and dissolved CO_2 is in equilibrium with CO_2 gas [$\text{CO}_{2(g)}$] (Equations. 1.7 and 1.8). The measurement of $\text{CO}_{2(g)}$ within waste-rock piles can provide insight into acid neutralization by carbonate-mineral dissolution (Amos et al., 2009, 2015).



Concurrent to calcite dissolution, the dissolution of (hydr)oxide and chemical weathering of silicate minerals also act to neutralize acid produced by sulfide oxidation (Jambor, 2003). The progression from carbonate-dominant, through (hydr)oxide-dominant to silicate-dominant neutralization produces a series of pH plateaus as the most favorable phase is depleted (Blowes and Ptacek, 1994). Dissolving carbonate minerals (e.g., Equations 1.5 – 1.8) maintains porewater pH in the range of 6.5 to >7.5 (Blowes and Ptacek, 1994; Lindsay et al., 2009). When available carbonate minerals are exhausted, secondary $\text{Al}(\text{OH})_3$ (Equation 1.9), formed during the carbonate-dissolution phase, dissolves and maintains pH from 4.0 – 4.3. When $\text{Al}(\text{OH})_3$ is consumed, secondary $\text{Fe}(\text{OH})_3$ dissolves at pH 3.5 or lower (analogous to Equation 1.9; Blowes and Ptacek, 1994). When these available phases are consumed, silicate-mineral dissolution becomes the dominant mechanism to neutralize acidity (e.g., Equation 1.10), including by congruent or incongruent chemical weathering, or complete dissolution (Blowes and Ptacek, 1994).



The forward reaction in Equation 1.9 represents the formation of a secondary aluminum hydroxide such as gibbsite $[Al(OH)_3]$, or an amorphous $Al(OH)_3$ phase, and the reverse reaction represents the dissolution of the hydroxide solid to neutralize acidity; $Fe(OH)_3$ formation and dissolution is analogous. Equation 1.10 illustrates the chemical weathering by hydrolysis of the plagioclase Ca-endmember anorthite $[CaAl_2Si_2O_8]$ to kaolinite $[Al_2Si_2O_5(OH)_4]$, which consumes H^+ and releases Ca. Phosphate minerals, particularly apatite [as hydroxyapatite $[Ca_5(PO_4)_3(OH)]$], can consume H^+ and release Ca and phosphate (e.g., as $H_2PO_4^-$) through a sequence of chemical reactions, which can be described by the overall reaction in Equation 1.11 (Dorozhkin, 2012; Langman et al., 2019; Sherlock et al., 1995).

The dissolution of carbonate, (hydr)oxide, silicate, and phosphate minerals to neutralize acidity produced by sulfide oxidation affects the pH of the porewater and drainage from mine waste, which in turn is a control on the formation of secondary minerals and trace element mobility.

Measurements of stable Ca isotopes have been applied to several riverine studies to apportion the contributions of carbonate and silicate minerals (Hindshaw et al., 2013; Moore et al., 2013; Jacobson et al., 2015; Lenh et al., 2017). Of the six stable calcium isotopes ^{40}Ca and ^{44}Ca are the most abundant in nature, at 96.98% and 2.056%, respectively (DePaolo 2004). Measurements of $^{44}Ca/^{40}Ca$, (reported in delta notation relative to seawater in per mil units (‰); Equation 1.12) on various lithologies and minerals illustrate a range of $\delta^{44/40}Ca$ values (Ryu et al., 2011; Jacobson et al., 2015). The formation of gypsum and calcite has been shown to preferentially incorporate the isotopically lighter (^{40}Ca) isotope (Lemarchand et al., 2004; Tipper et al., 2006; Tang et al., 2008; Brown et al., 2013; Nielsen and DePaolo, 2013; Harouaka et al., 2014). No studies applying stable Ca isotopes to mine-waste systems have been identified, but measurements of stable Ca isotopes may be applicable to mine-waste systems to distinguish calcite and silicate dissolution, and the effect of secondary Ca-bearing mineral formation and/or dissolution on aqueous chemistry.

$$\delta^{44/40}Ca = \left(\frac{(^{44}Ca/^{40}Ca)_{sample}}{(^{44}Ca/^{40}Ca)_{seawater}} - 1 \right) \times 1000 \quad (1.12)$$

1.1.2 Secondary minerals associated with pyrrhotite oxidation

The series of Fe-bearing alteration products from pyrrhotite can include Fe-deficient sulfides Fe_2S_3 , and FeS_2 (as marcasite) (Mycroft et al., 1995). The more common Fe-(oxyhydr)oxides and Fe-hydroxysulfates that can form include goethite [$\alpha\text{-Fe}(\text{OOH})$], ferrihydrite, lepidocrocite [$\gamma\text{-Fe}(\text{OOH})$], schwertmannite (e.g., $[\text{Fe}_8\text{O}_8(\text{OH})_{8-2x}, \text{SO}_4]_x \cdot n\text{H}_2\text{O}$, $1 < x < 1.75$); Schoepfer and Burton, 2021), and jarosite [$\text{KFe}_3(\text{SO}_4)_2(\text{OH})_6$] (Nordstrom et al., 2015). Of these secondary Fe-minerals, goethite is the most common mineral present in unsaturated zones (Jambor, 1994). The poorly crystalline ferrihydrite can form from direct precipitation (Jambor, 2003), and transform into goethite at $\text{pH} < 7$ and/or hematite [Fe_2O_3] at $\text{pH} 7 - 8$ (Schwertmann and Murad, 1983; Jambor and Dutrizac, 1998). Schwertmannite is typically fine-grained ($< 1.5 \mu\text{m}$; Dold and Fontboté, 2011) and metastable, transforming to goethite at $\text{pH} > 5$ (Schwertmann and Carlson, 2005). Jarosite formation is more typical in acidic mine-waste environments, forming at slightly lower pH values than schwertmannite (Jambor, 1994; Dutrizac and Jambor, 2000; Jamieson et al., 2005; Dold and Fontboté, 2011), but it has also been documented in mine waste with circumneutral porewater (Dockrey et al., 2014). Jarosite associated with mining wastes is typically fine-grained (e.g., generally $< 2 \mu\text{m}$; Desborough et al., 2010). Jarosite occurs as coatings or pseudomorphs of Fe-sulfide minerals in oxidized sulfide deposits (Dutrizac and Jambor, 2000; Jamieson et al., 2005); directly on oxidizing pyrrhotite (documented in laboratory experiments; Bhatti et al., 1993); and as a precipitate from supersaturated porewater in mine-waste systems (Alpers et al., 1989; Bigham and Nordstrom, 2000). Direct precipitation from porewater may be limited by kinetic barriers (Alpers et al., 1994). Due to structural defects, jarosite can transform to Fe-(oxyhydr)oxides, including goethite or hematite (Swayze et al., 2008; Lindsay et al., 2015). The secondary Fe-hydroxysulfate minerals can be a source of stored acidity, dissolving or transforming under changing geochemical conditions to release acidity. For example, the transformation of jarosite to goethite or hematite releases 3 mol H^+ per mol of jarosite, and the transformation of schwertmannite to goethite releases 2 – 6 mol of H^+ per mol of schwertmannite, depending on the schwertmannite formula (Dold and Fontboté, 2011; Lindsay et al., 2011).

In addition to the secondary Fe-(oxyhydr)oxides and Fe-hydroxysulfates, the Ca-sulfate mineral gypsum [$\text{CaSO}_4 \cdot 2\text{H}_2\text{O}$] is a common secondary mineral in waste-rock and tailings systems (Jambor, 1994). Gypsum can form in acidic and circumneutral mine-waste environments, and in stream channels impacted by mine drainage (Blowes et al., 1991, 2003; Jambor, 1994; Hammarstrom et al., 2005; Nordstrom 2011a). The formation of gypsum acts as a control on SO_4 concentrations produced by sulfide oxidation and Ca released by carbonate-mineral dissolution and/or silicate-mineral weathering (Equation. 1.2, 1.5 – 1.8, 1.10; Blowes et al., 2003). Gypsum can form large grains (e.g.,

> 1mm; Jambor 1994) from direct precipitation (Jambor 1994); cementing grains (Jambor 1994); and over-growths on calcite [CaCO_3] grains, which retards calcite dissolution (Booth et al., 1997; Al et al., 2000; Dubrovsky et al., 2000; Wilkins et al., 2001; Offeddu et al., 2015).

1.1.3 Trace elements associated with pyrrhotite oxidation

The Fe lattice in pyrrhotite can host impurities as Fe substitutions, or interstitial or admixed inclusions (Sakkopoulous et al., 1986). In pyrrhotite, nickel [Ni], cobalt [Co] and copper [Cu] are the most common impurities and can occur in ppm to wt% abundances (Arnold, 1967; Sakkopoulous et al., 1986; Paktunc et al., 1999; Becker et al., 2010; Smith et al., 2021). Nickel, Co and Cu can substitute in solid solution for Fe in the pyrrhotite lattice (Arnold and Reichen, 1962; Naldrett et al., 1967; Becker et al., 2010). Other trace elements measured in samples of natural pyrrhotite include antimony [Sb], arsenic [As], bismuth [Bi], cadmium [Cd], indium [In], iridium [Ir], lead [Pb], manganese [Mn], osmium [Os], selenium [Se], silver [Ag], tellurium [Te], and zinc [Zn] (Arnold and Reichen, 1962; Paktunc et al., 1990; Janzen et al., 2000; Vukmanovic et al., 2014; Smith et al., 2021). Commonly associated with pyrrhotite is pentlandite $[(\text{Fe},\text{Ni})_9\text{S}_8]$, which may exsolve during magmatic crystallization or metamorphism and form lamellae or fine grains within pyrrhotite (Naldrett et al., 1967; Cowden and Archibald, 1987; Vukmanovic et al., 2014). Similarly, the oxidation of other sulfide minerals release trace elements contained as impurities or as part of the mineral-forming components. In addition to pyrrhotite, the minerals pyrite, chalcopyrite $[\text{CuFeS}_2]$, arsenopyrite $[\text{FeAsS}]$, pentlandite, sphalerite $[(\text{Zn},\text{Fe})\text{S}]$, and galena $[\text{PbS}]$ are sulfide minerals commonly found in waste rock.

Trace elements incorporated into sulfide minerals are released to porewater when sulfide minerals oxidize. In addition, non-sulfide minerals in the mineral assemblage can contain trace elements, which can be released when these minerals weather (Nordstrom, 2011a). The mobility of the trace elements contained in various minerals depends on mineral reactivity, and hydrologic and geochemical conditions, particularly pH and redox potential (Jambor, 2003; Nordstrom, 2011a; Lindsay et al., 2015). At acidic pH values, metals such as aluminum [Al], Fe, Cd, Co, Cu, Mn, Ni, Pb and Zn can remain dissolved in high concentrations (e.g., Blowes et al., 1991; Alpers et al., 1992; Heikkinen et al., 2009; Nordstrom, 2011a,b). At circumneutral pH weakly hydrolyzing metals including Cd, Fe^{2+} and Ni, Zn, and metal(loid)s that form oxyanions, including As, molybdenum [Mo], Sb, Se, and U can remain in solution at elevated concentrations (e.g., Heikkinen et al., 2009; Lindsay et al., 2009; Nordstrom 2011b; Moncur and Smith, 2012; Lindsay et al., 2015; Sharafi et al., 2018).

The mobility of trace elements is affected by pH- and redox-dependent substitution, sorption and/or (co-)precipitation with secondary Mn-, Al- and Fe-(oxyhydr)oxides, carbonates, hydroxysulfates, phosphates, sulfides, and organic matter (McKenzie, 1980; Bruemmer et al., 1988; Cornell, 1991; McGregor et al., 1998; Scheinost et al., 2001; Lee et al., 2002; Manceau et al., 2007; Boujelben et al., 2008; Du Laing et al., 2009; Nordstrom, 2011a; Lindsay et al., 2015; Bao et al., 2021; Parigi et al., 2022). Sorption of As, Cd, Cr, Cu, Ni, Mn, Mo, Sb, and Zn to Fe-(oxyhydr)oxide and/or Fe-hydroxysulfate minerals has been identified or inferred by chemical extractions and/or electron-probe microanalyses of solid samples from mine tailings and waste rock (McGregor et al., 1998; Gunsinger et al., 2006; Smuda et al., 2007; Heikkinen et al., 2009; Moncur et al., 2009; Plante et al., 2010; Dold and Fontboté, 2011; Vriens et al., 2019; Cappuyns et al., 2021). Sorption of Co and Ni to Fe-(oxyhydr)oxides associated specifically with pyrrhotite oxidation in waste-rock samples has been identified by electron-probe microanalyses and/or synchrotron studies (Langman et al., 2015; Smith et al., 2021). Secondary Fe-(oxyhydr)oxides and Fe-hydroxysulfates can remove trace elements from porewater, however this reservoir may be transient if changing geochemical conditions promote the dissolution of the secondary phases and the release of associated trace elements.

Sulfide oxidation, the formation of secondary minerals, and the mobility of trace elements are affected by complex, interdependent geochemical processes that evolve over time. A better understanding of sulfide oxidation, the formation and stability of secondary minerals, the release and attenuation of trace elements, and the relative contribution of carbonate and silicate minerals to neutralizing acidity would improve predictive capabilities for the long-term geochemical behaviour of mining waste. Improved models inform management strategies, which can minimize negative environmental impacts of mining waste.

1.2 Detour Lake Mine

Detour Lake is an orogenic greenstone-hosted lode-gold deposit located in the Abitibi Greenstone Belt of eastern Ontario, Canada. During open-pit operations from 1983 – 1999 four waste-rock piles were constructed and covered with a single-layer cover (McNeill et al., 2020). Redevelopment of the mine commenced in 2006 and expansion of the open pit required the excavation and relocation of the historical waste-rock piles. The excavation of these piles provided an opportunity to collect waste-rock and porewater samples that had been weathering *in situ* for decades (Cash et al., 2014; Steinepreis, 2017; McNeill et al., 2020; Smith et al., 2021). The deposition history of the waste-rock piles was not documented. Lithologies at Detour Lake Mine exhibit typical greenstone mineralogy from regional metamorphism to lower amphibolite facies, hydrothermal alteration, and felsic

intrusives (Oliver et al., 2012). Samples collected from one of these historical waste-rock piles form the basis for this thesis.

1.3 Thesis structure

This thesis is presented as a series of four research papers that examine processes associated with pyrrhotite oxidation at the mineral-grain scale in porewater and solids samples. As a consequence of the research-paper format, there is some repetition in the concepts and background information presented in each of the research chapters. The chapters are organized to progress from a combined study that evaluates sulfide oxidation, neutralization, and the occurrence of secondary minerals and trace elements in mining waste rock, to individual chapters that focus on each of these topics.

Chapter 1 introduces the foundational concepts and research that were used in formulating the thesis research objectives and in interpreting the thesis research results.

Chapter 2, the first research chapter, evaluates the relationships among trace elements in sulfide minerals, sulfide-mineral oxidation, and porewater geochemistry from waste rock that has been stored subaerially for more than 30 years. Samples of porewater were extracted from waste-rock solids and analyzed for geochemical parameters. Sulfide grains and their alteration products from the solid samples were analyzed by optical microscopy, electron-probe microanalysis, and synchrotron X-ray absorption spectroscopy. The aqueous and solid-phase results were integrated to relate observed characteristics of solid-phase oxidation, and trace element occurrence in sulfide minerals and alteration products to co-located porewater chemistry.

Chapter 3 present results from an experiment using synchrotron X-ray absorption spectroscopy that was designed to identify changes in iron speciation at 1 μm increments across oxidizing pyrrhotite grains from waste-rock samples. The grains selected for analysis included pyrrhotite from freshly blasted waste rock, and grains from waste rock that had be weathering for more than 30 years. The two grains from the 30-year-old waste rock were selected from samples that had different oxidation characteristics. Analysis of the results includes interpretations and comparison of the presence of various iron-bearing alteration products, and ferric iron contents calculated by different methods.

Chapter 4 includes analysis and interpretation of aqueous and solid-sample chemistry collected specifically for this thesis, and new analyses and interpretations of large, multi-year datasets previously collected at the Detour Lake Mine and the Diavik Diamond mine (Bailey, 2013; Bailey et al., 2016; Hannam, 2012; Langman et al., 2017; McNeill 2016; McNeill et al., 2020; Smith et al., 2013). The analyses and interpretations focus on alkalinity and concentrations of major cations in solid and aqueous samples. Calculations to apportion the dissolved aqueous calcium to carbonate and

silicate sources, and measurements of stable calcium-isotope ratios on a subset of samples were used to attempt to identify the dominant acid-neutralizing mineral phase at both Detour Lake Mine and Diavik Diamond Mine.

Chapter 5 presents analyses of waste-rock solids characteristics by automated quantitative mineralogy (mineral liberation analysis), conventional static tests (whole rock analysis, four-acid digestions, total carbon and total sulfur), and electron-probe microanalysis. Results from the conventional techniques were used to interrogate and extend the results provided by quantitative mineralogical analysis. The analyses focused on secondary minerals, including identifying mineral associations and mineral habits to infer geochemical conditions, and using electron-probe microanalyses to quantify potential trace element reservoirs associated with secondary minerals.

Chapter 6 provides a summary of the thesis research results and contributions to science.

Chapter 2

Trace elements in sulfides and release to porewater from sulfide oxidation in a historical waste-rock pile, Ontario, Canada

This chapter is modified from:

Smith, L.J.D., Paktunc, D., Blowes, D.W. 2021. Trace elements in sulfides and release to porewater from sulfide oxidation in a historical waste-rock pile, Ontario, Canada. *Appl. Geochem.* 126, 14899. <https://doi.org/10.1016/j.apgeochem.2021.104899>.

2.1 Summary

Porewater chemistry and sulfide-mineral characteristics were evaluated in a waste-rock pile at the Detour Lake gold mine, Ontario, Canada, which had weathered *in situ* for more than 30 years. Geochemical characterization suggests that the waste rock would be potentially acid generating. Porewater extracted from the waste rock ranged in pH and alkalinity from 7.0 – 8.2, and 27 – 110 mg L⁻¹ as CaCO₃, respectively, suggesting on-going acid neutralization by carbonate-mineral dissolution. Of the trace elements, nickel occurs at the highest concentration in pyrrhotite (median of 2740 ppm in historical samples), the associated alteration rims, and in the porewater samples (median of 140 µg L⁻¹). Nickel:cobalt and nickel:iron ratios in the sulfide grains and alteration rims, together with the porewater data, suggest no preferential retention of nickel over cobalt, and that sorption sites were saturated. X-ray absorption near edge structure (XANES) spectroscopy measurements at the iron, sulfur and nickel K-edges also indicate trace-element associations within the sulfide grains and alteration rims, and the presence of oxidized species of iron and sulfur.

2.2 Introduction

Acid mine drainage (AMD) results from coupled physical and biogeochemical processes that occur when sulfide minerals are exposed to the atmosphere, such as in subaerial storage of waste rock and mill tailings from mining and mineral processing. Oxidation of the two most common sulfide minerals in waste rock, pyrite [FeS₂] and pyrrhotite [Fe_(1-x)S], release acidity [H⁺], sulfate [SO₄], iron [Fe], and trace elements through a complex series of microbially-mediated reactions (Nordstrom, 1982; Blowes et al., 2003; Langman et al., 2015; Steinepreis, 2017). Trace elements are released during sulfide oxidation when they occur as components or impurities in the sulfides, or by weathering of minerals containing trace elements in the non-sulfide mineral assemblage.

Sulfide oxidation is diffusion-limited at the particle scale, with the oxidant oxygen [O₂] or ferric iron [Fe³⁺] diffusing to the grain edge where oxidation occurs (Pratt et al., 1997; Thomas et al., 2001), leaving a series of alteration layers containing Fe-deficient sulfides, marcasite [FeS₂], and Fe-(oxyhydr)oxides (Mycroft et al., 1995), which could include schwertmannite [e.g., Fe₈O₈(OH)_{8-2x}, SO₄]_x·nH₂O, 1 < x < 1.75] (Schoepfer and Burton, 2021)], goethite [α -Fe(OOH)], ferrihydrite [nominally Fe₂O₃·9H₂O], lepidocrocite [γ -Fe(OOH)], or jarosite [KFe₃(SO₄)₂(OH)₆] (Nordstrom et al., 2015). The progressive thickening of reaction rims, which affects the ongoing rate of sulfide oxidation, can be described by the shrinking core model (Levenspiel, 1972; Cathles, 1979; Davis et al., 1986; Wunderly et al., 1996; Mayer et al., 2002; Mayer et al., 2003). Changing oxidation states of Fe and sulfur [S] in pyrrhotite oxidation may be related through electron trapping by metastable polysulfides (Thomas et al., 2001). In two studies of pyrrhotite oxidation using synchrotron radiation (Langman et al., 2015; Steinepreis, 2017) the S species marcasite, elemental S [S⁰], thiosulfate [S₂O₃²⁻], and sulfite [SO₃²⁻] were identified prior to release of S as SO₄ [SO₄²⁻].

Acidity released during sulfide oxidation can be neutralized by carbonate-, oxide- and silicate-mineral dissolution. Calcite [CaCO₃] is typically the most important neutralizing mineral (Plummer et al., 1978; Chou et al., 1989) because of its high solubility, and abundance in crustal rocks and sediments. Concomitant, but slower, dissolution of other carbonates, oxides and silicates (Jambor et al., 1998) can become important when calcite dissolution is insufficient to maintain a circumneutral pH (Blowes and Ptacek, 1994; Jurjovec et al., 2002; Blowes et al., 2003; Moncur et al., 2005; Smith et al., 2013). The neutralization of acidity to a circumneutral range reduces the mobility of many trace elements, e.g., arsenic [As], cadmium [Cd], copper [Cu], lead [Pb], nickel [Ni], zinc [Zn], by pH- and redox-dependent sorption and/or co-precipitation by secondary manganese- [Mn], aluminum- [Al], and Fe-(oxyhydr)oxides (McKenzie, 1980; Bruemmer et al., 1988; Cornell, 1991; Scheinost et al., 2001; Lee et al., 2002; Boujelben et al., 2008; Du Laing et al., 2009; Nordstrom, 2011). Gypsum [CaSO₄·2H₂O] precipitation is common in AMD systems and can exert a control on dissolved SO₄ concentrations (McGregor et al., 1998; Al et al., 2000; Blowes et al., 2003; Moncur et al., 2005; Sracek et al., 2004; Lindsay et al., 2009). These complex and interdependent geochemical processes can evolve over time as waste rock continues to be exposed to the atmosphere.

This study aims to improve our understanding of the release and attenuation of trace elements during weathering by evaluating the relationships between trace elements in primary sulfide minerals, sulfide oxidation products and porewater in waste rock that has been weathering subaerially for more than 30 years.

2.3 Experimental section

2.3.1 Site description

The Detour Lake Mine, located in the Abitibi Greenstone Belt of eastern Ontario, Canada, is an orogenic greenstone-hosted lode gold deposit. Four waste-rock piles were constructed from 1983 – 1999 during open-pit and underground mining. These historical waste-rock piles were re-contoured and closed with a single-layer cover. Redevelopment, which began in 2006, required the relocation of some of the waste-rock piles and provided an opportunity to collect and analyze waste-rock samples that have been weathering *in situ* for up to 30 years (Cash et al., 2014; Steinepreis, 2017; McNeill et al., 2020). Figure 2-1 illustrates the site location, the lithological distribution, historical pit outline and expansion pit outline.

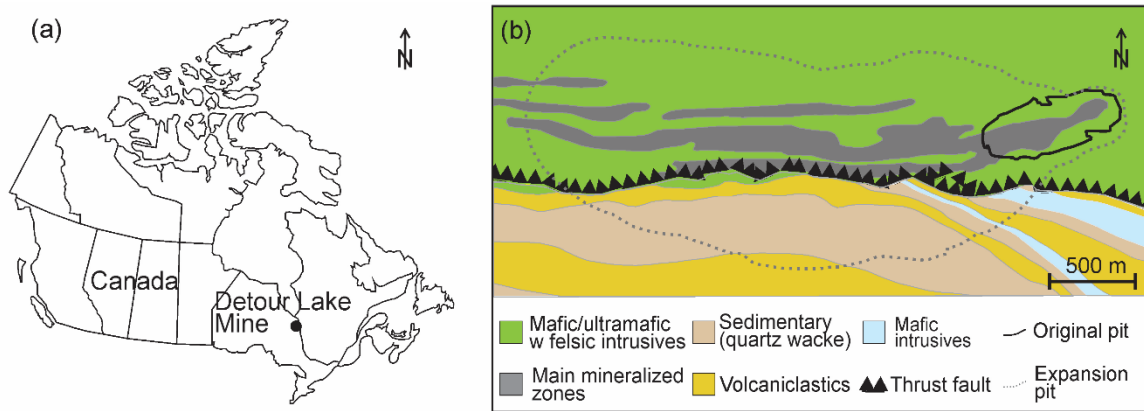


Figure 2-1: (a) Site location of the Detour Lake Mine and (b) lithological distribution, historical pit outline and current pit outline (modified from BBA and SGS, 2014).

2.3.2 Sample collection and analyses

The primary suite of samples for this study was collected in November 2015 from one waste-rock pile that was being relocated, and in December 2015 and January 2016 from waste rock that was freshly blasted adjacent to the perimeter of the original open pit. The waste-rock pile was 15 m high and had been partially removed and characterized for physical parameters (Cash et al., 2014). An excavator removed and discarded approximately 2 m of waste rock into the exposed face, before collecting a bucket from the freshly exposed waste rock for sampling. Samples were collected from the top (beneath the cover), middle and bottom at five locations, and one location from the middle only, and

across the exposed waste-rock face, to obtain approximately 15 L of the < 50 mm fraction for each sample.

Sample aliquots for mineralogical analyses were air dried under a fume hood for 48 h to reduce the possibility of phase transformations (Jambor, 1994). Thin sections were prepared from the 250 – 425 μm and < 425 μm size fractions for micro-analytical characterization. Aliquots of air-dried samples were sieved to obtain the fraction that passed the #40 sieve (425 μm) but retained on the #60 sieve (250 – 425 μm), and the fraction that passed the #40 sieve (< 425 μm). Samples of these fractions were prepared as thin sections by Spectrum Petrographics (Vancouver, USA). The samples were mounted on standard-sized Suprasil 2A quartz glass slides using a non-aqueous cyanoacrylate compound (Krazy Glue®) to reduce the possibility of mineralogical transformations of aqueous-sensitive phases. Thin sections were cut to a thickness of 30 μm , with double-sided, microprobe-quality polish. Supplementary thin sections were prepared from samples collected from the same, and an adjacent, waste-rock pile, which were oven-dried for a separate study (Cash et al., 2014). The supplementary thin sections were prepared by Vancouver Petrographics (Vancouver, Canada) on standard glass slides using a non-aqueous cyanoacrylate mounting medium (Loctite® 495), and with standard cut and polish to 30 μm thickness. Subsamples of the < 425 μm fraction were measured for total carbon [C] and total S by Leco Induction Furnace by SGS Canada Inc. (Burnaby, Canada).

Thin sections were evaluated by optical microscopy under reflected, transmitted, and cross-polarized light. Selected sulfide grains were studied at CanmetMINING (Ottawa, Canada) by a variable-pressure scanning electron microscope equipped with an energy-dispersive X-ray analyser (SEM/EDXA; Hitachi S-3200N with a Bruker Nano XFlash Detector 6 | 10), calibrated using the Bruker auto-calibration and the Cu signal from Cu-tape. The SEM/EDXA was used to confirm grain identification, observe weathering characteristics, and determine semi-quantitatively major and minor element concentrations at wt% level. Selected thin sections of the < 425 μm fraction were carbon-coated and sulfide grains and alteration rims were analyzed for chemical composition by electron-probe micro analysis (EPMA; JEOL 8230 SuperProbe) at the University of Ottawa, Ottawa, Canada. The EPMA had a 1 μm spot size to obtain concentrations at the ppm level of S, Fe, Cu, cobalt [Co], Ni, Zn, As and selenium [Se] in sulfide grains and their reaction rims. The EPMA method detection limit (MDL) varied by element: MDL of S was 129 ppm, Zn was 132 ppm, Se was 135 ppm, Cu was 163 ppm, Co was 169 ppm, Fe was 104 ppm, Ni was 108 ppm, and As was 218 ppm. Standards for sulfide analyses included marcasite, sphalerite [ZnS], Bi_2Se_3 , cubanite [CuFe_2S_3], pyrrhotite, pentlandite [$(\text{Fe,Ni})_9\text{S}_8$], and GaAs. EPMA was also used to measure Fe, calcium [Ca], strontium [Sr], magnesium [Mg] and Mn in carbonate grains, with MDLs of 242 ppm, 188 ppm, 563 ppm, 191 ppm,

and 186 ppm, respectively. EPMA standards for the carbonates included calcite, strontianite [SrCO₃], siderite [FeCO₃], Mn-bearing siderite [(Fe,Mn)CO₃], and dolomite [CaMg(CO₃)₂]. Spots reporting concentrations lower than the MDL, but higher than the limit of detection (LOD), were maintained in the datasets, but are considered estimates. Non-detect (ND) concentrations, i.e., concentrations < LOD, were maintained in the dataset and plotted at one half the LOD. The reported median statistic requires no assumptions for the value of the ND concentrations for statistical calculations; the reported mean values were calculated assuming ND concentrations were half the LOD.

Target points on pyrrhotite grains and their alteration rims were analyzed for S-, Fe-, Cu-, and Ni-species by micro-X-ray absorption spectroscopy (μ XAS) at the Canadian Light Source (CLS), beamline 06B-1 (SXRMB). SXRMB used an Si(111) monochromator for an incident beam energy range of 1.7 – 10 keV. The beam was focused to a spot size of approximately 10 μ m \times 10 μ m for micro-X-ray fluorescence (μ XRF) measurements. Additional targets on sulfides from the oven-dried supplementary samples were measured at the Advanced Photon Source (APS), beamline 13-ID-E for Fe, Cu, Ni, and Zn using the microprobe end station for a 1 μ m \times 1 μ m spot size. This beamline had an energy range of 2.4 – 28 keV, with an O₂-exclusion environment required for measurements in the S energy region, which was not employed for this study. Zinc could not be measured at SXRMB because the Zn K-edge energy occurs at the upper end of the beamline energy range, and Co could not be measured at either beamline because the very high concentration of Fe in the samples masked the Co K-edge response. Mapping of Cu by μ XRF was achievable, but concentrations of Cu were too low to obtain reliable XANES spectra. The ATHENA software package (Ravel and Newville, 2005) was used for XANES analyses and linear combination fitting (LCF). Standards for Fe included pyrrhotite (as Fe₇S₈ and as troilite [FeS]), pyrite, marcasite, ferrihydrite, goethite, hematite [Fe₂O₃], schwertmannite and Fe-foil [Fe⁰]. Standards for S included pyrrhotite (as Fe₇S₈ and as troilite), marcasite, Na₂S₂O₃, FeSO₄, Na₂SO₃, NiSO₄, K₂S₄O₆, and elemental sulfur [S⁰]. Standards for Ni included pentlandite, NiSO₄, Ni(OH)₂, NiS₂, NiO and Ni-foil [Ni⁰]. Standard spectra were measured at CLS SXRMB, with the exception of some Ni-standards, which were measured at APS 13-ID-E under the same conditions as μ XAS spectra.

Porewater was extracted from the historical waste rock by centrifugation. A clean stainless-steel scoop was used to obtain approximately 100 g of the < 25 mm fraction of each waste-rock sample. The sample was placed in Falcon® tubes with a hole pierced at the bottom and fitted to new, clean Nalgene® 60 mL HDPE sample bottles to collect the expelled porewater. Glass wool was placed at the hole-opening to minimize fine-grained fragments from entering the porewater collection bottle. Six aliquots of each sample were centrifuged at 8500 rpm for 30 min using a Thermo-Scientific

Sorvall Legent XT Centrifuge. The porewater collected from each aliquot was aggregated to form one sample. Moisture contents of the historical samples, following standard methods (ASTM, 2010), ranged from 6 – 13% (mean of 9%) and were in good agreement with moisture contents calculated from porewater extraction (7 – 13%, mean of 10%), suggesting centrifugation was an effective method of extracting porewater.

Paste pH of both oven-dried and air-dried waste rock were obtained by the standard method (ASTM, 2013) of mixing 10 g of sample and 10 mL of deionized (DI) water and letting stand for 1 h before measuring the pH. Paste pH was measured with a Cole Palmer combination electrode calibrated to standard buffers of pH 4.01, 7.00, and 10.01. Each aggregated porewater sample was analyzed for pH using an Orion Ross combination electrode calibrated to standard buffers of pH 4.01, 7.00, and 10.01; for Eh using an Orion Pt redox electrode checked with Zobell's solution (Nordstrom, 1977) and Light's solutions (Light, 1972); and for alkalinity using a Hach digital titrator with bromocresol green/methyl red indicator. Additional aliquots were filtered using a 0.45 µm cellulose acetate syringe filter, preserved to pH < 3 with trace-metals grade HNO₃ and analyzed for major cations by ICP-OES, and trace elements by ICP-MS. Aliquots for anion analysis were filtered using a 0.45 µm cellulose acetate filter and analyzed by ion chromatography. All aqueous analyses were conducted at the University of Waterloo; two blind duplicate samples for the set of 17 aqueous samples were submitted, with relative percent differences (RPD) of < ± 4% for major cations and typically < ± 20% for trace elements; RPD for Zn and Sb in duplicate samples were > 50%. QA/QC protocols followed EPA methods 6010C and 6020A for the ICP-OES and ICP-MS, respectively. Recoveries for internal calibration were 98 – 99% for major cations and 99 – 107 % for trace elements. Results from the geochemical analyses were modeled with the geochemical mass transfer model PHREEQC (v 3.0.6; Parkhurst and Appelo 2013) with the WATQ4F database, modified to include lepidocrocite, siderite and schwertmannite.

2.4 Results and discussion

2.4.1 Acid-base accounting

Neutralization potential (NP) and acid-generating potential (AP) values for the < 425 µm fraction calculated from the total C and total S concentrations, respectively, indicated that all historical samples, except one, were potentially acid generating or of uncertain acid-generating potential (Figure A-1). No primary or secondary siderite or ankerite [Ca(Fe,Mg,Mn)(CO₃)₂] were observed in any of the samples, and EPMA measurements of 13 carbonate grains indicated a median Fe concentration of 400 ppm (range of ND (< 93 ppm – 2300 ppm); thus Fe-carbonates species did not

bias the NP calculations based on total C concentrations. However, gypsum was identified by SEM/EDXA in some historical waste-rock samples, contributing to total S concentrations and AP in those samples.

Neither the calculated NP:AP, nor the observed degree of oxidation exhibits a spatial trend from top to bottom or along the transect (Figure 2-2), suggesting variations in *in situ* lithology and/or physicochemical properties impacted acid generation and neutralization. The exposed profile showed evidence of a cover comprising finer-grained sediment or soil, tip faces formed during waste-rock pile construction, and a historical traffic surface. These construction features can influence water and air movement, and, therefore, can influence mineral weathering (Strömberg and Banwart, 1999; Lefebvre et al., 2001; Smith and Beckie, 2003). Two freshly blasted waste-rock samples, mineralogically similar to the historical samples, had higher NP compared to the historical waste-rock samples, suggesting that the decades-long oxidation and neutralization processes have consumed carbonate minerals in the historical samples.

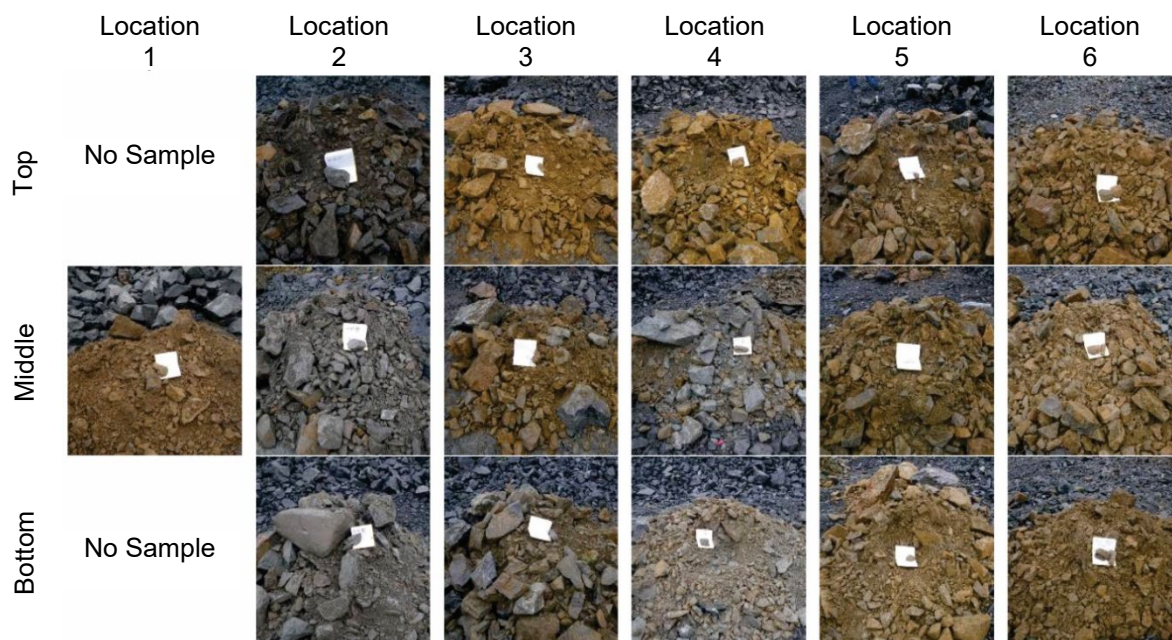


Figure 2-2: Waste-rock samples collected from profile locations illustrating visual oxidation characteristics. Samples collected from top (beneath cover), middle and bottom at six locations across a transect approximately 150 m long. White notebook in photos measures 24 × 18 cm.

Similar to the NP:AP difference between the fresh and historical samples, the paste pH measurements suggest the neutralization capacity of the historical waste-rock samples is depleted relative to the freshly blasted samples. A notable difference for both historical and fresh samples is

the paste pH of samples that were oven-dried were lower than the corresponding air-dried samples, with a greater difference in pH measurements for the historical waste-rock samples. Paste pH values of all oven-dried historical samples indicated more acidic conditions (pH 4.4 – 6.7) than the air-dried samples, which indicated circumneutral to slightly acidic conditions (pH 6.4 – 7.3). Because the moisture content values measured by the oven-drying method and those calculated from porewater extraction were in good agreement, the lower paste pH values of the oven-dried samples are attributed to the transformation during drying of ferrous iron [Fe^{2+}] to Fe^{3+} and precipitation as ferrihydrite, followed by the transformation of ferrihydrite to goethite (\pm hematite \pm jarosite). These mineralogical transformations as a result of oven-drying are consistent with observations using the Munsell® color-system. The oven-dried samples typically had more yellow and orange hues, with higher Munsell values (i.e., commonly 10 YR) compared to the air-dried samples (e.g., 2.5YR, 5Y, 10YR), suggesting the oven-dried samples had a higher proportion of Fe-(oxyhydr)oxides and/or Fe-hydroxysulfates (e.g., goethite and/or hematite, and possibly jarosite; Jambor and Dutrizac, 1998), compared to the air-dried samples. Because the observations of changes in paste pH and soil color with oven-drying were incidental, a rigorous examination of the Fe-species, i.e., by X-ray diffraction (XRD), in the oven-dried and air-dried samples was not conducted for this study. Nonetheless, the distinction between the paste pH of air-dried versus oven-dried samples is important, particularly for the historical waste-rock samples.

Measured porewater pH values were neutral to slightly alkaline (7.0 – 8.2), and slightly higher than the paste pH measurements of the air-dried samples, indicating acid neutralization predominantly by carbonate dissolution (Blowes and Ptacek, 1994) at 1:1 $\text{CaCO}_3\text{:H}^+$ molar ratio. Carbonate-dominant neutralization is consistent with the geochemistry of the extracted porewater: alkalinity was always present (27 – 110 mg L^{-1} as CaCO_3), dissolved aluminum [Al] concentrations were low (0.004 – 0.018 mg L^{-1}), and calculations by PHREEQC suggested samples with pH < 7.7 were undersaturated with respect to calcite (Figure 2-3) and dolomite, i.e., indicating a tendency for carbonate minerals to dissolve in response to H^+ generated by sulfide oxidation. Samples were near or at saturation with respect to gibbsite [$\text{Al}(\text{OH})_3$], and undersaturated with respect to amorphous $\text{Al}(\text{OH})_3$. Gibbsite formation may limit dissolved Al concentrations and the low Al porewater concentrations suggest the dissolution of $\text{Al}(\text{OH})_3$ phases was not consuming H^+ (Figure 2-3). Porewater samples were calculated to be near or at saturation with respect to gypsum and saturated with respect to barite [BaSO_4]. However, barite was not detected in the samples and was not expected to have significantly influenced SO_4 concentrations. See Figure A-2 for parameter concentrations used in the PHREEQC simulations and (Figure A-3) for the saturation indices of key secondary phases.

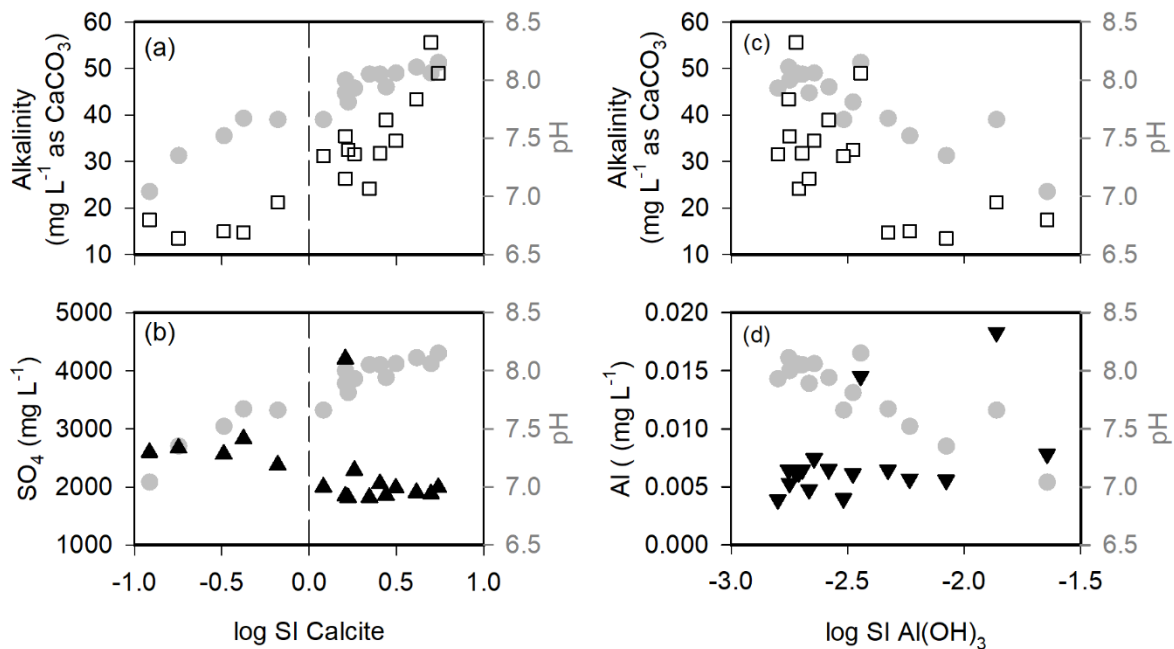


Figure 2-3: (a) alkalinity (open squares) and porewater pH (solid grey circles) vs. the log of the saturation index (SI) of calcite, (b) porewater pH (solid grey circles) and concentration of SO₄ (solid black upward triangles) vs. log[SI] of calcite; (c) alkalinity (open squares) and porewater pH (solid grey circles) vs. log[SI] of amorphous Al(OH)₃; (d) dissolved concentration of Al (solid black downward triangles) and pH (solid grey circles) vs. log[SI] of amorphous Al(OH)₃. Vertical dashed lined in (a) and (b) at log[SI] = 0 indicates saturation.

2.4.2 Mineralogical observations of sulfide oxidation characteristics

The principal sulfide minerals in the historical waste-rock samples were pyrrhotite and pyrite with lesser chalcopyrite [CuFeS₂] and a few small grains of sphalerite and pentlandite in some samples, including pentlandite lamellae in a few pyrrhotite grains. Pyrrhotite was typically the most abundant sulfide at approximately 1 – 3%, with pyrite abundances typically half that of pyrrhotite, per optical mineralogical observations. Two samples of freshly blasted waste rock had similar sulfide and silicate mineralogy to the historical waste-rock samples and were included in this study.

Partially and fully liberated pyrrhotite grains in the historical samples were typically strongly altered with oxidation propagating along basal parting planes. The degree of oxidation of pyrrhotite typically ranged from remnant pyrrhotite cores surrounded by thick rims of alteration products to pyrrhotite grains completely replaced by Fe-(oxyhydr)oxides, underscoring the heterogeneous nature of *in situ* weathering. Rarely, liberated pyrrhotite grains exhibited only thin alteration rims around a

mostly intact core. Pyrite grains exhibited lower degrees of oxidation than pyrrhotite, typically with thin alteration rims surrounding grains or along fractures, and occasionally with observable etch pits. (Figure 2-4).

Observations of gypsum in some historical samples (Figure A-4) were consistent with the porewater SO_4 concentrations and PHREEQC calculations and expected due to the decades-long sulfide oxidation under subaerial conditions. Conversely, no gypsum was identified by optical microscopy or SEM/EDX in the freshly blasted waste-rock samples. Extensive gypsum formation was not expected in the freshly blasted samples because the extent of sulfide oxidation and secondary sulfate-mineral formation would be limited by the short period of atmospheric exposure following blasting.

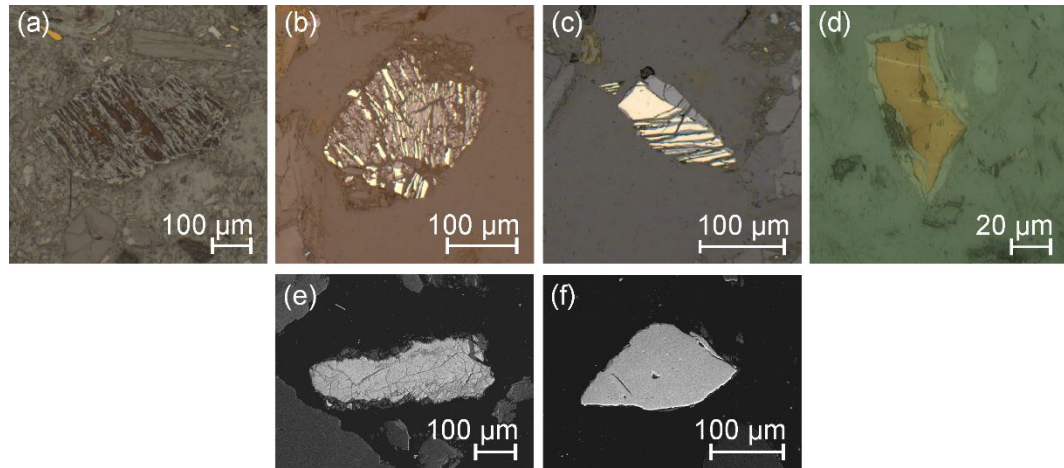


Figure 2-4: Sulfide oxidation characteristics in the historical samples with varying degrees of oxidation. Pyrrhotite grains in (a – d) in reflected light and pyrite grains in (e – f) as backscattered electron images.

(a) completely altered pyrrhotite; (b) strongly altered with remnant pyrrhotite cores; (c) slightly to moderately altered pyrrhotite; (d) mostly intact pyrrhotite grain with minor alteration rim; (e) pyrite oxidation propagating along fractures; (f) pyrite grain with minor etch pits.

2.4.3 Microanalysis of sulfide minerals

SEM/EDX microanalysis of residual sulfide grains suggested concentrations of Ni and Co were typically elevated, and Cu concentrations were occasionally elevated (e.g., Figure 2-5); concentrations of Zn and As were typically not discernable at the detection limit of the EDX.

EPMA was used to quantify trace elements in sulfide grains and alteration products in four historical samples that represent the range of porewater pH values of the sample suite, and one freshly blasted sample with mineralogy most similar to the historical samples. EPMA measurements of Ni in pyrrhotite in the historical samples ranged from < 108 – 5400 ppm (median of 2740 ppm, n = 79 for measured concentrations), and the Co concentrations ranged from < 169 – 3200 ppm (median of 225 ppm, n = 79). The pyrrhotite-mineral formula based on the median concentrations of Fe, Ni and Co is $(\text{Fe}_{0.862}\text{Ni}_{0.0039}\text{Co}_{0.00032})\Sigma_{0.866}\text{S}$ for all the historical samples, but with variation among samples (Table 2-1, Figure 2-6). The Ni and Co concentrations in pyrrhotite in the freshly blasted waste-rock sample were 144 – 4580 ppm (median of 3220 ppm, n = 72) and < 169 – 801 ppm (median of < 169 ppm, n = 72, with an estimated median concentration of 21 ppm based on measurements > LOD but < MDL), respectively, with a mineral formula of $(\text{Fe}_{0.855}\text{Ni}_{0.0045}\text{Co}_{0.00003})\Sigma_{0.859}\text{S}$, based on median concentrations of Fe, Ni and Co. The median Ni:Co ratios (based on molar ratios) in pyrrhotite were 0.75 (n = 65) and 9.56 (n = 39) in the historical and freshly blasted samples, respectively, but with variations within and among samples, particularly for Ni concentrations (Figure 2-6). Mann-Whitney rank sum tests suggest that Ni concentrations are not statistically significantly different among the samples with higher Ni concentrations, or among the samples with lower Ni concentrations, but are significantly different between all high/low sample combinations. The higher Ni concentrations occur in the freshly blasted sample, and the two historical samples with lower porewater pH and higher proportions of altered grains with remnant pyrrhotite cores. The group with lower Ni concentrations consists of the two samples with higher porewater pH and a larger proportion of liberated or partially liberated pyrrhotite grains. EPMA measurements on pyrrhotite alteration products illustrate similar groupings (Figure 2-6), however there were too few data points for statistical analyses. Concentrations of Co and Ni in the porewater were highly correlated ($r = 0.99$, $P < 0.05$; Figure 2-7). The porewater Ni concentrations measurements, together with the EPMA measurements, suggest that the difference in Ni concentrations in the alteration products is likely a result of the differences in the Ni and Co concentrations in original pyrrhotite mineral grains, rather than preferential release of Ni during pyrrhotite oxidation. Studies to date have not rigorously addressed the release rates of specific trace elements during pyrrhotite oxidation. One study on the effects of trace element substitution on oxidation rates suggests that pyrrhotite with higher trace element content may oxidize more slowly than pyrrhotite without impurities (Janzen et al., 2000).

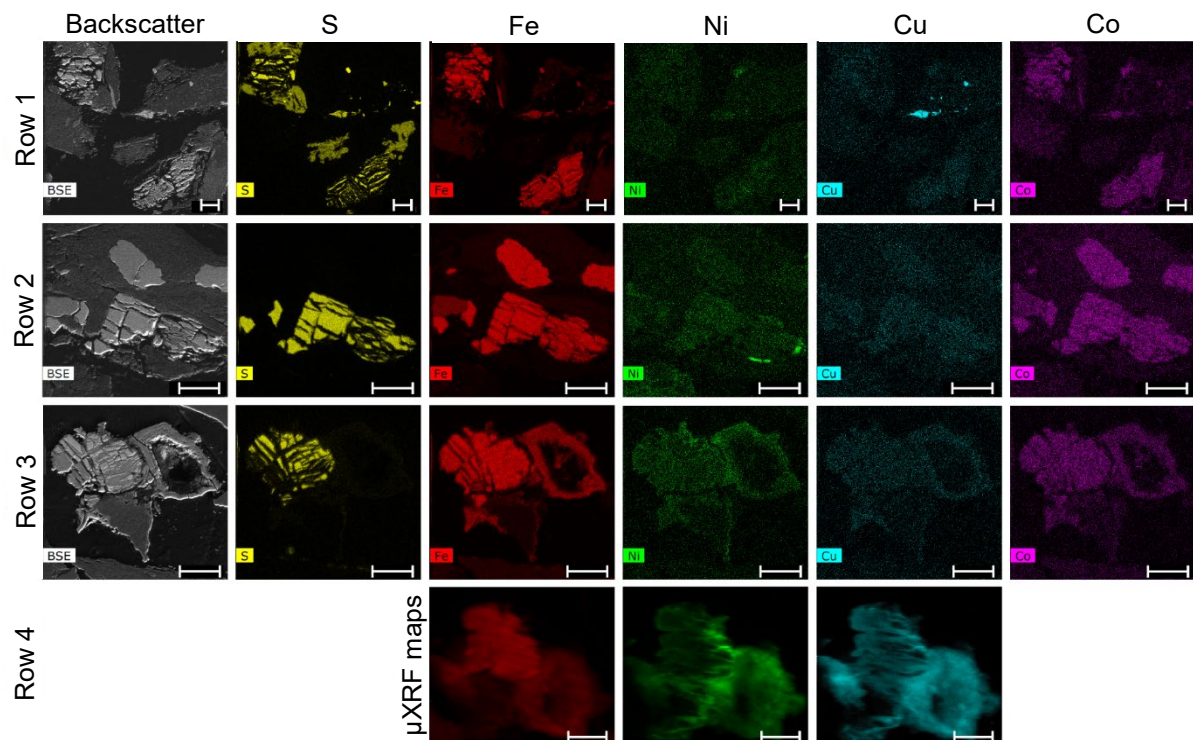


Figure 2-5: Rows 1 – 3 are SEM/EDX mapping of selected weathered sulfide grains, illustrating elevated cobalt (Co), nickel (Ni) and copper (Cu) concentrations in the unaltered cores and alteration rims. Row 1: two altered pyrrhotite grains (upper left and lower right) and smaller chalcopyrite flecks (evident in Cu map, with gypsum evident in the sulfur (S) plot (absent in the iron (Fe) map; see Figure A-4). Row 2: moderately altered pyrrhotite grain. Row 3: moderately to strongly altered pyrrhotite (upper left) and a separate alteration rim (right). The dark center of the alteration rim evident in the third row suggests a sulfide grain was plucked during slide preparation. Row 4: μXRF mapping (at beamline 13-ID-E) of the same grain as in Row 3. The μXRF maps are rotated approximately 35° clockwise from the SEM/EDX maps. Scale bars represent 60 μm.

Table 2-1: Summary of nickel (Ni) and cobalt (Co) concentrations in pyrrhotite grains. Historical samples are identified by their porewater pH values. Non-detect (ND) values of Co were assigned 1.5 ppm and half the limit of detection (LOD) for mean calculations of concentrations and Ni:Co. A single Ni measurement in sample with pH 7.0 was < LOD and assigned a value of 54, half the LOD. Concentrations > LOD but < MDL are considered estimates and are in provided in parentheses for median and mean values.

Ranges for Ni:Co ratios present the ratios calculated with Co concentrations > LOD, values in parentheses indicated the maximum Ni:Co when 1.5 ppm was assigned to Co concentrations < LOD, and the number of measurements with Co < LOD are noted.

Sample	Mineral formula based on median element concentrations	Ni range, mean, median, n (ppm)	Co range, mean, median, n (ppm)	Ni:Co range, mean, median, n < Co MDL (from ppm)
Freshly blasted	(Fe _{0.855} Ni _{0.0045} Co _{0.00003})Σ0.859S	144 – 4580, 2980 3220, 72	<169 – 801, <169 (107), <169 (21), 72	0.94 – 1050 (3050), 964, 107, 33
pH 8.1	(Fe _{0.863} Ni _{0.0011} Co _{0.00030})Σ0.864S	250 – 5100, 1860, 786, 34	<169 – 1440, 451, 218, 34	0.51 – 1250 (3400), 497, 3.58, 7
pH 7.8	(Fe _{0.873} Ni _{0.0009} Co _{0.00075})Σ0.875S	314 – 2840, 1080, 683, 9	<169 – 1140, 299, 531, 9	0.54 – 6.96 (1890), 4.14 1.24, 2
pH 7.4	(Fe _{0.858} Ni _{0.0048} Co _{0.00034})Σ0.863S	146 – 5400, 3250, 3440, 17	<169 – 3200, 519, 243, 17	0.046 – 333 (3210), 478, 10.1, 3
pH 7.0	(Fe _{0.852} Ni _{0.0052} Co _{0.00026})Σ0.858S	<108 – 4960, 3270, 3730, 19	<169 – 965, 299, 189, 19	0 (0.8) – 405 (2230), 280, 8.72, 17, 2
All historical	(Fe _{0.862} Ni _{0.0039} Co _{0.00032})Σ0.866S	<108 – 5400, 2410, 2740, 79	<169 – 3200, 391, 225, 79	0 (0.8) – 1250 (3400), 432, 6.95, 14

Nickel and Co are also the most abundant trace elements observed in the pyrite grains of the historical samples (n = 101, median values of 558 and 417 ppm, respectively), and the freshly blasted sample (n = 50, median values of 440 and < 169 ppm, respectively). Concentrations of Ni and Co vary within and among the pyrite grains, with no discernable groupings (Figure 2-6). Arsenic is commonly present in pyrite in the historical samples (< 218 – 5610 ppm), and in the freshly blasted sample (median of < 218 ppm with estimated value of 126 ppm, based on ND and measurements > LOD). Pyrite grains in both the historical and freshly blasted samples occasionally contain Cu, Zn and/or Se, typically at concentrations < 120 ppm (at 75th percentile). Because pyrite exhibits a lower degree of oxidation than pyrrhotite, fewer EPMA measurements were possible on the alteration products associated with pyrite grains (Figure 2-6), and the contributions of pyrite oxidation to Ni and Co concentrations in the porewater are considered minimal.

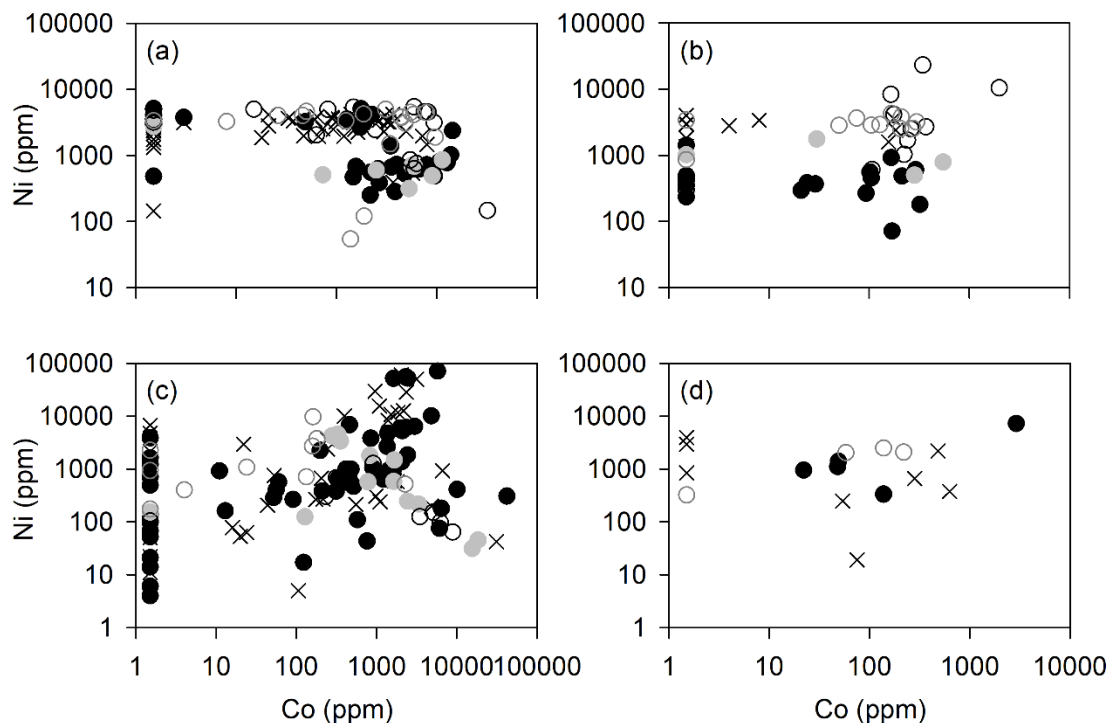


Figure 2-6: Nickel (Ni) and cobalt (Co) concentrations in historical and freshly blasted samples in (a) pyrrhotite grains and (b) pyrrhotite alteration rims, and (c) pyrite grains and (d) pyrite alteration rims. Co with ND measurements plotted at 1.5 ppm, half the LOD. Samples plotted by porewater pH: black filled circles = 8.1; grey filled circles = 7.8; black open circles = 7.4; grey open = 7.0; x = freshly blasted sample.

The relative proportion of trace elements in the sulfide grains was consistent with the porewater geochemistry ($n = 17$): typically low concentrations of As ($< 0.3 - 0.55 \mu\text{g L}^{-1}$, median of $0.36 \mu\text{g L}^{-1}$), and Se ($1.2 - 71.5 \mu\text{g L}^{-1}$, median of $5.4 \mu\text{g L}^{-1}$) and elevated concentrations of Cu, Zn, Ni and Co (Figure A-5). It appears that the oxidation of chalcopyrite, the third most abundant sulfide mineral in these samples, contributed most of the dissolved Cu in the porewater ($1.5 - 14.1 \mu\text{g L}^{-1}$, median of $7.2 \mu\text{g L}^{-1}$). The chalcopyrite grains measured by EPMA occasionally contained trace amounts of Zn, Se and/or Ni, and rarely contained As. Elevated concentrations of Zn ($5.2 - 185 \mu\text{g L}^{-1}$, median of $26.2 \mu\text{g L}^{-1}$) in some porewater samples can be attributed to, at least in part, the oxidation of sphalerite, which was present in trace amounts.

Nickel in the porewater was released primarily from the oxidation of pyrrhotite, which exhibited a higher degree of oxidation than pyrite. Samples with porewater pH of 7.0 and 7.4 had porewater Ni concentrations that were much higher (1030 and $1660 \mu\text{g L}^{-1}$, respectively) than samples with higher pH (Figure A-5). All porewater samples were undersaturated with respect to $\text{Ni}(\text{OH})_2$ and NiCO_3 .

(Figure A-3), suggesting Ni is not being sequestered by these potential secondary phases, neither of which were observed in these samples. Differences in Ni:Fe molar ratios in the alteration rims and the parent pyrrhotite grains were not statistically significant at a 95% confidence interval (Figure 2-7), with the exception of the sample with porewater pH 8.1, which had higher Ni:Fe in pyrrhotite grains compared to the alteration rims. Pentlandite inclusions and lamellae were not observed in proximity to these spot measurements, however, it is possible that very small inclusions or lamellae may have influenced the Ni concentrations. The Ni:Fe ratios in the alteration rims did not correlate to the degree of oxidation of the alteration rim, using the residual S concentration as a proxy for degree of alteration, though the data are limited (Figure 2-7). Aqueous phase Ni:Fe tracked the solid phase ratios, but at approximately four orders of magnitude higher (Figure 2-7). The higher concentrations of Ni compared to Fe in the aqueous phase are attributed to the removal of aqueous Fe as a secondary Fe-(oxyhydr)oxide precipitate, and suggests that Ni sorption sites were saturated, with the possible exception of the sample with porewater pH of 8.1. PHREEQC-calculated saturation indices for amorphous Fe(OH)₃ and goethite suggest that the porewaters from all samples were saturated with respect to these phases and that these phases were geochemically stable in this system. Surface complexation calculations also suggest the Ni sorption sites were saturated (Figure 2-8), based on the parameters of Dzombak and Morel (1990) for ferrihydrite (specific surface area of 600 m² g⁻¹, strong site density of 0.005 mol [mol Fe]⁻¹, weak site density of 0.2 mol [mol Fe]⁻¹) and the number of moles of precipitated goethite from the equilibrated porewater. Applying ferrihydrite parameters to goethite is considered conservative because of the more crystalline nature (and therefore fewer sorption sites) of goethite.

These solid and aqueous phase data suggest that concentrations of aqueous Ni were primarily influenced by the initial concentration of Ni in the sulfide minerals and the degree of sulfide oxidation, and sorption of Ni by accumulating Fe-(oxyhydr)oxides resulted in Ni:Fe ratios similar to the initial sulfide oxidizing grain. At circumneutral porewater pH values, elevated concentrations of Ni have been reported in porewater from unsaturated tailings (0.15 mg L⁻¹; Lindsay et al., 2009), and unsaturated waste-rock drainage (< 1 to > 5 mg L⁻¹; Smith et al., 2013; Sinclair et al., 2015). Nickel has been observed to be sorbed to Fe-(oxyhydr)oxide phases in solid samples associated with circumneutral waste-rock drainage (Langman et al., 2015), and sorbed to natural ferromanganese coatings (Manceau et al., 2007).

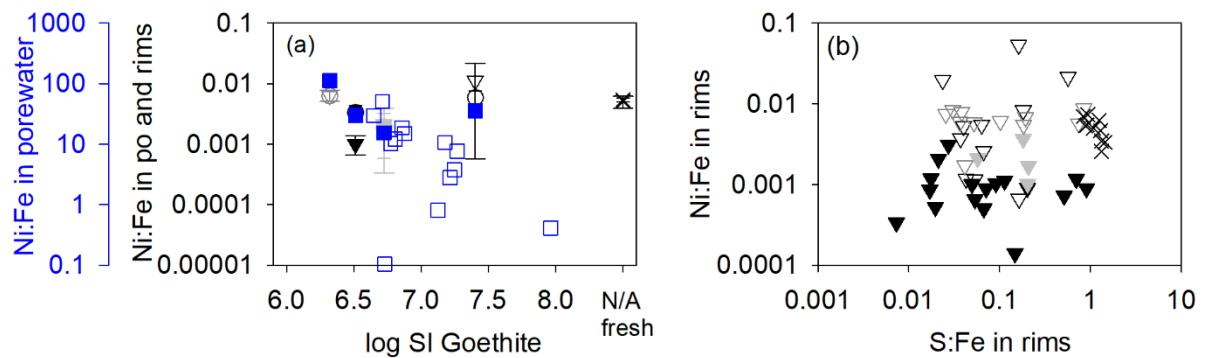


Figure 2-7: (a) Saturation indices in log scale (log[SI]) of goethite versus Ni:Fe molar ratios in pyrrhotite (“po”; circles), alteration rims (“rims”; triangles) and porewater (blue squares). (b) S:Fe molar ratios versus Ni:Fe molar ratios in alteration rims. Samples plotted by porewater pH: solid black symbols = 8.1; solid grey symbols = 7.8; open black symbols = 7.4; open grey symbols = 7.0; × = freshly blasted sample. Solid blue squares in (a) indicate porewater samples with corresponding EPMA measurements. Symbols plotted in (a) at median values and bars indicate 25th and 75th percentiles.

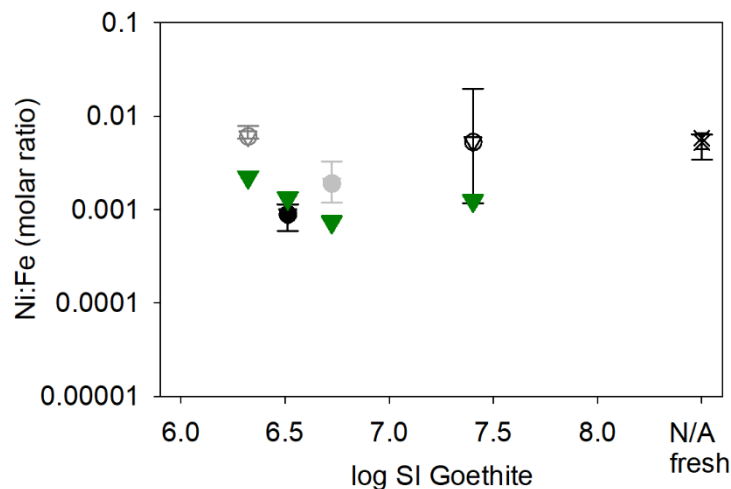


Figure 2-8: Saturation indices in log scale (log[SI]) of goethite versus Ni:Fe molar ratios in pyrrhotite (circles) and alteration rims (triangles) measured by EPMA, and PHREEQC-calculated molar ratios of Ni:Fe for Ni sorbed on alteration rims as ferrihydrite (green triangles). Samples plotted by porewater pH: solid black symbols = 8.1; solid grey symbols = 7.8; open black symbols = 7.4; open grey symbols = 7.0. Symbols for pyrrhotite and alteration rims are plotted as the median, and bars denote 25th and 75th percentiles.

Trace element associations in the sulfides and their alteration products measured by EPMA were consistent with μ XRF mapping at 13-ID-E and SXRMB that showed concentrations of Ni and Cu associated with some sulfide grains and their alteration products (e.g., bottom row in Figure 2-5, Figure 2-9). Zinc was also measured at 13-ID-E, but concentrations in the pyrite and pyrrhotite grains and the alteration products were typically too low (i.e., below the MDL of EPMA) to permit the acquisition of reliable spectra.

The partially altered pyrrhotite grain illustrated in Row 2 of Figure 2-5 was targeted for micro-spectroscopy measurements of Ni-Fe-, and S-XANES at SXRMB; Cu-XANES was attempted but concentrations were too low to obtain reliable spectra. The Ni-XANES spectrum collected from a spot with elevated Ni concentrations identified by μ XRF suggests that Ni occurs predominantly as NiS_2 , with a smaller component of NiSO_4 (Figure 2-9), consistent with the observed progressive oxidation of the pyrrhotite grains and release of Ni.

Although discriminating among Fe-(oxyhydr)oxide phases in natural samples has shown to be difficult with Fe-XANES analysis (Priest et al., 2007), LCF results provide a ratio of $\text{Fe}^{3+}:\text{Fe}^{2+}$ species in areas of the pyrrhotite grain areas that exhibit differing oxidation characteristics. Both Fe- and S-XANES LCF indicated a higher proportion of Fe^{3+} compounds compared to Fe^{2+} compounds and more oxidized S-species at Spots b and c (Table 2). The areas of the grains corresponding to μ XRF Spots b and c were observed by SEM and optical microscopy to be more extensively oxidized, and the higher degree of oxidation is consistent with EPMA measurements that detected S concentrations in grains and alteration rims (Figure 2-7). A higher proportion of pyrrhotite was suggested by both Fe- and S-XANES spectra and LCF than was apparent by SEM and optical microscopy. This discrepancy can be attributed to the depth of X-ray penetration and fluorescence emissions from phases underlying the surface visible to optical and SEM microscopy, and/or the $10\text{ }\mu\text{m} \times 10\text{ }\mu\text{m}$ beam spot measured adjacent unaltered grain areas in addition to the target altered zone. Linear combination fitting suggests that one or more phases not included in the LCF are likely contributing to the Fe pre-edge peaks and white lines, two sections of the Fe-spectra with a poor LCF fit using only Fe-sulfide and Fe-(oxyhydr)oxide standards. Including schwertmannite, the only sulfate-bearing Fe-XANES standard used in this study, improved the LCF fit, particularly in the more oxidized areas (Spots b and c; in Figure 2-9). Although most porewater samples in this study were calculated to be supersaturated with respect to schwertmannite, (Figure A-3), this secondary mineral has been shown to be metastable, progressively releasing sulfate and converting to goethite at $\text{pH} > 5$ (Schwertmann and Carlson, 2005), the porewater pH range measured in this study. Nonetheless, S

concentrations in altered rims measured by EPMA (Figure 2-7), and a better LCF fit obtained by including schwertmannite suggest the presence of an oxidized Fe-S-O-H species.

S-XANES LCF results suggested similar proportions of reduced Fe-S compounds (pyrrhotite + marcasite) to the Fe-XANES LCF results, as well as the presence of sulfate, sulfite, thiosulfate and/or tetrathionite species (Table 2-2), consistent with previous S-XANES observations of oxidizing pyrrhotite (Langman et al., 2015), and S-species produced during the pyrrhotite oxidation process (e.g., review by Belzile et al., 2004). These S species occur as intermediate Fe-S oxidation products during the pyrrhotite oxidation process (Schippers and Sand, 1999; Langman et al., 2015). The LCF goodness-of-fit in the Fe-XANES declines in areas where partial oxidation products are observed. Similar to the Fe-XANES LCF results, some white line areas in the higher oxidation state regions of the measured S-XANES spectra had a poorer fit (Figure 2-9), suggesting one or more S-phases with higher oxidation states, not included among the reference standards for this study, contributed to the measured spectra. LCF results, together with the measured Fe- and S-XANES spectra, indicate the need to quantify the abundance of key Fe- and S-species, which represent transitional Fe- and S- phases, and intermediate oxidation steps.

Table 2-2: Linear combination fitting results for Fe-, S- and Ni-XANES analyses at target spots illustrated in Figure 2-9. Standard spectra and sensitivity analyses are presented in Table A-1 through Table A-3.

		Spot a	Spot b	Spot c	Spot d	Spot e
Fe	Pyrrhotite	78%	63%	58%	42%	90%
	Marcasite	7%	13%	27%	34%	-
	Goethite	10%	14%	-	12%	5%
	Schwertmannite	5%	10%	15%	13%	5%
	<i>R-factor</i>	<i>4.55E-04</i>	<i>1.97E-04</i>	<i>5.01E-04</i>	<i>1.05E-03</i>	<i>3.69E-04</i>
	<i>Reduced Chi-squared</i>	<i>8.53E-05</i>	<i>3.71E-05</i>	<i>8.94E-05</i>	<i>1.89E-04</i>	<i>7.15E-05</i>
	<i>Fe³⁺:Fe²⁺</i>	<i>0.18</i>	<i>0.32</i>	<i>0.18</i>	<i>0.18</i>	<i>0.11</i>
S	Pyrrhotite	89%	86%	71%		90%
	Marcasite	-	3%	-		-
	Elemental S					4%
	Thiosulfate	5%	5%	12%		4%
	Tetrathionate	5%	7%	17%		2%
	Sulfate	0.4%	-	-		-
	<i>R-factor</i>	<i>3.60E-03</i>	<i>4.18E-03</i>	<i>1.12E-02</i>		<i>3.4E-03</i>
	<i>Reduced Chi-squared</i>	<i>5.72E-04</i>	<i>7.13E-04</i>	<i>1.99E-03</i>		<i>5.6E-04</i>
Ni	NiS ₂				85%	
	NiSO ₄				15%	
	<i>R-factor</i>				<i>1.08E-03</i>	
	<i>Reduced Chi-squared</i>				<i>2.48E-04</i>	

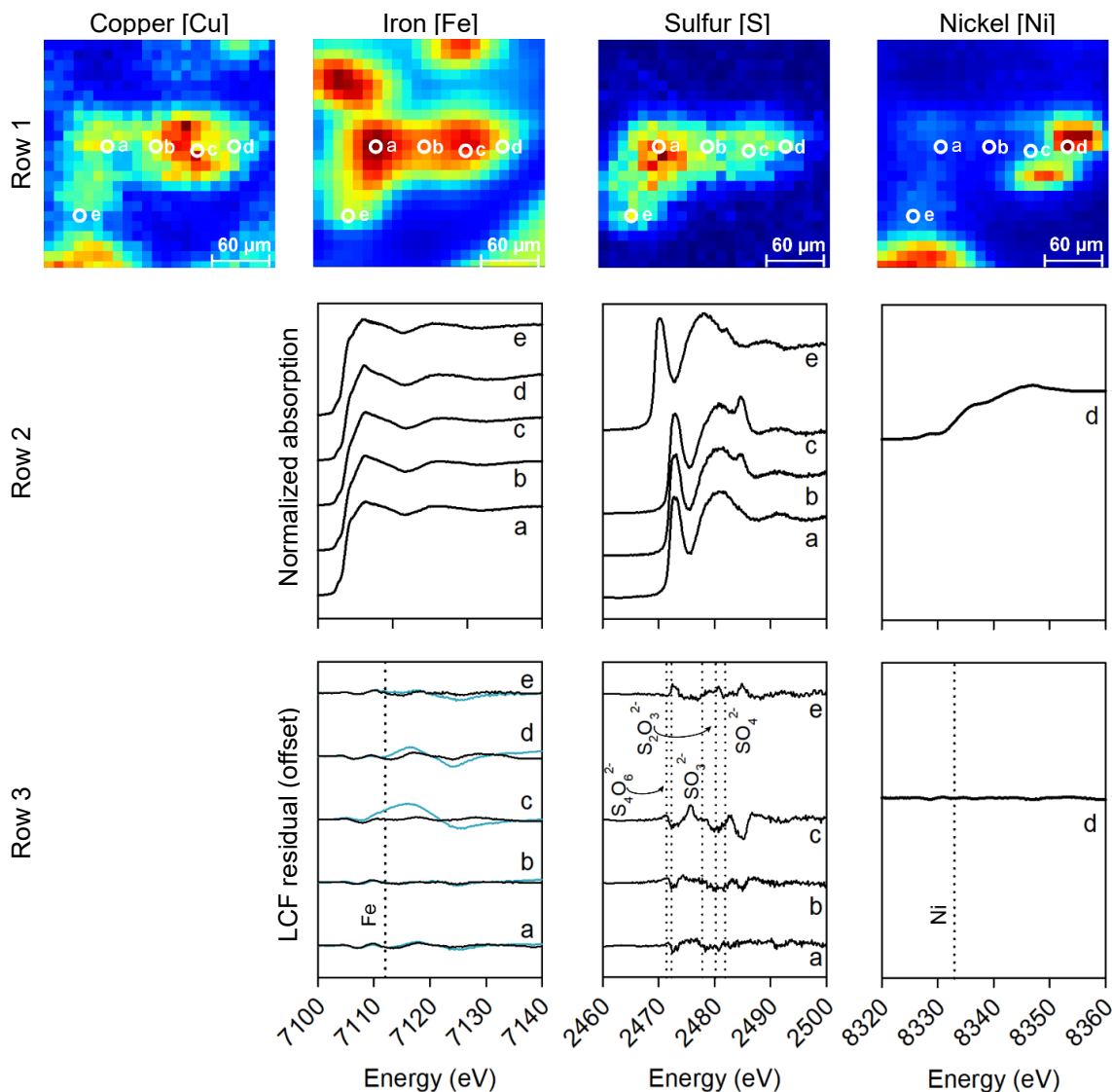


Figure 2-9: Row 1: μ XRF element maps of target pyrrhotite grain. Colour scale represents relative abundance by element, with red as highest concentration and blue as lowest. Row 2: XANES spectra for target spots identified in the element maps. Row 3: linear combination fitting (LCF) residual. Blue lines in Fe LCF residual indicate fit with only Fe-(oxyhydr)oxides and black line indicates fit that includes schwertmannite. Vertical dotted lines indicate K-edge energies. Standard spectra are provided in Figure A-6 and measured spectra plotted with LCF fits are presented in Figure A-7.

2.5 Conclusions

A variety of analytical techniques were used to provide insight into the behaviour of sulfur, iron and trace elements during sulfide oxidation in weathered waste rock. Synchrotron-based analyses were supported by calculated acid-generating potential and neutralization potential, electron-probe

microanalysis, observations of oxidation characteristics by optical microscopy and scanning electron microscopy with energy dispersive X-ray analysis, and porewater chemistry. Synchrotron-based analyses suggested the presence of nickel and mixed oxidation states of sulfur and iron associated with oxidizing pyrrhotite. Trace element concentrations in solid samples, measured by electron-probe microanalysis, and in porewater samples, combined with calculations using the speciation/mass-transfer model PHREEQC, suggested the porewater was undersaturated with respect to the secondary nickel phases included in the WATEQ4F database, and suggested that although nickel sorption to hydrous ferric oxide alteration rims was favoured, sorption sites were saturated. Porewater was circumneutral with measurable alkalinity and elevated concentrations of some trace metals, including nickel. Porewater was calculated to be saturated with the secondary minerals gypsum, amorphous $\text{Al}(\text{OH})_3$ and gibbsite, consistent with the measured alkalinity, pH, and metals concentrations. Together, these analyses suggested sulfide oxidation was proceeding, trace elements were released to porewater, and carbonate-mineral dissolution was the predominant acid-neutralizing mechanism in waste rock that had been stored subaerially for 30 years.

Chapter 3

Fe K-edge XANES across oxidizing pyrrhotite grains from natural samples of mining waste rock

Lianna J.D. Smith, Dogan Paktunc, David W. Blowes.

In preparation for submission to The Canadian Mineralogist.

3.1 Summary

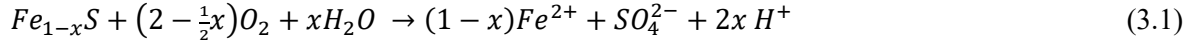
Iron K-edge X-ray absorption near edge spectra (XANES) were collected across transects of oxidizing pyrrhotite grains in natural samples of waste rock and compared to measurements conducted on standards of ferric iron, ferrous iron, and compounds of mixed oxidation states. The XANES spectra were analyzed by pre-edge centroid deconvolution and linear combination fitting. Linear combination fitting of the pre-edge region and energy range of the XANES spectra (7070 – 7220 eV) produced best fits with differing species and higher ferric iron contributions (difference of typically $f < 0.1$) than linear combination fitting of the XANES energy range. Deconvolution of the pre-edge centroids produced centroid energies that were correlated to the ferric iron contribution of the linear combination best fits of both the pre-edge and full spectrum, but a ferric iron content below a threshold value may affect the centroid energy. Ferrous iron standards that exhibited oxidation characteristics maintained a pre-edge centroid energy characteristic of ferrous iron species, and several transect spots at a calculated ferric iron contribution of $f \approx 0.2$ exhibited a 0.6 eV range in pre-edge centroid energies.

3.2 Introduction

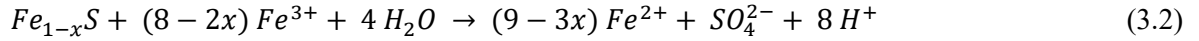
The oxidation of pyrrhotite $[\text{Fe}_{(1-x)}\text{S}]$ in mining waste rock can release acidity $[\text{H}^+]$, iron $[\text{Fe}]$, sulfate $[\text{SO}_4]$, and trace elements to the environment. Pyrrhotite is a non-stoichiometric Fe-sulfide that can form in monoclinic or hexagonal crystal systems based on a NiAs structure (Tokonami et al., 1972; Becker et al., 1997; Belzile et al., 2004). The Fe lattice positions are predominantly occupied by ferrous iron $[\text{Fe}^{2+}]$, with lesser ferric iron $[\text{Fe}^{3+}]$, both bonded to sulfur $[\text{S}]$ (Levinson and Treves, 1968; Pratt et al., 1994) in either 5-fold or 6-fold coordination (Tokonami et al., 1972). Ferric iron in the lattice provides thermodynamic stability, but Mössbauer spectra suggest Fe^{2+} and Fe^{3+} may not occur as separate species (Tokonami et al., 1972; Pratt et al., 1994). The Fe lattice contains ordered vacancies (Pierce and Buseck, 1974), other lattice defects, and impurities as Fe-substitutions, or

interstitial or admixed inclusions (Sakkopoulous et al., 1986). The lattice vacancies in monoclinic pyrrhotite causes strong ferromagnetic behaviour (Wang and Slaverson, 2005).

Pyrrhotite $[\text{Fe}_{1-x}\text{S}]$ can be oxidized by oxygen $[\text{O}_2]$ (Equation 3.1) or Fe^{3+} (Equation 3.2), according to:



and



In conditions with $\text{pH} > 3$, Fe^{2+} released from sulfide oxidation (Equation 3.1), in the presence of O_2 , can be oxidized to Fe^{3+} to perpetuate reaction 2 (at $\text{pH} < 3$; Equation 3.3), or precipitate as Fe^{3+} (oxyhydr)oxides (at $\text{pH} > 3$; Equation 3.4, with $\text{Fe}(\text{OH})_3$ representing a general Fe^{3+} (oxyhydr)oxide).



However, studies have indicated that the oxidation reactions in Equations 3.1 and 3.2 may not proceed to completion, with intermediate products that can include mixed oxidation states of S, Fe-deficient phases, various Fe-(oxyhydr)oxides, and possibly accumulated negative charge (Steger, 1982; Mycroft et al., 1995; Thomas et al., 1998, 2001; Janzen et al., 2000; Harries et al., 2013; Langman et al., 2015; Nordstrom et al., 2015; Steinepreis, 2017; Smith et al., 2021; Chapter 2).

Ratios of Fe^{2+} and Fe^{3+} were successfully determined in basaltic glasses using the pre-edge feature of synchrotron X-ray absorption near edge spectra (XANES) at the Fe K-edge, supported by Mössbauer spectra and/or wet chemical analysis (Berry et al., 2003, Cottrell et al., 2009; Fiege et al., 2017). The pre-edge features of Fe K-edge XANES spectra were analyzed in natural mineral samples and mechanical mixtures of phases consisting of varying proportions of Fe^{2+} and Fe^{3+} , and the interpretations included electron transition and Fe coordination of the deconvolution components, and pre-edge energy and intensity (Wilke et al., 2001). A study of Fe K-edge XANES in soil samples and synthetic mixtures of Fe minerals, Prietzel et al. (2007) concluded that pre-edge peak energies reasonably estimated Fe^{2+} and Fe^{3+} contributions but discriminating among specific Fe-oxyhydroxide

phases was not possible. These studies followed earlier work, which identified the pre-edge feature of Fe K-edge XANES spectra to represent the Fe oxidation state, bonding coordination and site geometry (White and McKinsty, 1966; Srivastava and Nigam, 1973; Shulman et al., 1976; Waychunas et al., 1980, 1983; Dräger et al., 1988).

The objective of this study was to evaluate Fe K-edge XANES features across transects of partially oxidized pyrrhotite grains from waste-rock samples. A better understanding of the distribution of mixed Fe oxidation states and bonding arrangements in partially oxidized pyrrhotite grains and their alteration products would improve our understanding of the pyrrhotite oxidation process in natural samples.

3.3 Experimental section

3.3.1 Sample description

The partially oxidized pyrrhotite grains analyzed in this study were obtained from one freshly blasted and two historical waste-rock samples from the Detour Lake Mine, Ontario, Canada. Samples 117, 3M and 4T in this study were obtained from subsamples of waste rock described in Smith et al., (2021) and Chapter 2. The waste rock was air-dried to minimize the potential for tertiary phase transformations and the pyrrhotite fraction from each sample was magnetically separated to increase the potential target grains. The median pyrrhotite compositions for pyrrhotite grains for samples 117 and 4T, identified by electron-probe microanalysis (EPMA) in a previous study (Smith et al., 2021; Chapter 2), correspond to approximately Fe_6S_7 , slightly Fe-deficient compared to the monoclinic, 4C-pyrrhotite composition of Fe_7S_8 . Pyrrhotite grains from sample 3M, not measured by Smith et al. (2021) or in Chapter 2, are expected to be of similar composition, based on similar formulae obtained for other samples from the same system.

The concentrated pyrrhotite samples were prepared as thin sections by Spectrum Petrographics (Vancouver, USA). The samples were mounted on Suprasil 2A quartz glass slides with cyanoacrylate (Krazy Glue®), a non-aqueous compound, to minimize mineral transformations during slide preparation. Slides were cut and polished to 30 μm thickness with double-sided, microprobe-quality finish.

3.3.2 Standards

Standards comprised natural and synthetic minerals with Fe^{2+} and Fe^{3+} phases that are commonly associated with sulfide oxidation in waste rock and tailings. Standards included ferrihydrite [nominally $5\text{Fe}_2\text{O}_3 \cdot 9\text{H}_2\text{O}$], goethite [$\alpha\text{-Fe}(\text{OOH})$], jarosite [$\text{KFe}_3(\text{SO}_4)_2(\text{OH})_6$], schwertmannite [e.g.,

$\text{Fe}_8\text{O}_8(\text{OH})_{8-2x}(\text{SO}_4)_x \cdot n\text{H}_2\text{O}$, $1 < x < 1.75$] (Schoepfer and Burton, 2021), hematite [Fe_2O_3], magnetite [Fe_3O_4], synthetic $\text{FeSO}_4 \cdot 7\text{H}_2\text{O}$, melanterite [$\text{FeSO}_4 \cdot 7\text{H}_2\text{O}$], marcasite [FeS_2], pyrite [FeS_2] and pyrrhotite [Fe_{1-x}S]. For clarity, synthetic $\text{FeSO}_4 \cdot 7\text{H}_2\text{O}$ is referred to by the chemical formula, and the natural mineral melanterite is referred to by the mineral name. The Fe-(oxyhydr)oxides were synthesized at the University of Waterloo according to the method of Schwertmann and Cornell (2000) and verified by X-ray diffraction (XRD) analysis. Any oxidation products on the Fe^{2+} standards were removed by leaching in 1 M HCl for 1 hr at 50°C under a fume hood, followed by three rinses with de-ionized (Milli-Q®) water, and a final rinse with methanol. The final products were dried in a vacuum desiccator. The Fe^{2+} and Fe^{3+} standards were applied and sealed as a thin layer to polyamide (Kapton®) tape. The standard tapes were cut and placed in random, overlapping orientations on a second layer of polyamide tape. XRD analysis of the marcasite standard produced peaks consistent with the presence of the partial oxidation product szomolnokite [$\text{FeSO}_4 \cdot \text{H}_2\text{O}$], and the diffractogram of the magnetite standards contained seven unidentified peaks (Figure B-1). Both marcasite and magnetite were maintained as standards in this study, recognizing the presence of either of these minerals in linear combination fitting (LCF) best fits may represent a contribution from the other phases. The natural melanterite standard originated from the Sherritt-Gordon Sherridon mine (Moncur et al., 2015a) archived in mineral oil. The melanterite crystals were ground using a ceramic mortar and pestle using sufficient mineral oil to isolate the melanterite from the atmosphere.

3.3.3 Fe K-edge data collection and analysis

The Fe K-edge X-ray absorption near edge structure (XANES) spectra of standards, target spots, and transects across partially oxidized pyrrhotite grains were collected at the Advanced Photon Source (APS; Argonne National Laboratory, USA), beamline 13-ID-E. The beamline has an energy range of 5.4 – 28 keV, suitable for measurements at the Fe K-edge. The beamline was equipped with a microprobe end station to provide a micro-focused spot size of $1 \mu\text{m} \times 1 \mu\text{m}$. Samples and standards were mounted at 45° to the incident beam. A Si (311) monochromator was used for this study. The energy step was set to 2.0 eV in the pre-edge region (–150 to –8 eV); to 0.1 eV in the edge region (–8 to +20 eV, which includes the pre-edge peak region); and in the post-edge region (+20 to +300) to $1/\text{\AA}$ to dynamically increase the energy steps from approximately 1 – 3.5 eV at increasing energy away from the edge. Counting time per point was set to 1 s. Standard spectra were collected in both fluorescence and transmission mode, and pyrrhotite spots and sample spectra were collected in fluorescence mode. The detector for fluorescence mode was a Vortex 4-element detector. Dead time was monitored to ensure acceptable levels were not exceeded, and a dead-time correction was applied

to the collected spectra using the processing software. A Fe-reference foil was used for internal calibration with the first-derivative peak calibrated to the Fe K-edge energy of 7110.8 eV.

Oxidation features in the spectrum of the pyrrhotite standard were observed during XANES data collection, suggesting oxidation products on the pyrrhotite standard had accumulated after the pre-treatment leach (Table 3-1 and Figure B-2). To acquire non-oxidized pyrrhotite spectra to be used as standards in data analysis, visually unaltered spots in the center of pyrrhotite grains in each in each of the samples were measured in fluorescence mode, and the white lines were evaluated for oxidation characteristics during spectra acquisition. The target grains were selected and registered using reflected light microscopy of the 13-ID-E Offline Sample Coordinate and Registration System (OSCAR).

All standards, except the melanterite paste and synthetic $\text{FeSO}_4 \cdot 7\text{H}_2\text{O}$, were prepared as multiple, randomly oriented thin layers mounted on polyamide tape for analysis during the same beamline session as the samples. The melanterite paste and $\text{FeSO}_4 \cdot 7\text{H}_2\text{O}$ were mounted in individual channels sealed with self-adhesive backing and affixed to the sample holder with polyamide tape. Standard spectra were acquired where standard thickness achieved 1 absorption length; two spectra were collected per standard.

Partially oxidized pyrrhotite grains were selected and registered using OSCAR. The target grains were mapped using the micro-X-ray fluorescence (μXRF) mapping function to identify Fe-concentration intensities of the target grains. Maps were collected with a 2 μm spot size and a counting time of 0.025 s per spot. Final transect start and end points were selected and registered from the μXRF map images. Fe K-edge XANES of transect spots were collected in fluorescence mode using a macro to move the fine stage at 1 μm step intervals along the delineated transect; one spectrum was collected per spot.

Spectra were normalized and analyzed using the X-ray absorption spectra (XAS) Viewer of Larch (V. 0.9.57; Newville, 2013). The E0 values for each collected standard, pyrrhotite and sample spectra were obtained as the energy that corresponded to the maximum peak of the normalized first derivative spectra. White line energies were obtained at the first maximum of the normalized spectra after E0.

Spectra from transect spots were analyzed by LCF from 7070 – 7220 eV, which included the pre-edge, edge and the main features of the post-edge regions; the LCF spanning 7070 – 7220 eV is referred to as the full-spectrum LCF, though this energy range truncates the beginning and end of the acquired XANES spectra. The pre-edge energy range (7104 – 7119 eV) was selected to capture the pre-edge features of the standards and transect spots. The pre-edge energy range was analyzed

separately by LCF to compare the ferrous and ferric iron components contributing the LCF best fit based on the spectral features of the pre-edge and XANES energy ranges. A maximum of four components were allowed to fit the unknown transect spectra to reduce the number of variables. LCF best fits were evaluated by comparing components and fit statistics for a given spot; comparing the consistency among components of calculated best fits of adjacent transect spots; and removing phases with low calculated contributions to evaluate the difference on the reduced χ^2 fit statistic for each spot across a transect. If removing the phase degraded the reduced χ^2 fit statistic (i.e., the reduced χ^2 value increased) by $> 5\%$ relative percent difference (RPD), the phase was considered to be a reasonable component of the LCF best fit.

The pre-edge peaks were analyzed by fitting a background curve several eV before and after the pre-edge feature using a spline function consisting of a linear function with a positive slope and a Lorentzian function. The pre-edge peaks were deconvoluted using pseudo-Voigt functions. When the Gaussian fraction was allowed to vary, the fraction of peaks fitted to the pyrrhotite standards ranged from 0.5 to 0.8, and from 0.1 to 0.7 for the standards. Spectra from sample transects illustrated a range of Gaussian contributions. A Gaussian contribution of 0.4 was selected to reduce the number of variables and was based on the Gaussian fraction for the magnetite peak when the fraction was allowed to vary. Magnetite was selected as the model compound for the Gaussian fraction because it comprises mixed oxidation states and both tetrahedral and octahedral Fe bonding arrangements. In this study, the consistent application of a 0.4 Gaussian fraction provided superior fits to pure Lorentzian or pure Gaussian functions, but fixing fractions between 0.3 and 0.6 had negligible effect on the fit statistics. The importance of constraining the Gaussian contribution, representing experimental conditions, to a pseudo-Voigt function is discussed by Farges et al., (2004). However, subsequent studies have fixed the Gaussian contributions between 0.5 and 1 based on best fits and reducing the number of variables (Wilke et al., 2001; Farges et al., 2004; Cottrell et al., 2009; Fiege et al., 2017). Fiege et al. (2017) emphasize the importance of the background fit in the pre-edge range over the deconvolution method; Berry et al. (2003) note that the choice of function is less important than consistent application; and Cottrell et al. (2009) report that both consistent application and choice of function affect spectral fitting.

3.4 Results and discussion

3.4.1 Standards

The standard spectra collected in transmission and fluorescence modes were compared to qualitatively identify over-absorption characteristics of the spectra collected in fluorescence mode.

The comparison was consistent with the expectation that over-absorption features are present in the fluorescence spectra, particularly in the white-line region for Fe^{3+} minerals (Figure B-2). The differences in calculated pre-edge energies between the two modes were similar but calculated pre-edge intensities were typically lower for the transmission spectra (Table B-1). The effect of over-absorption on the pre-edge centroid is consistent with the results from Cottrell et al., (2009) for the centroid energy, but that study identified higher centroid intensities for spectra that had been corrected for over-absorption.

The XANES spectrum of the pyrrhotite standard exhibited characteristics of oxidation, including a higher E0 value and a shifted white line of greater intensity than expected for a reduced Fe species (Table 3-1 and Figure B-2). Spectra of non-oxidized pyrrhotite (visually unaltered spots observed by reflected light microscopy) in each of the samples were acquired. Values of E0 varied by up to 1.6 eV from pyrrhotite grains measured within a waste-rock sample and among all samples (Table 3-1). Rather than merging the pyrrhotite spectra from each separate pyrrhotite spot in a sample to a single sample-specific pyrrhotite standard, the individual spectra were maintained and the multiple, sample-specific pyrrhotite standards were applied for LCF and for interpretation of the pre-edge peaks. Unlike the E0 and white line energies, the pre-edge centroid energies had little variation (0.2 eV) among all pyrrhotite samples. However, the centroid intensities were variable, with no correlation to centroid energy values, suggesting variable Fe-bonding symmetry among the sample pyrrhotite standards, either as primary mineral structure, or from early-stage oxidation (Table 3-1; Figure B-4).

The Fe^{2+} and Fe^{3+} standards had E0 and white line energies representative of their oxidation state (Table 3-1). The Fe^{3+} species had E0 energies > 7125 eV and white line energies > 7129 eV. The Fe^{2+} standards pyrite and marcasite maintained E0 (< 7116 eV) and white line (< 7119 eV) energies consistent with those expected for Fe^{2+} compounds. Magnetite, with mixed Fe oxidation states, had E0 of 7119.6 eV and white line energy of 7129.7 eV.

Deconvolution of the pre-edge centroid energies included peaks at higher energy than the main pre-edge centroid in ferrihydrite, goethite, schwertmannite and hematite (Figure 3-1). These components are not related to $1s \rightarrow 3d/4p$ transitions of the main pre-edge peak components and may represent long-range order of Fe; the centroid energies were calculated by excluding these components above 7115 eV (Wilke et al., 2001).

The pre-edge centroids of the ferrihydrite, goethite and hematite standards exhibit similar features, with main centroid energies consistent with expectation of values for Fe^{3+} species (Table 3-1; Figure B-3; Wilke et al., 2001). The pre-edge intensities calculated from the fluorescence spectra were ferrihydrite > hematite > goethite. Ferrihydrite is a nano-sized, poorly crystalline and metastable

phase with Fe vacancies and/or substitutions (Jambor and Dutrizac, 1998; Paktunc et al., 2013). In one model of ferrihydrite, all Fe occurs in octahedral coordination (Drits et al., 1993; Manceau, 2011); whereas another model proposed 20% of Fe occurring in tetrahedral coordination (Michel et al., 2007, 2010). Ferrihydrite transforms into the more crystalline phases goethite and/or hematite (Schwertmann and Murad, 1983; Jambor and Dutrizac, 1998; Schwertmann et al., 1999, 2004). Ferric iron occurs as Fe-O octahedra in both goethite and hematite, but with different octahedral arrangements, and greater Fe³⁺ vacancies and lattice distortion in goethite (Cornell and Schwertmann, 2003).

To assess the confidence in the pre-edge peak intensities of the standards, especially those that are contributed from octahedrally-coordinated Fe-O distances, bond-length data were extracted from crystal structures of goethite, hematite, ferrihydrite, schwertmannite and jarosite. Uncertainty values in Fe-O distances were calculated for each site in the structures (Table B-2). This uncertainty in the variability of Fe-O distances would represent some form of symmetry loss due to distortion in octahedral Fe and represent the source of the pre-edge peak intensities. In these calculations, the ferrihydrite structure is assumed to be composed entirely of Fe-O octahedral as per Drits et al., (1993). The greater calculated intensity of the pre-edge centroid of ferrihydrite compared to goethite and hematite is consistent with the uncertainty (standard deviation) of reported interatomic distances between Fe-O in these Fe³⁺ samples (Table 3-2, Figure 3-2). Regression analysis of the Fe³⁺ standards used in this study with the calculated uncertainty of Fe-O bond distances (jarosite, schwertmannite, ferrihydrite goethite, hematite), though a limited dataset, provides a linear trend with $R^2 = 0.84$ ($P < 0.05$) (Figure 3-2).

The FeSO₄·7H₂O standard that exhibited oxidation characteristics, with higher E0 and white line energies, and a more pronounced white line feature, and is referred to as FeSO₄·7H₂O(ox). A second FeSO₄·7H₂O sample exhibited a more pronounced white line in the fluorescence spectra, but not in the transmission spectra, and was maintained in the standard suite as FeSO₄·7H₂O (Table 3-1, Figure 3-1 and Figure B-2). Three maxima are observable in the pre-edge feature of the FeSO₄·7H₂O standard, consistent with expectations of Fe²⁺ in octahedral coordination in FeSO₄·7H₂O (Figure 3-1; Figure B-3; Wilke et al., 2001). The E0 and white line energies of melanterite and FeSO₄·7H₂O(ox) suggest the presence of Fe³⁺, but the centroid energies of melanterite and FeSO₄·7H₂O(ox) remain in the Fe²⁺ energy range (Table 3-1). Three maxima are tenuously observable in the melanterite and FeSO₄·7H₂O(ox) spectra (Figure 3-1), possibly illustrating increasing site distortion and shifting pre-edge features towards two maxima (Wilke et al., 2001). The pre-edge maxima together with the lower centroid intensities calculated for melanterite and FeSO₄·7H₂O(ox) compared to FeSO₄·7H₂O appear

to be a result of dehydration during spectra acquisition (Figure B-5). In addition, the full-energy spectra of melanterite and $\text{FeSO}_4 \cdot 7\text{H}_2\text{O}(\text{ox})$ show shifted E0 and white line energies, and more pronounced white line characteristics, consistent with oxidation characteristics (Figure B-2), despite the centroid energies reflecting a Fe^{2+} oxidation state. Because these standards had oxidized and likely dehydrated, they were not included as components in LCF. However, the discrepancy between the observed oxidation characteristics in the XANES spectra and the pre-edge centroid intensities is noteworthy, particularly because the same discrepancy was observed with the pyrrhotite standard.

The pre-edge intensities of pyrite and marcasite measured in this study are discordant with the expected relative intensities due to lattice symmetry (Table 3-1 and Figure B-3; Table B-1). Iron in both pyrite and marcasite is in octahedral coordination, however marcasite has lower lattice symmetry than pyrite (Schmøkel et al., 2014), and is more reactive than pyrite (Zhang et al., 2022), suggesting the pre-edge intensity of marcasite should be larger than that of pyrite. The discrepancy may be related to the presence of oxidation products in the marcasite standard, as identified by XRD. Both the pyrite and marcasite standards were maintained in the standard suite used for LCF.

Neither linear nor polynomial regression equations with a $R^2 > 0.7$ value could be obtained from the pre-edge centroid energy and intensity values of the standards, pyrrhotite spots, or a combined dataset (standards + transect spots; Figure 3-1). Ratios of $\text{Fe}^{3+}/[\text{Fe}^{2+} + \text{Fe}^{3+}]$ ($\text{Fe}^{3+}/\Sigma\text{Fe}$) for unknown transect spots could not be calculated based on the pre-edge centroid characteristics of the standards. Sample-specific regressions could be obtained using the sample-specific pyrrhotite spots and the Fe^{3+} standards only, however correlation remained poor with the regression and sample transect spots, illustrating the complexity of compounds where both oxidation state and coordination are variable.

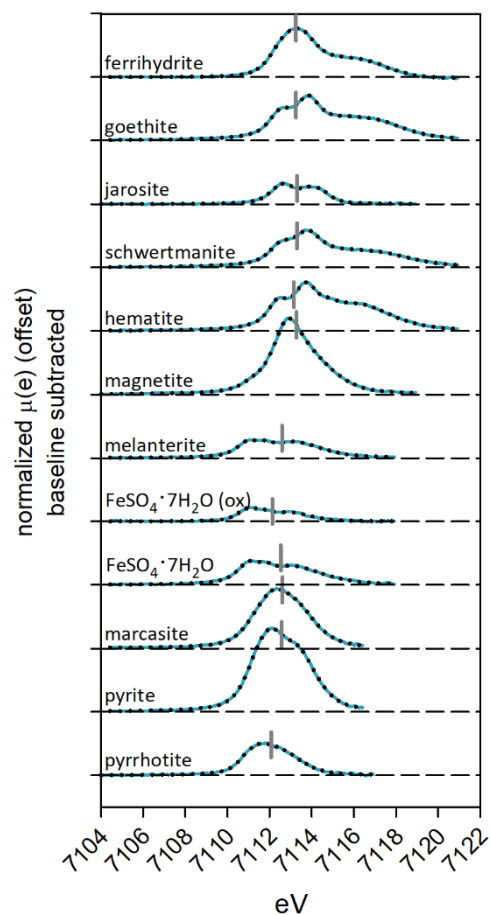


Figure 3-1: Pre-edge peaks (baseline-subtracted) for Fe^{2+} and Fe^{3+} standards. Blue curves represent measured spectra, black dotted curves represent deconvoluted spectra. Vertical grey bars illustrate centroid energy (of main peaks). Fit statistics provided in Figure B-3.

Table 3-1: E0, white line and pre-edge centroid (PEC) characteristics for standards in fluorescence mode.

Standard	E0 (eV)	White line (eV)	PEC energy (eV)	PEC intensity	PEC fit reduced Chi²
<i>Sample pyrrhotite spots (standards)</i>					
117b	7116.30	7121.61	7112.28	0.256	3.03E-7
117d	7117.51	7121.71	7112.23	0.265	2.73E-6
117e	7116.91	7121.51	7112.38	0.283	1.49E-7
117f	7115.91	7121.21	7112.25	0.274	1.45E-6
117g	7116.21	7121.51	7112.26	0.333	1.79E-7
3Ma	7116.31	7121.11	7112.24	0.232	1.62E-6
3Mb	7115.91	7121.81	7112.24	0.246	1.83E-6
3Mc	7116.41	7120.91	7112.21	0.283	3.41E-7
3Mf	7116.41	7121.71	7112.39	0.284	1.24E-7
4Ta	7116.31	7121.41	7112.28	0.320	2.44E-7
4Tb	7116.41	7121.51	7112.45	0.361	1.67E-7
4Tc	7116.41	7121.31	7112.25	0.278	8.04E-7
4Td	7116.71	7121.9	7112.32	0.291	1.81E-7
<i>Standards</i>					
Pyrrhotite	7118.52	7123.72	7112.08	0.170	2.44E-7
Pyrite	7116.62	7119.62	7112.58	0.485	3.12E-7
Marcasite	7116.92	7119.72	7112.60	0.337	2.58E-7
FeSO ₄ ·7H ₂ O	7119.83	7125.73	7112.53	0.185	2.73E-7
FeSO ₄ ·7H ₂ O (oxidized)	7118.42	7124.02	7112.13	0.077	2.85E-7
Melanterite (oxidized ± dehydrated)	7120.03	7126.32	7112.59	0.144	1.11E-7
Magnetite	7119.62	7130.42	7113.27	0.386	2.30E-7
Hematite	7122.12	7129.02	7113.16	0.155	1.88E-7
Schwertmannite	7125.92	7130.82	7113.31	0.102	1.25E-7
Jarosite	7127.12	7130.42	7113.31	0.100	1.46E-7
Goethite	7127.32	7131.97	7113.25	0.118	8.74E-8
Ferrihydrite	7122.02	7130.84	7113.26	0.221	2.16E-7

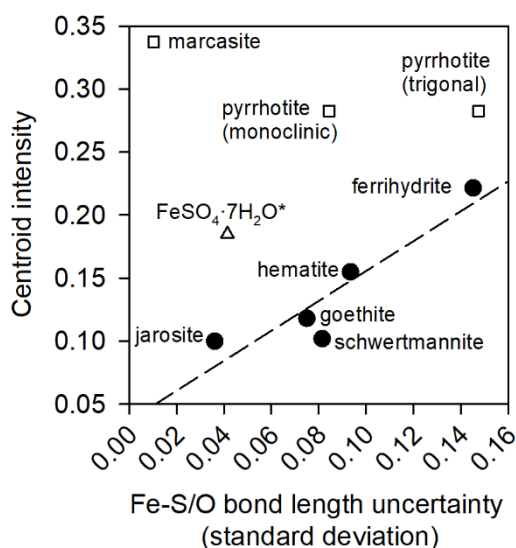


Figure 3-2: Calculated pre-edge centroid intensity (main peaks) vs. average standard deviations of the Fe-O bond lengths for Fe³⁺ minerals (circle symbols). Dashed line represents regression line for Fe³⁺ minerals with equation: [centroid intensity] = 0.037 + (1.19 × [standard deviation of Fe-O bond length]) with R² = 0.84. Included for information: Fe²⁺ minerals (square symbols) and FeSO₄·7H₂O* (triangle symbol); FeSO₄·7H₂O* plotted with the calculated pre-edge centroid intensity of the standard used in this study, at the bond length uncertainty of melanterite because of the poor-quality spectra of melanterite obtained in this study. References from which bond length uncertainty was calculated are provided in Table 3-2.

Table 3-2: Summary of Fe-O bond lengths and calculated standard deviations for Fe-O octahedra.

Mineral	System	n Fe sites	Average Fe-S/O length (Å)	Standard deviation	Reference
Pyrrhotite (Fe ₇ S ₈)	Trigonal	7	2.453	0.148	Fleet, 1971
Pyrrhotite (Fe ₇ S ₈)	Monoclinic	4	2.449	0.084	Tokonami et al., 1972
Marcasite	Orthorhombic	1	2.244	0.010	Buerger, 1937
Melanterite	Monoclinic	2	2.123	0.042	Peterson, 2003
Hematite	Trigonal	1	2.031	0.093	Finger and Hazen, 1980
Ferrihydrite	Trigonal	1	2.083	0.145	Drits et al., 1993
Goethite	Orthorhombic	1	2.022	0.075	Szytuła et al., 1968
Jarosite	Trigonal	1	2.000	0.031	Kato and Miura, 1977
Schwertmannite	Triclinic	10	2.033	0.082	Fernandez-Martinez et al., 2010

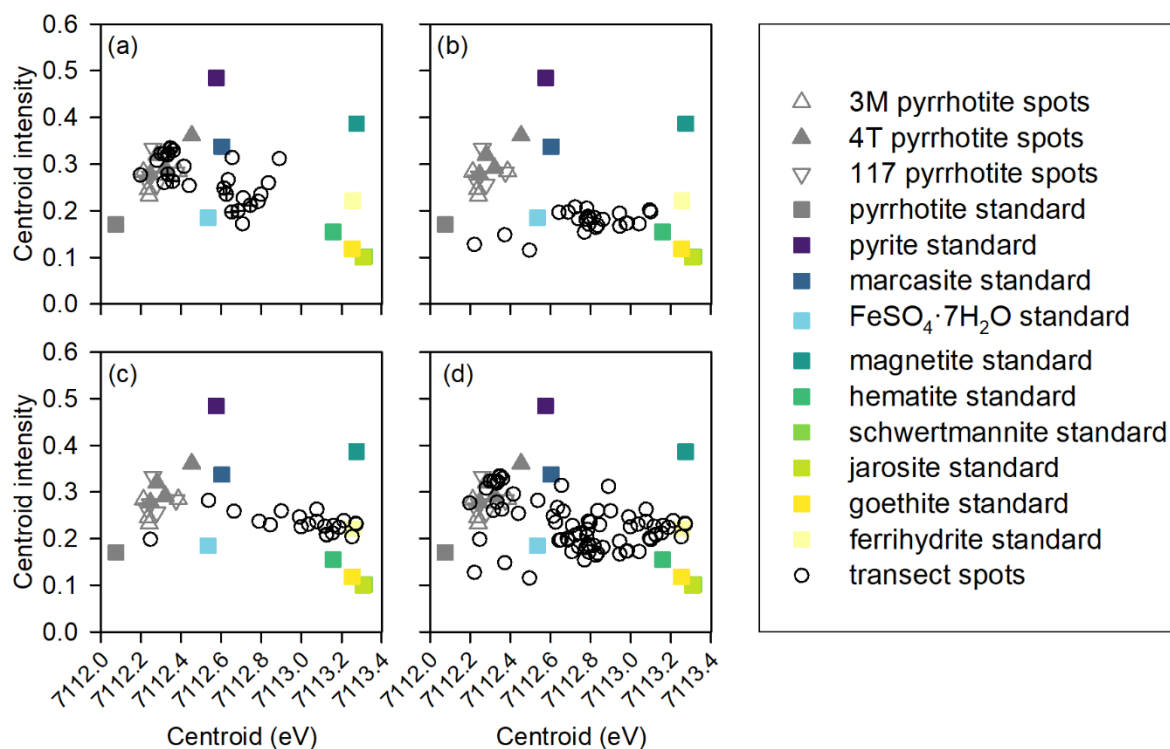


Figure 3-3: Pre-edge centroid energy vs. (main peak) intensity of standards and transect spots for (a) grain 117, (b) grain 3M, (c) grain 4T, and (d) transect spots from all three grains.

3.4.2 Transects across altered pyrrhotite grains

Grain 117 was obtained from a sample of freshly blasted waste rock, and grains 3M and 4T were obtained from samples of waste rock that had been weathering under ambient conditions for more than 30 years (Smith et al., 2021; Chapter 2). The bulk waste-rock sample from which grain 4T was obtained exhibited typically stronger oxidation characteristics than the sample from which grain 3M was obtained, with lower pore water pH and lower alkalinity concentrations, but a similar proportion of alteration products measured by quantitative mineralogical analysis (Smith et al., 2021, Chapter 2, Chapter 5). XANES spectral features from spots collected across transects of the three partially oxidized pyrrhotite grains suggest the presence of both Fe^{2+} and Fe^{3+} species, with variations across the transect of the partially oxidized grains (Figure 3-3 and Figure B-6). Deconvolution of the pre-edge centroids of the transect spots did not require extra peaks at energies > 7115 eV, as was required for the Fe^{3+} standards ferrihydrite, goethite, schwertmannite and hematite.

3.4.2.1 E0 and white line energies, and pre-edge centroid characteristics

The transect across grain 117 shows an abrupt increase to the white line energies, increasing pre-edge centroid energies, and decreasing centroid intensities as the proportion of Fe^{3+} species increase at the discrete transition from a visually unaltered pyrrhotite to an alteration zone. Values of E0 illustrate a more subdued increase, with some variation at the transition from the pyrrhotite grain to the alteration zone (Figure 3-4). The grains from the weathered waste-rock samples 3M and 4T, do not exhibit abrupt changes in white line energies, however E0 values from adjacent transect spots can change by several eV, particularly towards the center of the transect in grain 3M, and near the beginning, middle and end of the transect across 4T. These energy changes are reflected in the LCF fits of both the pre-edge and full spectrum, which included a higher proportion of Fe^{3+} minerals in the best fits for transects with higher E0 than the adjacent spots with lower E0 energies.

Centroid energies remain < 7113.0 eV in most transect spots of samples 117 and 3M, but range up to 7113.27 in sample 4T, generally consistent with the proportion of Fe^{2+} and Fe^{3+} species identified by LCF. Centroid intensities reflect the Fe-coordination symmetry, and the shifting intensities across transects suggest changing Fe coordination and lattice distortions across spots at the μm scale as pyrrhotite oxidizes and alteration products form and transform. The transect spots in 117 that are predominantly composed of pyrrhotite have the highest calculated centroid intensities of the transect spots, typically > 0.3 , and the lowest centroid energies, consistent with pyrrhotite-dominated mineralogy at those spots. These intensities are at the high end of those calculated for the sample-specific pyrrhotite measurements (Table 3-1). The lower centroid energies of the transect spots in grain 117 associated with alteration products, and most transect spots in 3M and 4T suggest decreasing Fe-coordination symmetry with formation of secondary $\text{Fe-O} \pm \text{OH} \pm \text{S}$ species as Fe-deficient sulfide phases (e.g., marcasite) and Fe-(oxyhydr)oxide phases form and transform as pyrrhotite oxidation progresses.

The centroid intensities are generally inverse to the centroid energies but show more variation. Although the correlation coefficients for the transect spots were moderate with samples 117 and 3M, ($r = -0.61$, $r = -0.57$, respectively, $P < 0.05$), there was no correlation for sample 4T ($r = -0.23$, $P > 0.05$), for the combined dataset of transect spots ($r = -0.40$, $P < 0.05$; Figure 3-3, Figure 3-4) or among sample-specific pyrrhotite standards + Fe^{3+} standards + transect spots (as in Section 3.3.2).

3.4.2.2 Linear combination fitting

The LCF best fits of the pre-edge and full-spectrum energy ranges suggested the presence of different phases associated with pyrrhotite alteration, though both spectral fits included phases that could reasonably be present.

Spots 1 – 6 of the transect across grain 117, associated with visually unaltered pyrrhotite, included small calculated (< 5%) pyrite contributions in both the pre-edge and full spectrum LCF best fits. Excluding pyrite from the LCF components at these spots degraded the reduced χ^2 fit parameter by 10 – 56% (RPD), suggesting the association of pyrrhotite with the Fe-deficient phase at these spots is reasonable. Similarly, excluding magnetite from the components for the full-spectrum LCF degraded the reduced χ^2 value by up to 25% (RPD).

Whereas the Fe^{3+} phases of the pre-edge LCF best fits for grains 117 and 3M were predominantly schwertmannite and ferrihydrite, the full-spectrum LCF fits included more prevalent ferrihydrite, goethite, and jarosite (Figure 3-4; LCF fits and statistics are provided in Figure B-7 through Figure B-12). LCF best fits for the pre-edge spectrum of grain 4T were obtained predominantly with ferrihydrite as the Fe-(oxyhydr)oxide species, whereas hematite dominated in the full spectrum LCF best fit. Fe- SO_4 phases were largely absent in both the pre-edge and full spectrum best fits for grain 4T, with exceptions at four spots in the pre-edge LCF best fits (Figure 3-4). The transformation of ferrihydrite to hematite is favored over goethite at pH 7 – 8 (Schwertmann and Murad, 1983), the pH range measured in pore water extracted from the weathered waste-rock samples 4T (Smith et al., 2021, Chapter 2). The presence of hematite favored in the full-spectrum LCF best fit of grain 4T compared to ferrihydrite calculated for grains 117 and 3M, suggest the transformation of secondary phases associated with grain 4T is more advanced than the other two grains. That grain 4T would exhibit more aged Fe-(oxyhydr)oxides is consistent with the sample origin from weathered waste rock: grain 117 was obtained from freshly blasted waste rock, and geochemical characteristics of pore water from sample 4T indicated a higher degree of oxidation and weathering than sample 3M (from Smith et al., 2021; Chapter 2).

$\text{FeSO}_4 \cdot 7\text{H}_2\text{O}$ was calculated to be present in small, but persistent contributions in the full spectrum LCF best fits for grain 3M, and spots associated with alteration characteristics in grain 117. Excluding $\text{FeSO}_4 \cdot 7\text{H}_2\text{O}$ from the LCF standards increased the reduced χ^2 statistic by up to 115% (RPD). In contrast, few spots in the pre-edge LCF best fits included $\text{FeSO}_4 \cdot 7\text{H}_2\text{O}$ and excluding this phase from the pre-edge LCF components degraded the reduced χ^2 fit statistic by < 5% (RPD), suggesting the LCF best fits of the pre-edge without a $\text{FeSO}_4 \cdot 7\text{H}_2\text{O}$ component was also reasonable. Spots with $\text{FeSO}_4 \cdot 7\text{H}_2\text{O}$ contributions typically, but not consistently, also included the Fe-deficient sulfide

marcasite. The pre-edge LCF best fits included a higher proportion of marcasite (Figure 3-4), with schwertmannite as the SO_4 phase providing a better fit, compared to the full-spectrum LCF best fits. The oxidation of marcasite is stoichiometric and produces polysulfides (Rinker et al., 1997), including ferrous sulfate (as FeSO_4 ; Zhang et al., 2022). Melanterite and/or other hydrated ferrous sulfate phases are commonly associated with marcasite oxidation (Rimstidt and Vaughan, 2003). These Fe- SO_4 phase(s) associated with sulfide oxidation have been identified by various techniques in studies of mining waste (Blowes et al., 1991; Jambor, 1994; Hammarstrom et al., 2004; Murray et al., 2004; Moncur et al., 2015a, 2015b). The considerable improvement in the reduced χ^2 fit statistic by including the $\text{FeSO}_4 \cdot 7\text{H}_2\text{O}$ standard for the full spectrum LCF of grains 117 and 3M, and the presence of a Fe-deficient sulfide phase, is consistent with the progression of pyrrhotite oxidation. The paucity of $\text{FeSO}_4 \cdot 7\text{H}_2\text{O}$ in most spots of grain 4T LCF full spectrum best fits is also consistent with that grain exhibiting a higher degree of oxidation from XANES analysis in this study, and geochemical and mineralogical analyses from previous studies (Smith et al., 2021; Chapter 2, Chapter 5).

Schwertmannite is a common precipitate in waters associated with sulfide oxidation, but typically forms distant from the site of sulfide oxidation (Schoepfer and Burton, 2021). This poorly crystalline phase forms as very fine grains and is metastable, aging to goethite at $\text{pH} > 5$ (Schwertmann and Carlson, 2005), the pH of the porewater extracted from waste-rock samples associated with grains 3M and 4T (Smith et al., 2021; Chapter 2). The schwertmannite crystal structure remains uncertain due to variable composition and metastability (Schoepfer and Burton, 2021), but Fernandez-Martinez et al., (2010) proposed a deformed structure with Fe^{3+} -O octahedra, with SO_4^{2-} forming both inner-sphere and outer-sphere complexes within the channel structures. Excluding schwertmannite and limiting the SO_4 -bearing standards to jarosite and $\text{FeSO}_4 \cdot 7\text{H}_2\text{O}$ degraded the value of the reduced χ^2 fit statistic by up to 64% (RPD) for the pre-edge LCF best fits for grains 3M and 117. Schwertmannite may be forming in microenvironments associated with pyrrhotite alteration. The presence of jarosite has been inferred by XRD and mineral liberation analysis to be forming in microenvironments associated with oxidizing pyrrhotite in samples of 3M and 4T (Chapter 5). Alternately, schwertmannite in the LCF fits in this study may represent a poorly crystalline Fe^{3+} -O-H phase with lattice distortions caused by associated S-species of indeterminate oxidation state, bonding arrangement, and possibly trapped electrons. These S species would affect Fe bonding and/or lattice distortion (e.g., Zhang et al., 2022), and, therefore, Fe K-edge XANES spectra. Previous studies of oxidizing pyrrhotite by S K-edge XANES identified or inferred the presence of mixed oxidation state S-species associated with oxidizing pyrrhotite (Langman et al., 2015; Steinepreis, 2017; Smith et al., 2021; Chapter 2).

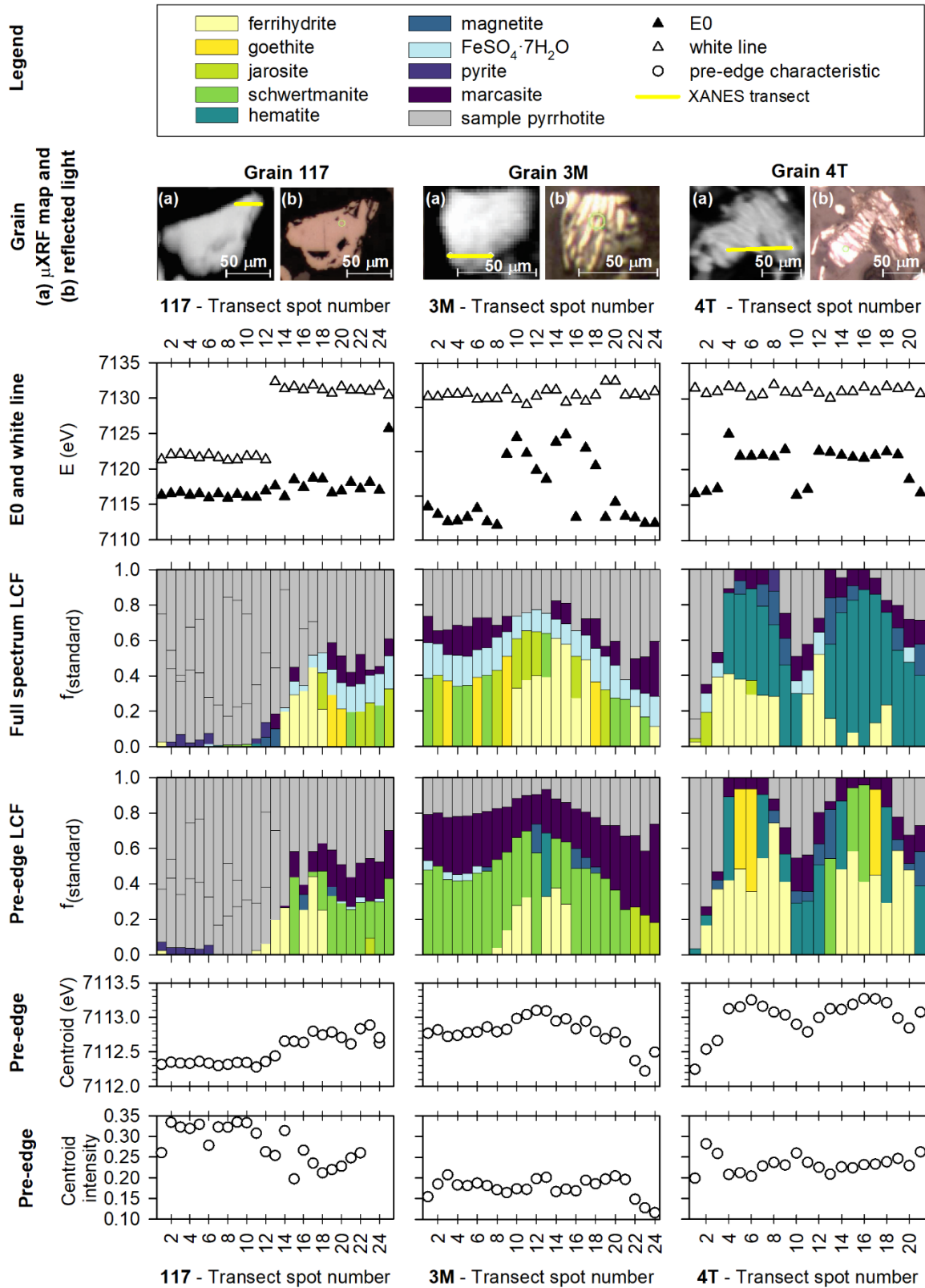


Figure 3-4: XANES features at transect spots across partially oxidized pyrrhotite grains 117, 3M and 4T. μ XRF maps of Fe in grain in (a) and reflected light images in (b) for each grain.

3.4.2.3 Ferric iron contributions ($\text{Fe}^{3+}/\Sigma\text{Fe}$)

Because a reasonable correlation could not be obtained from the ratio of $\text{Fe}^{3+}/\Sigma\text{Fe}$ and pre-edge centroid characteristics of the standards, an estimate of $\text{Fe}^{3+}/\Sigma\text{Fe}$ was calculated from LCF best fits for transect spots and compared to pre-edge centroid characteristics. Both the pre-edge and full spectrum LCF best fits included similar contributions from pyrrhotite in grains 117 and 4T. Grain 3M pre-edge LCF best fits had lower calculated pyrrhotite components and higher calculated marcasite components than the full spectrum (Figure 3-4). However, the pre-edge and full spectrum LCF best fits had similar $\text{Fe}^{3+}/\Sigma\text{Fe}$ for samples for all grains. The full spectrum LCF best fits contained Fe^{3+} contributions that were typically slightly lower than those calculated for the pre-edge. The discrepancies in $\text{Fe}^{3+}/\Sigma\text{Fe}$ contributions were typically < 0.08 with a maximum of 0.12 (e.g., transect spot 18 of grain 3M had a pre-edge LCF best fit with $\text{Fe}^{3+}/\Sigma\text{Fe} = 0.48$, whereas the pre-edge LCF best fit for the same spot calculated $\text{Fe}^{3+}/\Sigma\text{Fe} = 0.36$). Pre-edge LCF $\text{Fe}^{3+}/\Sigma\text{Fe}$ greater than those calculated from the full spectrum LCF best fits is consistent with the finding of Prietzel et al., (2001) that LCF of the pre-edge region under-estimated the Fe^{2+} component of mechanical mixtures of Fe^{2+} and Fe^{3+} minerals.

However, the pre-edge centroid energies of the pyrrhotite, melanterite and $\text{FeSO}_4 \cdot 7\text{H}_2\text{O}(\text{ox})$ standards maintained energies consistent with Fe^{2+} , despite the XANES spectra exhibiting oxidation characteristics. It is proposed here that the pre-edge centroid energies of oxidizing minerals can maintain the energy of the lower oxidation state of an oxidizing phase until a threshold Fe^{3+} contribution is surpassed. The combined dataset suggests the threshold value for these samples (analyzed in fluorescence mode with no over-absorption correction) is $\text{Fe}^{3+}/\Sigma\text{Fe} \approx 0.2$, based on the full spectrum LCF best fits (Figure 3-5). Centroid energies at $\text{Fe}^{3+}/\Sigma\text{Fe} \approx 0.2$ range from 7112.2 – 7112.9, and these data points include spots from each of the three analyzed grains.

The $\text{Fe}^{3+}/\Sigma\text{Fe}$ calculated from both the pre-edge and full-spectrum LCF best fits for the transect spots were highly correlated ($P < 0.05$) to the centroid energies in each grain transect, as well as the combined dataset (Figure 3-5). Centroid intensities were not correlated to $\text{Fe}^{3+}/\Sigma\text{Fe}$ (Figure 3-5), attributed to more intense pre-edge centroids of Fe^{3+} species dominating a combination that includes a less intense Fe^{2+} pre-edge centroid (Berry et al., 2003). Regression equations suggest $\text{Fe}^{3+}/\Sigma\text{Fe}$ from full-spectrum LCF best fits can be calculated from the pre-edge centroid energies. Both linear

regressions and second-order regressions provide $R^2 > 0.8$, with the second-order regressions providing marginally better fits (Table 3-3). The observation of a $\text{Fe}^{3+}/\Sigma\text{Fe}$ threshold value suggests any applied regression equation may have a larger error for $\text{Fe}^{3+}/\Sigma\text{Fe} < 0.2$, and the applicability of the regression equation calculated from the full dataset to partially oxidized pyrrhotite grains from other samples would need to be tested.

3.5 Conclusions

Linear combination fitting of Fe K-edge XANES spectra and deconvolution of the pre-edge centroids of transects across partially oxidized pyrrhotite grains provided insight into pyrrhotite oxidation. Results suggest phases at the 1 μm scale are a complex mixture of Fe-bonding symmetry and oxidation states as $\text{Fe-S} \pm \text{O} \pm \text{H}$ phases transform. These bonding arrangements are difficult to represent by discrete mineral phase standards in Fe K-edge XANES analyses. Oxidizing phases appear to retain the Fe^{2+} pre-edge centroid energy until oxidation produces a threshold Fe^{3+} contribution, which contributes to the complexity of XANES interpretation of spots associated with pyrrhotite oxidation in natural samples.

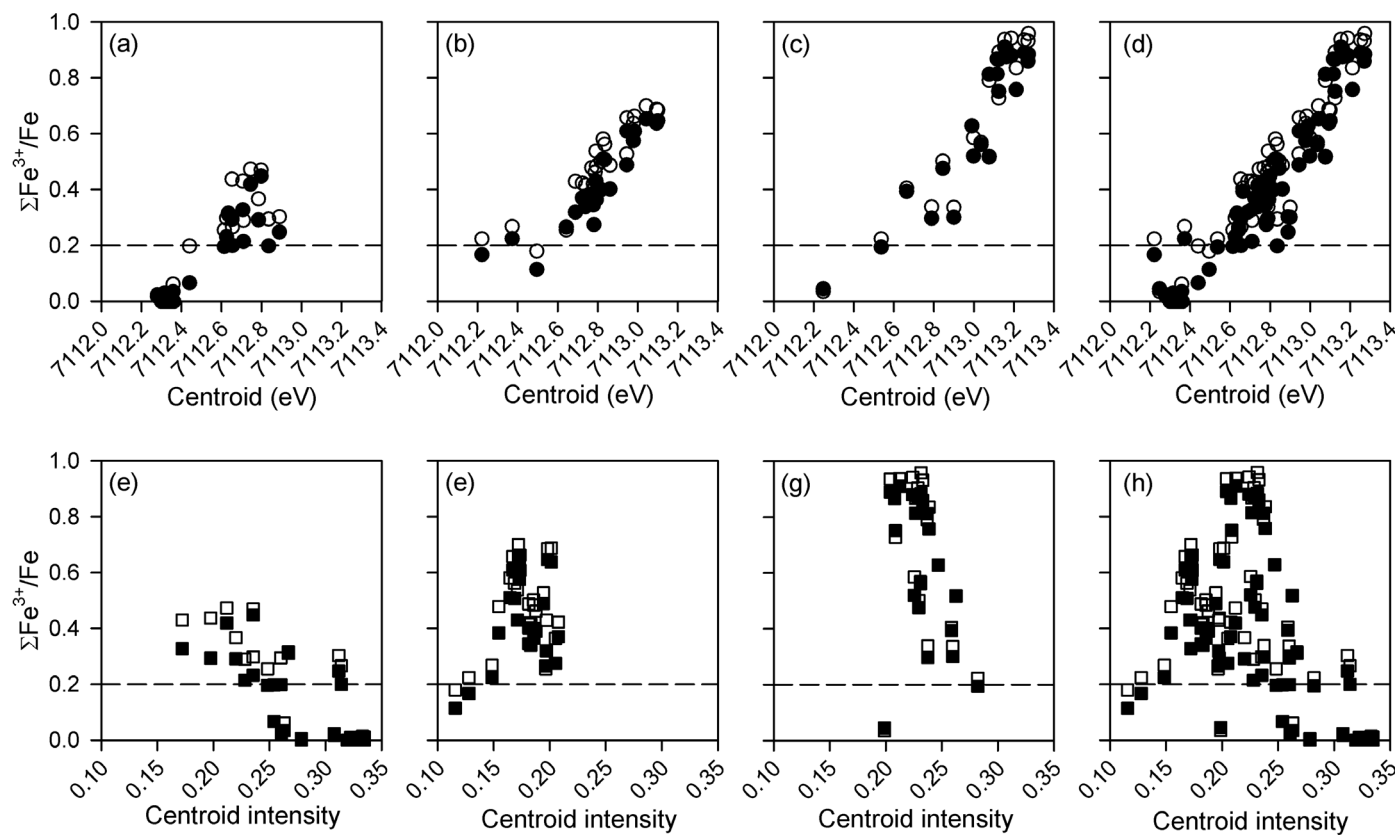


Figure 3-5: Pre-edge centroid energies vs. ratios of ferric iron to ferrous iron plus ferric iron ($\text{Fe}^{3+}/\Sigma\text{Fe}$) calculated from LCF fits of the pre-edge region (open circles), and the full spectrum (solid circles) for (a) grain 117, (b) grain 3M, (c) grain 4T and (d) the combined dataset. Pre-edge centroid intensities vs $\text{Fe}^{3+}/\Sigma\text{Fe}$ calculated from LCF fits of the pre-edge region (open squares), and the full spectrum (solid squares) for (e) grain 117, (f) grain 3M, (g) grain 4T, and (h) the combined dataset. Horizontal dashed line in all plots at $\text{Fe}^{3+}/\Sigma\text{Fe} = 0.2$.

Table 3-3: Linear and second order regressions for pre-edge centroid energies and ratios of ferric iron to ferrous iron plus ferric iron ($\text{Fe}^{3+}/\Sigma\text{Fe}$) calculated from linear combination fitting (LCF) best fits of the full energy XANES spectra (7070 – 7220 eV) , and separately the pre-edge energy range of the XANES spectra (7104 – 7119 eV) $P < 0.001$ for all regressions. C [eV] denotes centroid energy.

	Pre-edge LCF Linear regression	Second order regression	Full-spectrum LCF Linear regression	Second order regression
117	$C [\text{eV}] = 7112.3 + (1.052 \times \text{Fe}^{3+}/\Sigma\text{Fe}); R^2 = 0.84$	$C [\text{eV}] = 7112.3 + (1.766 \times \text{Fe}^{3+}/\Sigma\text{Fe}) - (1.751 \times (\text{Fe}^{3+}/\Sigma\text{Fe})^2); R^2 = 0.87$	$C [\text{eV}] = 7112.4 + (1.244 \times \text{Fe}^{3+}/\Sigma\text{Fe}); R^2 = 0.81$	$C [\text{eV}] = 7112.3 + (2.443 \times \text{Fe}^{3+}/\Sigma\text{Fe}) - (3.296 \times (\text{Fe}^{3+}/\Sigma\text{Fe})^2); R^2 = 0.89$
3M	$C [\text{eV}] = 7112.2 + (1.260 \times \text{Fe}^{3+}/\Sigma\text{Fe}); R^2 = 0.83$	$C [\text{eV}] = 7112.1 + (1.699 \times \text{Fe}^{3+}/\Sigma\text{Fe}) - (0.481 \times (\text{Fe}^{3+}/\Sigma\text{Fe})^2); R^2 = 0.83$	$C [\text{eV}] = 7112.3 + (1.231 \times \text{Fe}^{3+}/\Sigma\text{Fe}); R^2 = 0.81$	$C [\text{eV}] = 7112.1 + (2.140 \times \text{Fe}^{3+}/\Sigma\text{Fe}) - (1.097 \times (\text{Fe}^{3+}/\Sigma\text{Fe})^2); R^2 = 0.83$
4T	$C [\text{eV}] = 7112.4 + (0.880 \times \text{Fe}^{3+}/\Sigma\text{Fe}); R^2 = 0.86$	$C [\text{eV}] = 7112.2 + (1.884 \times \text{Fe}^{3+}/\Sigma\text{Fe}) - (0.876 \times (\text{Fe}^{3+}/\Sigma\text{Fe})^2); R^2 = 0.92$	$C [\text{eV}] = 7112.4 + (0.908 \times \text{Fe}^{3+}/\Sigma\text{Fe}); R^2 = 0.84$	$C [\text{eV}] = 7112.2 + (2.020 \times \text{Fe}^{3+}/\Sigma\text{Fe}) - (1.027 \times (\text{Fe}^{3+}/\Sigma\text{Fe})^2); R^2 = 0.90$
Combined dataset	$C [\text{eV}] = 7112.3 + (0.989 \times \text{Fe}^{3+}/\Sigma\text{Fe}); R^2 = 0.90$	$C [\text{eV}] = 7112.3 + (1.209 \times \text{Fe}^{3+}/\Sigma\text{Fe}) - (0.246 \times (\text{Fe}^{3+}/\Sigma\text{Fe})^2); R^2 = 0.91$	$C [\text{eV}] = 7112.4 + (1.015 \times \text{Fe}^{3+}/\Sigma\text{Fe}); R^2 = 0.89$	$C [\text{eV}] = 7112.3 + (1.462 \times \text{Fe}^{3+}/\Sigma\text{Fe}) - (0.522 \times (\text{Fe}^{3+}/\Sigma\text{Fe})^2); R^2 = 0.91$

Chapter 4

Major ion chemistry and calcium isotopic composition of waste rock and porewater in calcite-dominant and calcite-depleted systems

4.1 Summary

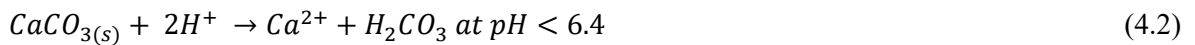
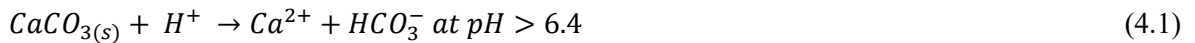
Sulfide mineral oxidation produces acid that can be neutralized by carbonate and non-carbonate minerals. Datasets and archived samples of waste-rock porewater and solids from two lithologically-distinct mines were analyzed with the objective of discriminating the relative contributions from carbonate-mineral and non-carbonate mineral dissolution to neutralizing acid produced by sulfide-mineral oxidation. Waste rock from Diavik Diamond Mine (Diavik) was composed of granite and metasediment, and porewater exhibited periods of alkalinity depletion. Waste rock from the Detour Lake Mine (Detour) was typical of greenstone gold deposits and porewater had measurable alkalinity for all samples analyzed. Major-ion ratios of solids and porewater samples suggest preferential release of calcium and/or retention in porewater. Calculations using measured geochemical parameters and calculated concentrations of dissolved inorganic carbon provided a lower bound of porewater calcium concentrations derived from carbonate-mineral dissolution; exsolution of carbon dioxide gas was not measured in these samples. A small subset of porewater and solid samples was analyzed to determine stable calcium isotope ratios ($^{44}\text{Ca}/^{40}\text{Ca}$). Waste-rock porewater from Diavik Diamond Mine exhibited alkalinity depletion and had $\delta^{44/40}\text{Ca}$ values that ranged from -1.51 to -1.08 ‰ (seawater). Porewater from Detour had measurable alkalinity and typically higher $\delta^{44/40}\text{Ca}$ values than the porewater from Diavik; Detour porewater had $\delta^{44/40}\text{Ca}$ values of -1.22 to -0.45 ‰. The $\delta^{44/40}\text{Ca}$ values of solid samples leached by acetic acid and samples digested by four-acid digestion from Detour were lower than the associated porewater samples, suggesting an isotope fractionation mechanism, likely the precipitation of secondary gypsum. Two-component mixing calculations of samples used to represent the carbonate fraction and the silicate fraction for the Diavik samples resulted in high contributions from carbonate-mineral dissolution, which are inconsistent with the extent of carbonate-mineral depletion. The solid-sample endmembers applied may not have been representative. Results suggest the geochemical evolution of porewater in waste-rock systems, particularly secondary-mineral formation, may confound the ability to apply simple two-component mixing or measured porewater geochemistry to discriminate contributions of carbonate-mineral

dissolution and silicate-mineral dissolution to acid neutralization. Additional measurements of $\delta^{44/40}\text{Ca}$ values of target mineralogical fractions within solid samples of secondary minerals may improve the mixing results.

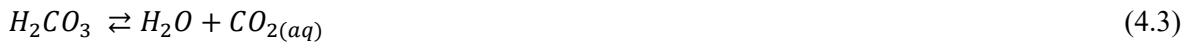
4.2 Introduction

The evolution of porewater geochemistry and mineral transformations in acidic and circumneutral waste-rock systems is complex because of concurrent sulfide-mineral oxidation; acid neutralization by the dissolution of carbonate, oxide and silicate minerals; secondary-mineral precipitation and/or dissolution; and/or cation sorption to secondary (oxyhydr)oxide minerals (e.g., Jambor et al., 2003). Quantifying the relative contributions of carbonate- and non-carbonate-mineral dissolution to the neutralization of the acid produced by sulfide oxidation could refine models and predictions of the evolution of drainage water from mine-waste systems, and, thus, its potential impact on the receiving environment.

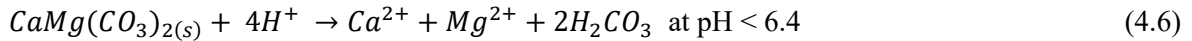
Of the minerals with potential neutralizing capacity, calcite [CaCO_3] is typically the most important in mining-waste systems because of its high solubility and typically high abundance in crustal rocks. Based on aqueous carbonate equilibria, the neutralization of acidity [H^+] by calcite is pH dependent. The predominant neutralization reaction at $\text{pH} > 6.4$ releases 1 mol bicarbonate [HCO_3^-] and one mol calcium [Ca, as the Ca^{2+} ion]. At $\text{pH} < 6.4$, the predominant aqueous carbonate species is carbonic acid [H_2CO_3]. Calcite dissolution releases 1 mol Ca^{2+} and 1 mol carbonate species per mol of CaCO_3 dissolved, regardless of pH (Equations 4.1 and 4.2).



Carbonic acid produced in the reaction described by Equation. 4.2, is in equilibrium with dissolved CO_2 [$\text{CO}_{2(aq)}$], which in turn is in equilibrium with the gas phase [$\text{CO}_{2(g)}$] (Equations 4.3 and 4.4). The measurement of $\text{CO}_{2(g)}$ within waste-rock piles can be an indication of acid neutralization by carbonate-mineral dissolution (Amos et al., 2009, 2015).



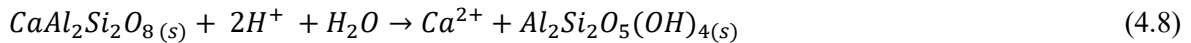
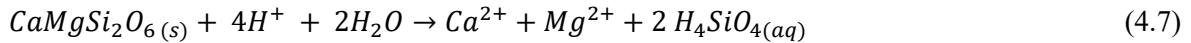
Dolomite [$\text{CaMg}(\text{CO}_3)_2$] is also considered a fast-dissolving carbonate mineral important in acid neutralization (Paktunc 1999; Jambor 2000). Dolomite dissolution releases one mole of each Ca^{2+} and magnesium [Mg, as the ion Mg^{2+}] in a ratio of 1 mol Ca^{2+} and 1 mol Mg^{2+} to 2 mol carbonate species (Equation 4.5 and 4.6). Busenberg and Plummer (1982) demonstrated that dolomite dissolution was non-stoichiometric in a brief early stage wherein the CaCO_3 component dissolved more rapidly than the MgCO_3 component, prior to dissolution becoming stoichiometric.



The Fe-bearing carbonate minerals ankerite [$\text{Ca}(\text{Fe,Mg})(\text{CO}_3)_2$] and siderite [FeCO_3] are common minerals in mine-waste systems. Ankerite dissolution is analogous to that of dolomite, producing 1 mol of Ca^{2+} and 2 mol of HCO_3^- during acid neutralization (at pH > 6.4). Siderite is a common primary carbonate mineral in quartz-carbonate vein deposits (Dubé and Gosselin, 2005). Siderite does not contain Ca. The dissolution of siderite releases HCO_3^- (or H_2CO_3) but contributes neither Ca nor consumes net acidity under aerobic condition; siderite dissolution first consumes H^+ , but then produces H^+ through Fe^{2+} oxidation and hydrolysis to $\text{Fe}(\text{OH})_3$ (Paktunc, 1999).

As the carbonate minerals dissolve to neutralize acid produced by the oxidation of sulfide minerals, non-carbonate minerals also dissolve and can act to neutralize acid, though the rate of silicate-mineral dissolution is kinetically limited (e.g., Jambor 2003; Price 2009). The dissolution of silicate minerals releases the major cations Ca, Mg, sodium [Na], potassium [K], as well as silicon [Si], aluminum [Al], and iron [Fe], along with any trace element impurities. The dissolution of available neutralizing minerals contributes to the development of pH-buffering plateaus described by Blowes and Ptacek (1994), which has been observed in several mine-waste systems (e.g., Johnson et al., 2000; Ljungberg and Öhlander 2001; Gunsinger et al., 2006; Smith et al., 2013a; Langman et al., 2015). Of the Ca-bearing silicate minerals, Ca-bearing plagioclase of the Ca-Na solid-solution series (with the calcic end-member anorthite [$\text{CaAl}_2\text{Si}_2\text{O}_8$]), the pyroxenoid wollastonite [CaSiO_3], and the clinopyroxene group (e.g., augite nominally as [$(\text{Ca,Na})(\text{Mg,Fe,Al})(\text{Si,Al})_2\text{O}_6$], and Ca endmembers diopside [$\text{CaMgSi}_2\text{O}_6$] and hedenbergite [$\text{CaFeSi}_2\text{O}_6$]) are among the faster-reacting silicate minerals, though have rates 4 – 5 orders of magnitude lower than calcite (Jambor 2000). For example, diopside dissolution by (e.g., by sulfuric acid) consumes 4 mol of H^+ and releases 1 mol Ca^{2+} (Equation 4.7).

Chemical weathering of 1 mol anorthite consumes 2 mol of H^+ and releases 1 mol of Ca^{2+} when H_2SiO_4 activity favors kaolinite $[Al_2Si_2O_5(OH)_4]$ formation (Equation 4.8).



Pertinent to Ca behavior in mine-waste systems is the common precipitation of the sparingly soluble mineral gypsum $[CaSO_4 \cdot 2H_2O]$, removing Ca from porewater. The formation of gypsum has been shown in laboratory experiments to retard the dissolution rate of calcite by forming on the calcite surface (Booth et al., 1997; Wilkins et al., 2001; Offeddu et al., 2015). A gypsum coating on carbonate surfaces was inferred in samples from a tailings impoundment (Dubrovsky et al., 1985; Al et al., 2000). Secondary siderite was identified as a coating on ankerite in samples from an anoxic tailings impoundment (Al et al., 2002), and in saturated tailings at near-neutral pH and with high concentrations of aqueous Fe^{2+} (Dubrovsky et al., 1985), suggesting the formation of secondary siderite would impede carbonate dissolution.

Several studies of rivers have apportioned Ca to silicate weathering by carbonic acid to evaluate atmospheric CO_2 consumption; these studies applied major ion ratios of the host silicate rocks and aqueous concentrations, commonly Ca/Na ratios with the assumption Na is derived from plagioclase (e.g., Blum et al., 1998; Gaillard et al., 1999; Galay and France-Lanord 1999; Anderson et al., 2000; Quade et al., 2003; Ryu et al., 2011; Moore et al., 2013). In rivers where aqueous Ca was calculated to exceed the Ca concentration of the host silicate assemblage, the “excess” Ca was attributed primarily to calcite and/or dolomite dissolution; secondary-mineral formation and/or dissolution, including non-stoichiometric dissolution, of Ca-bearing minerals also contributed to excess Ca (Blum et al., 1998; Galay and France-Lanord 1999; Oliva et al., 2004; Moore et al., 2013).

Moore et al., (2013) compared results from a mass-balance approach using Ca/Na ratios to $\delta^{44/40}Ca$ values of riverine water samples and rocks to apportion Ca between carbonate and silicate reservoirs. Calcium has six stable isotopes, of which ^{40}Ca and ^{44}Ca are the most abundant in nature, at 96.98% and 2.056%, respectively, with variations possible due to radiogenic ^{40}Ca contributions (DePaolo 2004). Lenh et al., (2017) applied $\delta^{44/40}Ca$ and $\delta^{44/42}Ca$ values, among other isotope geochemistry, to evaluate sources of mineral products in five Alaskan rivers. Other riverine studies used Ca isotopes to calculate mixing between calcite weathering, silicate weathering, and/or other input sources (Hindshaw et al., 2013; Moore et al., 2013; Jacobson et al., 2015). In addition to aqueous samples,

studies have measured $\delta^{44/40}\text{Ca}$ in samples of minerals (e.g., Ryu et al., 2011; Jacobson et al., 2015; Lehn et al., 2017). Fractionation of Ca isotopes during gypsum precipitation (Harouaka et al., 2014) and calcite precipitation has been demonstrated in laboratory experiments (Lemarchand et al., 2004; Tang et al., 2008), and in natural systems (Tipper et al., 2006; Brown et al., 2013; Nielsen and DePaolo 2013). However, Jacobson and Holmden (2008) suggest an equilibrium Ca-isotope fractionation factor very close to zero during calcite precipitation in a study of a carbonate aquifer.

This study evaluated major-ion ratios, and ratios of calculated dissolved inorganic carbon (DIC) to dissolved Ca concentrations for porewater samples, and analogous ratios for solid samples to provide a lower bound of carbonate-mineral dissolution. Calculation results were compared to a limited series of $^{44}\text{Ca}/^{40}\text{Ca}$ measurements on porewater and waste-rock solids in waste-rock systems that exhibited periods of alkalinity depletion, and waste-rock systems with measurable alkalinity. The objectives of this study were to evaluate if Ca and calculated DIC concentrations, and $^{44}\text{Ca}/^{40}\text{Ca}$ ratios could be used to apportion aqueous Ca to the dissolution of Ca-bearing carbonate and Ca-bearing silicate minerals in waste rock. A better understanding of the relative contributions of mineral types to neutralize acid produced by sulfide oxidation would improve models of long-term geochemical evolution of waste-rock piles and associated environmental impacts.

4.3 Experimental section

4.3.1 Site descriptions

Waste-rock porewater and drainage (collectively referred to as porewater samples), and solid-phase samples evaluated in this study were obtained from existing datasets and archived samples. Porewater and solids data were collected from multi-year field experiments at Diavik Diamond Mine (Diavik; Northwest Territories, Canada; Figure 4-1; Smith et al., 2013b). Porewater and solids data from Detour Lake Mine (Detour), a greenstone gold mine (Ontario, Canada; Figure 4-1), were collected from two historical waste-rock piles (McNeill 2016; McNeill et al., 2021; Smith et al., 2021; Chapter 2).

Waste rock at Diavik is Ca-poor, consisting of predominantly granitoids, with varying proportions of metasediment that is hosted in the granitic country rock as lenses and rafts. The granitic assemblage is K-feldspar [KAlSi_3O_8], plagioclase [$(\text{Na,Ca})\text{Al}(\text{Al,Si})\text{Si}_2\text{O}_8$, with Ca < 0.2 atomic proportion], and quartz [SiO_2] with < 5% each of biotite [nominally as $\text{K}(\text{Mg,Fe})_3\text{AlSi}_3\text{O}_{10}(\text{OH})_2$] and

muscovite $[\text{KAl}_2(\text{AlSi}_3\text{O}_{10})(\text{OH})_2]$, and < 2% apatite (as hydroxyapatite $[\text{Ca}_5(\text{PO}_4)_3(\text{OH})]$), with some local chloritization of biotite and sericitization of plagioclase (Jambor, 1997). The metasediment assemblage contains highly variable modes of predominantly quartz, plagioclase (with Ca < 0.3 atomic proportion), and biotite, common but irregular K-feldspar, and predominant accessory minerals of apatite and zircon $[\text{ZrSiO}_4]$, with occasional sillimanite $[\text{Al}_2(\text{SiO}_4)\text{O}]$ and tourmaline of undefined cation composition (Jambor 1997). Calcite in the Diavik waste rock is present as an accessory mineral, with carbon [C] concentrations estimated at < 0.2 wt% (0.04 – 2.14 wt%, median of 0.17 wt%, n = 34) in the < 40 mm particle fraction (Smith et al., 2013c).

The waste-rock samples from Detour exhibited a typical greenstone mineral assemblage metamorphosed to lower amphibolite facies, e.g., quartz, plagioclase, K-feldspar, chlorite [e.g., chlinochlore $(\text{Mg,Fe,Al})_6(\text{Si,Al})_4\text{O}_{10}(\text{OH})_8$], amphibole [e.g., actinolite $\text{Ca}_2(\text{Mg,Fe}^{2+})_5\text{Si}_8\text{O}_{22}(\text{OH})_2$], and clinopyroxene (Oliver et al., 2012). Both anorthite and albite contribute to the plagioclase mineral assemblage (McNeill (2016); Chapter 5; Appendix C). Carbonate minerals occur as interstitial calcite in mafic assemblages and from regional hydrothermal alteration (Oliver et al., 2012).



Figure 4-1: Locations of the Diavik Diamond Mine and the Detour Lake Mine.

4.3.2 Existing datasets

4.3.2.1 Porewater and drainage samples

Datasets and archived samples of porewater analyzed in this study from three Diavik systems that exhibited periods of alkalinity depletion, and one system that maintained measurable alkalinity. The system with measurable alkalinity was a 2-m scale active zone lysimeter (AZL) filled with waste rock

of lower metasediment proportion (system 1UW), and the alkalinity-depleted systems included a duplicate AZL filled with waste rock of lower metasediment proportion (system 1UE), two 2-m scale AZLs filled with waste rock of higher metasediment proportion (systems 3UE and 3UW), and a 15-m scale test pile constructed with waste rock of higher metasediment proportion that was covered with 1.5 m of till (glacial sediment recovered from the lake bottom) and 3 m of waste rock of lower metasediment proportion (the Covered test pile, CB; Hannam, 2012; Bailey 2013; Smith et al., 2013a; Langman et al., 2017). Sulfide-mineral content was predominantly associated with the metasediment lithology (Jambor, 1997), thus systems with higher metasediment compositions had higher concentrations of sulfur (Smith et al., 2013c; Bailey et al., 2016).

Porewater samples for Ca-isotope analysis from 1UE, 1UW, 3UW and CB were selected from archived cation samples by evaluating concentrations of major ions, pH and measured alkalinity. All but one sample were selected to represent depleted alkalinity concentrations, with saturation indices indicating undersaturation with respect to calcite but ranging from undersaturated to approaching saturation with respect to gypsum. One sample was selected with higher alkalinity and calculated to be supersaturated with respect to calcite and undersaturated with respect to gypsum, to represent conditions prior to alkalinity depletion (Table 4-1).

Datasets and archived porewater samples analyzed from the Detour waste-rock systems represented systems with measurable alkalinity and were collected by soil-water solution samplers (SWSS) installed in boreholes in an historical waste-rock pile at Detour (WRS#4, McNeill, 2016), and from porewater extracted from waste-rock samples collected from a second historical waste-rock pile at the Detour mine (WRS#1, Smith et al., 2021; Chapter 2). The depositional histories of the waste-rock piles were unknown. At the time of sampling, the waste-rock piles had single-layer soil covers that were vegetated with grasses, shrubs and trees, but the waste-rock piles had been partially excavated such that the pile profiles were exposed to the atmosphere; WRS#4 overlaid a peat layer (McNeil 2016). Samples collected from SWSS installed within the peat layer underlying WRS#4 were geochemically distinct from porewater obtained from within the waste rock and were not included in the analysis.

Table 4-1: Measured values of pH, alkalinity and dissolved calcium [Ca], and calculated saturation indices of calcite and gypsum for the porewater samples analyzed for Ca isotopes in this study. Data with * denotes data reported or presented in referenced study; reference with † indicates data presented in the supplementary material. Data with no symbols indicate this study is the first to present the value.

Sample origin	Sample type	Sample ID	Digestion or sample date	pH	Alkalinity (mmol L ⁻¹ CaCO ₃)	Ca (mmol L ⁻¹)	Log SI calcite	Log SI gypsum	δ ^{44/40} Ca (‰ seawater)	Reference for *data
Detour	Centrifuged porewater	2M-pw	24-Nov-15	8.1*	0.69*	15.5*	0.50*	0.039*	-0.84	Smith et al., 2021†, Appendix A
Detour	Centrifuged porewater	4T-pw	23-Nov-15	7.0*	0.35*	13.3*	-0.91*	0.01*	-0.62	Smith et al., 2021†, Appendix A
Detour	Centrifuged porewater	5M-pw	24-Nov-15	7.4*	0.27*	13.1*	-0.75*	0.007*	-0.82	Smith et al., 2021, Appendix A†
Detour	Centrifuged porewater	6B-pw	22-Nov-15	8.1*	1.11*	14.9*	0.70*	0.013*	-0.66	Smith et al., 2021†, Appendix A
Detour	<i>in situ</i> porewater	(4-2)-5.5	04-Sep-13	8.1*	1.31*	5.1*	0.43	-0.58	-1.22	McNeill, 2016
Detour	<i>in situ</i> porewater	(4-2)-10.5	24-Sep-12	8.0*	0.42*	12.4*	0.16	-0.070	-0.45	McNeill, 2016
Detour	<i>in situ</i> porewater	(4-2)-25.5	23-Sep-12	7.2*	6.11*	6.6*	0.42	-0.90	-1.03	McNeill, 2016
Detour	<i>in situ</i> porewater	(4-5)-15	04-Sep-13	8.1*	1.00*	11.9*	0.52	-0.074	-0.28	McNeill, 2016
Diavik	Waste-rock drainage	1UE-pw11	20-Oct-11	5.9*	0.015*	0.41*	-4.55*	-2.00	-1.39	Hannam, 2012
Diavik	Waste-rock drainage	1UE-pw13	01-Oct-13	5.0	0.025	1.1	-4.75	-1.36	-1.38	Not previously reported
Diavik	Waste-rock drainage	1UE-pw15	02-Jun-15	4.6	0.010	4.6	-4.68	-9.75	-1.42	Not previously reported
Diavik	Waste-rock drainage	1UW-pw11	20-Aug-11	8.6*	0.59*	1.1*	0.037*	-1.52	-1.20	Hannam, 2012
Diavik	Waste-rock drainage	3UW-pw15	20-Aug-15	3.5	0	5.8	—	-3.00	-1.51	Not previously reported
Diavik	Waste-rock drainage	CB-drn22	22-Nov-08	5.1*	0.032*	11.8*	-3.77*	-0.18*	-1.22	Bailey, 2013
Diavik	Waste-rock drainage	CB-drn28	28-Nov-08	4.8*	0.17*	10.8*	-3.53*	-0.21*	-1.23	Bailey, 2013
Diavik	Waste-rock drainage	CB-drn18	18-Sep-12	4.0*	0	7.4	—	-0.28	-1.08	Langman et al., 2017

All porewater samples had been measured for pH using an Orion Ross combination electrode calibrated to standards of pH 4.01, 7.00, and 10.01; for alkalinity on a filtered aliquot (0.45 µm syringe filter) by Hach digital titrator and bromocresol green/methyl red indicator (endpoint of pH 4.5); and for cations on a filtered aliquot (0.45 µm syringe filter) preserved to pH < 3 with trace-metals grade HNO₃ (McNeill, 2016). All porewater was analyzed for major cations at the University of Waterloo by ICP-OES, with QA/QC protocols following EPA method 6010C. Archived samples had been stored in a cold room (4 °C) and did not exhibit evidence of evaporation or secondary mineral precipitation by visual observation. The saturation indices (SI; as log SI) and speciation were calculated for this study using PHREEQCi v.3.3.12.12704 (Parkhurst and Appelo, 2013) using the WATEQ4F database. Inputs included field-measured pH, Eh, and alkalinity, major cations, Al, Fe, manganese [Mn], and the anions sulfate [SO₄], nitrate [NO₃], and chloride [Cl].

4.3.2.2 Solid samples

The Detour solid samples in this study were reported by McNeill (2016) and in Chapter 5. For this study the data were converted from oxide to elemental concentrations, and individual measurements of the < 425 µm size fractions of the waste-rock samples were included. The Detour solids dataset comprised 299 data points. Solid-sample data from the Diavik waste-rock systems were limited to measurements on grain-size fractions from five samples with lower sulfur concentrations and 28 samples with higher sulfur concentrations. Sample preparation and chemical composition were summarized as particle-size weighted average concentrations in the < 5 mm fraction in Bailey et al. (2016), and Bailey (2013). The same dataset was applied in this study; however, the oxide concentrations were converted to elemental concentrations, and individual measurements from the grain-size fractions < 630 µm, the sieve size closest to the < 425 µm sieve size used for Detour samples, were applied. The resulting Diavik solids dataset comprised 15 data points for the lower sulfur samples, and 64 data points for the higher sulfur samples.

Waste-rock samples from both the Diavik and the Detour waste-rock piles that hosted the SWSS were analyzed by energy dispersive X-ray fluorescence spectroscopy (ED-XRF) at the University of Waterloo using a PanAnalytical Minipal4 desktop analyzer (Bailey et al., 2016; McNeill, 2016). Solid samples obtained from the Detour waste-rock pile profile, from which porewater was extracted by centrifugation (Smith et al., 2021; Chapter 2; Chapter 5), were analyzed by whole-rock analysis with lithium metaborate fusion with ICP-MS finish (WRA) at SGS Canada (Burnaby, Canada). Results from WRA conducted by SGS Canada are presented in Table D-2.

It is important to note that the solid samples analyzed from Diavik were collected prior to the construction of the waste-rock piles and had not weathered under ambient conditions prior to analysis (Smith et al., 2013b; Bailey et al., 2016). In contrast, the Detour solid samples were collected from excavated pits and profiles of waste-rock piles that had weathered *in situ* for approximately 30 years (Cash, 2014; McNeill et al., 2016, Smith et al., 2021).

4.3.3 Solid samples: additional analyses

Carbonate-mineral grains from four thin sections of waste-rock samples from Detour (Smith et al., 2021; Chapter 2) were analyzed by electron probe micro-analysis (EPMA) with a 1 μm spot size (JEOL 8230 Superprobe, University of Ottawa, Canada). Standards included calcite, dolomite, Mn-bearing siderite [FeCO_3 , with 2.95 wt% Mn] and strontianite [SrCO_3]. Detection limits for carbonate analysis for Ca was 134 ppm, Sr was 476 ppm, Fe was 188 ppm, Mn was 144 ppm, and Mg was 115 ppm.

4.3.4 Solid samples: treatments for calcium-isotope analyses

The solid samples for Ca-isotope analyses included plagioclase grains and waste-rock matrix from Diavik, and waste-rock matrix and massive calcite from Detour. The plagioclase grains from Diavik were separated manually under a microscope from archived samples of the waste rock with lower sulfur concentrations. The plagioclase grains were first leached by acetic acid to remove any accumulated carbonate-mineral phases and the acetic-acid rinsate was discarded. The rinsed plagioclase grains were digested using the four-acid approach (hydrofluoric acid, nitric + perchloric acids, *aqua regia*), evaporated to dryness, and then reconstituted with HNO_3 for cation and Ca-isotope analyses. The calcite sample from Detour was a ~500 g solid calcite sample provided by the Detour geology department. The origin of the calcite sample was not provided, but the morphology suggested the sample was obtained from a hydrothermal vein, common on the mine property. The solid samples of waste rock consisted of air-dried fractions obtained by sieving (Smith et al., 2021; Chapter 2). An aliquot of the sieved Diavik waste-rock sample was leached with acetic acid to target the carbonate-mineral fraction, with the leachate retained and analyzed. This solid fraction was subsequently digested by the four-acid approach, evaporated to dryness and reconstituted with HNO_3 . The acetic leach of the Detour waste-rock samples and the four-acid digestions on all solid samples were conducted by AGAT Laboratories (Mississauga, ON). Acetic leaches of the Detour calcite, the Diavik waste rock, and the pre-rinse of the Diavik plagioclase were conducted at the University of

Waterloo: 2 g of the < 425 µm fraction of waste rock were leached with 30 mL of 1 M sodium acetate brought to pH 4.5 with glacial acetic acid. The samples were placed in an orbital rotator for 2 hr at 40 rpm and filtered through a 0.2 µm syringe filter. summarizes the solid samples and the leaching/digestion treatments. Rinsate and leachate were analyzed for major cations at the University of Waterloo by ICP-OES using the same protocols as the porewater samples.

4.3.5 Isotope analysis

Porewater samples, acetic-acid rinsate, and digested solid samples were analyzed at the University of Saskatchewan (Saskatoon, Canada) for $^{44}\text{Ca}/^{40}\text{Ca}$ isotopic ratios by multicollector thermal ionization mass spectrometry (MC-TIMS) using a double-spike technique, following the procedure described by Jacobsen et al., (2015). Values are reported relative to OSIL seawater in delta notation and per mil units (‰):

$$\delta^{44/40}\text{Ca} = \left(\frac{(^{44}\text{Ca}/^{40}\text{Ca})_{\text{sample}}}{(^{44}\text{Ca}/^{40}\text{Ca})_{\text{OSIL seawater}}} - 1 \right) \times 1000 \quad (4.9)$$

Standard reference material (SRM) from the National Institute of Standards and Technology (NIST) 915a and 915b were analyzed during the analyses to assess accuracy and reproducibility and results are considered reasonable when compared to long-term data for $\delta^{44/40}\text{Ca}_{915a}$ (-1.862 ± 0.006 ‰) and $\delta^{44/40}\text{Ca}_{915b}$ (-1.129 ± 0.004 ‰) reported by Jacobson et al. (2015; Table 4-2).

Table 4-2: Standard reference material from the National Institute of Standards and Technology measured during sample analyses

Standard	Measured $\delta^{44/40}\text{Ca}$ (seawater)	2 standard error
915b	-1.14	0.02
915b	-1.12	0.02
915b	-1.13	0.02
915b	-1.15	0.03
915a	-1.86	0.03

4.4 Results and discussion

4.4.1 Major cations

The concentrations of major cations in the Diavik porewater reflect the predominant felsic mineralogy, with higher concentrations of Na and K compared to the mafic and Ca-dominated mineralogy of the Detour waste rock (Figure 4-2). Major ions in the porewater samples analyzed for Ca isotopes were consistent with the relative cation concentrations of the larger datasets (Figure 4-2). Relative contributions of Ca, and to a lesser extent, Mg were typically higher in porewater samples than the solid samples for both the Diavik and Detour systems (Figure 4-2; Figure C-1), indicating preferential Ca release from mineral weathering and/or preferential retention of Ca in porewater. The concentrations measured in the Detour solid samples represents minerals that have undergone some degree of weathering (Figure C-2), which may include non-stoichiometric or preferential dissolution. The Detour porewater dataset maintained a higher proportion of Ca than the solid samples, suggesting ongoing preferential release of Ca from mineral weathering and/or retention of Ca in porewater. Molar proportions of Ca to the major cations $\text{Ca} + \text{Mg} + \text{Na} + \text{K}$ ($\text{Ca}/\sum\text{cations}$) in the Diavik porewater ranged from 0.06 – 0.74, with median of 0.27. The $\text{Ca}/\sum\text{cations}$ of the Detour porewater was higher, ranging from 0.23 – 0.77 with median of 0.62. No trends were evident between $\text{Ca}/\sum\text{cations}$ and porewater pH or measured alkalinity (Figure 4-2); these relationships did not provide insight into the relative contributions of carbonate- and non-carbonate- mineral dissolution to acid neutralization in either Ca-poor or Ca-abundant systems.

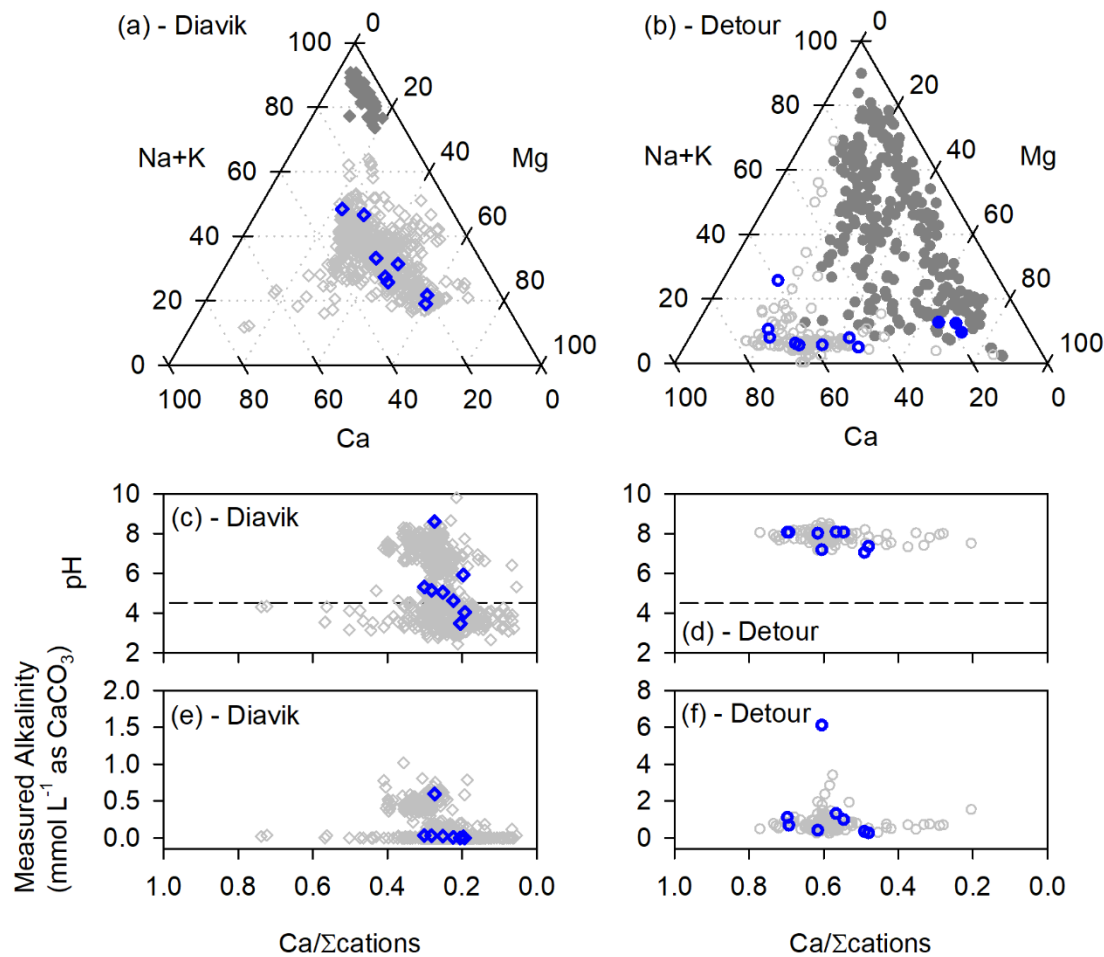


Figure 4-2: Ternary plots for (a) Diavik and (b) Detour showing molar proportions of calcium (Ca), magnesium (Mg) and sodium plus potassium (Na + K). Molar proportions of calcium to the sum of major cations ($\text{Ca}/\Sigma\text{cations}$) vs. pH for (c) Diavik and (d) Detour. $\text{Ca}/\Sigma\text{cations}$ vs. measured alkalinity for (e) Diavik and (f) Detour. Note different y-axes scales in (e) and (f). Diavik waste rock (solid dark-grey diamonds), porewater (open light-grey diamonds), Detour waste rock (solid dark-grey circles) and porewater (open light-grey circles). Porewater samples analyzed for calcium isotopes are illustrated with blue outlines. Detour waste-rock samples with extracted porewater analyzed for calcium isotopes are illustrated with solid blue symbols. Note the x-axes in (c) – (f) in reverse order to correspond to Ca-axes of ternary diagrams.

4.4.2 Secondary minerals

Mineral weathering releases the major cations Ca, Mg, Na, and K to porewater, and the oxidation of sulfide minerals releases SO_4 . Removal of Ca, Mg, Na, K and/or SO_4 by the formation of secondary minerals could affect $\text{Ca}/\Sigma\text{cations}$ ratios, and, thus, affect apportioning dissolved Ca to carbonate- and non-carbonate minerals. All Diavik and Detour porewater samples in this dataset were calculated to be undersaturated with respect to the secondary Mg-bearing phases brucite $[\text{Mg}(\text{OH})_2]$, epsomite $[\text{MgSO}_4 \cdot 7\text{H}_2\text{O}]$, and nesquehonite $[\text{Mg}(\text{CO}_3) \cdot 3\text{H}_2\text{O}]$. All samples analyzed for Ca isotopes, and all porewater samples in the Diavik dataset were calculated to be undersaturated with respect to magnesite $[\text{MgCO}_3]$. A small number of Detour samples ($n = 7$ of the 117 samples from above the peat layer) were calculated to be supersaturated with respect to this phase; PHREEQC calculations indicated Mg removal by secondary minerals was not expected, and therefore would not affect the Ca molar proportions. Similarly, removal of Mg by incorporation as an impurity in precipitating calcite and aragonite $[\text{CaCO}_3]$ has been shown to be low at Mg/Ca ratios similar to those measured in the Detour sample set for samples collected above the peat layer (0.21 – 1.31, median of 0.50, $n = 117$; e.g., Davis et al., 2004; De Choudens-Sánchez and González, 2009).

Jarosite $[\text{KFe}_3(\text{SO}_4)_2(\text{OH})_6]$ is a common secondary mineral in acidic mine-drainage waters (Dutrizac and Jambor, 2000). The formation of jarosite could remove K from the water and therefore amplify the $\text{Ca}/\Sigma\text{cations}$ ratio. None of the Detour samples collected above the peat layer was calculated to be saturated with respect to jarosite, however, another study of the Detour solids from waste-rock pile WRS#1 suggested the presence of jarosite at modal abundances $< 1\%$ (Chapter 5). Of the samples from the Diavik dataset, $n = 157$ of 793 were calculated to be supersaturated with respect to jarosite, including sample 3UW-pw15, analyzed for Ca-isotope ratios (Table 4-1). This sample had a $\text{Ca}/\Sigma\text{cations}$ ratio within the range of the Diavik dataset. There was no observable trend between $\text{Ca}/\Sigma\text{cations}$ ratios and the calculated jarosite saturation indices for either dataset (Figure 4-3). The calculated saturation indices of Mg- and K-bearing secondary phases suggest that secondary-mineral formation was not measurably amplifying the $\text{Ca}/\Sigma\text{cations}$ ratios.

Contrary to the formation of secondary Mg- and K-bearing minerals amplifying $\text{Ca}/\Sigma\text{cations}$ ratios, gypsum formation can cause the ratios to decrease by removing Ca from porewater. Gypsum is a common secondary mineral in mine-waste systems and many Diavik and Detour porewater samples were calculated to be approaching saturation, or supersaturated, with respect to gypsum, including samples analyzed for Ca isotopes (Figure 4-3). Gypsum has been identified in Detour waste-rock

samples from WRS#1 (Smith et al., 2021; e.g., Figure A-4). Like gypsum, the precipitation of secondary calcite would remove Ca from porewater. Most samples (n = 112 of 135) were calculated to be supersaturated with respect to calcite, however rates of calcite precipitation at saturation indices near equilibrium (log SI of 0 – 0.2) have been shown to be very low and may be inhibited by trace impurities (Plummer and Busenberg, 1999). Nonetheless, calculated saturation indices for calcite at saturation appear to indicate a solubility control (Figure 4-3d).

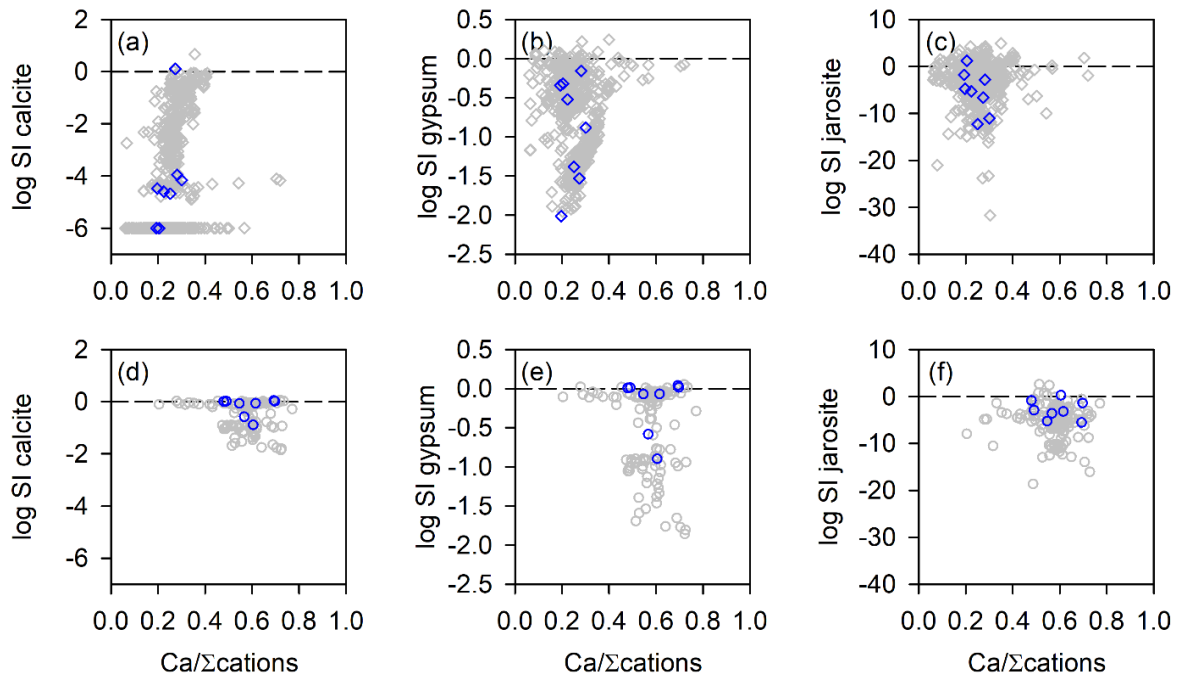


Figure 4-3: Relationship between calcium concentrations as molar proportion ($\text{Ca}/\Sigma\text{cations}$) and the calculated saturation indices (log SI) of the Diavik porewater dataset of (a) calcite, (b) gypsum and (c) jarosite; and for the Detour porewater dataset of (d) calcite, (e) gypsum, and (f) jarosite. Open grey symbols identify porewater values and open blue symbols identify samples analyzed for Ca isotopes. Data points at or above dashed horizontal line at log SI = 0 are calculated to be (super)saturated with respect to the mineral phase. Samples with no measurable alkalinity are plotted at log SI calcite = -6 for display.

4.4.3 Alkalinity

Drainage from Diavik waste rock exhibited periods of alkalinity depletion, and periods with measurable alkalinity (Hannam 2012; Smith et al., 2013a; Bailey et al., 2016; Figure C-3), whereas *in situ* porewater from Detour had measurable alkalinity for all samples obtained (McNeill 2016; Figure C-4) Centrifuged porewater from Detour waste rock also contained measurable alkalinity (Figure A-2; Smith et al., 2021; Chapter 2). Samples in both datasets had $\text{pH} < 8.3$ (Figure 4-4), with few exceptions, indicating the predominant carbonate species was H_2CO_3 and/or HCO_3^- . Alkalinity measured by titration (as measured in the datasets used in this study) includes non-carbonate species and species that contribute to “negative alkalinity” or acidity (see Kirby and Cravotta 2005a,b for detailed discussion). Alkalinity and the contribution of various species to alkalinity were calculated by PHREEQC. For samples with measured alkalinity $> 0 \text{ mg L}^{-1}$ as CaCO_3 the calculated total concentrations equaled the measured total alkalinity, and PHREEQC provided calculated concentrations of DIC species. Negative alkalinities and no DIC species were calculated for inputs with measured alkalinity $= 0 \text{ mg L}^{-1}$ as CaCO_3 . Of note are a number of Diavik samples ($n = 54$ of 793 samples) with $\text{pH} < 4.5$ but measured alkalinity $> 0 \text{ mg L}^{-1}$ as CaCO_3 . At $\text{pH} < 4.5$ acidity provided by H^+ and other protonated species is expected to equal or exceed concentrations of species that contribute to alkalinity and a positive alkalinity measured by titration is not expected; the dominant DIC species in aqueous carbonate equilibria at this pH range is H_2CO_3 , which does not contribute to alkalinity. The discrepancy may be due to samples not being at equilibrium at the time of analysis but is likely a result of field-sampling error and/or measurement sensitivity; these data points are discussed further in the calculation section (Section 4.4.4) and included in Figure C-6.

Plots of measured alkalinities (in units of mol L^{-1} as CaCO_3), and PHREEQC-calculated total alkalinity and total DIC, excluding samples with $\text{pH} < 4.5$ and measurable alkalinity, are provided in Figure 4-4. There were no observable trends between any of the alkalinity-related parameters and pH for the Detour dataset. Calculated alkalinities increased from negative values as pH increased to > 4.5 in the Diavik dataset. There were no observable trends between pH and calculated DIC for $\text{pH} < 4.5$ or $\text{pH} > 6.3$ in the Diavik dataset, but for $4.5 < \text{pH} < 6.3$, and $\text{DIC} > 0 \text{ mmol L}^{-1}$ the calculated DIC concentrations appear to increase with decreasing pH (Figure 4-4c). An exponential decay (in the form $y = a^{-bx}$) regression produced a moderate correlation of $R^2 = 0.73$, but with standard error greater than the calculated “a” coefficient. The higher calculated DIC concentrations at pH values approaching 4.5 may be an artefact of the PHREEQC calculation requiring DIC species to balance

calculated alkalinity species and H^+ as a result of disequilibrium within the sample and/or field measurement error near pH 4.5.

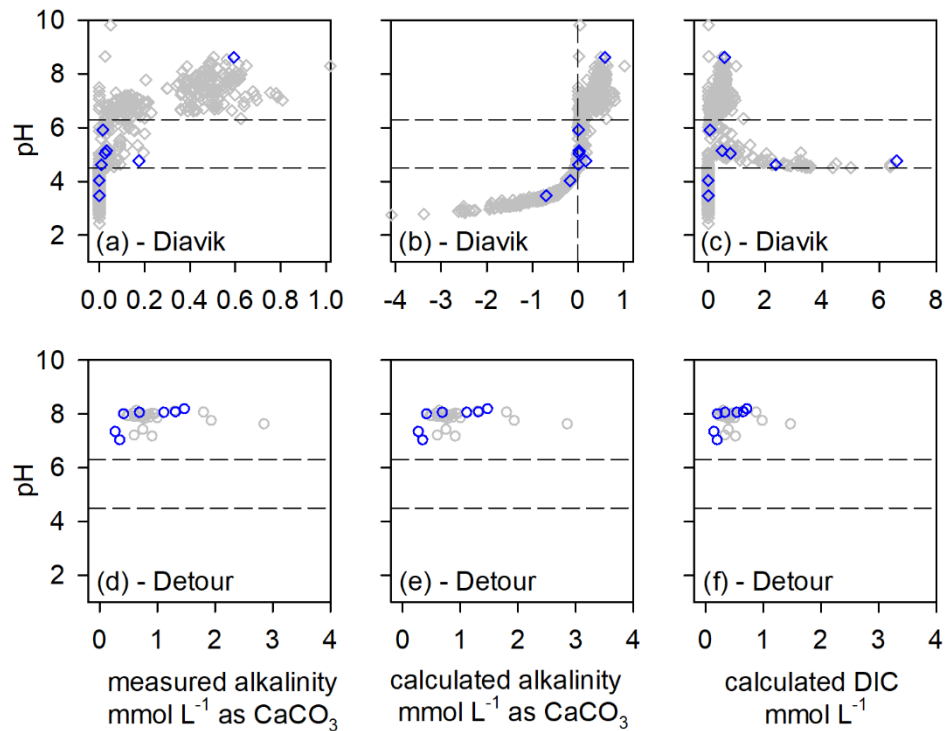


Figure 4-4: Measured alkalinity, PHREEQC-calculated alkalinity, and PHREEQC-calculated dissolved inorganic carbon (DIC) concentrations for (a – c) the Diavik porewater dataset; and (d - f) the Detour porewater dataset. Open grey symbols indicate porewater samples, open blue symbols indicate samples analyzed for Ca-isotope values. Horizontal dashed line at pH = 4.5 and pH = 6.3 in all plots. Vertical dashed line in (b) at alkalinity concentration of 0 mmol L⁻¹ as CaCO₃.

4.4.4 Calcium derived from carbonate-mineral dissolution: lower-bound calculations

Measured concentrations of Ca and PHREEQC-calculated concentrations of DIC were used to estimate a lower bound for contributions of Ca from carbonate minerals dissolving to neutralizing acidity produced by sulfide oxidation. DIC exsolved as CO_{2(g)} (i.e., per Eq. 4.2 – 4.4) was not measured, which precluded a full mass-balance calculation of carbonate-derived DIC in the systems. As lower-bound calculations, DIC was applied as a proxy for Ca derived from carbonate-mineral dissolution, based on the assumption that each mol of C is released in 1:1 ratio with Ca for calcite

dissolution (Equation 4.1), or a 2:1 ratio for dolomite (\pm ankerite) dissolution (Equation 4.5), regardless of pH. Ratios based on the assumption that calcite was the only carbonate mineral contributing Ca were calculated by Equation 4.10 and denoted as ($Ca_{cal-diss}/Ca_{pw}$). Ratios based on the assumption that dolomite (for Detour samples only) was the only carbonate mineral contributing Ca were calculated by Equation 4.11 and denoted as ($Ca_{dol-diss}/Ca_{pw}$).

$$\Sigma(DIC\ species)/\Sigma(Ca\ aqueous\ species); \text{ denoted } (Ca_{cal-diss}/Ca_{pw}) \quad (4.10)$$

$$\left[\frac{1}{2}\Sigma(DIC\ species)\right]/\Sigma(Ca\ aqueous\ species); \text{ denoted } (Ca_{dol-diss}/Ca_{pw}) \quad (4.11)$$

Analogous calculations were made for the solid samples of concentrations of C to Ca as mol [kg waste rock]⁻¹ as an indication of the contribution of calcite and dolomite to Ca concentrations in the solid samples ($Ca_{cal-min}/Ca_{sol}$) and ($Ca_{dol-min}/Ca_{sol}$), respectively. These ratios represent the proportion of Ca in the solid sample attributable to Ca-bearing carbonate minerals for the assumption that no other C sources (e.g., organics) were present. The assumption is reasonable for Diavik systems 1UE, 1UW, 3UE and 3UW because calcite was identified as the only carbonate mineral present (Jambor 1997), and the waste-rock samples were obtained directly from freshly blasted waste rock (Smith et al., 2013b). System CB, the 15-m high waste-rock pile, included a till cover constructed from till recovered from a lake bottom (Smith et al., 2013b), which may plausibly contain organic C. Geochemical characterization of the till has not been conducted, but if present organic C can contribute organic alkalinity to total alkalinity (e.g., Cantrell et al., 1990), and therefore over-calculate DIC of the porewater.

Analysis by EPMA of 13 carbonate grains from two Detour waste-rock samples collected from WRS#1 (samples described in Smith et al., 2021; Chapter 2) did not identify dolomite, however 18 of 29 grains measured from freshly blasted waste rock within the Detour pit were identified as dolomite (Table C-1). McNeill (2016) identified the presence of dolomite in waste-rock samples collected from WRS#1 for that study, and quantitative mineralogical analyses of separate samples from WRS#1 (Chapter 5) suggested the presence of dolomite, with modal abundances of dolomite > calcite in seven of nine samples. Ankerite [Ca(Fe,Mg)(CO₃)₂] was not identified by EPMA but was identified as part of the hydrothermal alteration mineral assemblage in the mafic rocks at Detour (Oliver et al., 2012). Like dolomite, ankerite has a CO₃:Ca ratio of 2:1, and Ca released during ankerite dissolution is analogous to dolomite dissolution. Siderite has not been identified in Detour samples in this, or other studies of Detour lithologies, (Chapter 5; Oliver et al., 2012; McNeill 2016; McNeill et al.,

2020), despite its common occurrence in mineral deposits. For this study, siderite was assumed to be absent, based on the mineralogical studies, and any reference to Ca contributions from dolomite dissolution implicitly includes the potential for an ankerite component. However, if present in significant quantities, ignoring siderite would over-ascribe Ca from calcite-dolomite-ankerite dissolution in the DIC-based calculation method, and produce erroneously high $\text{Ca}_{\text{cal-diss}}/\text{Ca}_{\text{pw}}$. Ratios calculated assuming only dolomite was dissolving were lower than ratios calculated assuming only calcite was dissolving for a given measured Ca concentration.

For the Diavik sample set, the $\text{Ca}_{\text{cal-min}}/\text{Ca}_{\text{sol}}$ in the solid samples had a similar range to the $\text{Ca}_{\text{cal-diss}}/\text{Ca}_{\text{pw}}$ ratios in the porewater (Figure 4-5). The $\text{Ca}_{\text{cal-min}}/\text{Ca}_{\text{sol}}$ ratios were < 0.5 ($n = 79$, range of 0.07 – 0.52, and median of 0.19). Half of the porewater samples in the Diavik dataset had no measurable alkalinity ($n = 401$ of 793 samples), and therefore $\text{Ca}_{\text{cal-diss}}/\text{Ca}_{\text{pw}} = 0$. The 54 suspect Diavik porewater samples with $\text{pH} < 4.5$ but measurable alkalinity produced high PHREEQC-calculated DIC concentrations ($> 4 \text{ mmol L}^{-1}$, with $n = 31$ of 54 samples $> 10 \text{ mmol L}^{-1}$; Figure C-6), and therefore high, suspect $\text{Ca}_{\text{cal-diss}}/\text{Ca}_{\text{pw}}$ ratios (range 0.37 – 77.7, median 1.23; Figure C-6). Additional analyses, including pCO_2 measurements, would be required to better quantify DIC concentrations in porewater with $\text{pH} < 4.5$. Samples with $\text{pH} > 4.5$ and measurable alkalinity had $\text{Ca}_{\text{cal-diss}}/\text{Ca}_{\text{pw}}$ range of 0.002 – 1.86 and median of 0.16. Ratios of $\text{Ca}_{\text{cal-diss}}/\text{Ca}_{\text{pw}} > 1$ are incompatible with the conceptual model that all DIC was contributed by carbonate-mineral dissolution in a 1:1 molar ratio with Ca, i.e., suggesting an excess of Ca from carbonate-mineral dissolution over the measured concentration of dissolved Ca. The three Diavik samples with $\text{pH} > 4.5$, measurable alkalinity and calculated $\text{Ca}_{\text{cal-diss}}/\text{Ca}_{\text{pw}} > 1$ had pH near 4.5 and low measured alkalinity, suggesting that, like samples with $\text{pH} < 4.5$ and measurable alkalinity, the porewater of these samples was likely not at equilibrium, or the field-measured alkalinity or pH values were erroneous. Excluding the three samples with $\text{pH} > 4.5$, measured alkalinity, and calculated $\text{Ca}_{\text{cal-diss}}/\text{Ca}_{\text{pw}} > 1$ produced a range of 0.002 – 0.96 with a median of 0.11 ($n = 334$; Figure 4-5). These lower-bound calculations suggest calcite dissolution commonly contributed to porewater Ca concentrations. Calcite dissolution was also indicated by the calculated saturation indices, with only 4 of 793 Diavik porewater samples calculated to be supersaturated with respect to calcite (Figure 4-3). Similar to the apparent trend of pH with DIC for samples with $4.5 < \text{pH} < 6.3$, the $\text{Ca}_{\text{cal-diss}}/\text{Ca}_{\text{pw}}$ ratios appear to decrease with increasing pH (Figure 4-5), consistent with ongoing calcite dissolution to neutralize acidity.

The $\text{Ca}_{\text{cal-diss}}/\text{Ca}_{\text{pw}}$ ratios for porewater samples from the Detour dataset at < 25 m depth ranged from 0.02 – 0.75, with a median of 0.06, lower than the median value calculated for the Diavik samples. Higher concentrations of Ca in Detour porewater and/or lower DIC concentrations would cause lower $\text{Ca}_{\text{cal-diss}}/\text{Ca}_{\text{pw}}$ ratios. In a system where both calcite and dolomite dissolution contribute to porewater Ca concentrations, $\text{Ca}_{\text{cal-diss}}/\text{Ca}_{\text{pw}}$ overestimates, and $\text{Ca}_{\text{dol-diss}}/\text{Ca}_{\text{pw}}$ underestimates the minimum contribution of carbonate dissolution to Ca porewater concentrations. The range and median values of the $\text{Ca}_{\text{dol-diss}}/\text{Ca}_{\text{pw}}$ ratios were half that of the $\text{Ca}_{\text{cal-diss}}/\text{Ca}_{\text{pw}}$ ratios (0.01 – 0.37 with median value of 0.03). The range bounded by each of these carbonate-mineral contributions in the Detour samples is illustrated in Figure 4-5. There was no observable trend between $\text{Ca}_{\text{cal-diss}}/\text{Ca}_{\text{pw}}$ ratios and pH (Figure 4-5).

Whereas correlating ratios with common components can results in Pearson’s “spurious correlations” (Chayes, 1971), deviations from the regression lines of ratio correlations can be informative. There was no trend in calculated DIC concentrations with $\text{Ca}_{\text{cal-diss}}/\text{Ca}_{\text{pw}}$ ratios for the Diavik dataset as a whole (Figure 4-5). However, evaluating the datasets by excluding data points with $\text{pH} < 4.5$ and measurable alkalinity (i.e., suspect, high $\text{Ca}_{\text{cal-diss}}/\text{Ca}_{\text{pw}}$ values), and considering each waste rock-system separately, four of the five waste-rock systems produced highly correlated regressions (Figure C-7). System 1UW did not produce a high correlation coefficient. All porewater samples from 1UW were circumneutral ($\text{pH} 6.3 - 8.6$; median of 7.5, $n = 138$). The $\text{Ca}_{\text{cal-diss}}/\text{Ca}_{\text{pw}}$ values for 1UW samples appear to be independent of DIC concentrations, suggesting the higher ratios are caused by relatively lower porewater Ca concentrations rather than relatively higher DIC concentrations. At circumneutral pH, like in the 1UW system, pH is expected to be buffered by carbonate-mineral dissolution, and this system typically had the highest median value of $\text{Ca}_{\text{cal-diss}}/\text{Ca}_{\text{pw}}$ (0.21) among the Diavik systems.

For $n = 123$ of 135 samples in the Detour dataset, both $\text{Ca}_{\text{cal-diss}}/\text{Ca}_{\text{pw}}$ and $\text{Ca}_{\text{dol-diss}}/\text{Ca}_{\text{pw}}$ increase with increasing DIC concentrations along regression curves with the same slope, but with different intercepts, illustrating the shift as a result of the 2:1 molar ratio of C:Ca in dolomite (Figure 4-5). Where the trends in $\text{Ca}_{\text{cal-diss}}$ and $\text{Ca}_{\text{dol-diss}}$ are similar, the term $\text{Ca}_{\text{minl-diss}}$ denotes the contribution of Ca from carbonate-mineral dissolution, and is used in the discussion to refer to both $\text{Ca}_{\text{cal-diss}}$ and $\text{Ca}_{\text{dol-diss}}$. Samples plotting above the regression lines in Figure 4-5 show increasing $\text{Ca}_{\text{minl-diss}}/\text{Ca}_{\text{pw}}$ at relatively constant (respective) $\text{Ca}_{\text{minl-diss}}$ concentrations, illustrating that the higher ratios were caused by relatively lower Ca concentrations rather than relatively higher DIC concentrations, similar to the

trend from the Diavik system 1UW. Of the 12 samples that suggest the $Ca_{\text{minl-diss}}/Ca_{\text{pw}}$ was higher as a result of relatively lower Ca concentrations, seven were collected from SWSS installed at < 5.5 m depth. These shallow samples were calculated to be supersaturated with respect to calcite, but undersaturated with respect to gypsum. Seven of the eight samples were calculated to be supersaturated with respect to dolomite, however, the precipitation of dolomite would not be expected (Busenberg and Plummer, 1982). The lower Ca and SO_4 porewater concentrations measured in these porewater samples from < 5.5 m depth (McNeill, 2016) suggest a compositional or physical difference affecting waste rock in the upper 2 – 5 m compared to the deeper portions of the waste-rock pile. The compositional difference may be a result of waste-rock pile construction (i.e., different waste-rock lithologies placed at the top of the pile during pile construction), the influence of the cover material, and/or the downward propagation of a sulfide-oxidation front depleting sulfide minerals with carbonate minerals dissolving to (super)saturation to neutralize the acid. The physical difference may be related to the hydrologic conditions in the upper ~5 m, where capillarity tension may be affecting the equilibrium constants for secondary minerals, particularly gypsum precipitation (Pedretti et al., 2015). Ratios of $Ca_{\text{minl-diss}}/Ca_{\text{pw}}$ would be amplified by removal of Ca from porewater by gypsum formation.

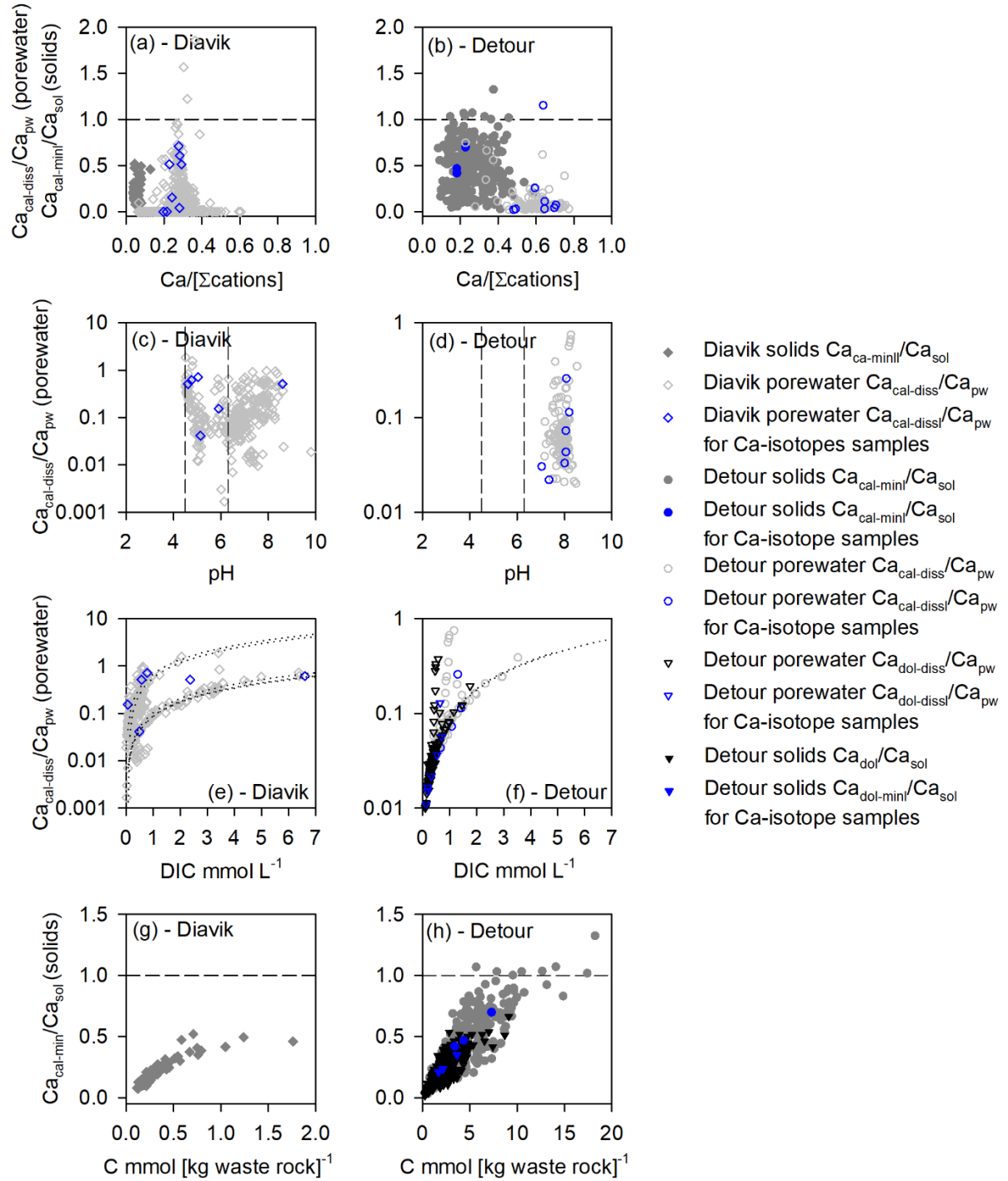


Figure 4-5: (a) Diavik and (b) Detour datasets of Ca-molar proportion of cations ($\text{Ca}/\Sigma\text{cations}$) vs. the calculated proportion of dissolved Ca in porewater contributed by calcite dissolution ($\text{Ca}_{\text{cal-diss}}/\text{Ca}_{\text{pw}}$), and the calculated proportion of Ca from calcite in the total concentration of Ca ($\text{Ca}_{\text{cal-minI}}/\text{Ca}_{\text{sol}}$) in solid

samples. (c) Diavik (e) Diavik dataset of pH vs. ($\text{Ca}_{\text{cal-diss}}/\text{Ca}_{\text{pw}}$). (e) Diavik and (f) Detour datasets of dissolved inorganic carbon (DIC) vs. $\text{Ca}_{\text{mini-diss}}/\text{Ca}_{\text{pw}}$. $\text{Ca}_{\text{mini-diss}}/\text{Ca}_{\text{pw}}$ indicates ratio calculated assuming calcite dissolution or dolomite dissolution. (g) Diavik and (h) Detour dataset of the calculated proportion of Ca from calcite or dolomite in the total concentration of Ca ($\text{Ca}_{\text{mini}}/\text{Ca}_{\text{sol}}$) in solid samples. Axes denoted $\text{Ca}_{\text{mini}}/\text{Ca}_{\text{sol}}$ indicates the ratio of carbonate calculated as $[\text{mol calcite}]/[\text{kg waste rock}]^{-1}$, or as $[\text{mol dolomite}]/[\text{kg waste rock}]^{-1}$ to the concentration of Ca as $[\text{mol Ca}]/[\text{kg waste rock}]^{-1}$. Horizontal dashed line in (a) and (e) at a molar ratio of 1. Vertical dashed lines in (c) and (d) at pH 4.5 and 6.3. Dotted lines in (e) and (f) are the regression lines for $\text{Ca}_{\text{cal-diss}}/\text{Ca}_{\text{pw}}$ vs. DIC for the various systems. Dashed horizontal lines at 1 indicate all Ca measured is attributable to carbonate-mineral presence (for solid samples), or dissolution (for aqueous samples) for this calculation approach.

4.4.5 $\delta^{44/40}\text{Ca}$ values of porewater

Samples of drainage from Diavik waste rock had $\delta^{44/40}\text{Ca}$ values that were more negative than those of porewater samples from Detour waste rock (Table 4-1). The range of $\delta^{44/40}\text{Ca}$ values for Diavik porewater samples was -1.51 to -1.08 ‰, and for Detour samples above the peat layer was -1.22 to -0.45 ‰, with median values of -1.31 ‰ and -0.82 ‰, respectively. The sample collected from within the peat layer, with a measured value of -1.03 ‰ was not included in the interpretation of Ca-isotope values, but the value is maintained in figures and tables for information.

4.4.6 Porewater $\delta^{44/40}\text{Ca}$ values and ion ratios

The $\delta^{44/40}\text{Ca}$ values of the Diavik samples appear to be independent of both the Ca/Na and Ca/K ratios (Figure 4-6), suggesting a possible influence on the $\delta^{44/40}\text{Ca}$ value from a Ca source other than the weathering of Ca-poor minerals such as, Na-bearing plagioclase, K-feldspar, and K-bearing micas. In addition to calcite dissolution, the dissolution of apatite in acid-neutralizing reactions was likely contributing to the porewater concentrations of Ca in the Diavik samples (Langman et al., 2019). Ca-isotope measurements were not conducted on apatite samples, and dissolution of this mineral may be influencing the $\delta^{44/40}\text{Ca}$ values of the Diavik porewater.

The $\delta^{44/40}\text{Ca}$ values of the Detour samples do not exhibit a trend with Ca/K or Ca/Mg ratios, but $\delta^{44/40}\text{Ca}$ values increase with Ca/Na ratios (Figure 4-6), likely from plagioclase dissolution. The solid-solution minerals that include Ca and Mg, and the K-bearing mineral assemblage obscure any weathering relationships.

The $\delta^{44/40}\text{Ca}$ values appear to increase with increasing Ca/SO_4 ratios for the Diavik sample set, whereas the $\delta^{44/40}\text{Ca}$ values appear to be independent of the Ca/SO_4 ratios for the Detour dataset (Figure 4-6). Porewater SO_4 concentrations were attributed to sulfide oxidation in both systems. A regression line with moderate correlation can be calculated for $\delta^{44/40}\text{Ca}$ to Ca/SO_4 of the Diavik samples ($R^2 = 0.55$). The Detour dataset suggests a possible control on the Ca and SO_4 concentrations, likely gypsum formation, which confounded apportioning porewater Ca to carbonate-mineral and silicate-mineral sources. Furthermore, capillarity tension in models of waste-rock piles has been shown to increase the equilibrium constant of gypsum and promote gypsum formation (Pedretti et al., 2015). This process may be occurring in both the Diavik and Detour systems, which would influence the Ca reservoirs of each system, and which would not be indicated by the saturation indices calculated by PHREEQC. However, the dataset is small and correlations and apparent trends should be interpreted with caution.

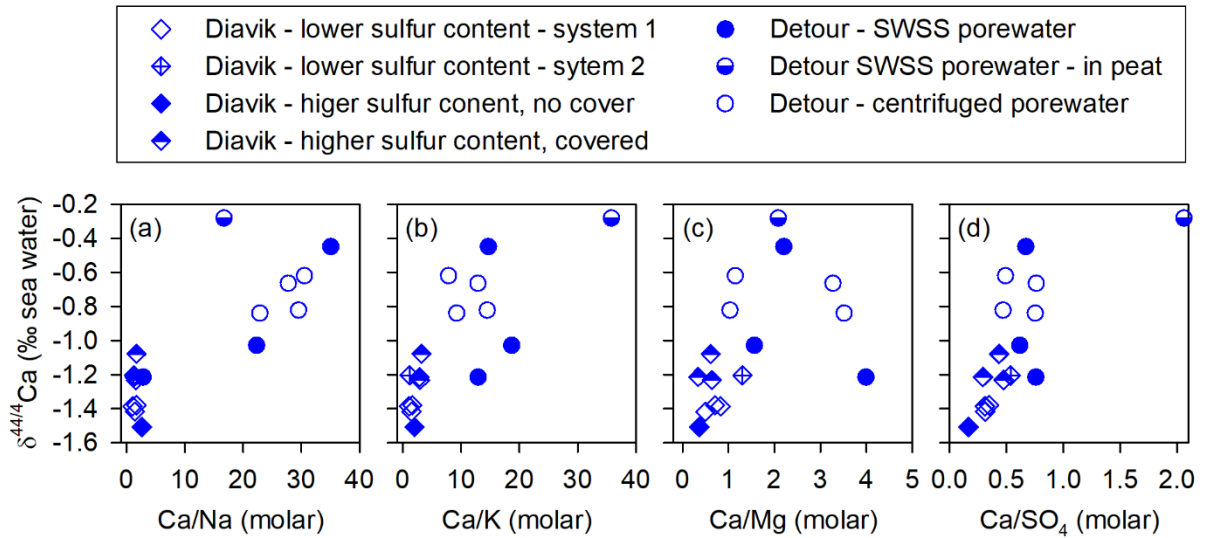


Figure 4-6: Molar ratios of calcium (Ca) to (a) sodium (Na); (b) potassium (K); (c) magnesium (Mg); and sulfate (SO₄).

4.4.7 Apportioning calcium to carbonate and silicate fractions using $\delta^{44/40}\text{Ca}$ values

An apparent trend between $\text{Ca}_{\text{cal-diss}}/\text{Ca}_{\text{pw}}$ and the measured $\delta^{44/40}\text{Ca}$ values for samples with $\text{DIC} > 0$ for the combined (Detour + Diavik) dataset (Figure 4-7) suggests $\delta^{44/40}\text{Ca}$ values and $\text{Ca}_{\text{cal-diss}}/\text{Ca}_{\text{pw}}$ calculations may be promising approaches to apportion carbonate-mineral contributions of Ca to aqueous concentrations of Ca in these datasets. However, the regression calculation provided only a moderate correlation coefficient ($R^2 = 0.41$), suggesting these results should be interpreted with caution. The $\text{Ca}/\Sigma\text{cations}$ and the measured $\delta^{44/40}\text{Ca}$ values of the combined dataset (Diavik + Detour) and moderate correlation ($R^2 = 0.62$) can be calculated (Figure 4-7). The dataset is small, and the Diavik and Detour groupings appear to be influencing the regression calculation. Any interpretations of potential correlations between or within the datasets are tenuous. As separate groups, the Diavik and Detour data each illustrate values of $\delta^{44/40}\text{Ca}$ that appear to be independent of the $\text{Ca}/\Sigma\text{cations}$ ratio. Variable $\delta^{44/40}\text{Ca}$ values at relatively constant $\text{Ca}/\Sigma\text{cations}$ ratios suggests a mechanism(s) influencing the $\delta^{44/40}\text{Ca}$ values that has little effect on $\text{Ca}/\Sigma\text{cations}$ ratios.

The $\delta^{44/40}\text{Ca}$ values appear to increase with increasing log SI calcite to calcite saturation for porewater samples with measurable alkalinity for a dataset that includes both Diavik and Detour samples (Figure 4-7). A regression line with high correlation can be calculated for $\delta^{44/40}\text{Ca}$ to the calculated saturation indices of calcite ($R^2 = 0.94$). When evaluated separately, the Diavik system for samples with measurable alkalinity and $[\log \text{SI calcite}] < 0$, maintains a mutually increasing relationship with a very similar regression line and high correlation coefficient ($R^2 = 0.84$) but over a very small range of log SI calcite values. The calculated saturation indices of calcite for the larger Diavik porewater datasets (Figure 4-3) illustrates the limited range of the Ca-isotope samples, again cautioning that the interpretation of a correlation on small, weighted datasets is tenuous. The Diavik samples were calculated to be undersaturated with respect to gypsum and show no relationship between $\delta^{44/40}\text{Ca}$ values in porewater and the calculated saturation indices of gypsum (Figure 4-7).

The Detour samples were calculated to be at or approaching saturation with respect to calcite and gypsum, and the $\delta^{44/40}\text{Ca}$ values appear to be independent of the calculated saturation indices (Figure 4-7). The one Detour sample with a lower calculated saturation index for gypsum was collected from a SWSS at 5 m depth and was consistent with the shallow (~2 – 5 m deep) SWSS samples of the porewater dataset of that had lower Ca porewater concentrations (McNeill 2016); these shallow samples were also calculated to be undersaturated with respect to gypsum.

Despite the small datasets, the relationships of $\delta^{44/40}\text{Ca}$ porewater values with calculated saturation indices do not preclude the possibility that gypsum formation influences $\delta^{44/40}\text{Ca}$ porewater values in systems where that phase may be forming. The $\delta^{44/40}\text{Ca}$ value of gypsum would depend on the $\delta^{44/40}\text{Ca}$ values of the porewater from which it was forming, and isotopic fractionation during gypsum formation. A laboratory study of abiotic gypsum precipitation reported an isotopic fraction factor ($\Delta^{44/40}\text{Ca}_{\text{solid-fluid}} = \delta^{44/40}\text{Ca}_{\text{solid}} - \delta^{44/40}\text{Ca}_{\text{fluid}}$) of -2.25‰ to -0.82‰ , with the lighter isotope preferentially partitioned into the forming gypsum (Harouaka et al., 2014).

Because the Diavik, Detour, and combined datasets of $\delta^{44/40}\text{Ca}$ are small, interpretations of potential correlations are not robust. However, the trends and implications identified in this study warrant further investigation on additional samples. Evaluations should include the relationship between $\delta^{44/40}\text{Ca}$ values and non-carbonate- and carbonate-mineral dissolution, secondary-mineral formation and dissolution, and the influence of the geochemical and organic composition of a cover system.

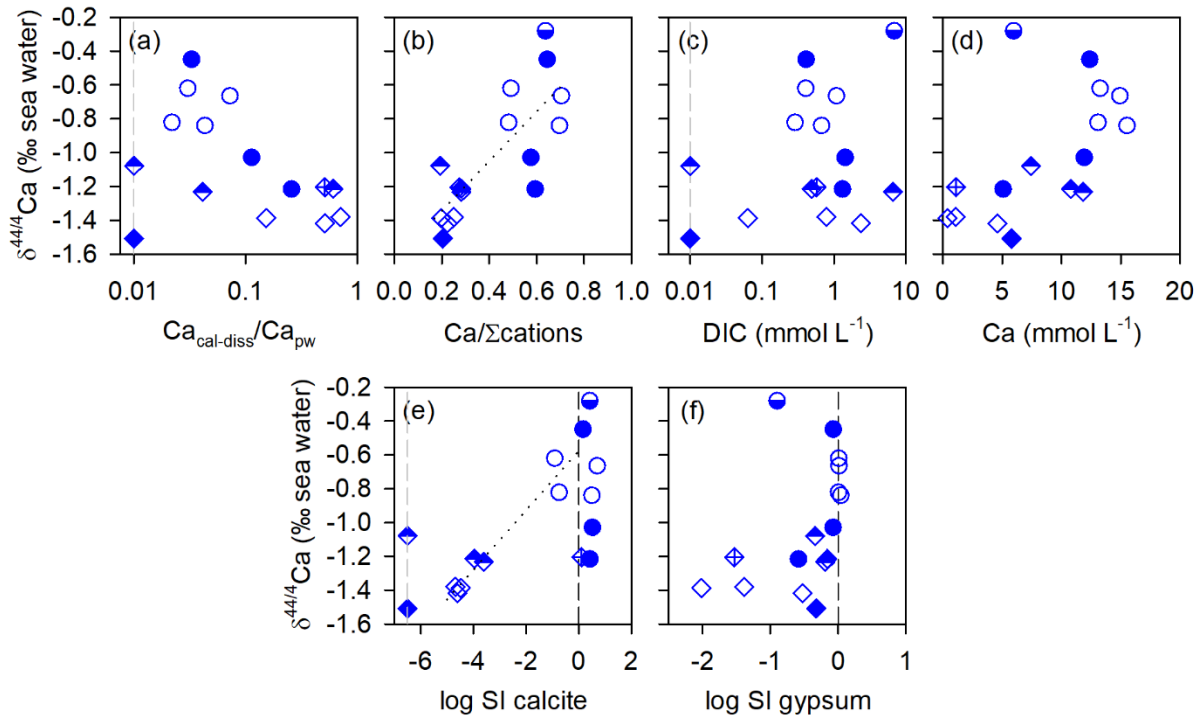


Figure 4-7: $\delta^{44/40}\text{Ca}$ values as a function of (a) calculated molar proportion of calcium [Ca] in porewater attributed to alkalinity, based on calcite dissolution ($\text{Ca}_{\text{cal-diss}}/\text{Ca}_{\text{pw}}$) in log scale; (b) calcium concentrations as molar proportion ($\text{Ca}/\Sigma\text{cations}$); (c) calculated dissolved inorganic carbon (DIC) in mmol L^{-1} ; (d) Ca concentration; (e) log saturation index (log SI) of calcite; and (f) log SI of gypsum. For display purposes, samples with no measurable alkalinity are plotted at vertical grey dashed lines in (a) at

0.01 proportion Ca from alkalinity, in (c) at DIC concentration of 0.01 mmol L⁻¹, and in (e) at log SI of -6.5. Vertical black dashed lines in (e) and (f) at log SI = 0 (saturation). Dotted lines in (b) and (e) are regression lines with R² of 0.62 and 0.94 (P < 0.005), respectively. Legend the same as in Figure 4-6.

4.4.7.1 Solid phase leaches and digestions

Acetic acid leaches and four-acid digestions of solid samples () were intended to represent carbonate- and silicate-mineral endmembers, respectively, in two-component mixing calculations. Diavik plagioclase sample T1-pl-4a had a $\delta^{44/40}\text{Ca}$ value of -3.84 ‰ (by four-acid digestion;) much lower than measured values for Icelandic basalt (-1.07 ‰ to -1.04 ‰ seawater) measured by Jacobson et al., (2015) and granites (-1.44 ‰ and -1.39 ‰ seawater) measured by Ryu et al., (2011), but higher than the measured value of K-feldspar (-9.62 ‰ seawater) reported by Ryu et al., (2011). The single Diavik sample representing carbonate minerals was sample T1-aa ($\delta^{44/40}\text{Ca}$ values of -0.92 ‰), the sample of the lower sulfur waste-rock system that was screened to pass the #35 sieve (500 μm) and leached with acetic acid. The measured $\delta^{44/40}\text{Ca}$ values of -0.92 ‰ of the Diavik waste-rock sample leached by acetic acid was within the range of values for Icelandic calcite measured by Jacobson et al., (2015; -1.18 ‰ to -0.59 ‰ seawater).

Diavik plagioclase sample T1-pl-4a (four-acid digestion) and acetic-acid leach T1-aa were used as endmembers in two-component mixing calculations for all Diavik porewater samples. Results appear contrary to the typical and expected geochemical evolution, and inconsistent with lower-bound calculations using calculated DIC concentrations. Two component mixing results suggested a greater proportion of carbonates were contributing to the $\delta^{44/40}\text{Ca}$ value for all samples, including those with lower calculated DIC concentrations, when a greater non-carbonate proportion would be expected (Table 4-4). The discrepancies suggest (i) one or both end members were not representative of the individual samples, (ii) a separate Ca source was contributing to the porewater Ca concentrations, (iii) the dissolution of carbonate minerals produced different Ca-isotope values over time, and/or (iv) gypsum was acting as a Ca reservoir.

Though these Diavik samples were calculated to be undersaturated with respect to gypsum, Ca-isotope values in gypsum would reflect the porewater Ca-isotope value at the time of formation, and fractionation during gypsum formation or dissolution. In a study of downward transport of rainfall in Ca-sulfate soils, Ewing et al., (2008) interpreted Ca-isotope negative fractionation factors (dissolved

phase isotopically heavier than solid phase). They concluded *in situ* Ca isotopic fractionation during mineral precipitation and dissolution occurred and was highly dependent on water recharge, solution chemistry, and transport. Diavik waste-rock systems experience repeated wetting and drying cycles as precipitation recharges the waste-rock piles, and seasonal variations in solute chemistry (Hannam 2013; Neuner et al., 2013; Smith et al., 2013a; Bailey et al., 2016; Collette, 2017), suggesting *in situ* Ca isotope fractionation due to secondary-mineral formation may also be plausible in unsaturated waste-rocks systems.

Table 4-3: Descriptions of solid samples and measured values of $\delta^{44/40}\text{Ca}$.

Sample origin	Sample type	Sample ID	Digestion or sample date	$\delta^{44/40}\text{Ca}$ (seawater)
Diavik	Acetic acid leach on < #35 sieve fraction	T1-aa	30-Aug-17	-0.92
Detour	Acetic acid leach on < #40 sieve fraction	2M-aa	30-Aug-17	-1.14
Detour	Acetic acid leach on < #40 sieve fraction	5M-aa	30-Aug-17	-1.37
Detour	Acetic acid leach on pan fraction	4T-aa	22-Jun-16	-1.24
Detour	Acetic acid leach on pulverized sample	DT-calcite-aa	21-Jul-16	-1.82
Diavik	Four-acid digestion of acetic-acid leached plagioclase grains	T1-pl-4a	04-Jul-16	-3.84
Detour	Four-acid digestion of < #40 sieve fraction	2M-4a	28-Aug-17	-1.03
Detour	Four-acid digestion of < #40 sieve fraction	5M-4a	28-Aug-17	-1.17
Detour	Four-acid digestion on < #200 sieve fraction	4T-4a	22-Jun-16	-1.12

The Detour acetic leach samples of waste rock (-1.37 ‰ and -1.14 ‰), and the massive (presumed hydrothermal) calcite sample from Detour (-1.82 ‰) were lower than the Diavik sample subjected to acetic leach and the measured values of calcite reported by Jacobson et al. (2015). The four-acid digested samples of Detour waste rock, which were not leached by acetic acid prior to digestion, had measured $\delta^{44/40}\text{Ca}$ values of -1.17 ‰, -1.12 ‰, and -1.03 ‰, lower than the values for Icelandic basalt reported by Jacobson et al. (2015) and hornblende measured by Ryu et al. (2011;

−0.84 ‰), but higher than the values measured by Ryu et al. (2011) for biotite (−1.52 ‰) and chlorite (−1.63 ‰). The waste rock leached by acetic acid and digested by the four-acid method have $\delta^{44/40}\text{Ca}$ values lower than the porewater samples extracted by centrifuging waste-rock solids (sample prefixes 2M, 4T and 5M; Table 4-1 and Table 4-3).

Fractionation factors ($\Delta^{44/40}\text{Ca}$) between the acetic-acid leach and porewater, and four-acid digestion and porewater were calculated by Equations 4.12 and 4.13, respectively. The porewater of these three samples was calculated to be saturated with respect to gypsum (Table 4-1), suggesting the preferential incorporation of the lighter ^{40}Ca isotope into gypsum, causing the remaining porewater to have a higher $\delta^{44/40}\text{Ca}$ value. This fractionation trend is consistent with fractionation measured during gypsum formation in the laboratory experiments of Harouaka et al. (2014), and the interpretations of *in situ* fractionation by Ewing et al. (2008). The endmember values are higher than the porewater values, likely due to the presence of gypsum and fractionation associated with gypsum formation. The four-acid digestion results without an acetic acid pre-leach precluded two-component mixing calculations for the Detour samples.

$$\Delta^{44/40}\text{Ca}_{[\text{acetic acid leach}]\text{-porewater}} = \delta^{44/40}\text{Ca}_{[\text{acetic acid leach}]} - \delta^{44/40}\text{Ca}_{\text{porewater}} \quad (4.12)$$

$$\Delta^{44/40}\text{Ca}_{[\text{four-acid digestion}]\text{-porewater}} = \delta^{44/40}\text{Ca}_{[\text{four-acid digestion}]} - \delta^{44/40}\text{Ca}_{\text{porewater}} \quad (4.13)$$

Cation geochemistry of the acetic leach fractions was used to estimate the proportion of leachable Ca-bearing phases that may have been extracted by the acetic acid leach by assuming the Mg was contributed wholly by dolomite, the sulfur [S] was contributed wholly by gypsum, and the remaining Ca was contributed by calcite (Table 4-6). These calculations did not immediately identify a trend between the measured $\delta^{44/40}\text{Ca}$ values and the estimated contribution of calcite, dolomite, or gypsum, though the dataset is small. The assumption of the mineral contributions to each element is a large source of error, particularly for the Diavik sample T1-aa, which has a calculated dolomite fraction of 0.87, despite that phase not being identified in the Diavik mineral assemblage. Hong et al. (2018) have noted that gypsum may be partially dissolved by acetic acid during an acetic-acid leach. Additional sample treatments should be included for future studies to target gypsum separately from the carbonate minerals.

Table 4-4: Two-component mixing results for the Diavik samples. The $\delta^{44/40}\text{Ca}$ value (-3.84‰) from four-acid digestion sample T1-pl-4a was used as the silicate value and the $\delta^{44/40}\text{Ca}$ value (-0.92‰) from the acetic leach sample T1-aa was used as the carbonate value. Calculated silicate and carbonate components from $\text{Ca}_{\text{cal-diss}}/\text{Ca}_{\text{pw}}$ are summarized for comparison.

Sample	$\delta^{44/40}\text{Ca}$ (‰ seawater)	Two-component mixing			$\text{Ca}_{\text{cal-diss}}/\text{Ca}_{\text{pw}}$	
		Calculated DIC (mmol L ⁻¹)	Calculated silicate component	Calculated carbonate component	Calculated maximum silicate component	Calculated minimum carbonate component
1UE-pw11	-1.39	0.063	0.16	0.84	0.85	0.15
1UE-pw13	-1.38	0.78	0.16	0.84	0.29	0.71
1UE-pw15	-1.42	2.37	0.17	0.83	0.49	0.51
1UW-pw11	-1.20	0.57	0.10	0.90	0.49	0.51
3UW-pw11	-1.51	0	0.20	0.80	1	0
CBdrn-28	-1.23	6.61	0.11	0.89	0.39	0.61
CBdrn-22	-1.22	0.49	0.10	0.90	0.96	0.04
CBdrn-18	-1.08	0	0.05	0.95	1	0

Table 4-5: Fractionation factors ($\Delta^{44/40}\text{Ca}$) for the three Detour samples with measured values of for porewater, acetic acid leached solids and four-acid digested solids.

Sample prefix	$\Delta^{44/40}\text{Ca}_{[\text{acetic acid leach}]-\text{porewater}}$	$\Delta^{44/40}\text{Ca}_{[\text{four-acid digestion}]-\text{porewater}}$
2M	-0.30 ‰	-0.19 ‰
4T	-0.62 ‰	-0.50 ‰
5M	-0.55 ‰	-0.35 ‰

Table 4-6: Apportioned calcium (Ca) to soluble mineral phases in acetic acid leach based on magnesium [Mg], sulfur [S] and Ca concentrations.

	T1-aa	2M-aa	5M-aa	4T-aa
$\delta^{44/40}\text{Ca}$ (‰ seawater)	-0.92	-1.14	-1.37	-1.24
Ca (mmol g ⁻¹)	0.0061	0.27	0.34	0.31
Mg (mmol g ⁻¹)	0.0053	0.02	0.016	0.017
S (mmol g ⁻¹)	0.0021	0.043	0.35	0.28
Proportion Ca as dolomite	0.87	0.072	0.047	0.054
Proportion Ca as gypsum	0.34	0.16	1.02	0.89
Proportion Ca as calcite	-0.21	0.77	-0.07	0.051
MLA dolomite proportion		0.31	0.21	0.18
MLA gypsum proportion		0.05	0.62	0.8
MLA calcite proportion		0.64	0.17	0.02

4.5 Conclusions

Molar-ion ratios of aqueous and solid samples from two lithologically-distinct mines illustrated a higher calcium proportion in aqueous samples than associated solid samples, suggesting preferential release from the solids and/or preferential retention of Ca in porewater. Calculations based on measured alkalinity and calcium and calculated dissolved inorganic carbon concentrations provided lower-bound contributions of calcium in aqueous samples from carbonate-mineral dissolution and non-carbonate mineral dissolution for data points with measurable alkalinity and $\text{pH} > 4.5$, and measured alkalinity of 0 mg L^{-1} as CaCO_3 and $\text{pH} < 4.5$. Porewater $\delta^{44/40}\text{Ca}$ values, measured alkalinity inputs and calculated concentrations of dissolved inorganic carbon, major cation ratios, and two-component mixing calculations did not identify any clear trends between the extent of carbonate-mineral dissolution and measured $\delta^{44/40}\text{Ca}$ values. Though a limited dataset of $^{44}\text{Ca}/^{40}\text{Ca}$ measurements, $^{44}\text{Ca}/^{40}\text{Ca}$ isotope analyses could not sufficiently discriminate carbonate-dominant vs. silicate-dominant acid neutralization in these mine-waste systems. Confounding factors may include incongruent primary- and secondary-mineral dissolution with respect to Ca-release, the formation of secondary minerals, and Ca-isotope fractionation during mineral dissolution and/or precipitation. Porewater $\delta^{44/40}\text{Ca}$ values from Diavik were typically lower than those from Detour across the range of alkalinity values, suggesting that the Ca-bearing mineralogy influenced $\delta^{44/40}\text{Ca}$ values in porewater, in addition to the degree of geochemical evolution, including precipitation and dissolution of Ca-bearing secondary minerals. Fractionation factors between waste rock leached by acetic acid (presumed carbonate-mineral component) and porewater samples were -0.62 ‰ , -0.55 ‰ , -0.30 ‰ for the three sets of co-located samples. The fractionation was likely caused by gypsum formation in the mine-waste system. Additional analyses of various solid samples, including discrete mineral phases, could refine an acid-neutralization model based on $\delta^{44/40}\text{Ca}$, which would avoid many of the assumptions required for the calculation method based on measured alkalinity and calculated dissolved inorganic carbon. Calcium-bearing secondary minerals and their influence on $\delta^{44/40}\text{Ca}$ values in water draining from mining-waste rock requires further investigation.

Chapter 5

Secondary mineral formation and trace-element reservoirs in weathered waste rock: Integration of quantitative mineralogy and conventional mineralogical techniques

Lianna J.D. Smith, Dogan Paktunc, and David W. Blowes. In preparation for submission to
Journal of Geochemical Exploration.

5.1 Summary

Sulfide minerals and secondary minerals associated with sulfide oxidation were characterized using automated quantitative mineralogy techniques in samples of weathered and freshly blasted waste rock from the Detour Lake Mine, Ontario, Canada. Associations and mineral habit of secondary minerals suggest heterogeneous and dynamic geochemical conditions within the historical waste-rock pile, and the formation of secondary minerals in microenvironments associated with oxidizing sulfide minerals. Electron-probe microanalyses of sulfide grains and alteration rims applied to the modal mineralogy determined by quantitative mineralogy permitted a calculation of trace elements in these reservoirs. The calculations revealed an under-estimation of trace elements by quantitative mineralogy when mass-balance calculations were considered.

5.2 Introduction

Waste rock from mining that is stored subaerially in waste-rock piles can generate acid mine drainage when sulfide minerals in the waste rock oxidize. Trace elements, which occur as components or impurities in sulfide, oxide and/or silicate minerals, can be released to porewater during sulfide oxidation, acid neutralization, and mineral weathering. As these reactions proceed, secondary minerals may precipitate and sequester elements and/or dissolve and release elements, which affects the concentration and speciation of major ions and trace elements in the porewater and drainage. Alteration rims surrounding partially oxidized sulfide minerals are composed of iron [Fe], oxygen [O], and, commonly, sulfur [S] of mixed oxidation states (e.g., Mycroft et al., 1995; Langman et al., 2015; Nordstrom et al., 2015; Steinepreis, 2017; Smith et al., 2021; Chapter 2). These Fe-(oxyhydr)oxide and Fe-hydroxysulfate minerals have the propensity to sorb trace elements that were

released during mineral dissolution (e.g., McKenzie et al., 1980; Bruemmer et al., 1988; Scheinost et al., 2001; Lee et al., 2002; Tian et al., 2017; Smith et al., 2021; Chapter 2).

Reliable and common bulk characterization techniques for quantifying elements in waste rock include whole rock analysis (WRA) by lithium metaborate fusion, *aqua regia* digestion, four-acid digestion, total sulfur and total carbon analyses and/or modified acid-base accounting (ABA). Bulk-characterization methods provide limited information about the mineral hosts containing potentially hazardous trace elements. Targeted mineralogical analyses commonly used to support bulk characterization include evaluations of mineral abundance and habit by optical microscopy, elemental concentrations at the ppm level by electron-probe microanalysis (EPMA), and mineral characterization by scanning electron microscopy with energy dispersive X-ray microanalyzer (SEM/EDX). X-ray diffraction (XRD) provides the mineralogical composition. These techniques are limited by the number of particles that are analyzed. The application of Rietveld refinement to XRD analyses can provide semi-quantitative mineral abundances, but can be limited in mineralogically-complex samples, including those from metamorphic terranes that include minerals with solid solutions, and platy or amorphous minerals; these types of samples produce complex patterns of overlapping peaks that can make quantification of phases difficult.

Mineral Liberation Analysis (MLA) is an automated technique for identifying minerals, determining mineral quantities, and distinguishing mineral associations. Development of automated systems for quantitative mineralogy began in the 1970s, including those based on image analysis and EPMA (Petruk, 1987, 1989; Sylvester et al., 2012). The Mineral Liberation Analyzer, the instrument used in this study, uses SEM to collect backscattered electrons (BSE) to identify minerals and mineral boundaries based on grey-scale brightness, and EDX to verify mineral identification using a reference database (Sylvester, 2012). MLA has become routine in ore-process mineralogy (e.g., Lotter et al., 2018; Sousa et al., 2018), and has been increasingly applied to waste-rock studies. Automated mineralogical quantification has been demonstrated to be a useful tool for pre-screening ore samples for the potential to form acid rock drainage using a calculated acid rock drainage (CARD) risk ratio based on the particle areas of sulfide and carbonate minerals, and relative mineral reactivities (Parbhakar-Fox et al., 2017). CARD risk ratios have been determined on samples of mine tailings to evaluate the physical, mineralogical, and geochemical characteristics of hardpan formation (Redwan et al., 2012). Barazzuol et al. (2009) applied the automated technique to humidity cell charges of mining-waste rock to confirm sulfide- and carbonate-mineral species in humidity cell charges, to

evaluate the relationships between sulfide grain size and liberation, and various minerals determined by MLA, and to determine sulfate release rates from humidity cells. Another study of waste rock compared acid-generating potential and neutralization potential obtained from standard acid-base accounting tests to those calculated using mineral liberation data (Elghali et al., 2018). St-Arnault et al., (2019) used MLA in a comprehensive study of waste rock that evaluated mineralogical controls on porewater chemistry from a field experiment.

Combining standard bulk techniques and targeted mineralogical techniques with automated mineral quantification provides an opportunity to better understand secondary-mineral formation and trace-element reservoirs. This study evaluates samples of waste rock from a historical waste-rock pile and freshly blasted waste rock from Detour Lake Gold Mine, a greenstone gold mine in Ontario, Canada (Figure 5-1). The objectives of this study were to apply MLA to characterize secondary-mineral assemblages, to combine results from EPMA and MLA measurements to quantify trace-element reservoirs associated with sulfide minerals and alteration products, and to compare results to bulk chemical analyses.

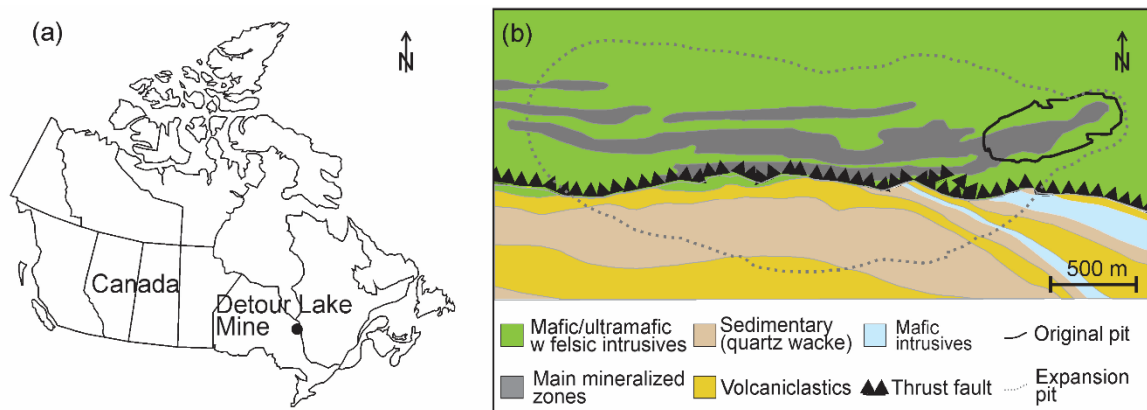


Figure 5-1: (a) Site location of Detour Lake Mine and (b) local geology with original pit and expansion pit outline (modified from BBA and SGS, 2014).

5.3 Experimental section

Samples for this study were obtained from a historical waste-rock pile and freshly blasted waste rock from the Detour Lake Mine, Ontario, Canada (Figure 5-1). Detour Lake Mine is an open-pit gold mine in the Abitibi Greenstone Belt of Ontario, Canada. The mine operated from 1983 – 1999, with

re-development commencing in 2006. The deposition of waste rock during the first stage of development was not documented, and the provenance and depositional history of the waste rock is poorly known. During closure the initial waste-rock piles were re-contoured and covered with a single layer of soil (McNeill et al., 2020). The second stage of mining required excavation and relocation of the historical waste-rock piles, providing an opportunity to collect *in situ* samples from waste rock that had been weathering for up to 30 years (Cash et al., 2014; McNeill et al., 2020; Smith et al., 2021).

Whole-rock analyses, total carbon and total sulfur, MLA, optical microscopy, X-ray Diffraction (XRD), and EPMA analyses were conducted on samples from the historical waste-rock pile that had been partially excavated, and samples from waste rock that was recently blasted from areas immediately adjacent to the original open pit. The waste-rock and porewater samples evaluated in this study were the same samples as those described in Chapter 2 and in Smith et al. (2021). The historical waste-rock samples were collected in November 2015, and the freshly blasted waste-rock samples were collected in December 2015 and January 2016. The < 425 µm fractions of freshly blasted and historical waste rock were evaluated in this study. Samples for thin sections and laboratory analyses were air dried in a fumehood for 48 h to reduce the possibility of tertiary mineral transformations (Jambor, 1994), sieved using a #40 (425 µm) sieve, and subsampled by coning and quartering.

Thin sections were prepared by Spectrum Petrographics (Vancouver, USA). Samples were mounted using a non-aqueous compound, cut to 30 µm thickness and finished with microprobe-quality polish on Suprasil 2A quartz glass slides. Thin sections were carbon coated for MLA analysis. MLA analysis was conducted at Memorial University (St. John's, Canada) by an experienced technician using a Mineral Liberation Analyzer and a standard database. Reported values for modal mineralogies are valid to +/- 0.01 wt% (Grant, D., pers. comm., 19 March 2019). XRD analyses were conducted at CanmetMINING (Ottawa, Canada) on splits of the < 425 µm sample fractions micronized to < 5 µm in a McCrone micronizing mill. XRD analyses were conducted with a Rigaku D/MAX 2500 rotating-anode powder diffractometer with monochromatic CuK α radiation at 40 kV, 200 mA, a step-scan of 0.02°, and a scan rate at 1° per minute in 2 Θ from 5 to 70°. Rietveld refinement was attempted, but the mineralogical complexity, talc component and the large quantity of solid-solution minerals, which have shifting peak positions depending on the composition, provided results of low confidence. EPMA was conducted at the University of Ottawa (Ottawa, Canada) using a JEOL 8230 SuperProbe with a 1 µm spot size. Sulfide grains and reaction rims were analyzed for

sulfur [S], iron [Fe], copper [Cu], cobalt [Co], nickel [Ni], zinc [Zn], arsenic [As] and selenium [Se], with standards of marcasite [FeS₂], sphalerite [ZnS], Bi₂Se₃, cubanite [CuFe₂S₃], pyrrhotite [Fe_{1-x}S], pentlandite [(Fe,Ni)₉S₈], and GaAs.

Calculations for mineral associations were based on mineral-boundary lengths calculated from each mineral grain identified by MLA. The proportion of the grain boundary of “mineral a” that is in contact with “mineral b” was normalized by the boundary lengths of “mineral b” in the sample. A mineral-association ratio greater than 1 indicates the contact between mineral a and mineral b is greater than would be expected based on bulk mineral-boundary lengths, and a ratio less than 1 suggests a lower degree of association. Minerals with modal abundances < 0.01 wt% were excluded from the calculation. This approach is analogous to the association index proposed by Lund et al. (2015) and applied by St-Arnault et al. (2019) but used mineral boundary lengths rather than MLA-calculated wt% associations. The boundary-length approach was applied here to remove any assumptions about mineral-phase densities and is proposed to be more representative for secondary minerals and for particles composed of numerous mineral grains of variable composition.

Splits of samples were subjected to four-acid digestion (hydrofluoric acid, nitric + perchloric acids, *aqua regia*), evaporated to dryness, and then reconstituted with trace-metals grade HNO₃ by AGAT Laboratories (Mississauga, Canada). The digestate was analyzed at the University of Waterloo for major cations by ICP-OES and for trace elements by ICP-MS, with QA/QC protocols following EPA methods 6010C (ICP-OES) and 6020A (ICP-MS). Total carbon and total sulfur were measured on the solid samples by induction furnace, conducted by SGS (Burnaby, Canada).

Maximum possible modal mineralogies for chalcopyrite, pentlandite and sphalerite were calculated from the four-acid digestion concentrations of Cu, Ni and Zn, respectively. The calculations assumed that all measured Cu was contributed by chalcopyrite, all measured Ni was contributed by pentlandite, and all measured Zn was contributed by sphalerite. The calculation results were checked by assuming the MLA-calculated pyrite and pyrrhotite abundances were representative, and then apportioning S to pyrite, pyrrhotite and the calculated maximum chalcopyrite, pentlandite and sphalerite abundances, and the residual S (from the induction furnace measurements) to the MLA-calculated abundances of gypsum, jarosite ± Ca-Fe-sulfate phase. Results were consistent with total S concentrations (Table D-1).

5.4 Results and discussion

5.4.1 Modal mineralogy

MLA-quantified modal mineralogy of the historical samples, together with optical microscopy observations, suggest the waste-rock samples were derived from similar mafic to ultramafic lithologies within the historical pit (Table 5-1). Two of the freshly blasted samples (samples 117 and 119) exhibited modal mineralogies similar to the historical samples. The remaining three freshly blasted samples suggest more felsic lithologies than the other samples and are likely derived from the felsic intrusives that occur within the mafic and ultramafic units (Oliver et al., 2012; Figure 5-1).

The freshly blasted felsic samples had lower abundances of sulfide minerals (Table 5-1). All freshly blasted samples, both felsic and mafic, had higher abundances of carbonate minerals and lower abundance of secondary minerals than the historical samples. Total S measured by induction furnace, and MLA-reported total S were in very good agreement, and total C was typically within a factor of two (Table 5-2). The discrepancy in the C concentrations may be related to the presence of C-containing particles not detected by MLA, e.g. (i) graphite, which has been documented at gold deposits within the Abitibi Greenstone belt (e.g., Dinel et al., 2008); (ii) carbonate grains $< 1.5 \mu\text{m}$, the resolution of the MLA; (iii) organic material; and/or (iv) other C-containing minerals not included in the MLA database. The MLA modal mineralogies, and total S and total C abundances by induction furnace are consistent with the expectation that the carbonate minerals would be depleted in the historical samples due to dissolution *via* acid neutralization in response to acid produced during sulfide oxidation. Ongoing formation of secondary minerals, which including sulfate-bearing phases, would be expected to occur throughout the weathering of the waste rock over the 30-year period of subaerial exposure.

Table 5-1: MLA-derived modal mineralogy for key minerals in wt%. “Qtz-plg-mix” denotes a mixture of quartz and plagioclase and was not included in the database for all MLA analyses. Gypsum was not included for sample 119. MLA-labeled mineral yavapaiite has been interpreted to occur in the samples as jarosite (See Section 3.2.1.3). Bulk chemical compositions for major elements are provided in Appendix D. Freshly-blasted samples 117 and 119 exhibited mafic to ultramafic lithology, whereas the remaining freshly blasted samples exhibited felsic lithology.

wt%	Historical									Freshly blasted					
	2M	3B	3M	3T	4Mb	4T	5B	5M	5T	117	119	090	223	224	25-26
Quartz	13.6	15.9	14.9	18.3	18.7	7.3	19.3	11.1	17.9	9.3	14.0	32.4	29.4	29.0	37.3
Qtz-plg-mix				1.5	1.3		0.98		1.3		1.3				
Plagioclase	7.8	8.2	8.0	11.5	12.6	5.5	11.3	8.0	11.5	7.2	9.1	20.3	20.1	19.7	21.8
Albite	2.7	1.9	3.1	1.2	1.3	2.1	1.1	2.4	1.4	0.84	1.3	5.1	3.7	5.0	5.3
Orthoclase	2.5	2.8	3.4	4.3	4.1	1.4	3.1	2.3	3.8	1.4	2.0	8.8	7.1	8.4	9.1
Chlorite-Fe	2.1	1.7	0.89	4.7	2.9	0.69	3.0	0.85	3.2	1.1	2.9	0.28	1.1	1.3	0.56
Chlorite-Mg	<0.01	<0.01	<0.01	7.2	8.3	<0.01	9.5	<0.01	10.3	<0.01	15.3	<0.01	<0.01	<0.01	<0.01
Chamosite (+Mg)	14.4	16.9	17.5	2.3	3.2	22.7	2.5	18.5	3.1	19.7	4.1	0.63	0.95	3.7	1.3
Clinopyroxene	12.3	13.1	15.5	11.5	11.6	17.1	8.6	13.9	10.6	7.2	8.5	3.2	2.3	4.2	2.7
Orthopyroxene	2.2	3.7	5.1	4.6	3.1	4.5	2.9	5.4	2.8	0.84	0.59	0.20	0.60	1.2	0.59
Hornblende	14.2	12.0	7.4	7.6	9.1	6.7	9.3	4.7	8.1	11.0	4.4	6.2	13.0	10.6	7.2
Amphibole - K rich	2.4	2.0	2.7	2.3	1.6	1.7	1.1	2.1	1.6	1.5	0.47	10.3	3.1	3.3	2.9
Muscovite	0.70	0.53	0.46	0.40	0.36	0.34	0.78	0.27	0.64	0.28	1.1	0.52	0.42	0.77	0.48
Biotite	1.7	1.6	1.8	2.5	6.3	7.0	3.0	4.4	3.3	3.6	1.8	0.47	1.3	1.1	0.45
Epidote	1.1	0.74	0.60	0.44	0.53	0.35	0.58	0.39	0.55	0.46	0.13	1.3	1.5	1.8	1.5
Talc	8.5	5.2	7.2	4.9	6.0	10.3	9.3	11.4	8.5	21.5	17.3	0.11	0.14	1.7	0.37
Calcite	1.9	0.63	0.48	0.34	0.48	0.55	0.38	0.06	0.81	5.0	2.9	1.8	7.8	2.8	1.6
Dolomite	1.7	0.98	1.1	1.5	1.7	1.4	2.1	1.1	1.3	4.0	5.2	6.0	3.8	2.3	4.2
Pyrrhotite	2.6	1.9	1.00	0.24	0.33	0.98	1.1	0.63	1.1	2.0	3.7	0.08	0.45	0.34	0.13
Pyrite	0.88	0.56	0.15	0.36	0.53	0.42	0.91	0.04	0.46	0.71	0.59	0.28	0.42	0.44	0.04
Chalcopyrite	0.14	0.27	0.16	0.11	0.09	0.23	0.27	0.17	0.18	0.11	0.33	<0.01	0.02	<0.01	0.01
Pentlandite	0.03	0.03	0.03	<0.01	0.01	0.03	0.04	0.01	0.03	0.08	0.11	<0.01	<0.01	<0.01	<0.01
Sphalerite	<0.01	<0.01	<0.01	<0.01	<0.01	<0.01	<0.01	<0.01	<0.01	<0.01	<0.01	<0.01	<0.01	<0.01	<0.01
Altered Fe-sulfide	1.3	1.1	0.93	1.2	0.59	0.87	1.2	1.5	1.0	<0.01	0.05	<0.01	0.02	<0.01	0.09
Gypsum	0.24	2.5	2.9	6.7	1.2	3.4	3.1	4.2	2.6	0.12		0.03	0.05	0.08	0.06
Yavapaiite (jarosite)	0.16	0.15	0.15	0.20	0.37	0.27	0.13	0.58	0.20	<0.01	0.06	<0.01	<0.01	<0.01	<0.01
Ca-Fe-sulfate	0.04	0.17	0.19	0.18	0.03	0.11	0.06	0.21	0.14	0.02	0.03	<0.01	<0.01	<0.01	<0.01

Table 5-2: Carbon [C] and sulfur [S] concentrations calculated by mineral liberation analyzer (MLA) and measured by induction furnace (IF). “n.a.” denotes not analyzed.

	MLA C (wt%)	MLA S (wt%)	IF C (tot) (wt%)	IF S (tot) (wt%)
<i>Historical</i>				
2M	0.45	1.94	0.88	1.52
3B	0.20	1.91	0.66	1.88
3M	0.20	1.34	0.78	1.32
3T	0.23	1.92	0.47	1.89
4Mb	0.28	0.90	0.53	0.89
4T	0.25	1.60	0.53	1.72
5B	0.31	1.92	0.41	1.90
5M	0.15	1.65	0.41	1.67
5T	0.26	1.53	0.57	1.40
<i>Freshly blasted</i>				
090	0.99	0.19	2.19	0.12
117	1.11	1.25	1.52	1.29
119	1.02	1.91	0.94	1.35
223	1.42	0.42	2.09	0.55
224	0.64	0.38	n.a.	n.a.
25-26	0.73	0.11	1.26	0.12

5.4.2 Secondary sulfate minerals

5.4.2.1 Gypsum

Gypsum is a common secondary mineral in waste rock and stream channels impacted by mine drainage. Porewaters extracted from waste-rock samples analyzed in this study were calculated to be saturated with respect to gypsum (Smith et al., 2021 with plots in Supplementary Material therein; Chapter 2). MLA provided a higher calculated abundance of gypsum in the weathered waste-rock samples than the freshly blasted samples (Table 5-1), as would be expected from ongoing sulfate release from sulfide oxidation in the older samples, compared to samples where sulfide minerals have not been extensively exposed to water and air. The grain-size distribution (as maximum diameter) of gypsum provided by MLA indicated d50 grain sizes of 133 – 227 μm (median = 189 μm , n = 9) in the historical samples (recall in the sample size fraction was < 425 μm), suggesting prolonged conditions that were geochemically favorable to gypsum precipitation in most historical samples. Conversely,

grain-size distributions of gypsum in the freshly blasted samples were finer (66 – 145 μm , median = 124 μm , $n = 5$), consistent with the expectation of limited gypsum formation in those samples.

Evaluating the MLA-calculated mineral grain sizes (as maximum diameter) of gypsum with respect to MLA-calculated modal abundance, and porewater pH and calculated saturation indices (Smith et al., 2021; Figure A-3), suggest dynamic and heterogeneous geochemical conditions in the historical waste-rock pile. Among the historical samples, sample 2M had the smallest d50 (132 μm), lowest calculated modal mineralogy (0.24 wt%), smallest free-boundary length, highest calculated saturation index (SI) for gypsum ($\log \text{SI} = 0.04$; Smith et al., 2021; Figure A-3), and the highest calculated modal mineralogy of pyrrhotite (2.6 wt%). Furthermore, this sample was the only historical sample to have a boundary association > 1 for gypsum and the altered Fe-sulfide phase [MLA-ascribed formula of $[(\text{FeO}(\text{OH}) \cdot n\text{H}_2\text{O})(\text{Fe}^{2+}\text{S}_2)]$ (Figure 5-2, Figure D-1). These characteristics and associations suggest gypsum formation was occurring proximal to oxidizing sulfide grains, where local concentrations of SO_4 may be higher than within the bulk porewater. An evaluation of the MLA-produced particle images of sample 2M showed most gypsum grains had irregular boundaries and/or occurred as cementing grains; well-formed crystal habits would be expected for prolonged geochemical conditions favorable to gypsum precipitation from porewater (Figure 5-3a). Together the MLA-calculated modal abundances, free-boundary lengths and MLA-produced images suggest sulfide oxidation and gypsum formation were in their infancy in sample 2M, and there remains a high potential for ongoing sulfide oxidation and related gypsum formation. The sample with the second smallest d50 (147 μm) for gypsum, sample 4Mb, had low modal abundances of both gypsum (1.2 wt%) and pyrrhotite (0.33 wt%; Table 5-1), a porewater pH of 8.1 (Smith et al., 2021; Chapter 2) and a calculated $\log \text{SI} < 0$. However, the calculated free-boundary lengths were similar to those measured for the other historical samples, and MLA-produced images illustrate common well-formed gypsum crystals with a high proportion of grains with no or few included minerals (Figure 5-3b). Together, these observations on sample 4Mb suggest an evolution from prolonged conditions favorable to gypsum formation to porewater that was undersaturated with respect to gypsum at the time of sampling. In addition, the degree of association between gypsum and the altered Fe-sulfide phase was low (Figure 5-2, Figure D-1), suggesting previous conditions within the bulk porewater were favorable to gypsum precipitation and accumulation, rather than limited gypsum formation proximal to oxidizing sulfide minerals in microenvironments, as interpreted for the sample 2M with d50 of 132 μm .

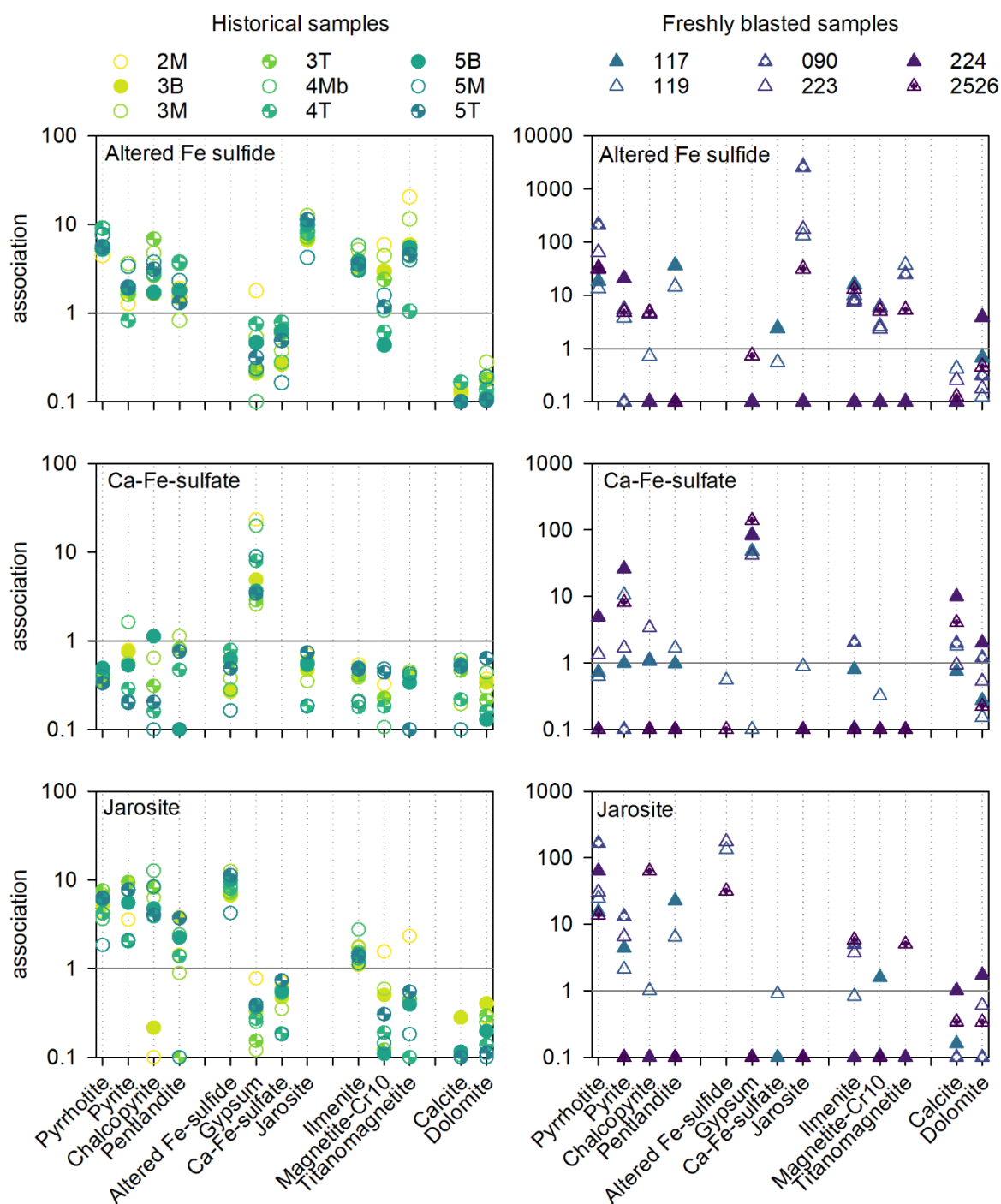


Figure 5-2: Calculated mineral associations for altered Fe-sulfides, Ca-Fe-sulfate and yavapaiite (jarosite). Minerals with <0.01 wt % modal abundance not included in the calculations.

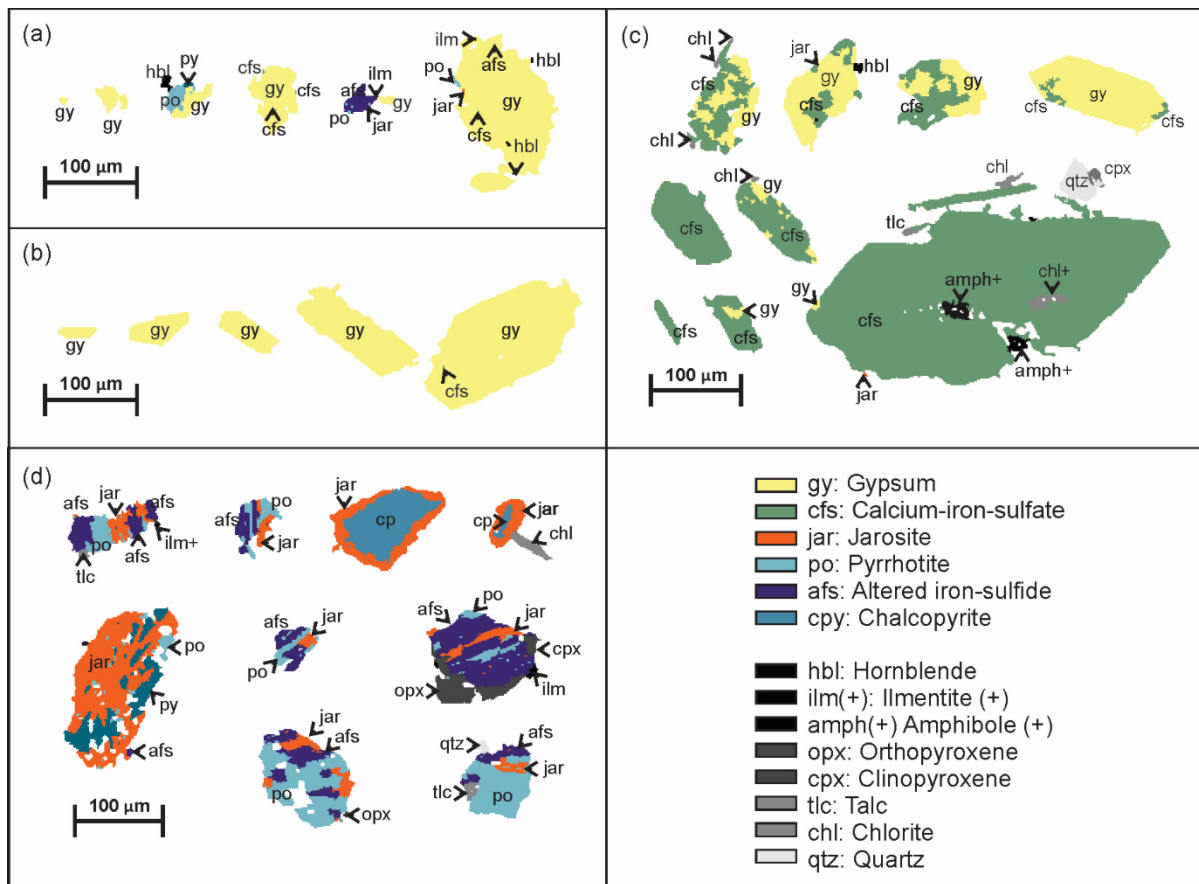


Figure 5-3: MLA-produced grain images. (a) Typical gypsum habit in sample 2M with smallest d50; (b) typical gypsum habit in sample 4Mb with second smallest d50; (c) typical occurrence of Ca-Fe-sulfate in various grains and samples; (d) distributions and associations of jarosite in various grains and samples.

5.4.2.2 Calcium-iron-sulfate phase

A calcium-iron-sulfate phase identified as Ca-Fe-sulfate [no ascribed formula] in the MLA database had mineral boundaries that were highly associated with gypsum for all samples (Figure 5-2; one freshly blasted sample did not have gypsum included in the MLA database during analysis). Mineral-boundary associations with Fe-bearing minerals, including the altered Fe-sulfide phase, were typically low. The typically small grain sizes (d50 range of 20 – 60 µm with median of 61 µm for historical samples, and 22 – 45 µm with median of 30 µm for freshly blasted samples), and MLA-modal abundances were low.

An evaluation of the MLA-produced particle images suggests grains of Ca-Fe-sulfate had similar habit to gypsum, particularly larger grains, distribution patterns consistent with cementing gypsum (e.g., Jambor 1994), appearing as continuation of gypsum grains, or as blebs in, or associated with, gypsum (Figure 5-3). Rather than a discrete phase, the MLA-ascribed Ca-Fe-sulfate phase in these samples is interpreted to be predominantly gypsum with an associated Fe species such as Fe-(oxyhydr)oxide precipitate on gypsum, sorbed Fe species on gypsum grains (e.g., Melliti et al., 2021), or as a gypsum surface coating on underlying Fe-bearing phase(s); the Fe-bearing phases may include partially oxidized sulfides that contributed SO_4 and Fe to the secondary phase.

Gypsum had the highest calculated degree of mineral association with the Ca-Fe-sulfate phase in the freshly blasted samples, however, unlike the historical samples, a Ca-Fe-sulfate phase was also associated with pyrite and/or pyrrhotite, and four of the six samples demonstrated a high degree of association with calcite \pm dolomite (Figure D-2). These relationships, the smaller particle sizes, and habit of gypsum in the freshly blasted samples indicate that the early-time formation of gypsum, and the associated Ca-Fe-sulfate phase was driven by the release of Fe and SO_4 by oxidizing sulfide minerals, and interaction with Ca which was likely predominantly derived from carbonate-mineral dissolution.

5.4.2.3 Jarosite

MLA assigned the phase yavapaiite [$\text{KFe}^{3+}(\text{SO}_4)_2$] to grains in some samples. Yavapaiite is interpreted here to occur in the samples as the hydrated form jarosite [$\text{KFe}^{3+}_3(\text{SO}_4)_2(\text{OH})_6$]. Yavapaiite is a rare primary mineral that is not stable in the temperature regime of greenschist to lower amphibolite facies, or typical hydrothermal temperatures (Forray et al., 2005). Jarosite is a common secondary mineral in mine tailings and waste rock where pH values are acidic (Dutrizac and Jambor, 2000; Jambor, 1994; Jamieson et al., 2005), and one study identified jarosite in a circumneutral waste-rock system (Dockrey et al., 2014). Jarosite can precipitate from supersaturated porewater in mine waste-rock systems (Alpers et al., 1989; Bigham and Nordstrom, 2000), can form coatings or pseudomorphs of Fe-sulfide minerals in oxidized sulfide deposits (Dutrizac and Jambor, 2000; Jamieson et al., 2005), and has been reported to form on pyrrhotite surfaces during oxidation in laboratory experiments (Bhatti et al., 1993). XRD analyses identified jarosite as possibly present in the historical samples, but not in the freshly blasted sample measured by that technique.

In the historical samples, jarosite was predominantly associated with altered Fe-sulfides, sulfide minerals, the Ca-Fe-sulfate phase, \pm gypsum (Figure 5-3; Figure D-3). Only sample 119 had an MLA-reported modal mineralogy of jarosite > 0.01 wt% (0.06 wt%), an order of magnitude lower than those calculated for the historical samples (Table 5-1). This freshly blasted sample had MLA associations consistent with those for the historical waste rock, suggesting the presence of jarosite. The blasting and collection history of this sample is undocumented, but modal abundances of sulfides, carbonates, and the presence of measurable secondary phases suggest this sample has undergone limited, but continuing, sulfide oxidation.

MLA-produced particle images illustrate the spatial distribution and habit of jarosite as occurring as small, discrete grains, and irregular blebs and patches intimately associated with pyrite, pyrrhotite and/or the altered Fe-sulfide phase (Figure 5-3). MLA-calculated grain sizes in the historical and freshly blasted samples had d50 ranges of 19 – 40 μm (median of 30 μm , $n = 9$), and 9 – 32 μm (median of 20 μm), respectively (Figure 5-3), consistent with observations that jarosite associated with mining wastes is fine grained, typically < 45 μm , and often < 0.5 μm (Desborough et al., 2006, 2010). The small, discrete grains may represent nucleation from a supersaturated solution in a microenvironment in close proximity to an oxidizing grain, though precipitation from supersaturated porewater has been reported to be limited by kinetic barriers (Alpers et al., 1994). The larger discrete grains, and the blebs and patches indicate jarosite formed directly on the sulfide surface during oxidation, with K^+ in the porewater derived from silicate mineral weathering. The presence of jarosite is difficult to observe by optical microscopy and was not noted in this study, but in the study described in Chapter 3, jarosite was included as a component of the best fits of linear combination fitting of Fe X-ray absorption near edge spectra (XANES) of an oxidizing pyrrhotite grain from sample 3M. Jarosite occurrence in other studies of mining waste suggest this phase formed in close association with mixture of secondary Fe-(oxy)hydroxides and Fe-hydroxysulfates from sulfide weathering (Blowes et al., 2014; Desborough et al., 2010), which can include schwertmannite [e.g., $\text{Fe}^{3+}_{16}\text{O}_{16}(\text{SO}_4)_2(\text{OH})_{12}\cdot 20\text{H}_2\text{O}$, $n = 10 - 12$], ferrihydrite [nominally $\text{Fe}_2\text{O}_3\cdot 9\text{H}_2\text{O}$], goethite [$\alpha\text{-Fe}(\text{OOH})$], and/or lepidocrocite [$\gamma\text{-Fe}(\text{OOH})$] (Bigham and Nordstrom, 2000; Blowes et al., 2014; Dockrey et al., 2014). The association between jarosite and the Fe-(oxyhydr)oxides is a consequence of an alteration sequence associated with sulfide oxidation and the aging of the associated Fe \pm S-bearing secondary minerals (Jambor et al., 2000).

Porewater extracted from the historical samples was circumneutral and calculated to be undersaturated with respect to jarosite (Smith et al., 2021; Chapter 2; Figure A-3). However, based on the identification of a $\text{K-Fe}^{3+}\text{SO}_4$ phase by MLA, the MLA-produced images, the MLA-reported associations of jarosite, and supporting evidence from XRD and XANES linear combination fitting from Chapter 3, it is interpreted here that the developing sulfide alteration products can include jarosite forming in acidic microenvironments, intimately associated with secondary Fe-(oxyhydr)oxide and Fe-hydroxysulfates (e.g., Figure 5-3). Similarly, occurrences of As-bearing secondary phases that are only stable at acidic pH values have been documented in mine tailings with circumneutral porewaters (DeSisto et al., 2011).

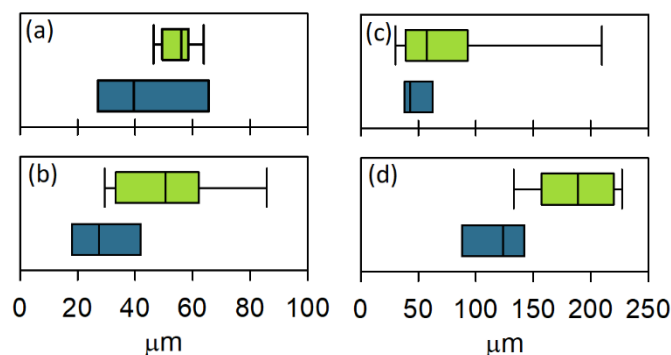


Figure 5-4: Distribution of d50 values of (a) altered Fe-sulfides; (b) yavapaiite (jarosite); (c) Ca-Fe-sulfate; (d) gypsum. Top boxes (green fill) in each frame are data from historical samples, bottom boxes (blue fill) are from freshly blasted samples. Boxes represent 25th and 75th percentiles, with median line; whiskers represent 5th and 95th percentile.

5.4.2.4 Fe-(oxyhydr)oxides

Consistent with the formation of Fe-(oxyhydr)oxides and Fe-hydroxysulfates, predominantly as alteration product from sulfide oxidation, MLA data suggest altered Fe-sulfides were associated predominantly with pyrrhotite, and to a lesser degree pyrite, chalcopyrite and pentlandite in all samples (Figure 5-2; Figure D-4). As reported in a previous study of these samples (Smith et al., 2021; Chapter 2), pyrite exhibited a lower degree of oxidation than pyrrhotite grains, as observed by optical microscopy, SEM/EDX and EPMA. Chalcopyrite grains were calculated to have a higher

degree of association with altered Fe-sulfide phases than pyrite in all but two historical samples, suggesting a higher degree of alteration in chalcopyrite, and consistent with optical microscopy observations. Grain sizes of chalcopyrite were calculated to be smaller than those of pyrite (median d50 value for chalcopyrite of 45 μm ; median d50 value of pyrite of 108 μm in historical samples), which may be an artefact of the limited modal abundance of chalcopyrite. However, small grain sizes can contribute to a higher degree of susceptibility to oxidation and/or illustrate a shrinking sulfide grain due to oxidation. Free-surface areas calculated by MLA suggest pyrite had a higher proportion free surface than chalcopyrite for both historical and freshly blasted samples. Pyrite and pyrrhotite had a high degree of association (Figure D-5), consistent with pyrite to pyrrhotite transition at conditions of greenschist to amphibolite facies exhibited at Detour (Phillips and Powel, 2010; Oliver et al., 2012; Dubosq et al., 2018). This close association can cause galvanic interactions between pyrite and pyrrhotite during weathering, with the enhanced oxidation of pyrrhotite over pyrite in this couple. Increased oxidation of chalcopyrite compared to pyrite due to galvanic interactions between pyrrhotite and pyrite may be contributing to the MLA-calculated associations of chalcopyrite and altered Fe-sulfide that were higher than associations between pyrite and altered Fe-sulfides, and the higher degree of alteration of chalcopyrite than pyrite observed by optical microscopy and SEM/EDX. Pyrrhotite and pentlandite had a high degree of association in all historical samples, consistent with typical occurrences of pentlandite as inclusions and/or exsolution lamellae in pyrrhotite, and as observed in these samples by optical microscopy (Smith et al., 2021; Chapter 2). However, in the MLA-produced mineral-particle images pentlandite typically occurred as blebs rather than lamellae, suggesting the resolution of the MLA (approximately 1.5 μm) was insufficient to capture pentlandite lamellae, and, therefore, the MLA-calculated modal mineralogy for pentlandite may be lower than the actual occurrence.

Notable associations with the altered Fe-sulfide phase, in addition to the secondary sulfates and sulfides, were the oxides ilmenite [MLA database formula as $\text{Fe}^{2+}\text{TiO}_3$], Cr-bearing magnetite [as $\text{Fe}_{2.5}\text{Cr}_{0.5}\text{O}_4$] and titanomagnetite [as $(\text{Fe}_{0.9}\text{Ti}_{0.1})_3\text{O}_4$] (Figure 5-3). Ilmenite has been identified as part of the lower amphibolite facies mineral assemblage at Detour Lake Mine (Oliver et al., 2012). In addition to altered Fe-sulfides, ilmenite typically had a degree of association with the S-bearing minerals jarosite in most samples, and with pyrrhotite and chalcopyrite in some samples, but with no consistency among the relationships (Figure D-1 through Figure D-5). The WRA-measured titanium [Ti] concentrations were lower than the MLA-calculated Ti elemental distribution for the historical

samples, but similar for the freshly blasted samples (Table D-2 and Table D-3). Studies of Fe ore by automated mineralogy have found distinguishing between Fe-ore minerals of similar composition to be problematic (Figueroa, et al., 2011; Donskoi et al., 2013). The MLA-calculated association between the Fe-oxides and altered Fe-sulfides in this study is interpreted to predominantly represent Fe-oxide phases in association with pyrrhotite that oxidized to form the MLA-identified phase altered Fe-sulfide.

5.4.3 Trace elements reservoirs

The liberation of minerals in which trace elements are incorporated will impact the release rate of trace elements to porewater. Encapsulation of sulfide minerals by silicate minerals and the accumulation of secondary minerals on surfaces can affect the diffusion rates of oxidants and reaction products, and thus impact the rate of sulfide oxidation and solute release. This rate dependence is commonly described conceptually and mathematically by the shrinking core model (e.g., Davis et al., 1986; Wunderly et al., 1996). MLA data of the historical and freshly blasted waste rock suggest that typically < 10% of sulfide grains were fully encapsulated (Figure D-6) by either rock-forming minerals or sulfide-oxidation products. The degree of liberation is expected to impact the overall rate of sulfide oxidation of the grain; however, oxidation is still expected to propagate through the entirety of partially encapsulated grains, but at a lower overall rate because of the narrowed oxidation front. As such, the entire trace-element load associated with a partially liberated grain would be available to be released to the environment.

The MLA database provided idealized mineral formulae that do not account for trace-element substitutions in the crystal lattice or surface sorption and makes assumptions about the composition of minerals with solid solution. Concentrations of Zn and Ni calculated by MLA were an order of magnitude, or more, lower than concentrations measured by four-acid digestion whereas Cu concentrations calculated by MLA were typically within a factor of two lower (Table 5-3). The MLA database ascribed Cu only to chalcopyrite [CuFeS_2], Ni only to pentlandite [$\text{Ni}_4.5\text{Fe}_{4.5}\text{S}_8$], and Zn only to sphalerite [ZnS]. The trace elements Se, Co and As were not included in the MLA-calculated elemental assay because they did not occur in the formulae of the minerals included in the MLA database.

Chalcopyrite and pentlandite were calculated by MLA to be present at ≤ 0.3 wt%, with sphalerite at < 0.01 wt% (Table 5-1). Low MLA-reported modal abundances may be an artefact of the resolution

and/or sample size used by MLA; i.e., the total number of particles analyzed by MLA is considerably lower than the number of particles analyzed by bulk chemical techniques, and particles smaller than the MLA resolution (1.5 μm) would escape identification by MLA (e.g., potentially pentlandite lamellae in pyrrhotite, or sphalerite grains). These “missing” particles may be contributing to the discrepancy between trace-element concentrations calculated by MLA and those measured by four-acid digestion (Table 5-3). The concentrations of Cu, Ni and Zn measured by four-acid digestion were used to calculate maximum abundances of chalcopyrite, pentlandite and sphalerite, respectively. Maximum calculated modal mineralogies of chalcopyrite were typically higher than those calculated by MLA by a factor of two, and pentlandite and sphalerite abundances were typically higher by an order of magnitude (Table 5-4). These maximum concentrations calculated using four-acid digestion concentrations are still considered “trace” (≤ 0.5 wt%), consistent with optical microscopy observations (Smith et al., 2021; Chapter 2), and are considered a reasonable maximum bound.

Combining modal mineralogy with EPMA data provides an opportunity to quantify and interpret trace-element reservoirs associated with sulfide minerals and their Fe-(oxyhydr)oxide \pm S alteration rims; these associated trace elements may be released to porewater as geochemical conditions evolve as a result of ongoing acid production by sulfide oxidation and neutralization by carbonate- and silicate-mineral dissolution. EPMA measurements were collected from grains of pyrite ($n = 101$ in historical samples, $n = 83$ in freshly blasted samples), pyrrhotite ($n = 79$ in historical samples, $n = 85$ in freshly blasted samples), chalcopyrite ($n = 41$ in historical samples, $n = 7$ in freshly blasted samples) and pentlandite ($n = 5$ in historical samples, $n = 2$ in freshly blasted samples) to identify and quantify trace-element substitutions in these minerals, which could be released during sulfide oxidation. Trace elements were measured in alteration rims associated with pyrrhotite ($n = 50$ in historical samples, $n = 12$ in freshly blasted samples) and pyrite ($n = 10$ in historical samples, $n = 5$ in freshly blasted samples) (Smith et al., 2021; Chapter 2) to quantify the trace-element reservoir that may act as both a sink and source for trace elements in porewater, based on the geochemical stability of the secondary Fe-(oxyhydr)oxide \pm S phases, which may fluctuate in response to changing *in situ* conditions.

5.4.3.1 Pyrite and pyrrhotite

The trace elements Ni and Co were measured by EPMA at the highest concentration in both pyrrhotite and pyrite, but with trace concentrations of Cu, Zn, Se and As detected in many grains

(Smith et al., 2021; Chapter 2). Applying median and 75th percentile concentrations measured by EPMA to the modal abundance of pyrite and pyrrhotite reported by MLA provided an estimate of the trace-element reservoirs in sulfide minerals and alteration products in the < 425 µm fraction of the historical waste rock that was not captured by MLA (Figure 5-5; Table D-4 and Table D-5). Pyrrhotite was calculated to contribute up to 103 ppm Ni and up to 15 ppm Co, and pyrite was calculated to contribute up to 16 ppm Ni and up to 18 ppm Co from the < 425 µm fraction of the bulk waste rock, in addition to the MLA-calculated Ni reservoir, and quantifying a Co reservoir not identified by MLA (Table D-4 and Table D-5).

5.4.3.2 Sulfide alteration products

Trace elements associated with the MLA-calculated modal abundances of altered Fe-sulfides were calculated using EPMA measurements of alteration rims associated with pyrrhotite and pyrite grains from four historical samples (n = 57 measurements), and one freshly blasted sample (n = 19 measurements). Trace-element concentrations not accounted for by MLA-ascribed mineral formulae were calculated to be Ni > Cu > Co > Zn > As > Se in the historical samples (Table 5-3). This sequence is broadly consistent with the modal abundances of sulfide minerals and their trace-element concentrations.

Of the trace elements, Ni had the highest concentration measured by EMPA in pyrrhotite (median of 2740 ppm, 75th percentile of 3990 ppm, n = 79), pyrite (median of 558 ppm, 75th percentile of 1790 ppm, n = 101), and the alteration rims associated with pyrrhotite and pyrite (median of 963 ppm, 75th percentile of 2510 ppm, n = 60). MLA-calculated Ni concentrations were based only on the occurrence of pentlandite, with the database formula of $\text{Fe}^{2+}_{4.5}\text{Ni}_{4.5}\text{S}_8$, underestimating the Ni concentration contributed by sulfide minerals and alteration products in the < 425 µm fraction of historical waste rock by up to 89 ppm, a factor of two (30 – 99% relative percent difference, RPD) when median Ni concentrations from EPMA were applied (Figure 5-5; Table D-4). Including the Ni reservoirs in pyrite, pyrrhotite and alteration rims, calculated using the median EPMA concentrations, increased the calculated concentrations of Ni associated with these reservoirs in the waste rock by up to a factor of two. When the 75th percentile concentrations measured by EPMA were applied, the discrepancy in Ni concentrations associated with sulfide mineral and alteration products increased by up to 152 ppm (60 – 170% RPD; Figure 5-5; Table D-5).

The median Cu concentration measured by EPMA on pyrite and pyrrhotite alteration rims ($n = 60$) was 1700 ppm (75th percentile of 5700 ppm). Median and 75th percentile concentrations were 24 ppm and 132 ppm ($n = 79$) in pyrrhotite and < 2 ppm and 99 ppm in pyrite ($n = 101$). Sorption of Cu on Fe-(oxyhydr)oxides has been observed in circumneutral mine drainage waters (Johnson, 1986; Lee et al., 2002), the pH range measured in porewater extracted from these samples (Smith et al., 2021; Chapter 2). Chalcopyrite was observed by optical microscopy to have a higher degree of alteration than pyrite in the historical samples (Smith et al., 2021; Chapter 2), suggesting chalcopyrite and alteration rims were the primary source of Cu in the historical samples.

Zinc concentrations measured by EPMA in the alteration rims of pyrrhotite and pyrite grains ($n = 60$) from the historical samples had a median concentration of 293 ppm, higher than median and 75th percentile concentrations measured in pyrite (< 2 ppm, 152 ppm, respectively; $n = 101$) and pyrrhotite (< 2 ppm, 159 ppm, respectively; $n = 79$), and higher than the median, but within the 75th percentile measured in chalcopyrite (39 ppm, 322 ppm, respectively; $n = 41$) in these samples. The higher concentration in alteration rims suggests Zn was released from weathering sphalerite, chalcopyrite, and possibly silicate minerals, and sorbed to the secondary Fe-(oxyhydr)oxide minerals associated with pyrite and pyrrhotite oxidation.

5.4.3.3 Trace sulfides by MLA: chalcopyrite, pentlandite and sphalerite

Chalcopyrite, pentlandite and sphalerite were characterized qualitatively by optical microscopy as occurring in minor or trace amounts (Smith et al., 2021; Chapter 2), whereas MLA quantified abundances of chalcopyrite and pentlandite, and estimated abundances of sphalerite. These quantifications permit a calculation of the reservoirs of Cu, Ni and Zn in mineral-crystal structures, and when combined with EPMA measurements, trace elements incorporated as impurities.

EPMA measurements of trace elements obtained from chalcopyrite and pentlandite were used to calculate the concentration of trace elements present as impurities; no sphalerite grains were encountered during the EPMA analyses. Chalcopyrite in the historical samples ($n = 42$) had estimated (i.e., $< \text{MDL}$ but $> \text{LOD}$) median Zn concentrations of 39 ppm (range of $< \text{LOD} - 4.64 \text{ wt\%}$), and an estimated median Ni concentration of 6 ppm (range of $< \text{LOD} - 726 \text{ ppm}$). Arsenic, Se and Co were detected in some grains, but median concentrations were $< \text{LOD}$ (ranges of $< \text{LOD} - 171 \text{ ppm}$; $< \text{LOD} - 456 \text{ ppm}$; $< \text{LOD} - 408 \text{ ppm}$, respectively). Chalcopyrite grains from two freshly blasted samples had order of magnitude differences in Zn, though with a limited number of measurements

(< LOD for all n = 3 in sample 117; and median of 345 ppm with range of < LOD – 506 ppm, n = 4 in sample 090), and Se (median of 248 ppm, range of < LOD – 380 ppm n = 3 in sample 117; and median of 48 ppm, range of < LOD – 132 ppm, n = 4 in sample 090).

Few pentlandite grains (n = 5 for historical, n = 2 for freshly blasted) were measured by EPMA; pentlandite grains in the historical waste rock had a median Se concentration of 212 ppm (range of 113 (estimate) – 467 ppm for historical; 3 ppm (estimate) and 243 ppm in freshly blasted), an estimated median As concentration of 103 ppm (range < LOD – 564 ppm for historical; 92 ppm (estimate) and 214 ppm for freshly blasted), and median Co concentration of 3.70 wt% (range of 0.76 – 4.51 wt% for historical; 1.57 wt% and 2.04 wt% for freshly blasted; Cu was not detected in any of the pentlandite grains measured, consistent with expected Cu partitioning during sulfide formation and subsequent metamorphism. The presence of Co in wt% abundances is notable, despite the low modal abundance of pentlandite, because the MLA database has no mineral formulae that contain Co, therefore neglecting a reservoir of an element of potential concern in mine-drainage waters. The measured concentrations of trace elements in pyrrhotite and pentlandite are reasonable when compared to EPMA measurements on sulfide grains from the Bushveld complex, and various Canadian deposits (Paktunc et al., 1990).

Trace-element concentrations associated with sphalerite were based only on the MLA-estimated sphalerite mineral abundances. Because no grains were encountered during EPMA, no assumptions or calculations were made about possible trace element impurities; however, it is expected that Cd, a common trace element in sphalerite solid solution (e.g., Cook et al., 2009), would be present in sphalerite, possibly in wt% abundances. Porewater extracted from corresponding historical samples had concentrations of Zn of 5.4 – 42.0 $\mu\text{g L}^{-1}$ and Cd concentrations of < 0.05 – 1.3 $\mu\text{g L}^{-1}$ (Smith et al., 2021; Chapter 2). The low concentration of Cd is consistent with the paucity of sphalerite in these samples. In addition to sphalerite, Zn can occur as an impurity in silicates, such as the amphiboles, pyroxenes and/or micas (Mihaljev and Farges, 1999; Salminen et al., 1998), which together comprise up to 37 wt% of the samples in this study, as calculated by MLA (Table 5-1).

5.4.3.4 Bulk assay: Comparison to MLA and trace sulfide calculations

The concentrations of Ni, Co, and Zn measured by four-acid digestion were consistent for felsic and mafic to ultramafic lithologies (Table 5-3; Mielke, 1979; Yaroshevsky, 2006). The discrepancy between the bulk measurement and calculated concentrations in sulfide and alteration-product

reservoirs may be artefacts of MLA sample size and resolution, (e.g., undercounting trace sulfides) and/or that these trace elements may be present as an impurity in ferromagnesian minerals (e.g., Carr and Turekian 1961). Copper concentrations measured by four-acid digestion were a factor of two to an order of magnitude higher than concentrations reported for crustal rocks (Yaroshevsky, 2006), suggesting chalcopyrite was present in the waste rock at elevated abundances, consistent with the association of chalcopyrite with gold mineralization at Detour Lake Mine (Oliver et al., 2012).

Calculated modal mineralogies by bulk chemistry of chalcopyrite were typically within a factor of two of the MLA-calculated modal mineralogies (Table 5-1; Table 5-4). The modal mineralogies of pentlandite and sphalerite calculated by four-acid digestion results were typically an order of magnitude higher than those calculated by MLA (Table 5-1; Table 5-4), but still at concentrations considered “trace” (< 0.5 wt%). The calculations based on four-acid digestion results ignored the contribution of Cu, Ni and Zn as impurities or sorbed species associated with pyrite, pyrrhotite and altered Fe-sulfides, but is considered a reasonable estimate of maximum possible mineral abundances. The chalcopyrite, pentlandite and sphalerite modal mineralogies calculated by MLA and four-acid digestion are interpreted here to represent the lower and upper bounds, respectively, of the plausible concentrations of these minerals in the samples, recognizing that trace-element substitutions in silicate minerals may also be contributing to the discrepancy between the MLA-calculated elemental concentrations and concentrations measured by four-acid digestion.

The trace elements Co, Se and As were not included in any MLA-ascribed mineral formula but were measured by four-acid digestion in the bulk waste-rock samples, and by EPMA as trace elements associated with sulfide minerals and their alteration products. Applying the EPMA-measured concentrations to the MLA-calculated modal mineralogy provided an estimate of these trace elements that could be released to the environment from sulfide oxidation. The calculated concentrations of As and Se using the median and 75th percentile EPMA concentrations applied to the calculated chalcopyrite, pentlandite and sphalerite modal abundances were similar to the concentrations measured by four-acid digestion. However, the Co concentrations in the historical samples calculated by this method were approximately an order of magnitude lower than those measured by four-acid digestion (Table 5-3; Table 5-5; Table D-4 and Table D-5). Concentrations of Co calculated using EPMA concentrations and the modal abundances of pentlandite and chalcopyrite were similar to those measured by four-acid digestion, suggesting pentlandite, which was measured to contain wt% abundance of Co (Smith et al., 2021; Chapter 2), was under-reported by MLA.

5.5 Conclusions

Quantitative mineralogy (mineral liberation analysis; MLA) integrated with conventional microscopy and mineral identification techniques suggest the persistence of heterogeneous and dynamic geochemical conditions in a historical waste-rock pile, including microenvironments that were geochemically favorable for secondary minerals to precipitate. Combining trace-element concentrations measured by electron-probe microanalysis to abundances of sulfide minerals and sulfide-oxidation products reported by mineral liberation analysis provide a quantification of trace-element reservoirs in the waste-rock samples. Calculations reveal that trace-element concentrations were undercalculated by quantitative mineralogy, when compared to standard bulk-chemical analysis; the discrepancy may be due to limitations on MLA sample size, resolution, and/or trace element impurities in silicate minerals.

Table 5-3: MLA- calculated assay based on assigned mineral formulae vs. trace elements measured by four-acid digestion. Concentration of the trace elements zinc [Zn], selenium [Se], copper [Cu], cobalt [Co], nickel [Ni], and arsenic [As]. The detection limit for Se was 2.2 ppm. “n.a.” denotes the sample was not analyzed by four-acid digestion. All concentrations in ppm.

	MLA-calculated elemental assay						Four-acid digestion concentrations					
	Zn	Se	Cu	Co	Ni	As	Zn	Se	Cu	Co	Ni	As
<i>Historical</i>												
2M	7	-	489	-	89	-	112	2.29	765	92.1	448	6.63
3B	1	-	951	-	88	-	123	2.72	1810	108	644	6.28
3M	36	-	554	-	96	-	106	2.38	740	90.4	700	5.04
3T	0	-	378	-	33	-	n.a.	n.a.	n.a.	n.a.	n.a.	n.a.
4MB	4	-	317	-	46	-	n.a.	n.a.	n.a.	n.a.	n.a.	n.a.
4T	0.4	-	801	-	91	-	158	2.74	924	2060	1490	7.93
5B	8	-	925	-	151	-	n.a.	n.a.	n.a.	n.a.	n.a.	n.a.
5M	0.3	-	588	-	43	-	184	2.79	1050	201	1640	5.94
5T	7	-	622	-	105	-	105	< 2.2	774	73.6	564	5.04
<i>Freshly blasted</i>												
117	63	-	384	-	291	-	196	< 2.2	429	86.2	642	6.71
119	59	-	1140	-	388	-	n.a.	n.a.	n.a.	n.a.	n.a.	n.a.
90	10	-	29	-	0.5	-	38.3	< 2.2	62.3	9.8	32.6	1.64
223	35	-	79	-	0.2	-	67	< 2.2	139	25.2	49.6	18.1
224	12	-	25	-	3	-	n.a.	n.a.	n.a.	n.a.	n.a.	n.a.
25-26	2	-	41	-	1	-	2.22	< 2.2	113	15.4	44.9	2.22

Table 5-4: Abundances of sphalerite, chalcopyrite and pentlandite based on zinc, copper and nickel concentrations, respectively, measured by four-acid digestion. “n.a.” denotes the sample was not analyzed by four-acid digestion.

	Calculated abundances from 4AD (wt%)		
	Sphalerite	Chalcopyrite	Pentlandite
<i>Historical</i>			
2M	0.02	0.22	0.14
3B	0.02	0.52	0.20
3M	0.02	0.21	0.22
3T	n.a.	n.a.	n.a.
4MB	n.a.	n.a.	n.a.
4T	0.02	0.27	0.47
5B	n.a.	n.a.	n.a.
5M	0.03	0.30	0.51
5T	0.02	0.22	0.18
<i>Freshly blasted</i>			
117	0.03	0.12	0.20
119	n.a.	n.a.	n.a.
090	0.01	0.02	0.01
223	0.01	0.04	0.02
224	n.a.	n.a.	n.a.
25-26	0.01	0.03	0.01

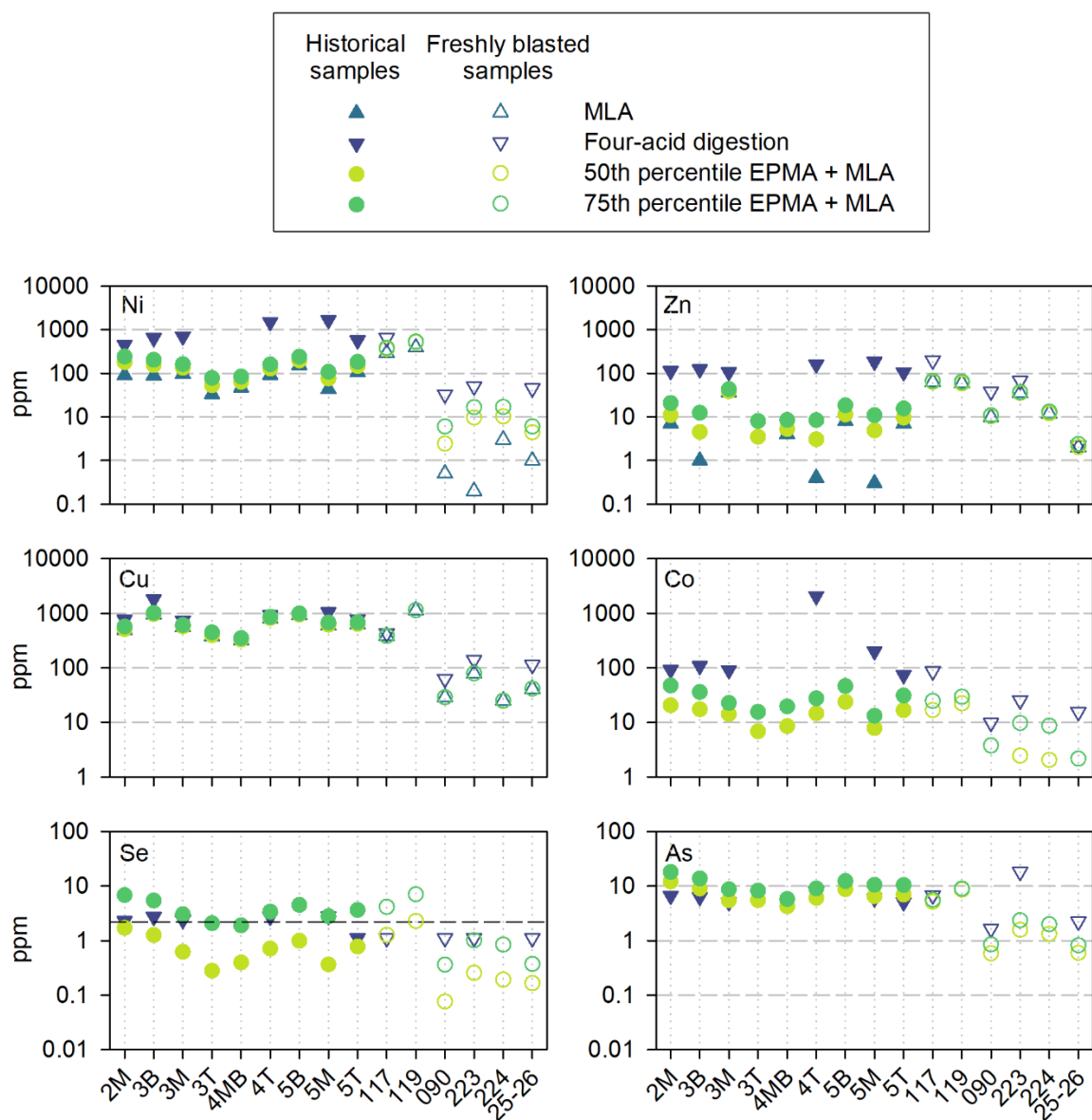


Figure 5-5: Concentrations of trace elements provided by MLA compared to concentrations measured by four-acid digestion, and calculated concentrations using median and 75th percentile concentrations measured by electron-probe micro analysis (EPMA) and applied to the MLA-provided modal mineralogies for pyrrhotite, pyrite, chalcopyrite, pentlandite and altered Fe-sulfides. Sphalerite excluded because MLA modal abundance considered an estimate and no sphalerite grains encountered during EPMA analysis. Recall that freshly blasted samples 117 and 119 had mafic to ultramafic lithologies,

whereas the other freshly blasted samples had felsic lithologies. All concentrations in ppm of waste-rock fraction < 425 µm, i.e., [mg trace element] [kg < 425 µm fraction of waste rock]⁻¹.

Table 5-5: Concentrations of selenium [Se], cobalt [Co] and arsenic [As] measured by electron-probe microanalysis (EPMA) applied to modal abundances of pentlandite and chalcopyrite calculated by four-acid digestion (4AD) concentrations. Includes contributions from pyrite, pyrrhotite and altered Fe-sulfide calculated based on MLA modal abundance. “n.a.” denotes sample not analyzed by four-acid digestion. All concentrations in ppm of waste-rock fraction < 425 µm, i.e., [mg trace element] [kg < 425 µm fraction of waste rock]⁻¹.

	Median EPMA applied to sulfide abundances (ppm)			75 th percentile EPMA applied to sulfide abundances		
	Se	Co	As	Se	Co	As
<i>Historical</i>						
2M	2.4	36	12	7.4	121	18
3B	2.7	44	9.2	6.4	132	14
3M	1.5	43	5.7	3.8	121	9.0
3T	n.a.	n.a.	n.a.	n.a.	n.a.	n.a.
4MB	n.a.	n.a.	n.a.	n.a.	n.a.	n.a.
4T	2.2	89	6.5	4.9	229	9.7
5B	n.a.	n.a.	n.a.	n.a.	n.a.	n.a.
5M	2.1	96	7.0	4.7	232	11
5T	1.6	37	7.1	4.2	111	11
<i>Freshly blasted</i>						
117	1.4	38	5.4	4.4	49	5.8
119	n.a.	n.a.	n.a.	n.a.	n.a.	n.a.
090	0.1	2.4	0.6	0.4	4.8	0.9
223	0.3	5.2	1.6	1.1	7.7	2.4
224	n.a.	n.a.	n.a.	n.a.	n.a.	n.a.
25-26	0.2	3.2	0.6	0.4	3.4	0.8

Chapter 6

Conclusions and contributions to science

6.1 Summary of results

This study has applied a variety of analytical techniques to investigate the key processes associated with pyrrhotite oxidation occurring in waste rock that has been weathering for more than 30 years.

Porewater extracted from waste rock that had been weathering subaerially for more than 30 years remained circumneutral (pH 7.0 – 8.2) with measurable alkalinity (27 – 110 mg L⁻¹ as CaCO₃), and elevated concentrations of sulfate (1800 – 4200 mg L⁻¹, median of 2000 mg L⁻¹), nickel (1 – 1660 µg L⁻¹; median of 120 µg L⁻¹), cobalt (2 – 81 µg L⁻¹; median of 6 µg L⁻¹), copper (1 – 14 µg L⁻¹; median of 7 µg L⁻¹) and zinc (5 – 185 µg L⁻¹; median of 26 µg L⁻¹) consistent with on-going sulfide oxidation and acidity neutralized predominantly by carbonate-mineral dissolution. Microanalysis of pyrrhotite grains confirmed oxidation and the presence of secondary minerals, and provided concentrations of trace elements associated with sulfide minerals and the oxidation products. Of the trace elements measured, nickel occurred at the highest concentration in pyrite (median of 558 ppm) and pyrrhotite (median of 2740 ppm) and the alteration rims (median of 963 ppm) from samples of weathered waste rock. Calculations suggested that sorption sites on the alteration rims were saturated with respect to nickel. Synchrotron X-ray absorption spectra revealed the presence of phases of mixed oxidation states of iron, sulfur and nickel associated with alteration rims. Results from this study suggest sulfide oxidation was proceeding and releasing trace elements to porewater, with some attenuation by sorption onto secondary phases, and carbonate minerals were dissolving to maintain circumneutral porewater pH.

Synchrotron-based data collected across oxidizing pyrrhotite grains provided insight into pyrrhotite oxidation at 1 µm intervals. Iron species in the alteration phases occurred as mixtures of ferric and ferrous iron species. Linear combination fitting of spectra from the least oxidized pyrrhotite grain included contributions of iron hydroxysulfate species whereas the iron species in the alteration products of the weathered sample consisted of predominantly iron (oxyhydr)oxides; these results are consistent with the aging of iron hydroxysulfates to iron hydroxides and circumneutral pH. Results from linear combination fitting were used to estimate the relative proportions of ferric iron and ferrous iron, and the results were compared to the pre-edge centroid characteristics. The pre-edge

centroids of some standards exhibited oxidation-state characteristics different from those inferred by edge and white line energies, and a clustering of data points from the pyrrhotite transects occurred at ferric iron fraction of 0.2. Together, these data suggest that the pre-edge centroids maintained the energy of ferrous iron until a threshold ferric iron contribution was exceeded.

Porewater chemistry, solids chemistry and stable calcium isotopes were analyzed to attempt to identify the relative contributions of carbonate- and silicate-mineral weathering to the neutralization of acid produced by sulfide oxidation. Multi-year porewater chemistry data from Detour Lake Mine, with supplementary data from the Diavik Diamond Mine were used to calculate lower bounds of carbonate-mineral contributions based on measured alkalinity and concentrations of dissolved calcium and calculated concentrations of dissolved inorganic carbon. The Detour and Diavik samples had calculated medians of carbonate-mineral contribution of 0.18 and 0.59 (as lower bounds), respectively. These results were consistent with expectations based on the respective system lithologies. Ratios of the stable calcium isotopes ^{44}Ca and ^{40}Ca were measured in a small number of porewater and solid samples from each system. Porewater from Diavik had lower $\delta^{44/40}\text{Ca}$ values (range of -1.51 to -1.08 ‰) than porewater from Detour (range of -1.22 to -0.45 ‰). Two-component mixing based on solids and porewater samples from the Diavik system suggested a carbonate-mineral contribution of up to 0.90, much higher than expected for the calcite-poor waste-rock system. Calcium isotope values from Detour solids and porewater samples suggested gypsum precipitation was preferentially incorporating the lighter (^{40}Ca) isotope and was confounding interpretation of the dataset. Additional analyses on solid samples would provide additional insight into the applicability of using stable calcium isotopes to apportion carbonate-mineral contributions to acid neutralization in mining waste rock.

Automated quantitative mineralogy (mineral liberation analysis, MLA) was used to identify and quantify characteristics of sulfide and secondary minerals. Porewater associated with the weathered waste-rock samples was calculated to be saturated with respect to gypsum. The abundance, mineral habit and grain sizes of gypsum varied among the historical samples and suggested heterogeneous and dynamic geochemical conditions within the waste-rock pile. The presence of jarosite in the MLA results were supported by X-ray diffraction analyses, despite calculations that showed porewater was undersaturated with respect to that phase. The grain size and associations produced by MLA suggested that jarosite formed in acidic microenvironments adjacent to oxidizing sulfide grains.

Concentrations of trace elements measured by electron-probe microanalysis were applied to MLA modal mineralogy to quantify potential trace-element reservoirs and compared to concentrations measured by four-acid digestion. Arsenic, selenium and cobalt were measured by electron-probe microanalysis in sulfide grains and alteration rims but were not included in the MLA-calculated elemental assay because no mineral formulae in the MLA database contained these elements. Copper, nickel and zinc occur as the main components of chalcopyrite, pentlandite and sphalerite, respectively, and as impurities in pyrite and pyrrhotite. These trace elements were under-reported by up to an order of magnitude when compared to calculations applying electron-probe microanalytical results to MLA modal mineralogy, and to four-acid digestion concentrations. The discrepancy between bulk chemical assay and MLA-calculated element concentrations may be caused by trace-element solid solution with silicate minerals not considered by MLA mineral formulae, and/or the sample size and resolution limitations of MLA.

6.2 Contributions to science

The evolution of porewater geochemistry and mineral transformations in acidic and circumneutral mine-waste systems are complex because of concurrent sulfide-mineral oxidation, acid neutralization by the dissolution of carbonate- and non-carbonate minerals, secondary-mineral precipitation and/or dissolution, and/or trace-element release to porewater and sorption to secondary minerals. A better understanding of these processes contributes to more rigorous characterization and prediction of the quality and persistence of mine drainage, and, therefore, evaluation of environmental risk. Research presented in this study evaluated waste-rock solids and porewater and furthered our understanding of these processes.

The first research chapter demonstrates the value of characterizing sulfide oxidation characteristics from the solid-phase and co-located porewater samples using solid-phase and aqueous geochemistry, data collected from microanalytical techniques, and mass-transfer models. Analysis of trace elements and the speciation of iron and sulfur in partially oxidized sulfide grains and associated alteration rims provides insight into the pyrrhotite oxidation process in waste rock that had been weathering for 30 years. Interpreting characteristics of weathered waste-rock solids and porewater together contributes to a better understanding of the evolution of sulfide mineral oxidation and oxidation products in mine-drainage water. This approach can be extended to a variety of mine-waste systems to improve drainage chemistry predictions for more robust mine-waste management strategies. An incidental but

broadly applicable finding emphasizes the importance of proper sample handling to reduce the possibility of tertiary phase transformations, which may affect measured geochemical parameters and subsequent interpretations and predictions.

The synchrotron-based research described in the second chapter evaluated the spatial distribution at the 1 μm scale of iron species associated with pyrrhotite oxidation. The possibility of oxidizing ferrous-iron species retaining a ferrous-iron pre-edge centroid energy until a threshold ferric-iron component has been surpassed suggests the possibility of a pyrrhotite-oxidation mechanism that has not yet been identified and/or confirmed. This research forms the basis for (i) future studies to interrogate the sulfide-oxidation model using synchrotron-based techniques and (ii) evaluating adjustments to the shrinking-core model based on secondary phases in reactive transport modelling.

This research is believed to be the first study to apply stable calcium-isotope measurements to mine-waste systems and provided values of $\delta^{44/40}\text{Ca}$ from samples from two lithologically-distinct waste rock systems. Samples included porewater extracted from waste rock, massive calcite (presumed hydrothermal), plagioclase, acetic-leached fractions of waste rock, and waste rock digested by the four-acid method. A better understanding of the relative contributions of carbonate- and non-carbonate minerals to neutralizing acid produced by sulfide oxidation is important for predicting the geochemical evolution of drainage chemistry. Additional porewater samples, and analyses targeting carbonate mineral, gypsum, and silicate fractions of waste rock would confirm the applicability of using stable calcium isotopes to inform acid neutralization mechanisms in heterogeneous geochemical systems.

A mass-balance calculation using measured porewater chemistry and a mass-transfer model to apportion dissolved calcium concentrations to carbonate-mineral and silicate-mineral sources provides a lower-bound of calcium concentrations from carbonate-mineral dissolution. Additional characterization parameters would be required for a complete mass-balance approach and to confidently apply the results to unsaturated, subaerially exposed waste-rock systems. The presented calculation approach can form the basis for reactive transport modelling and can be refined with the incorporation of pore-gas composition data.

Results from automated quantitative mineralogy provide insight into the distribution, association and habit of secondary minerals, which are not evident by standard techniques. Characteristics of secondary minerals provides insight into the geochemical conditions within the mine-waste system,

which are not necessarily evident from porewater chemistry or standard analytical methods. Trace-element concentrations calculated from modal abundances measured by automated quantitative mineralogy must be interpreted with caution. Combining quantitative modal abundances and trace-element concentrations measured by conventional microanalytical techniques provides a distribution of trace elements among sulfide-mineral and alteration-product reservoirs. Comparing these results to results from conventional bulk assays reveals limitations in applying automated quantitative mineralogy for characterizing trace-element reservoirs. Quantitative mineralogy provides large, comprehensive datasets that are not practicably obtainable by conventional methods, and is becoming a routine and important analytical method for mine-waste characterization. This research emphasizes the value of applying quantitative mineralogy to mine-waste systems. However, this research also emphasizes the necessity for understanding the assumptions and system limitations of quantitative mineralogy when interpreting the results, particularly for environmentally important trace elements, which may not be adequately represented by standard mineral databases.

Research presented in this thesis demonstrates the value of integrating field-based measurements, and microanalytical and quantitative techniques to interpret sulfide-oxidation characteristics, secondary-mineral formation, and the behaviour of trace elements in solids and porewater. Research outcomes can be extended to future studies to contribute to improving our understanding of the development and persistence of drainage chemistry, and, thus, reducing environmental risk from mine waste.

References

- Al, T.A., Martin, C.J., Blowes, D.W. 2000. Carbonate-mineral/water interactions in sulfide-rich mine tailings. *Geochim. Cosmochim. Acta.* 64, 3933–3948. [https://doi.org/10.1016/S0016-7037\(00\)00483-X](https://doi.org/10.1016/S0016-7037(00)00483-X).
- Alpers, C.N., Nordstrom, D.K., Ball, J.W. 1989. Solubility of jarosite solid solutions precipitated from acid mine waters, Iron Mountain, California, U.S.A. *Sci. Geol. Bull.*, 42, 4, 281–298.
- Alpers, C.N., Blowes, D.W., Nordstrom, D.K., Jambor, J.L. 1994. Secondary minerals in acid mine-water chemistry. In: Jambor, J.L., Blowes, D.W. (Eds.), *Environmental Geochemistry of Sulfide Mine-Waste*. Mineralogical Association of Canada Short Course, vol. 22. Mineralogical Association of Canada, Canada, 247–270.
- Amos, R.T., Blowes, D.W., Smith, L., Sego, D.C. 2009. Measurement of wind-induced pressure gradients in a waste-rock pile. *Vadose Zone J.* 8, 953–962. <https://doi.org/10.2136/vzj2009.0002>.
- Amos, R.T., Blowes, D.W., Bailey, B.L., Sego, D.C., Smith, L., Ritchie, A.I.M. 2015. Waste-rock hydrology and geochemistry. *Appl. Geochem.* 57, 140–156. <http://dx.doi.org/10.1016/j.apgeochem.2014.06.020>.
- Alpers, C.N., Nordstrom, D.K., Ball, J.W. 1989. Solubility of jarosite solid solutions precipitated from acid mine waters, Iron Mountain, California, U.S.A. *Sci. Geol. Bull.*, 42, 4, 281–298.
- Alpers, C.N., Nordstrom, D.K., Burchard, J.M. 1992. Compilation and interpretation of water-quality and discharge data for acidic mine waters at Iron Mountain, Shasta County, California, 1940–91. *Water-Resources Investigations Report 91-4160*. U.S. Geological Survey, Sacramento, California.
- Alpers, C.N., Blowes, D.W., Nordstrom, D.K., Jambor, J.L. 1994. Secondary minerals in acid mine-water chemistry. In: Jambor, J.L., Blowes, D.W. (Eds.), *Environmental Geochemistry of Sulfide Mine-Waste*. Mineralogical Association of Canada Short Course, Vol. 22. Mineralogical Association of Canada, Canada, 247–270.
- Anderson, S.P., Drever, J.I., Frost, C.D., Holden, P. 2000. Chemical weathering in the foreland of a retreating glacier. *Geochim. Cosmochim. Acta.* 64, 1173–1189. [https://doi.org/10.1016/S0016-7037\(99\)00358-0](https://doi.org/10.1016/S0016-7037(99)00358-0).

- Arnold, R.G., Reichen, L.E. 1962. Measurement of the metal content of naturally-occurring, metal-deficient, hexagonal pyrrhotite by an X-ray spacing method. *Amer. Mineral.* 47, 105–111.
- ASTM International. 2010. Standard test methods for laboratory determinations of water (moisture) content of soil and rock by mass. Standard D2216-10, ASTM International, West Conshohocken, United States.
- ASTM International 2013. Standard test method for pH of soils. Standard D4972-13, ASTM International, West Conshohocken, United States.
- Bailey, B.L 2013. Geochemical and microbiological characterization of effluent and pore water from low-sulfide content waste rock. Ph.D. Thesis. University of Waterloo. Waterloo, Canada.
- Bailey, B.L., Blowes, D.W., Smith, L., Sego, D.C. 2016. The Diavik Waste Rock Project: Geochemical and microbiological characterization of low sulfide content large-scale waste rock test piles. *Appl. Geochem.* 65, 54–72. <https://doi.org/10.1016/j.apgeochem.2015.10.010>.
- Bao, Z., Al, T., Couillard, M., Poirier, G., Bain, J., Shrimpton, H.K., Finfrock, Y.Z., Lanzirrotti, A., Paktunc, D., Saurette, E., Hu, Y., Ptacek, C.J., Blowes, D.W. 2021. A cross scale investigation of galena oxidation and controls on mobilization of lead in mine waste rock. *J. Hazard. Mat.* 412, 125130. <https://doi.org/10.1016/j.jhazmat.2021.125130>.
- Bao, Z., Bain, J., Saurette, E., Finfrock, Y.Z., Hu, Y., Ptacek, C.J., Blowes, D.W. 2022. Mineralogy-dependent sulfide oxidation *via* polysulfide and thiosulfate pathways during weathering of mixed-sulfide bearing mine waste rock. *Geochim. Cosmochim. Acta.* 317, 523–537. <https://doi.org/10.1016/j.gca.2021.10.012>.
- Barazzuol, L., Sexsmith, K., Bucknam, C., Lopez, D. 2009. Application of an advanced mineralogical technique: Sulphide mineral availability and humidity cell interpretations based on MLA analysis. Proceedings of the 8th International Conference on Acid Rock Drainage (ICARD), Skelleftea, Sweden, June 2009.
- BBA and SGS. 2014. Detour Lake Mine NI 43-101 Technical Report. 4 February 2014.
- Becker, M., de Villiers, J., Bradshaw, D. 2010. The mineralogy and crystallography of pyrrhotite from selected nickel and PGE ore deposits. *Econ. Geol.* 105, 1025–1037. <https://doi.org/10.2113/econgeo.105.5.1025>.

- Becker, U. Munz, A.W., Lennie, A.R., Thronton, G., Vaughn, D.J. 1997. The atomic and electronic structure of the (001) surface of monoclinic pyrrhotite (Fe_7S_8) as studied using STM, LEED and quantum mechanical calculations. *Surf. Sci.* 389, 66–87, [https://doi.org/10.1016/S0039-6028\(97\)00370-1](https://doi.org/10.1016/S0039-6028(97)00370-1).
- Belzile, N., Chen, Y-W., Cai, M-F., Li, Y., 2004. A review on pyrrhotite oxidation. *J. Geochem. Explor.* 84, 64–76, <https://doi.org/10.1016/j.gexplo.2004.03.003>.
- Berry, A.J., O'Neill, H. St.C., Jayasuriya, K.D., Campbell, S.J., Foran, G.J. 2003. XANES calibration for the oxidation state of iron in silicate glass. *Am. Mineral.* 88, 967–977. <https://doi.org/10.2138/am-2003-0704>.
- Bhatti, T.M., Bigham, J.M., Carlson, L., Tuovinen, O.H. 1993. Mineral products of pyrrhotite oxidation by *Thiobacillus ferrooxidans*. *Appl. Environ. Microbiol.*, 59, <https://doi.org/10.1128/aem.59.6.1984-1990.1993>.
- Bigham, J.M., Nordstrom, D.K. 2000. Iron and aluminum hydroxysulfates from acid sulfate waters. In: Alpers, C.N., Jambor, J.L., Nordstrom, D.K. *Sulfate Minerals: Crystallography, Geochemistry, and Environmental Significance. Reviews in Mineralogy and Geochemistry*, Vol. 40. Mineralogical Society of America, USA, 351– 403. <https://doi.org/10.2138/rmg.2000.40.7>.
- Bird, G. 2016. The influence of the scale of mining activity and mine site remediation on the contamination legacy of historical metal mining activity. *Environ. Sci. Pollut. Res.* 23, 23456–23466. <https://doi.org/10.1007/s11356-016-7400-z>.
- Blowes, D.W., Reardon, E.J., Jambor, J.L., Cherry, J.A. 1991. The formation and potential importance of cemented layers in inactive sulfide mine tailings. *Geochim. Cosmochim. Acta.* 55, 965–978.
- Blowes, D.W., Ptacek, C.J. 1994, Acid neutralization reactions in mine tailings. In: Jambor, J.L., Blowes, D.W. (Eds.), *Environmental Geochemistry of Sulfide Mine-Wastes*, vol. 22. Mineral. Assoc. Can. Short Course, pp. 271–292.
- Blowes, D.W., Ptacek, C.J., Jambor, J.L., Weisener, C.G., 2003. The geochemistry of acid mine drainage. In: Lollar, B.S., Holland, H.D., Turekian, K.K., Exec (Eds.), *Treatise on Geochemistry*, Vol. 9. Elsevier-Pergamon, Oxford, pp. 149–204. <https://doi.org/10.1016/B0-08-043751-6/09137-4>.

- Blum, J.D., Gazis, C.A., Jacobson A.D., Chamberlain, C.P. 1998. Carbonate versus silicate weathering in the Raikhot watershed within the high Himalayan crystalline series. *Geology*. 26, 411–414. [https://doi.org/10.1130/0091-7613\(1998\)026<0411:CVSWIT>2.3.CO;2](https://doi.org/10.1130/0091-7613(1998)026<0411:CVSWIT>2.3.CO;2).
- Booth, J., Hong, Q., Compton, R.G., Prout, K., Payne, R.M. 1997. Gypsum overgrowths passivate calcite to acid attack. *J. Colloid Interf Sci.* 192, 207–214. <https://doi.org/10.1006/jcis.1997.4978>.
- Boujelben, N., Bouzid, J., Elouear, Z., 2008. Adsorption of nickel and copper onto natural iron oxide-coated sand from aqueous solutions: study in single and binary systems. *J. Hazard Mater.* 163, 376–382. <https://doi.org/10.1016/j.jhazmat.2008.06.128>.
- Brown, S.T., Kennedy, B.M., DePaolo, D.J., Hurwitz, S., Evans, W.C. 2013. Ca, Sr, O and D isotope approach to defining the chemical evolution of hydrothermal fluids: Example from Long Valley, CA, USA. *Geochim Cosmochim Acta.* 122, 209–225. <https://doi.org/10.1016/j.gca.2013.08.011>.
- Bruemmer, G.W., Gerth, J., Tiller, K.G., 1988. Reaction kinetics of the adsorption and desorption of nickel, zinc and cadmium by goethite. I. Adsorption and diffusion of metals. *J. Soil Sci.* 39, 37–52. <https://doi.org/10.1111/j.1365-2389.1988.tb01192.x>.
- Buerger, M.J. 1937. Interatomic distances in marcasite and notes on the bonding in crystals of lollingite, arsenopyrite, and marcasite types. *Z. Krystallog. Krist.* 97, 504–513. <https://doi-org.proxy.lib.uwaterloo.ca/10.1524/zkri.1937.97.1.504>.
- Busenberg, E., Plummer, N. 1982. The kinetics of dolomite in CO₂-H₂O systems at 1.5 to 65°C and 0 to 1 atm pCO₂. *Am. J. Sci.* 282, 45–78.
- Byrne, P. Reid, I., Wood, P.J. 2010. Sediment geochemistry of streams draining abandoned lead/zinc mines in central Wales: the Afon Twymyn. *J. Soils Sediments.* 10, 683–697. <https://doi.org/10.1007/s11368-009-0183-9>.
- Cánovas, C.R., Macías, F., Basallote, M.D., Olías, J., Nieto, J.M., Pérez-López, J. 2021. Metal(loid) release from sulfide-rich wastes to the environment: The case of the Iberian Pyrite Belt (SW Spain). *Curr. Opin. Environ. Sci. Health.* 20, 100240. <https://doi.org/10.1016/j.coesh.2021.100240>.
- Cantrell, K.J., Serkiz, S.M., Perdue, E.M. 1990. Evaluation of acid neutralizing capacity data for solutions containing natural organic acids. *Geochem. Cosmochim. Acta.* 54, 1247–1254. [https://doi.org/10.1016/0016-7037\(90\)90150-J](https://doi.org/10.1016/0016-7037(90)90150-J).

- Cappuyns, V., Van Campen, A., Helser, J. 2021. Antimony leaching from soils and mine waste from the Mau Due antimony mine, North-Vietnam. *J. Geochem. Explor.* 220, 106663.
<https://doi.org/10.1016/j.gexplo.2020.106663>.
- Carpenter, R.H., Desborough, G.A. 1964. Range in solid solution and structure of naturally occurring troilite and pyrrhotite. *Am. Mineral.* 49, 1350– 365.
- Carr, M.H., Turekian, K.K. 1961. The geochemistry of cobalt. *Geochim. Cosmochim. Acta.* 23, 9–60.
[https://doi.org/10.1016/0016-7037\(61\)90087-4](https://doi.org/10.1016/0016-7037(61)90087-4)
- Cash, A. 2014. Structural and hydrologic characterization of two historic waste rock piles. M.Sc. thesis. University of Alberta, Edmonton, Canada.
- Cathles, L.M., 1979. Predictive capabilities of a finite difference model of copper leaching in low grade industrial sulfide waste dumps. *Math. Geol.* 11, 175–191.
<https://doi.org/10.1007/bf01028964>.
- Chayes, F. 1971. *Ratio Correlation: A Manual for Students of Petrology and Geochemistry*. The University of Chicago Press, Chicago, USA.
- Collette, L. 2017. Cryohydrology of a covered waste rock pile in a permafrost environment. M.Sc. thesis. The University of British Columbia, Vancouver, Canada.
- Cook, N.J., Ciobanu, C.L., Pring, A., Skinner, W., Shimizu, M., Danyushevsky, L., Saini-Eidukat, B., Melcher, F. 2009. Trace and minor elements in sphalerite: A LA-ICPMS study. *Geochim. Cosmochim. Acta.* 73, 4761–4791. <https://doi.org/10.1016/j.gca.2009.05.045>.
- Cornell, R.M., 1991. Simultaneous incorporation of Mn, Ni and Co in the goethite structure. *Clay Miner.* 26, 427–430. <https://doi.org/10.1180/claymin.1991.026.3.11>.
- Cottrell, E., Kelley, K.A., Lanzirotti, A., Fischer, R.A. 2009. High-precision determination of iron oxidation state in silicate glasses using XANES. *Chem. Geol.* 268, 167–179.
<https://doi.org/10.1016/j.chemgeo.2009.08.008>.
- Cowden, A., Archibald, N.J. 1987. Massive-sulfide fabrics at Kambalda and their relevance to the inferred stability of monosulfide solid-solution. *Can. Mineral.* 25, 34–50.

- Davis, G.B., Doherty, G., Ritchie, A.I.M., 1986. A model of oxidation in pyritic mine wastes: Part 2: Comparison of numerical and approximate solutions. *Appl. Math. Model.* 10, 323–329.
[https://doi.org/10.1016/0307-904X\(86\)90091-0](https://doi.org/10.1016/0307-904X(86)90091-0).
- Davis, K.J., Dove, P.M., Wasylenki, L.W., De Yoreo, J.J. 2004. Morphological consequences of differential Mg^{2+} incorporation at structurally distinct steps on calcite. *Am. Mineral.* 89, 714–720.
<https://doi.org/10.2138/am-2004-5-605>.
- De Choudens-Sánchez, V., González, L.A. 2009. Calcite and aragonite precipitation under controlled instantaneous supersaturation: Elucidating the role of CaCO_3 saturation state and Mg/Ca ratio on calcium carbonate polymorphism. *J. Sediment. Res.* 79, 363–376.
<https://doi.org/10.2110/jsr.2009.043>
- DePaolo, D.J. 2004. Calcium isotopic variations produced by biological, kinetic, radiogenic and nucleosynthetic processes. *Rev. Mineral. Geochem.* 55, 255–288.
<https://doi.org/10.2138/gsrmg.55.1.255>.
- Desborough, G.A., Smith, K.S., Lowers, H.A., Swayze, G.A., Hammarstrom, .M., Diehl, S.F., Driscoll, R.L., Leinz, R.W. 2006. The use of synthetic jarosite as an analog for natural jarosite. In: *Proceedings of the Seventh International Conference on Acid Rock Drainage*. St. Louis, Missouri, pp 458–465. <https://doi.org/10.21000/JASMR06020458>.
- Desborough, G.A., Smith, K.S., Lowers, H.A., Swayze, G.A., Hammarstrom, J.M., Diehl, S.F., Leinz, R.W., Driscoll, R.L. 2010. Mineralogical and chemical characteristics of some natural jarosites. *Geochim. Cosmochim. Acta.* 74, 1041–1056. <https://doi.org/10.1016/j.gca.2009.11.006>.
- DeSisto, S.L., Jamieson, H.E., Parsons, M.B. 2011. Influence of hardpan layers on arsenic mobility in historical gold mine tailings. *Appl. Geochem.* 26, 2004–2018.
<https://doi.org/10.1016/j.apgeochem.2011.06.030>.
- Dinel, E., Fowler, A.D., Ayer, J., Still, A., Tylee, K., Barr, E. 2008. Lithogeochemical and stratigraphic controls on gold mineralization within the metavolcanic rocks of the Hoyle Pond Mine, Timmins, Ontario. *Econ. Geol.* 103, 1341–1363.
<https://doi.org/10.2113/gsecongeo.103.6.1341>.
- Dockrey, J.W., Lindsay, M.B.J., Mayer, K.U., Beckie, R.D., Norlund, K.L., Warren, L.A., Southam, G. 2014. Acidic microenvironments in waste rock characterized by neutral drainage: Bacteria-

- mineral interactions at sulfide surfaces. *Minerals*, 4, 170–190.
<https://doi.org/10.3390/min4010170>.
- Dold, B., Fontboté, L. 2011. Element cycling and secondary mineralogy in porphyry copper tailings as a function of climate, primary mineralogy, and mineral processing. *J. Geochem. Expl.* 74, 3–55.
[https://doi.org/10.1016/S0375-6742\(01\)00174-1](https://doi.org/10.1016/S0375-6742(01)00174-1).
- Donskoi, E., Manuel, J.R., Austin, P.I., Poliakov, A., Peterson, M.J., Hapugoda, S. 2013. Comparative study of iron ore characterisation using a scanning electron microscope and optical image analysis. *Trans. Inst. Min. Metall. B: Appl. Earth Sci.* 122, 217–229.
<https://doi.org/10.1179/1743275814Y.0000000042>.
- Dorozhkin, S.V., 2012. Dissolution mechanism of calcium apatites in acids: a review of literature. *World J. Methodol.* 2, 1–17. <https://doi.org/10.5662/wjm.v2.i1.1>.
- Dräger, G., Frahm, R., Materlik, G., Brümmer, O. 1988. On the multipole character of the X-ray transitions in the pre-edge structure of Fe K absorption spectra. *Phys. Stat. Sol.*, 146, 287–294.
<https://doi.org/10.1002/pssb.2221460130>.
- Drits, V.A., Sakharov, B.A., Salyn, A.L., Manceau, A. 1993. Structural model for ferrihydrite. 1993. *Clay Min.* 28, 185–207. <https://doi.org/10.1180/claymin.1993.028.2.02>.
- Du Laing, G., Rinklebe, J., Vandecasteele, B., Meers, E., Tack, F.M.G., 2009. Trace metal behavior in estuarine and riverine floodplain soils and sediments: a review. *Sci. Total Environ.* 407, 3972–3985. <https://doi.org/10.1016/j.scitotenv.2008.07.025>.
- Dubé, B., Gosselin, P. 2007. Greenstone-hosted quartz-carbonate vein deposits. In: Goodfellow, W.E, (Ed.), *Mineral Deposits of Canada: A Synthesis of Major Deposit-Types, District Metallogeny, the Evolution of geological Provinces, and Exploration Methods: Geological Association of Canada, Mineral Deposits Division, Special Publication No. 5*, p 49–73.
- Dubosq, R., Lawley, C.J.M., Rogowitz, A., Schneider, D.A., Jackson, S. 2018. Pyrite deformation and connections to gold mobility: Insight from micro-structural analysis and trace element mapping. *Lithos.* 310–311, <https://doi.org/10.1016/j.lithos.2018.03.024>.
- Dubrovsky, N.M., Cherry, J.A., Reardon, E.J., Vivyurka, A.J. 1985. Geochemical evolution of inactive pyritic tailings in the Elliot Lake uranium district. *Can Geotech J.* 22, 110–128.
<https://doi.org/10.1139/t85-011>.

- Dutrizac, J.E., Jambor, J.L. 2000. Jarosites and their application in hydrometallurgy. In: Alpers, C.N., Jambor, J.L., Nordstrom, D.K. Sulfate Minerals: Crystallography, Geochemistry, and Environmental Significance. Reviews in Mineralogy and Geochemistry, Vol. 40. Mineralogical Society of America, USA, 405–452. <https://doi.org/10.2138/rmg.2000.40.7>.
- Dzombak, D.A., Morel, F.M.M., 1990. Surface Complexation Modeling: Hydrous Ferric Oxide. John Wiley & Sons, New York.
- Elghali, A., Benzaazoua, M., Bouzahzah, H., Bussière, B., Villarraga-Gómez, H. 2018. Determination of the available acid-generating potential of waste rock, part I : Mineralogical approach. Appl. Geochem. 99, 31–41. <https://doi.org/10.1016/j.apgeochem.2018.10.021>.
- Ewing, S.A., Yang, W., DePaolo, D.J., Michalski, G., Kendall, C., Stewart, B.W., Thiemens, M., Amundson, R. 2008. Non-biological fractionation of the stable Ca isotopes in soils of the Atacama Desert, Chile. Geochim. Cosmochim. Acta. 72, 1096–1110. <https://doi.org/10.1016/j.gca.2007.10.029>.
- Farges, F., Lefrère, Y. Rossano, S., Berthereau, A., Calas, G., Brown Jr., G.E. 2004. The effect of redox state on the local structural environment of iron in silicate glasses: a combined XAFS spectroscopy, molecular dynamics, and bond valence study. J. Non-cryst. Solids. 344, 176–188. <https://doi.org/10.1016/j.jnoncrysol.2004.07.050>.
- Fernandez-Martinez, A., Timon, V., Roman-Ross, G., Cuello, G.J., Daniels, J.E., Ayora, C. 2010. The structure of schwertmannite, a nanocrystalline iron oxyhydroxysulfate. Am. Mineral. 95, 1312–1322. <https://doi.org/10.2138/am.2010.3446>.
- Fiege, A., Ruprecht, P., Simon, A.C., Bell, A.S., Göttlicher, J., Newville, M., Lanzirrotti, T., Moore, A. 2017. Calibration of Fe XANES for high-precision determination of Fe oxidation state in glasses: Comparison of new and existing results obtained at different synchrotron sources. Am. Mineral. 102, 369–380. <https://doi.org/10.2138/am-2017-5822>.
- Figueroa, G., Moeller, K., Buhot, M., Gloy, G., Haberlah, D. 2011. Proceedings, 10th International Congress for Applied Mineralogy (ICAM), Trondheim, Norway, August 2011.
- Finger, L.W., Hazen, R.M. 1980. Crystal structure and isothermal compression of Fe₂O₃, Cr₂O₃, and V₂O₃ to 50 kbars. J. Appl. Phys. 51, 5362. <https://doi.org/10.1063/1.327451>.

- Fleet, M.E. 1971. The crystal structure of a pyrrhotite (Fe_7S_8). *Acta Cryst.* B27, 1864–1867.
<https://doi.org/10.1107/S0567740871004990>.
- Forray, F.L., Drouet, C., Navrotsky, A. 2005. Thermochemistry of yavapiite $\text{KFe}(\text{SO}_4)_2$: formation and decomposition. *Geochim. Cosmochim. Acta.*, 69, 2133–2140.
<https://doi.org/10.1016/j.gca.2004.10.018>.
- Galay, A., France-Lanord, C. 1999. Weathering processes in the Ganges-Brahmaputra basin and the riverine alkalinity budget. *Chem. Geol.* 159, 3–30. [https://doi.org/10.1016/S0009-2541\(99\)00033-9](https://doi.org/10.1016/S0009-2541(99)00033-9).
- Gunsinger, M.R., Ptacek, C.J., Blowes, D.W., Jambor, J.L., Moncur, M.C. 2006. Mechanisms controlling acid neutralization and metal mobility within a Ni-rich tailings impoundment. *Appl. Geochem.* 1301–1321. <https://doi.org/10.1016/j.apgeochem.2006.06.006>.
- Hammarstrom, J.M.; Seal, R.R. II; Meier, A.L.; and Kornfeld, J.M. 2005. Secondary sulfate minerals associated with acid drainage in the eastern US: recycling of metals and acidity in surficial environments. *Geochemistry of Sulfate Minerals: A Tribute to Robert O. Rye*. Paper 2.
<http://digitalcommons.unl.edu/usgsrye/2>.
- Hannam, S.E.S. 2012. Diavik Waste Rock Project: Geochemical and mineralogical investigations of waste-rock weathering. M.Sc. thesis. University of Waterloo. Waterloo, Canada.
- Harouaka, K., Eisenhauer, A., Fantle, M.S. 2014. Experimental investigation of Ca isotopic fractionation during abiotic gypsum precipitation. *Geochim. Cosmochim. Acta.* 129, 157–176.
<https://doi.org/10.1016/j.gca.2013.12.004>.
- Harries, D., Pollock, K., Lagenhorst, F. 2013. Oxidative dissolution of 4C- and NC-pyrrhotite: Intrinsic reactivity differences, pH dependence, and the effect of anisotropy. *Geochim. Cosmochim. Acta.* 102, 23–44. <http://dx.doi.org/10.1016/j.gca.2012.10.021>.
- Harouaka, K., Eisenhauer, A., Fantle, M.S. 2014. Experimental investigation of Ca isotopic fractionation during abiotic gypsum precipitation. *Geochim. Cosmochim. Acta.* 129, 157–176.
<https://doi.org/10.1016/j.gca.2013.12.004>.
- Heikkinen, P.M., Räisänen, M.L., Johnson, R.H. 2009. Geochemical characterisation of seepage and drainage water from two sulfide mine tailings impoundments: Acid mine drainage versus neutral mine drainage. *Mine Water Environ.* 28, 30–49. , <http://dx.doi.org/10.1007/s10230-008-0056-2>.

- Hiemstra, T. 2013 Surface and mineral structure of ferrihydrite. *Geochim. Cosmochim. Acta*. 105 316–325. <http://dx.doi.org/10.1016/j.gca.2012.12.002>.
- Hindshaw, R.S., Bourdon, B., Pogge von Strandmann, P.A.E., Vigier, N., Burton, K.W. The stable calcium isotopic composition of rivers draining basaltic catchments in Iceland. *Earth. Plant. Sci. Lett.* 374, 173–184. <http://dx.doi.org/10.1016/j.epsl.2013.05.038>.
- Hong, D., Fan, M., Yu, L., Cao, J. 2018. An experimental study simulating the dissolution of gypsum rock. *Energy Explor. Exploit.* 36, 942–954. DOI:10.1177/0144598717751927.
- Jacobson, A.D., Holmden, C. 2008. $\delta^{44}\text{Ca}$ evolution in a carbonate aquifer and its bearing on the equilibrium isotope fractionation factor for calcite. *Earth. Planet. Sci. Lett.* 270, 349–353. <https://doi.org/10.1016/j.epsl.2008.03.039>.
- Jacobson, A.D., Andrews, M.G., Lehn, G.O., Holmden, C. 2015. Silicate versus carbonate weathering in Iceland: New insights from Ca isotopes. *Earth. Planet. Sci. Lett.* 416, 132–142. <https://doi.org/10.1016/j.epsl.2015.01.030>.
- Jambor, J.L. 1994. Mineralogy of sulfide-rich tailings and their oxidation products. In: Jambor, J.L., Blowes, D.W. (Eds.), *Environmental Geochemistry of Sulfide Mine-Waste*. Mineralogical Association of Canada Short Course, Vol. 22. Mineral. Assoc. Canada, Canada, 59–102.
- Jambor, J.L. 1997. Mineralogy of the Diavik Lac de Gras kimberlites and host rocks. Report to Diavik Diamond Mines Ltd. Yellowknife, Northwest Territories.
- Jambor, J.L. 2000. The relationship of mineralogy to acid- and neutralization-potential values in ARD. In: Cotter-Howells, J.D., Campbell, L.S., Valsami-Jones, E., Batchelder, M. (Eds.). *Environmental Mineralogy: Microbial Interactions, Anthropogenic Influences, Contaminated Land and Waste Management*. Mineral Society Series, 9, Mineralogical Society, London, England.
- Jambor, J.L., Nordstrom, D.K., Alpers, C.N. 2000. Metal-sulfate salts from sulfide mineral oxidation. In: Alpers, C.N., Jambor, J.L., Nordstrom, D.K. (Eds.). *Sulfate Minerals: Crystallography, Geochemistry, and Environmental Significance*. Reviews in Mineralogy and Geochemistry, vol. 40. Mineralogical Society of America, USA, 303–350. <https://doi.org/10.2138/rmg.2000.40.6>.

- Jambor, J.L. 2003. Mine-waste mineralogy and mineralogical perspectives of acid-base accounting
In: Jambor, J.L., Blowes, D.W., Ritchie, A.I.M. (Eds.). *Environmental Aspects of Mine Wastes*.
Mineral. Assoc. Canada, Short Course Series 31, Ottawa, Canada, 117–142.
- Jambor, J.L., Blowes, D.W., 1998. Theory and applications of mineralogy in environmental studies of
sulfide-bearing mine wastes, in: Cabri, L.J., Vaughn, D.J., (Eds.), *Modern approaches to ore and
environmental mineralogy*, Mineralogical Association of Canada short course, Mineralogical
Association of Canada: Canada, Vol 27, pp 367–401.
- Jambor, J.L., Dutrizac, J.E. 1998. Occurrence and constitution of natural and synthetic ferrihydrite, a
widespread iron oxyhydroxide. *Chem. Rev.* 98, 2549–2586. <https://doi.org/10.1021/cr970105t>.
- Jamieson, H.E., Robinson, C., Alpers, C.N., McCleskey, R.B., Nordstrom, D.K., Peterson, R. 2005.
Major and trace element composition of copiapite-group minerals and coexisting water from the
Richmond mine, Iron Mountain, California. *Chem. Geol.*, 215, 387–405.
<https://doi.org/10.1016/j.chemgeo.2004.10.001>.
- Janzen, M.P., Nicholson, R.V., Scharer, J.M. 2000. Pyrrhotite reaction kinetics: Reaction rates for
oxidation by oxygen, ferric iron, and for nonoxidative dissolution. *Geochim. Cosmochim. Acta*.
64, 1511–1522. [https://doi.org/10.1016/S0016-7037\(99\)00421-4](https://doi.org/10.1016/S0016-7037(99)00421-4).
- Jin, L., Koulialias, D., Schnedler, M., Gehring, A.U., Pósfai, M., Ebert, P., Charilaou, M., Schäublin,
R.E., Jia, C-L., Löffler, J.F., Dunn-Borkowski, R.E. 2021. Atomic-scale characterization of
commensurate and incommensurate vacancy superstructures in natural pyrrhotites. *Am. Mineral.*
106, 82–96. <https://doi.org/10.2138/am-2020-7479CCBY>.
- Johnson, C.A. 1986. The regulation of trace element concentrations in river and estuarine waters
contaminated with acid mine drainage: The adsorption of Cu and Zn on amorphous Fe
oxyhydroxides. *Geochim. Cosmochim. Acta*, 50, 2433–2438. [https://doi.org/10.1016/0016-7037\(86\)90026-8](https://doi.org/10.1016/0016-7037(86)90026-8).
- Johnson, R.H., Blowes, D.W., Robertson, W.D., Jambor, J.L. 2000. The hydrogeochemistry of the
Nickel Rim mine tailings impoundment, Sudbury, Ontario. *Contam. Hydrol.* 41, 49–81.
[https://doi.org/10.1016/S0169-7722\(99\)00068-6](https://doi.org/10.1016/S0169-7722(99)00068-6).
- Kato T., Miura, Y. 1977. The crystal structures of jarosite and svanbergite. *Mineralogical Journal.* 8,
419–430. <https://doi.org/10.2465/minerj.8.419>.

- Kirby, C.S., Cravotta III, C.A. 2005a. Net alkalinity and net acidity 1: Theoretical considerations. *Appl. Geochem.* 20, 1920–1940. <https://doi.org/10.1016/j.apgeochem.2005.07.002>.
- Kirby, C.S., Cravotta III, C.A. 2005b. Net alkalinity and net acidity 2: Practical considerations. *Appl. Geochem.* 20, 1941–1964. <https://doi.org/10.1016/j.apgeochem.2005.07.003>.
- Langman, J.B., Blowes, D.W., Veeramani, H., Wilson, D., Smith, L., Sego, D.C., Paktunc, D. 2015. The mineral and aqueous phase evolution of sulfur and nickel with weathering of pyrrhotite in a low sulfide, granitic waste rock. *Chem. Geol.* 401, 169–179. <https://doi.org/10.1016/j.chemgeo.2015.02.024>.
- Langman, J.B., Veeramani, H., Blowes, D.W., Bailey, B., Wilson, D., Smith, L., Sego, D.C., Amos, R.T., Holland, S.P. 2017. Waste rock biogeochemistry in a permafrost environment; Examination of a cover design for a low-sulfide, granitic waste rock. *Geomicrobiol. J.* 34, 656–669. <https://doi.org/10.1080/01490451.2016.1238978>.
- Langman, J.B., Sinclair, S., Amos, R.T., Wilson, D., Ptacek, C.J., Sego, D.C., Smith, L., Blowes, D.W. 2019. Alkalinity generated from weathering of accessory calcite and apatite and acid drainage neutralization in an Archean granitoid waste rock. *J. Geochem. Explor.* 205, 106341. <https://doi.org/10.1016/j.gexplo.2019.106341>.
- Lee, G., Bingham, J.M., Faure, G., 2002. Removal of trace metals by coprecipitation with Fe, Al and Mn from natural waters contaminated with acid mine drainage in the Ducktown mining district, Tennessee. *Appl. Geochem.* 17, 569–581. [https://doi.org/10.1016/S0883-2927\(01\)00125-1](https://doi.org/10.1016/S0883-2927(01)00125-1).
- Lefebvre, R., Hockley, D., Smolensky, J., Lamontagne, A., 2001. Multiphase transfer processes in waste rock piles producing acid mine drainage 2: Applications of numerical simulation. *J. Contam. Hydrol.* 52, 165–186. [https://doi.org/10.1016/S0169-7722\(01\)00157-7](https://doi.org/10.1016/S0169-7722(01)00157-7).
- Lehn, G.O., Jacobson, A.D., Douglas, T.A., McClelland, J.W., Barker, A.J., Khosh, M.S. 2017. Constraining seasonal active layer dynamics and chemical weathering reactions occurring in North Slope Alaskan watersheds with major ion and isotope ($\delta^{34}\text{S}_{\text{SO}_4}$, $\delta^{13}\text{C}_{\text{DIC}}$, $\delta^{44/40}\text{Ca}$, $\delta^{44/42}\text{Ca}$) measurements. *Geochim. Cosmochim. Acta.* 217, 399–420. <https://doi.org/10.1016/j.gca.2017.07.042>.

- Lemarchand, D., Wasserburg, G.J., Papanastassiou, D.A. 2004. Rate-controlled isotope fractionation in synthetic calcite. *Geochim. Cosmochim. Acta.* 68, 4665–4678.
<https://doi.org/10.1016/j.gca.2004.05.029>.
- Levinson, L.M., and Treves, D. 1968. Mössbauer study of the magnetic structure of Fe₇S₈. *J. Phys. Solids.* 29, 2227–2231. [https://doi.org/10.1016/0022-3697\(68\)90019-X](https://doi.org/10.1016/0022-3697(68)90019-X).
- Levenspiel, O., 1972. *Chemical Reaction Engineering*. J. Wiley, New York.
<https://doi.org/10.1002/aic.690190143>.
- Light, T.S. 1972. Standard solution for redox potential measurements. *Anal. Chem.* 44, 1038–1039.
<https://doi.org/10.1021/ac60314a021>.
- Lindsay, M.B.J., Condon, P.D., Jambor, J.L., Lear, K.G., Blowes, D.W., Ptacek, C.J., 2009. Mineralogical, geochemical, and microbial investigation of a sulfide-rich tailings deposit characterized by neutral drainage. *Appl. Geochem.* 24, 2212–2221.
<https://doi.org/10.1016/j.apgeochem.2009.09.012>.
- Lindsay, M.B.J., Moncur, M.C., Bain, J.G., Jambor, J.L., Ptacek, C.J., Blowes, D.W. 2015. Geochemical and mineralogical aspects of sulfide mine tailings. *Appl. Geochem.* 57, 157–177.
<https://doi.org/10.1016/j.apgeochem.2015.01.009>.
- Ljungberg, J., Öhlander, B. 2001. The geochemical dynamics of oxidizing mine tailings at Laver, northern Sweden. *J. Geochem. Explor.* 75, 57–72. [https://doi.org/10.1016/S0375-6742\(01\)00175-3](https://doi.org/10.1016/S0375-6742(01)00175-3).
- Lotter, N.O., Baum, W., Reeves, S., Arrué, C., Bradshaw, D.J. 2017. The business value of best practice process mineralogy. *Miner. Eng.* 116, 226–238.
<http://dx.doi.org/10.1016/j.mineng.2017.05.008>.
- Luís, A.T., Alexander, A.C., Almeida, S.F.P., da Silva, E.F., Culp, J. 2013. Benthic diatom communities in streams from zinc mining areas in continental (Canada) and Mediterranean climates (Portugal). *Water Pollut. Res. J. Can.* 48.2, 180–191.
<https://doi.org/10.2166/wqrjc.2013.043>.
- Lund, C., Lamerg, P., Lindberg, T. 2015. Development of a geometallurgical framework to quantify mineral textures for process prediction. *Miner. Eng.* 82, 61–77,
<https://doi.org/10.1016/j.mineng.2015.04.004>.

- Malmström, M., Banwart, S., Lewenhagen, J., Duro, L., Bruno, J. 1996. The dissolution of biotite and chlorite at 25°C in near-neutral pH region. *J. Contam. Hydrol.* 21, 201–213.
[https://doi.org/10.1016/0169-7722\(95\)00047-X](https://doi.org/10.1016/0169-7722(95)00047-X).
- Manceau, A., Lanson, M., Geoffroy, N., 2007. Natural speciation of Ni, Zn, Ba, and as in ferromanganese coatings on quartz using X-ray fluorescence, absorption, and diffraction. *Geochem. Cosmochim. Acta.* 71, 95–128. <https://doi.org/10.1016/j.gca.2006.08.036>.
- Manceau, A. 2011. Critical evaluation of the revised akdalaite model for ferrihydrite. *Amer. Mineral.* 96, 521–533. <https://doi.org/10.2138/am.2011.3583>.
- Mayer, K.U., Frind, E.O., Blowes, D.W., 2002. Multicomponent reactive transport modelling in variably saturated porous media using a generalized formulation for kinetically controlled reactions. *Water Resour. Res.* 38, 1174–1195. <https://doi.org/10.1029/2001WR000862>.
- Mayer, K.U., Frind, E.O., Blowes, D.W., 2003. Advances in reactive-transport modelling. In: Jambor, J.L., Blowes, D.W., Ritchie, A.I.M. (Eds.), *Environmental Aspects of Mine Wastes*, Mineralogical Association of Canada Short Course, Vol. 31. Mineralogical Association of Canada, Canada, 383–302.
- McGregor, R.G., Blowes, D.W., Jambor, J.L., Robertson, W.D. 1998. The solid-phase controls on the mobility of heavy metals at the Copper Cliff tailings area, Sudbury, Ontario, Canada. *J. Contam. Hydrol.* 33, 247–271. [https://doi.org/10.1016/S0169-7722\(98\)00060-6](https://doi.org/10.1016/S0169-7722(98)00060-6).
- McKenzie, R.M., 1980. The adsorption of lead and other heavy metals on oxides of manganese and iron. *Aust. J. Soil Res.* 18, 61–73. <https://doi.org/10.1071/SR9800061>.
- McNeill, B. 2016. Geochemical and microbiological characterization of the historic waste rock piles at the Detour Lake gold mine. M.Sc. thesis. University of Waterloo. Waterloo, Canada.
- McNeill, B., Pakostova, E., Bain, J.G., Gould, W.D., Amos, R.T., Wilson, G.W., Ptacek, C.J., Blowes, D.W. 2020. Microbial community structure within a weathered waste-rock pile overlain by a monolayer soil cover. *Appl. Geochem.* 114, 104531.
<https://doi.org/10.1016/j.apgeochem.2020.104531>.
- Melliti, E., Touati, K., Van der Bruggen, B., Elfil, H. 2021. Effect of Fe²⁺ ions on gypsum precipitation during bulk crystallization of reverse osmosis concentrates. *Chemosphere.* 263, 127866. <https://doi.org/10.1016/j.chemosphere.2020.127866>.

- Michel, F.M., Ehm, L., Antao, S.M., Lee, P.L., Chupas, P.J., Liu, G., Strongin, D.R., Schoonen, M.A.A., Phillips, B.L., and Parise, J.B. 2007. The structure of ferrihydrite, a nanocrystalline material. *Science*. 316, 1726–1729. <https://doi.org/10.1126/science.1142525>.
- Michel, F.M., Barrón, V., Torrent, J., Morales, M.P., Serna, C.J., Boily, J.F., Liu, Q., Ambrosini, A., Cismasu, A.C., and Brown, G.E. Jr. 2010. Ordered ferromagnetic form of ferrihydrite reveals links among structure, composition, and magnetism. *Proc. Natl. Acad. Sci.* 107, 2787–2792. <https://doi.org/10.1073/pnas.0910170107>
- Mielke, J.E. 1979. Composition of the Earth's crust and distribution of the elements. In: Siegel, F.R. (Ed.). *Review of research on modern problems in geochemistry*. International Association for Geochemistry and Cosmochemistry. Earth Science Series No. 16. UNESCO Report SC/GEO/544/3, Paris, 13–77.
- Mihaljev, and Farges, F. 1999. Zinc. In: Fairbridge R.W., Marshall CP (Eds.). *Encyclopedia of Geochemistry*. 1st ed. 1999. Kluwer Academic; 1999. <https://doi.org/10.1007/1-4020-4496-8>.
- Moncur, M.C., Ptacek, C.J., Blowes, D.W., Jambor, J.L. 2005. Release, transport and attenuation of metals from an old tailings impoundment. *Appl. Geochem.* 20, 639–659. <https://doi.org/10.1016/j.apgeochem.2004.09.019>.
- Moncur, M.C., Jambor, J.L., Ptacek, C.J., Blowes, D.W. 2009. Mine drainage from the weathering of sulfide minerals and magnetite. *Appl. Geochem.* 24, 2362–2373. <https://doi.org/10.1016/j.apgeochem.2009.09.013>.
- Moncur, M.C., Ptacek, C.J., Blowes, D.W., Peterson, R.C. 2015a. The occurrence and implications of efflorescent sulfate minerals at the former Sherritt-Gordon Zn-Cu mine, Sherridon, Manitoba, Canada. *Can. Mineral.* 53, 961–977. <https://doi.org/10.3749/canmin.1500092>.
- Moncur, M.C. Ptacek, C.J., Lindsay, M.B.J., Blowes, D.W., Jambor, J.L. 2015b. Long-term mineralogical and geochemical evolution of sulfide mine tailings under a shallow water cover. *Appl. Geochem.* 57, 178 – 193. <http://dx.doi.org/10.1016/j.apgeochem.2015.01.012>.
- Moore, J., Jacobson, A.D., Holmden, C., Craw, D. 2013. Tracking the relationship between mountain uplift, silicate weathering, and long-term CO₂ consumption with Ca isotopes: Southern Alps, New Zealand. *Chem. Geol.* 341, 110–127. <http://dx.doi.org/10.1016/j.chemgeo.2013.01.005>.

- Morimoto, N., Nakazawa, H., Nishiguchi, K., Tokonami, M. 1970. Pyrrhotites: Stoichiometric compounds with composition $\text{Fe}_{n-1}\text{S}_n$ ($n \geq 8$). *Science*. 168, 964–966.
<https://doi.org/10.1126/science.168.3934.964>.
- Moreno-González, R., Macías, F., Olías, M., Cánovas, C.R. 2022. Temporal evolution of acid mine drainage (AMD) leachates from the abandoned tharsis mine (Iberian Pyrite Belt, Spain). *Environ. Pollut.* 295, 118697. <https://doi.org/10.1016/j.envpol.2021.118697>.
- Murray, J., Kirschbaum, A., Bold, B., Guimaraes, E.M. Miner, E.P. 2014. Jarosite versus Soluble Iron-Sulfate Formation and Their Role in Acid Mine Drainage Formation at the Pan de Azúcar Mine Tailings (Zn-Pb-Ag), NW Argentina. *Minerals*. 4, 477–502.
<https://doi.org/10.3390/min4020477>.
- Mycroft, J.R., Nesbitt, H.W., Pratt, A.R. 1995. X-ray photoelectron and Auger electron spectroscopy of air-oxidized pyrrhotite: Distribution of oxidized species with depth. *Geochim. Cosmochim. Acta*. 59, 721–733. [https://doi.org/10.1016/0016-7037\(94\)00352-M](https://doi.org/10.1016/0016-7037(94)00352-M).
- Naldrett, A.J., Craig, J.R., Kullerud, G. 1967. The central portion of the Fe-Ni-S system and its bearing on pentlandite exsolution in iron-nickel sulfide ores. *Econ. Geol.* 62, 826–847.
<https://doi.org/10.2113/gsecongeo.62.6.826>.
- Neilsen, L.C., DePaolo, D.J. 2013. Ca isotope fractionation in a high-alkalinity lake system: Mono Lake, California. *Geochim. Cosmochim. Acta*. 118, 276–294.
<https://doi.org/10.1016/j.gca.2013.05.007>.
- Neuner, M., Smith, L., Blowes, D.W., Sego, D.C., Smith, L.J.D., Fretz, N., Gupton, M. 2013. The Diavik waste rock project: Water flow through mine waste rock in a permafrost terrain. *Appl. Geochem.* 36, 222–233. <http://dx.doi.org/10.1016/j.apgeochem.2012.03.011>.
- Newville, M. 2013. Larch: An analysis package for XAFS and related spectroscopies. *J. Phys.: Conf. Ser.* 430 012007. <https://doi.org/10.1088/1742-6596/430/1/012007>.
- Nordstrom, D.K., 1977. Thermochemical redox equilibria of Zobell's solution. *Geochim. Cosmochim. Acta*. 41, 1835–1841. [https://doi.org/10.1016/0016-7037\(77\)90215-0](https://doi.org/10.1016/0016-7037(77)90215-0).
- Nordstrom, D.K. 1982. Aqueous pyrite oxidation and the consequent formation of secondary minerals. In: Kittrick, A., Fanning, D.S., Hossner, L.R. (Eds.), *Acid Sulphate Weathering*. Soil Sci. Soc. Am. Special Pub. 10, 37–56. <https://doi.org/10.2136/sssaspecpub10.c3>.

- Nordstrom, D.K. 2011a. Hydrogeochemical processes governing the origin, transport and fate of major and trace elements from mine wastes and mineralized rock to surface waters. *Appl. Geochem.* 26, 1777–1791. <https://doi.org/10.1016/j.apgeochem.2011.06.002>.
- Nordstrom, D.K., 2011b. Mine waters: acidic to circumneutral. *Elements* 7, 393–398. <https://doi.org/10.2113/gselements.7.6.393>.
- Nordstrom, D.K., Southam, G. 1997. Geomicrobiology of sulfide mineral oxidation. In: Banfield, J.F., Nealson, K.H. (Eds.), *Geomicrobiology: Interactions between Microbes and Minerals*, Vol. 35, *Reviews in Mineralogy*, Min. Soc. Am. Washington, DC, 361–390. <https://doi.org/10.1021/es990646v>.
- Nordstrom, D.K., Blowes, D.W., Ptacek, C.J. 2015. Hydrogeochemistry and microbiology of mine drainage: An update. *Appl. Geochem.* 57, 3–16. <http://dx.doi.org/10.1016/j.apgeochem.2015.02.008>.
- Nordstrom, D.K., Alpers, C.N., Ptacek, C.J., Blowes, D.W. 2000. Negative pH and Extremely Acidic Mine Waters from Iron Mountain, California. *Environ. Sci. Technol.* 34, 254–258. <https://doi.org/10.1021/es990646v>.
- Offeddu, F.G., Cama, J., Soler, J.M., Dávila, G., McDowell, A., Craciunescu, T., Tiseanu, I. 2015. Processes affecting the efficiency of limestone in passive treatments for AMD: Column experiments. *J. Environ. Chem. Eng.* 3, 304–316. <https://doi.org/10.1016/j.jece.2014.10.013>.
- Oliva, P., Dupré, B., Martin, F., Viers, J. 2004. The role of trace minerals in chemical weathering in a high-elevation granitic watershed (Esibère, France : Chemical and mineralogical evidence. *Geochim. Cosmochim. Acta.* 68, 2223–2244. <https://doi.org/10.1016/j.gca.2003.10.043>.
- Oliver, J., Ayer, J., Dubé, Aubertin, R., Burson, M., Panneton, G., Friedman, R., Hamilton, M. 2012. Structure, stratigraphy, U-Pb geochronology and alteration characteristics of gold mineralization at the Detour Lake Gold Deposit, Ontario, Canada. *Explor. Min. Geol.*, 20, 1–30.
- Paktunc, A.D., Hulbert, L.J., Harris, D.C. 1990. Partitioning of the platinum-group and other trace elements in sulfides from the Bushveld Complex and Canadian occurrences of nickel-copper sulfides. *Can. Mineral.* 28, 475–488.

- Paktunc, A.D. 1999. Mineralogical constraints on the determination of neutralization potential and prediction of acid mine drainage. *Environ. Geol.* 39, 103–112.
<https://doi.org/10.1007/s002540050440>.
- Paktunc, D., Manceau, A., Dutrizac, J. 2013. Incorporation of Ge in ferrihydrite: Implications for the structure of ferrihydrite. *Am. Mineral.* 98, 848–858. <https://doi.org/.2138/am.2013.4312>.
- Parbhakar-Fox A., Lottermoser B., Hartner R., Berry R.F., Noble T.L. 2017. Prediction of Acid Rock Drainage from Automated Mineralogy. In: Lottermoser B. (Eds.) *Environmental Indicators in Metal Mining*. Springer, Cham. https://doi.org/10.1007/978-3-319-42731-7_8
- Parigi, R., Chen, N., Reid, J.W., Ptacek, C.J., Blowes, D.W. 2022. Nickel isotope fractionation during precipitation of Ni secondary minerals and synchrotron-based analysis of the precipitates. *Geochim. Cosmochim. Acta.* 317, 91–105. <https://doi.org/10.1016/j.gca.2021.10.027>.
- Parkhurst, D.L., Appelo, C.A.J. 2013. Description of input and examples for PHREEQC version 3 — a computer program for speciation, batch-reaction, one-dimensional transport, and inverse geochemical calculations: U.S. Geological Survey Techniques and Methods. Book 6, Ch. A43, 497 pp., available only at <https://pubs.usgs.gov/tm/06/a43>.
- Pedretti, D., Lassin, A., Beckie, R.D. 2015. Analysis of the potential impact of capillarity on long-term geochemical processes in sulphidic waste-rock dumps. *Appl. Geochem.* 62, 75–83.
<http://dx.doi.org/10.1016/j.apgeochem.2015.03.017>.
- Peterson, R.C. 2003. The relationship between Cu content and distortion in the atomic structure of melanterite from the Richmond mine, Iron Mountain, California. *Can. Mineral.* 41, 937–949.
<https://doi.org/10.2113/gscanmin.41.4.937>.
- Petruk, W. 1987. The MP-SEM-IPS image analysis system. Ottawa, Canada. CANMET report 87-1E.
<https://doi.org/10.4095/307078>.
- Petruk, W. 1989. The MP-SEM-IPS image analysis system: short course handbook. In: *Image Analysis to Mineral and Earth Sciences*. W. Petruk (Ed.). Mineralogical Association of Canada Short Course, vol. 16. Mineralogical Association of Canada, Canada, 37–42.
- Phillips, G.N., Powell, R. 2010 Formation of gold deposits: a metamorphic devolatilization model. *J. Metamorphic. Geol.*, 28, 689–718. <https://doi.org/10.1111/j.1525-1314.2010.00887.x>.

- Pierce, L., Buseck, P.R. 1974. Electron imaging of pyrrhotite superstructures. *Science*. 186, 1209–1212. <https://doi.org/10.1126/science.186.4170.1209>.
- Plante, B., Benzaazoua, M., Bussière, B., Biesinger, M.C., Pratt, A.R. 2010. Study of Ni sorption onto Tio mine waste rock surfaces. *Appl. Geochem.* 25, 1830–1844. <https://doi.org/10.1016/j.apgeochem.2010.09.010>.
- Plummer, L.N., Busenberg, E. 1982. The solubilities of calcite, aragonite and vaterite in CO₂-H₂O solutions between 0 and 90°C, and an evaluation of the aqueous model for the system CaCO₃-CO₂-H₂O. *Geochim. Cosmochim. Acta*. 46, 1011–1040. [https://doi.org/10.1016/0016-7037\(82\)90056-4](https://doi.org/10.1016/0016-7037(82)90056-4).
- Plummer, L.N., Busenberg, E. 1999. Data on the crystal growth of calcite from calcium bicarbonate solutions at 34°C and CO₂ partial pressures of 0.101, 0.0156 and 0.00102 atmospheres. U.S. Geological Survey Open-File Report 99–247. Reston, Virginia, U.S.A.
- Plummer, L.N., Wigley, T.M.L., Parkhurst, D.L., 1978. The kinetics of calcite dissolution in CO₂-water systems at 5° to 60°C and 0.0 to 1.0 atm CO₂. *Am. J. Sci.* 278, 179–216. <https://doi.org/10.2475/ajs.278.2.179>.
- Plummer, L.N., Parkhurst, D.L., Wigley, T.M.L. 1979. Critical review of the kinetics of calcite dissolution and precipitation. In: Jenne, E.A. (Ed.). *Chemical Modeling in Aqueous Systems*. American Chemical Society Symposium Series, Vol. 93, 537–573. <https://doi.org/10.1021/bk-1979-0093>.
- Pratt, A.R., Nesbitt, H.W., 1997. Pyrrhotite leaching in acid mixtures of HCl and H₂SO₄. *Am. J. Sci.* 297, 807–828. <https://doi.org/10.2475/ajs.297.8.807>.
- Pratt, A.R., Muir, I.J., Nesbitt, H.W. 1994. X-ray photoelectron and Auger electron spectroscopic studies of pyrrhotite and mechanism of air oxidation. *Geochim. Cosmochim. Acta*. 58, 827–841, [https://doi.org/10.1016/0016-7037\(94\)90508-8](https://doi.org/10.1016/0016-7037(94)90508-8).
- Price, W.A. 2009. Prediction manual for drainage chemistry from sulphidic geologic materials. CANMET Mining and Mineral Sciences Laboratories. MEND Report 1.20.1. December 2009.
- Prietzl, J., Thieme, J., Eusterhues, K., Eichert, D., 2007. Iron speciation in soils and soil aggregates by synchrotron-based X-ray microspectroscopy (XANES, μ -XANES). *Eur. J. Soil Sci.* 58, 1027–1041. <https://doi.org/10.1111/j.1365-2389.2006.00882.x>.

- Quade, J., English, N., DeCelles, P.G. 2003. Silicate versus carbonate weathering in the Himalaya: a comparison of the Arun and Seti River watersheds. *Chem. Geol.* 202, 275–296.
<https://doi.org/10.1016/j.chemgeo.2002.05.002>.
- Ravel, B., Newville, M. 2005. ATHENA, ARTEMIS, HEPHAESTUS: Data analysis for X-ray absorption spectroscopy using IFEFFIT. *J. Synchrotron Radiat.* 12, 537–541.
<https://doi.org/10.1107/S0909049505012719>.
- Redwan, M., Rammlmair, D., Meima, J. 2012. Application of mineral liberation analysis in studying micro-sedimentological structures within sulfide mine tailings and their effect on hardpan formation. *Sci. Total. Environ.* 414, 480–493. <https://doi.org/10.1016/j.scitotenv.2011.10.038>.
- Rimstidt, J.D., Vaughan, D.J. 2003. Pyrite oxidation: A state-of-the-art assessment of the reaction mechanism. *Geochim. Cosmochim. Acta.*, 67, 873–880. [https://doi.org/10.1016/S0016-7037\(02\)01165-1](https://doi.org/10.1016/S0016-7037(02)01165-1).
- Rinker, M.J., Nesbitt, H.W., Pratt, A.R. 1997. Marcasite oxidation in low-temperature acidic (pH 3.0) solutions: Mechanism and rate laws. *Am. Mineral.* 82, 900–912. <https://doi.org/10.2138/am-1997-9-1007>.
- Ryu, J-S., Jacobson, A.D., Holmden, C., Lundstrom, C., Zhaofeng Zhang. 2011. The major ion, $\delta^{44}/^{40}\text{Ca}$, $\delta^{44}/^{42}\text{Ca}$, and $\delta^{26}/^{24}\text{Mg}$ geochemistry of granite weathering at pH=1 and T=25 °C: power-law processes and the relative reactivity of minerals. *Geochim. Cosmochim. Acta.* 75, 6004–6026. <https://doi.org/10.1016/j.gca.2011.07.025>.
- Sakkopoulos, S., Vitoratos, E., Argyreas, T. 1986. Impurity-band conduction in natural pyrrhotite. *J. Appl. Phys.* 55, 595–597. <https://doi.org/10.1063/1.333071>.
- Salminen, R.; Tarvainen, T.; Demetriades, A.; Duris, M.; Fordyce, F.M.; Gregorauskiene, V.; Kahelin, H.; Kivisilla, J.; Klaver, G.; Klein, H.; Larson, J.; Lis, J.; Locutura, J.; Marsina, K.; Mjartanova, H.; Mouvet, C.; O'Connor, P.; Odor, L.; Ottonello, G.; Paukola, T.; Plant, J.A.; Reimann, C.; Schermann, O.; Siewers, U.; Steenfelt, A.; Van der Sluys, J.; De Vivo, B.; Williams, L.. 1998 FOREGS Geochemical Mapping Field Manual. Espoo, Finland, Geological Survey of Finland, 38pp. Geological Survey of Finland Guide 47.
- Scheinost, A.C., Abend, S., Pandya, K.I., Sparks, D.L., 2001. Kinetic controls on Cu and Pb sorption by ferrihydrite. *Environ. Sci. Technol.* 35, 1090–1096. <https://doi.org/10.1021/es000107m>.

- Schippers, A., Sand, W., 1999. Bacterial leaching of metal sulfides proceeds by two indirect mechanisms via thiosulfate or via polysulfides and sulfur. *Appl. Environ. Microbiol.* 65(1), 319–321. <https://doi.org/10.1128/AEM.65.1.319-321.1999>.
- Schippers, A., 2004. Biogeochemistry of metal sulfide oxidation in mining environments, sediments and soils. In: Amend, J.P., Edwards, K.J., Lyons, T.W. (Eds.), *Sulfur Biogeochemistry — Past and Present*. Special Paper, 379. Geological Society of America, Boulder, Colorado, USA, pp. 49–62.
- Schmøkel, M.S., Berg, L., Cenedese, S., Jørgensen, M.R.V., Chen, Y-S., Overgaard, J., Iversen, B.B. 2014. Atomic properties and chemical bonding in the pyrite and marcasite polymorphs of FeS₂: a combined experimental and theoretical electron density study. *Chem. Sci.*, 5, 1408. <https://doi.org/10.1039/c3sc52977k/>.
- Schoepfer, V.A., Burton, E.D. 2021. Schwertmannite: A review of its occurrence, formation, structure, stability and interactions with oxyanions. *Earth-Sci. Rev.* 221, 103811. <https://doi.org/10.1016/j.earscirev.2021.103811>.
- Schwertmann, U., Cornell, R.M. 2000. *Iron oxides in the laboratory: Preparation and characterization*. Second. Ed. John Wiley & Sons. <https://doi.org/10.1002/9783527613229>.
- Schwertmann, U., Carlson, L. 2005. The pH-dependent transformation of schwertmannite to goethite at 25°C. *Clay Miner.* 40, 63–66. <https://doi.org/10.1180/0009855054010155>.
- Schwertmann, U., Murad, E. 1983. Effect of pH on the formation of goethite and hematite from ferrihydrite. *Clays Clay Miner.* 31, 27–248. <https://doi.org/10.1346/CCMN.1983.0310405>.
- Schwertmann, U., Friedl, J., Stanjek, H. 1999. From Fe(III) ions to ferrihydrite and then to hematite. *J. Colloid Interface Sci.* 209, 215–223. <https://doi.org/10.1006/jcis.1998.5899>.
- Schwertmann, U., Stanjek, H., Becher, H.-H. 2004. Long-term in vitro transformation of 2-line ferrihydrite to goethite/hematite at 4, 10, 5 and 25°C. *Clay Min.* 29, 433–438. <https://doi.org/10.1180/0009855043940145>.
- Seal, R.R. II., Hammarstrom J.M. 2003. Geoenvironmental models of mineral deposits: Examples from massive sulfide and gold deposits. In: Jambor, J.L., Blowes, D.W., Ritchie, A.I.M. (Eds.), *Environmental Aspects of Mine Wastes*. Mineralogical Association of Canada Short Course, Vol. 31. Mineralogical Association of Canada, Canada, 11–50.

- Sharafi, A., Ardejani, F.D., Rezaei, B., Sargheini, J. 2018. Environmental geochemistry of near-neutral waters and mineralogy of zinc and lead at the Angouran non-sulphide zinc mine, NW Iran. *J. Geochem. Explor.* 186, 77–93. <https://doi.org/10.1016/j.gexplo.2017.11.020>.
- Sherlock, E.J., Lawrence, R.W., Poulin, R., 1995. On the neutralization of acid rock drainage by carbonate and silicate minerals. *Environ. Geol.* 25, 43–54. <https://doi.org/10.1007/BF01061829>.
- Shulman, G.R., Yafet, Y., Eisenberger, P., Blumberg, W.E. 1976. Observations and interpretation of x-ray absorption edges in iron compounds and proteins. *Proc. Natl. Acad. Sci. USA.* 73, 1384–1388. <https://doi.org/10.1073/pnas.73.5.1384>.
- Sinclair, S.A., Pham, N., Amos, R.T., Sego, D.C., Smith, L., Blowes, D.W., 2015. Influence of freeze-thaw dynamics on internal geochemical evolution of low sulfide waste rock. *Appl. Geochem.* 61, 160–174. . <https://doi.org/10.1016/j.apgeochem.2015.05.017>.
- Sjöberg, E.L., Rickard, D.T. 1984. Calcite dissolution kinetics: Surface speciation and the origin of the variable pH dependence. *Chem. Geol.* 42, 119–136. [https://doi.org/10.1016/0009-2541\(84\)90009-3](https://doi.org/10.1016/0009-2541(84)90009-3).
- Smith, L., Beckie, R., 2003. Hydrologic and geochemical transport processes in mine waste rock, in: Jambor, J.L., Blowes, D.W., Ritchie, A.I.M., (Eds.), *Environmental Aspects of Mine Wastes*. Mineralogical Association of Canada short course, Mineralogical Association of Canada: Canada, 2003, Vol 31, pp 51–72.
- Smith, L.J.D., Bailey, B.L., Blowes, D.W., Jambor, J.L., Smith, L., Sego, D.C. 2013a. The Diavik Waste Rock Project: Initial geochemical response from a low sulfide waste rock pile. *Appl. Geochem.* 36, 210–221. <https://doi.org/10.1016/j.apgeochem.2012.06.008>.
- Smith, L.J.D., Moncur, M.C., Neuner, M., Gupton, M., Blowes, D.W., Smith, L., Sego, D.C. 2013b. The Diavik Waste Rock Project: Design, construction, and instrumentation of field-scale experimental waste-rock piles. *Appl. Geochem.* 36, 187–199. <https://doi.org/10.1016/j.apgeochem.2011.12.026>.
- Smith, L.J.D., Blowes, D.W., Jambor, J.L., Smith, L., Sego, D.C., Neuner, M. 2013c. The Diavik Waste Rock Project: Particle size distribution and sulfur characteristics of low-sulfide waste rock. *Appl. Geochem.* 36, 200–209. <https://doi.org/10.1016/j.apgeochem.2013.05.006>.

- Smith, L.J.D., Paktunc, D., Blowes, D.W. 2021. Trace elements in sulfides and release to porewater from sulfide oxidation in a historical waste-rock pile, Ontario, Canada. *Appl. Geochem.* 126, 14899. <https://doi.org/10.1016/j.apgeochem.2021.104899>.
- Smuda, J., Dold, B., Friese, K., Morgenstern, P., Glaesser, W. 2007. Mineralogical and geochemical study of element mobility at the sulfide-rich Excelsior waste rock dump from the polymetallic Zn-Pb-(Ag-Bi-Cu) deposit, Cerro de Pasco, Peru. *J. Geochem. Explor.* 92, 97–110. <https://doi.org/10.1016/j.gexplo.2006.08.001>.
- Sousa, R., Simons, b., Bru, K., Botelho de Sousa, A., Rollinson, G., Anderson, J., Martin, M., Leite, M.M. 2018. Use of mineral liberation quantitative data to assess separation efficiency in mineral processing – Some case studies. *Miner. Eng.* 127, 134–142. <https://doi.org/10.1016/j.mineng.2018.08.004>.
- Stracek, O., Choquette, M., Gélinas, P., Lefebvre, R., Nicholson, R.V., 2004. Geochemical characterization of acid mine drainage from a waste rock pile, Mine Doyon, Québec, Canada. *J. Contam. Hydrol.* 69, 45–71. [https://doi.org/10.1016/S0169-7722\(03\)00150-5](https://doi.org/10.1016/S0169-7722(03)00150-5).
- Srivastava, U.C., Nigam, H.L. 1973. X-ray absorption edge spectrometry (XAES) as applied to coordination chemistry. *Coord. Chem. Rev.* 9, 275–310. [https://doi.org/10.1016/S0010-8545\(00\)82080-9](https://doi.org/10.1016/S0010-8545(00)82080-9).
- St-Arnault, M., Vriens, B., Klein, B., Mayer, K.U., Beckie, R.D. 2019. Mineralogical controls on drainage quality during the weathering of waste rock. *Appl. Geochem.* 108, 104376. <https://doi.org/10.1016/j.apgeochem.2019.104376>.
- Steger H.F. 1982. Oxidation of sulfide minerals VII: Effect of temperature and relative humidity on the oxidation of pyrrhotite. *Chem. Geol.* 35, 281–295. [https://doi.org/10.1016/0009-2541\(82\)90006-7](https://doi.org/10.1016/0009-2541(82)90006-7).
- Steinepreis, M., 2017. Investigation of gas transport rates through a covered waste rock pile and synchrotron studies on the sulfide oxidation reaction. M.Sc. thesis, University of Waterloo.
- Strömberg, B., Banwart, S., 1999. Experimental study of acid-consuming processes in mining waste rock: some influences of mineralogy and particle size. *Appl. Geochem.* 14, 1–16. [https://doi.org/10.1016/S0883-2927\(98\)00028-6](https://doi.org/10.1016/S0883-2927(98)00028-6).

- Swayze, G.A., Desborough, G.A., Smith, K.S., Lowers, H.A., Hammarstrom, J.M., Diehl, S.F., Leinz, R.W., Driscoll, R.L., 2008. Understanding Jarosite – from Mine Waste to Mars. United States Geological Survey Circular 1328, pp. 8–13.
- Sylvester, P.J. 2012. Use of the Mineral Liberation Analyzer for studies of sediments and sedimentary rocks. Mineralogical Association of Canada Short Course 42, 1–16.
- Szytuła, A., Burewicz, A., Dimitrijević, Ž., Kraśnicki, S., Rżany, H., Todorović, J., Wanic, A., Wolski, W. 1968. Neutron diffraction studies of α -FeOOH. *Physica status solidi*, 26, 429–434. <https://doi.org/10.1002/PSSB.19680260205>.
- Tang, J., Dietzel, M., Böhm, Köhler, Eisenhauer. 2008. Sr²⁺/Ca²⁺ and ⁴⁴Ca/⁴⁰Ca fractionation during inorganic calcite formation: II. Ca isotopes. *Geochim. Cosmochim. Acta*. 72, 3733–3745. <https://doi.org/10.1016/j.gca.2011.10.039>.
- Thomas, J.E., Jones, C.F., Skinner, W.M., Smart, R. St.C. 1998. The role of surface sulfur species in the inhibition of pyrrhotite dissolution in acid conditions. *Geochim. Cosmochim. Acta*. 62, 1555–1565. [https://doi.org/10.1016/S0016-7037\(98\)00087-8](https://doi.org/10.1016/S0016-7037(98)00087-8).
- Thomas, J.E., Skinner, W.E., St. C. Smart, R. 2001. A mechanism to explain sudden changes in rates and products for pyrrhotite dissolution in acid solution. *Geochim. Cosmochim. Acta*. 66, 1–12, [https://doi.org/10.1016/S0016-7037\(00\)00503-2](https://doi.org/10.1016/S0016-7037(00)00503-2).
- Tian, L., Shi, Z., Lu, Y, Dohnalkova, A.C., Lin, Z., Dang, Z. 2017. Kinetics of cation and oxyanion adsorption and desorption on ferrihydrite: Roles of ferrihydrite binding sites and a unified model. *Environ. Sci. Technol.* 51, 10605–10614. <https://doi.org/10.1021/acs.est.7b03249>.
- Tipper, E.T., Galay, A., Bickle, M.J. 2006. Riverine evidence for a fractionated reservoir of Ca and Mg on the continents: Implications for the oceanic Ca cycle. *Earth. Planet. Sci. Lett.* 247, 267–279. <https://doi.org/10.1016/j.epsl.2006.04.033>.
- Tokonami, M, Nishiguchi, K., Morimoto, N. 1972. Crystal structure of a monoclinic pyrrhotite (Fe₇S₈). *Am. Mineral.* 57, 1066–1080.
- Vriens, B., Peterson, H., Laurenzi, L., Smith, L., Aranda, C., Mayer, U., Beckie, R.D. 2019. Long-term monitoring of waste-rock weathering at the Antamina mine, Peru. *Chemosphere*. 215, 858–869. <https://doi.org/10.1016/j.chemosphere.2018.10.105>.

- Vukmanovic, Z., Reddy, S.M., Godel, B., Barnes, S.J., Fiorentini, M.L., Barnes, S.-J., Kilburn, M.R. Relationship between microstructures and grain-scale trace element distribution in komatiite-hosted magmatic sulphide ores. *Lithos*. 184–187, 42–61.
<http://dx.doi.org/10.1016/j.lithos.2013.10.037>.
- Wang, H., Salveson I. 2005. A review on the mineral chemistry of the non-stoichiometric iron sulphide, Fe_{1-x}S ($0 \leq x \leq 0.125$): polymorphs, phase relations and transitions, electronic and magnetic structures. *Ph. Transit.* 78, 547–567. <https://doi.org/10.1080/01411590500185542>.
- Waychunas, G.A., Apter, M.J., Brown Jr., G.E. 1983. X-Ray K-Edge Absorption Spectra of Fe Minerals and Model Compounds: Near-Edge Structure. *Phys. Chem. Minerals*, 10, 1–9.
<https://doi.org/10.1007/BF01204319>.
- White, A.F., Bullen, T.D., Vivit, D.V., Schulz, M.S., Clow, D.W. 1999. The role of disseminated calcite in the chemical weathering of granitoid rocks. *Geochim. Cosmochim. Acta*. 63, 1939–1953.
- White, A.F. Schulz, M.S., Lowenstern, J.B., Vivit, D.V., Bullen, T.D. 2005. The ubiquitous nature of accessory calcite in granitoid rocks: Implications for weathering, solute evolution, and petrogenesis. *Geochim. Cosmochim. Acta*. 69, 1455–1471.
<https://doi.org/10.1016/j.gca.2004.09.012>.
- White, E.W. McKinstry, H.A. 1966. Chemical Effect on X-Ray Absorption-Edge Fine Structure. In: Mallett G.R., Fay M.J., Mueller W.M. (Eds.) *Advances in X-Ray Analysis*. Springer, Boston, MA.
https://doi.org/10.1007/978-1-4684-7633-0_34.
- Wilke, M., Farges, F., Petit, P.-E., Brown Jr., G.E., Martin, F. 2001. Oxidation state and coordination of Fe in minerals: An Fe K-XANES spectroscopic study. *Am. Mineral.* 86, 714–730.
<https://doi.org/10.2138/am-2001-5-612>.
- Wilkins, S.J., Compton, R.J., Taylor, M.A., Viles, H.A. 2001. Channel flow cell studies of the inhibiting action of gypsum on the dissolution kinetics of calcite: A laboratory approach with implications for field monitoring. *J. Colloid Interf Sci.* 236, 354–361.
<https://doi.org/10.1006/jcis.2000.7418>.

- Wunderly, M.D., Blowes, D.W., Frind, E.O., Ptacek, C.J., 1996. Sulfide mineral oxidation and subsequent reactive transport of oxidation products in mine tailings impoundments: A numerical model. *Water Resour. Res.* 32, 3173–3187. <https://doi.org/10.1029/96WR02105>.
- Yaroshevsky A.A. 2006. Abundances of chemical elements in the Earth's crust. *Geochem. Int.* 44, 48–55. <https://doi.org/10.1134/S001670290601006X>.
- Zhang, J., Li, Y., Chen, J. 2022. Water-oxygen interaction on marcasite (101) surface: DFT calculation. *Int. Min. Sci. Technol.* 32, 191–199. <https://doi.org/10.1016/j.ijmst.2021.11.01>.

Appendices

Appendix A

Supplementary Material for Chapter 2

Trace elements in sulfides and release to porewater from sulfide oxidation in a historical waste-rock pile, Ontario, Canada

Figures

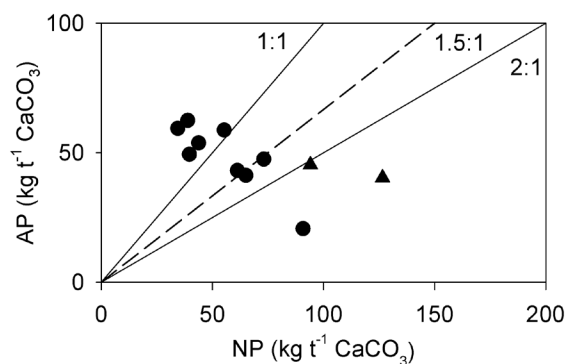


Figure A-1: Ratios of neutralization potential (NP) to acid-generating potential (AP) (NP:AP) of samples from historical waste rock (samples) and freshly blasted waste rock (triangles). Lines at 1:1, 1.5:1 and 2:1 represent designations of acid-generating potential. Samples with NP:AP < 1:1 are typically designated “potentially acid generating”. Samples with 1:1 < NP:AP < 2:1 are typically designated “of uncertain acid-generating potential”. Samples with NP:AP > 2:1 are typically designated “non-acid generating.”. Detour Lake Mine designates samples with NP:AP > 1.5:1 as “non-acid generating”.

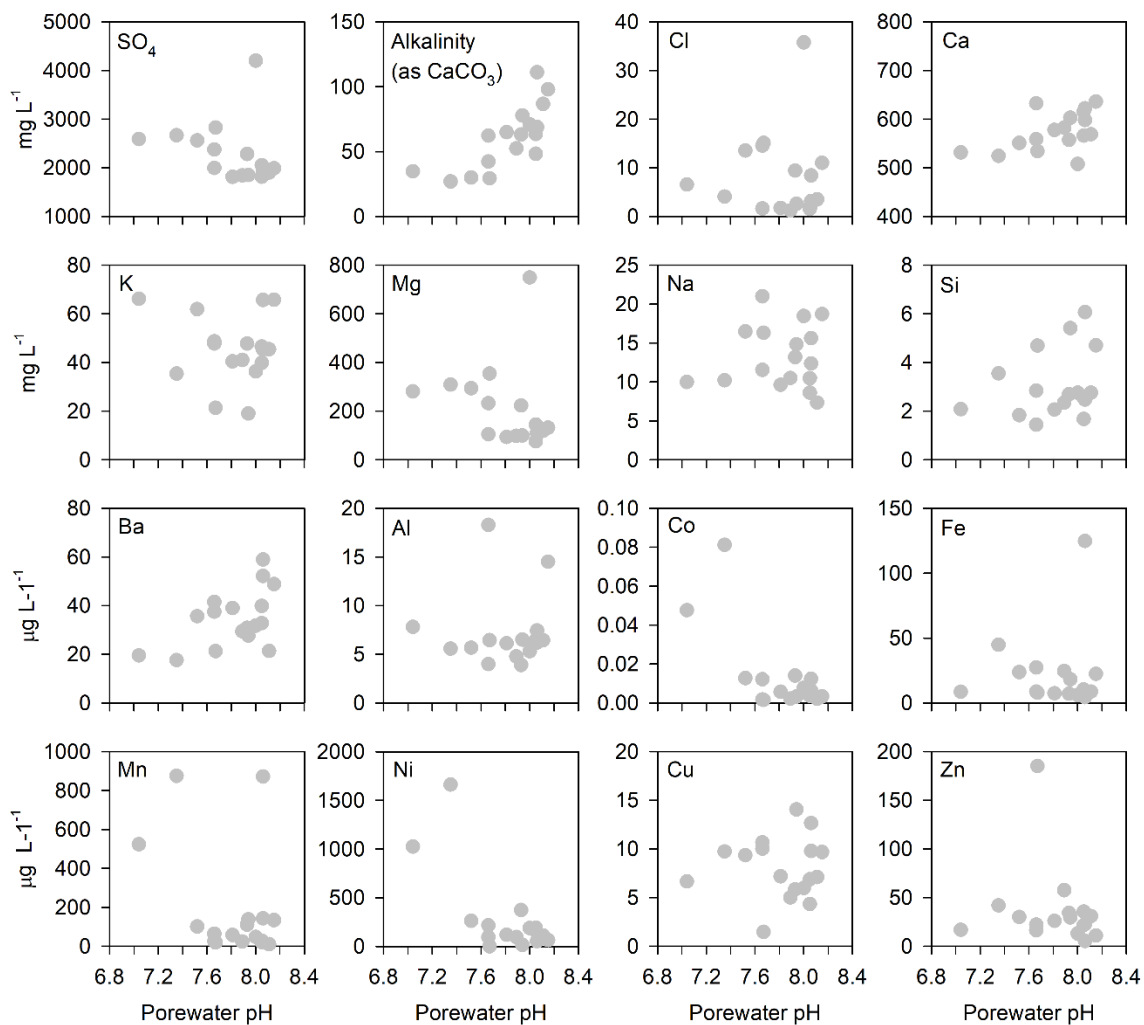


Figure A-2: Porewater concentrations of major ions and key trace elements.

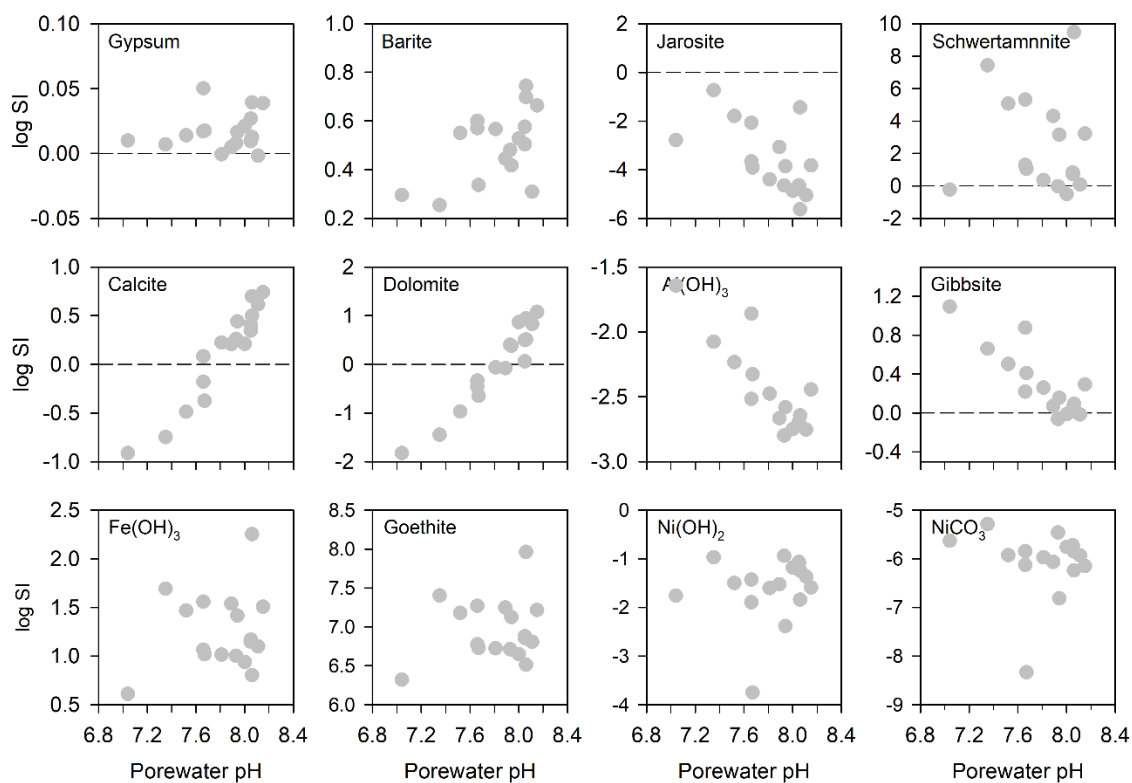


Figure A-3: Saturation indices (SI) of key secondary phases calculated by PHREEQC.

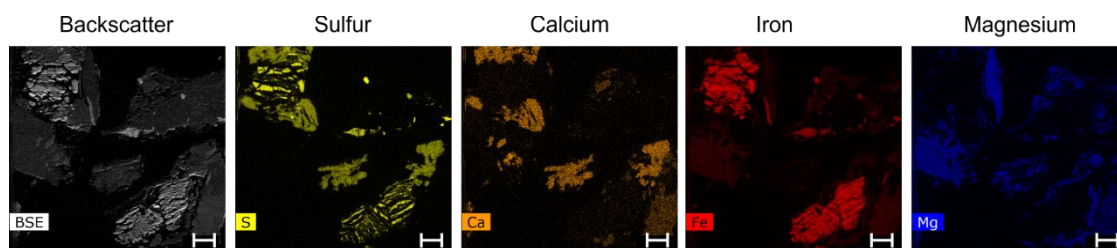


Figure A-4: SEM/EDX maps of two altered pyrrhotite grains (upper left and lower right in each frame), and gypsum grains or coatings evident in the Sulfur and Calcium maps. Scale bar represents 60 μm .

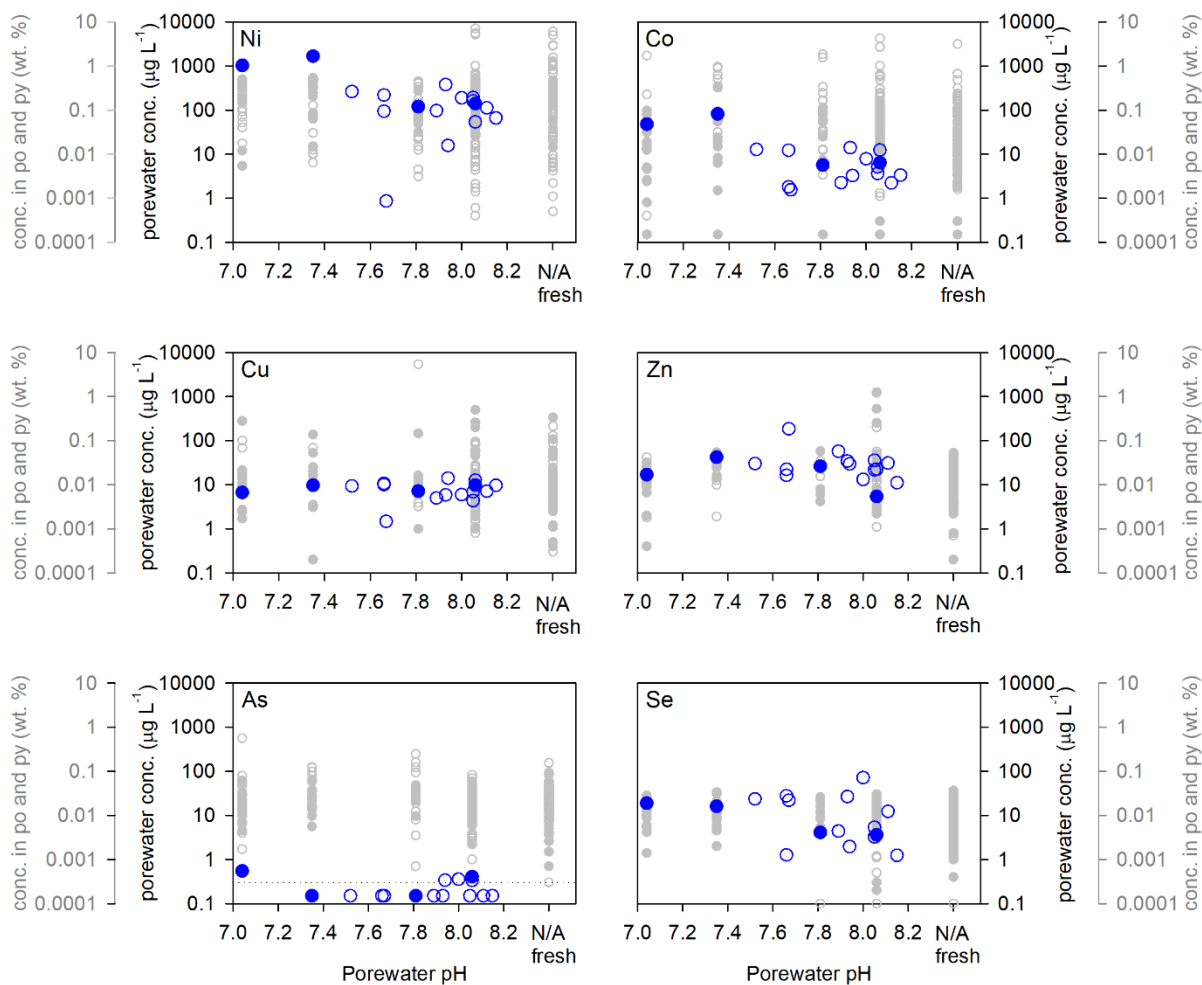


Figure A-5: Concentrations of trace metals measured by EPMA in pyrrhotite ("po", filled grey circles), and pyrite ("py", open grey circles), and measured in porewater (blue circles). Filled blue circles represent porewater samples with corresponding EPMA measurements of po and py, open blue circles represent porewater samples with no corresponding EPMA measurements. Grey circles plotted at "N/A fresh" on the x-axis represent EPMA measurements on po and py in the freshly blasted sample most similar to the historical samples. Dotted line in the As and Se plots identify the method detection limits for the aqueous samples.

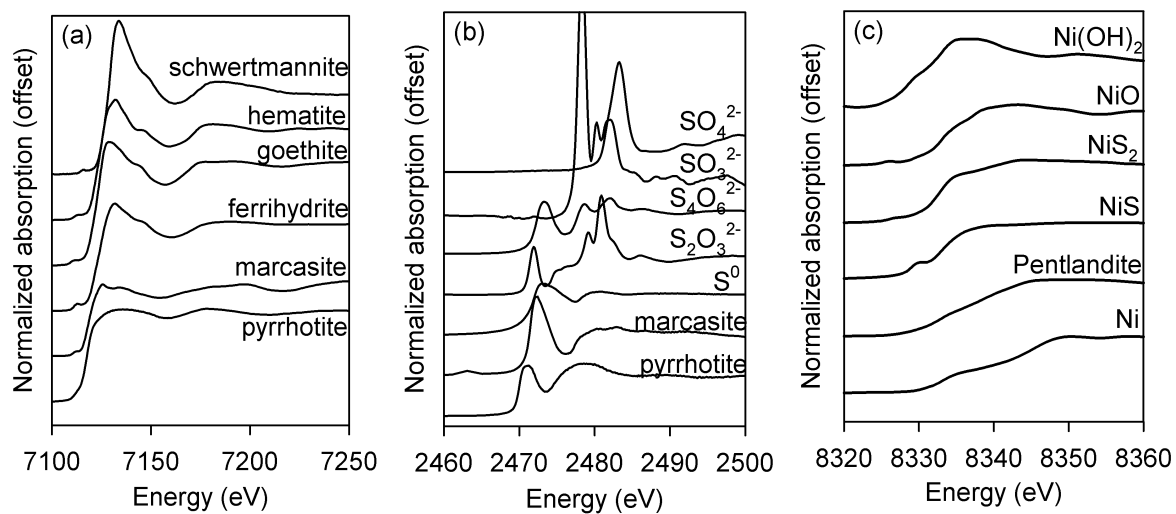


Figure A-6: Standard spectra for (a) iron-XANES, (b) sulfur-XANES, and (c) nickel-XANES.

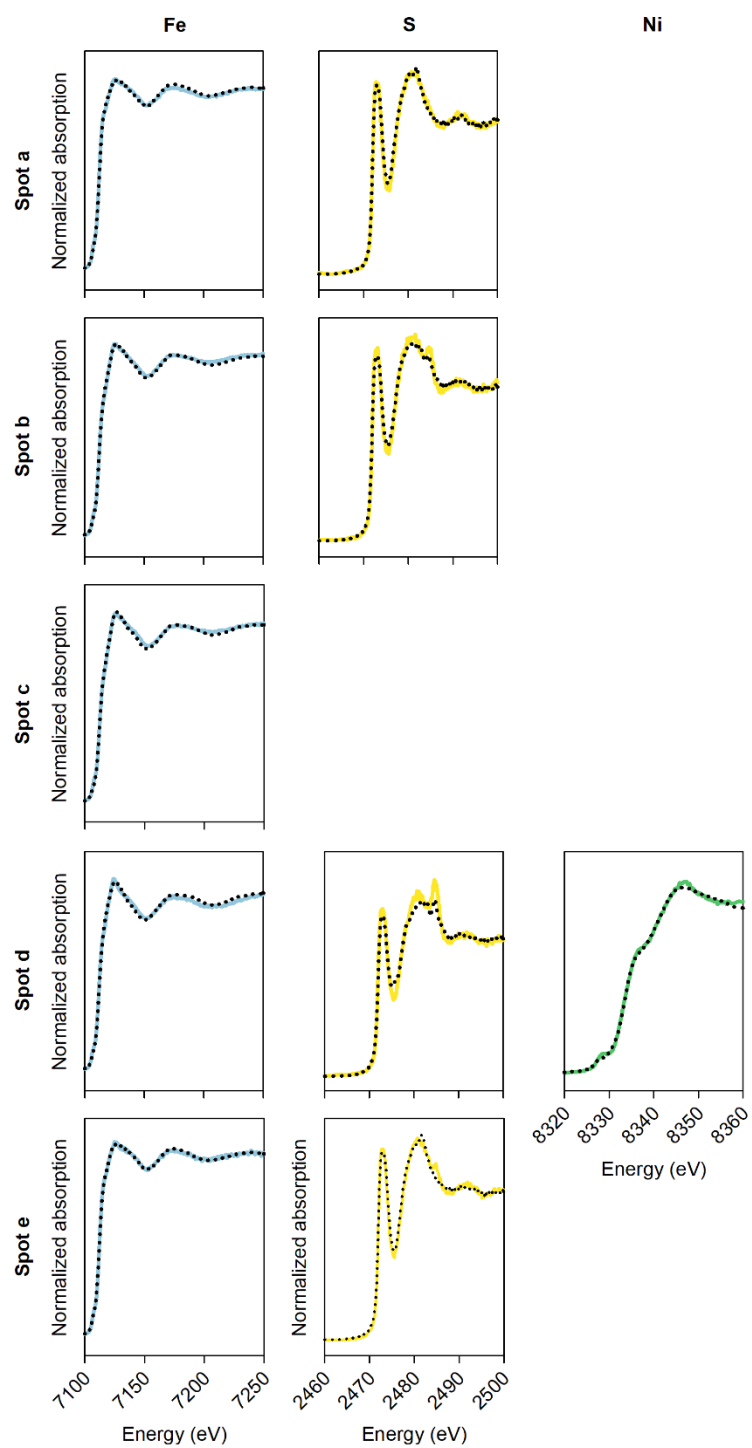


Figure A-7: Measured spectra of iron (Fe; blue lines); sulfur (S; yellow lines); and nickel (Ni, green lines) and linear combination fitting results (dotted lines)

Tables

Table A-1: Sensitivity analyses for linear combination fitting (LCF) for X-ray absorption near edge spectra of iron (Fe-XANES). The % improvement in fit statistics compares the LCF combination in the previous column for the measured spot. “N.I.” in schwertmannite row indicates “not included”.

Standard	Spot a			Spot b				Spot c			Spot d			Spot e		
Pyrrhotite	100%	96%	78%	100%	88%	80%	63%	100%	86%	58%	100%	86%	42%	100%	98%	90%
Marcasite			7%		12%	8%	13%		14%	27%		14%	34%			
Goethite		4%	10%				13%						12%		2%	5%
Ferrihydrite																
Schwertmannite		N.I.	5%		N.I.	N.I.	10%		N.I.	15%		N.I.	13%		N.I.	5%
<i>R-factor</i>	1.63E-03	9.80E-04	4.55E-04	7.65E-03	1.82E-03	4.97E-04	1.97E-04	2.09E-02	1.62E-02	5.01E-04	9.09E-03	5.99E-03	1.05E-03	2.38E-03	2.19E-03	3.69E-04
<i>Reduced Chi-squared</i>	3.02E-04	1.81E-04	8.53E-05	1.41E-03	3.36E-03	9.27E-05	3.71E-05	3.69E-03	6.00E-01	8.94E-05	1.62E-03	1.06E-03	1.89E-04	4.56E-04	4.20E-04	7.15E-05
% improvement in fit statistic		40%	54%		76%	73%	60%		22%	97%		34%	82%		8%	83%

Table A-2: Sensitivity analyses for linear combination fitting (LCF) for X-ray absorption near edge spectra of sulfur (S-XANES). The % improvement in fit statistics compares the LCF combination in the previous column for the measured spot. Grey font represents insufficient improvement in fit statistic to include phases < 5%.

Standard	Spot a				Spot b				Spot c				Spot d	Spot e		
Pyrrhotite	100%	94%	93%	89%	100%	88%	85%	86%	100%	88%	71%	69%	No data	100%	90%	90%
Marcasite								3%								
Elemental S															6%	4%
Thiosulfate		6%	6%	5%			7%	5%		12%	12%	13%			9%	4%
Tetrathionate				5%		12%	8%	7%			17%	17%				2%
Sulfite												1%				
Sulfate			2%	0.4%												
<i>R-factor</i>	8.94E-03	9.12E-03	8.83E-03	3.60E-03	1.13E-02	1.03E-02	4.67E-03	4.18E-03	2.93E-02	1.30E-02	1.12E-02	1.08E-02		1.14E-02	4.62E-03	3.40E-03
<i>Reduced Chi-squared</i>	1.42E-03	1.49E-03	1.40E-03	5.72E-03	1.90E-03	1.72E-03	7.91E-03	7.13E-04	5.14E-03	2.28E-03	1.99E-03	1.93E-03		1.85E-03	7.53E-03	5.60E-04
%improvement in fit statistics		2%	3%	59%		9%	54%	11%		56%	14%	3%			60%	26%

Table A-3: Sensitivity analyses for linear combination fitting (LCF) for X-ray absorption near edge spectra of nickel (Ni-XANES). The % improvement in fit statistics compares the LCF combination in the previous column for the measured spot. Grey font represents insufficient improvement in fit statistic to include to include phases < 5%.

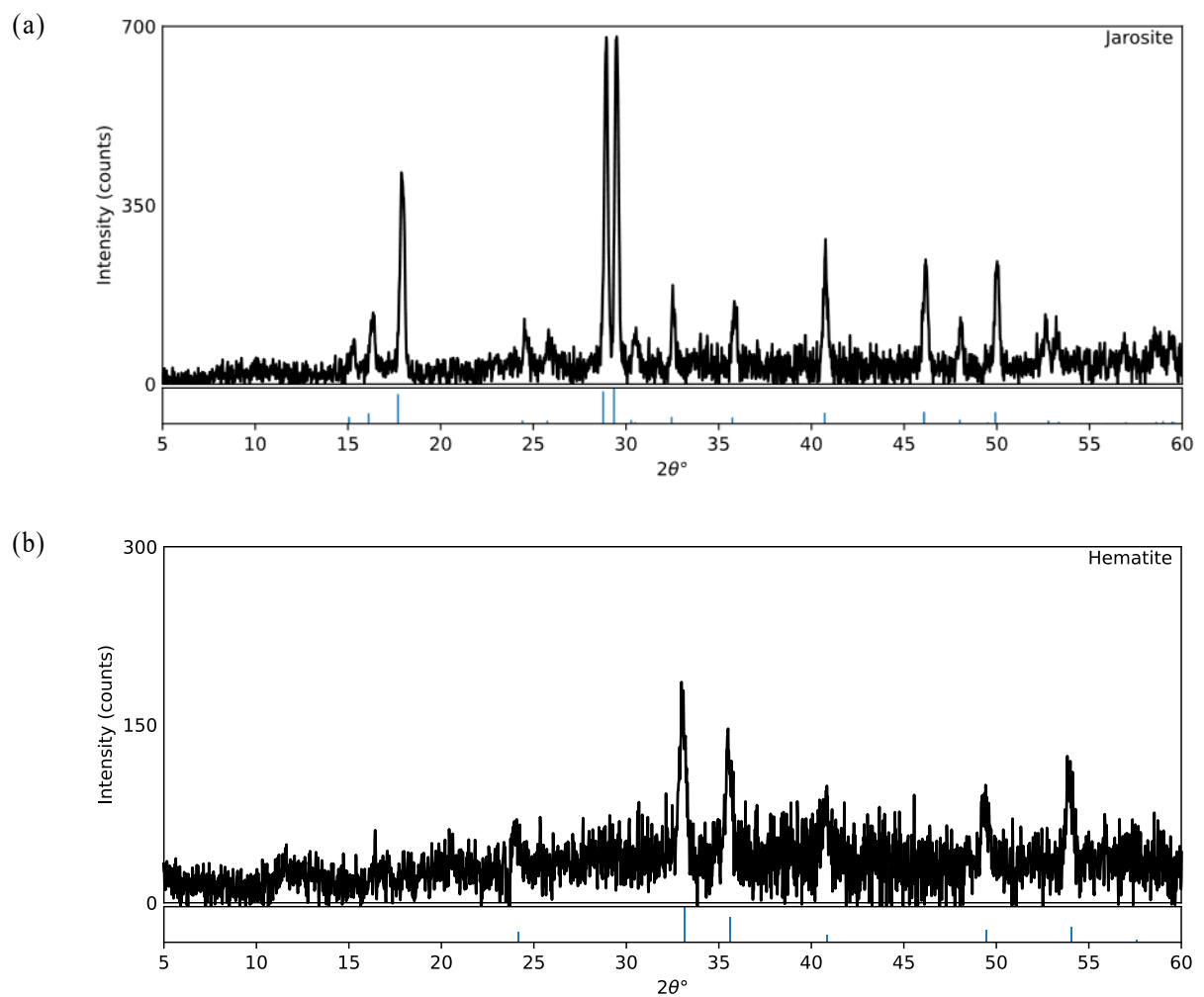
Standard	Spot d			
Pentlandite	100%			
NiS ₂		100%	85%	84%
NiS				
NiSO ₄			15%	15%
NiO + Ni(OH) ₂				1%
<i>R-factor</i>	<i>3.49E-02</i>	<i>2.87E-02</i>	<i>1.08E-03</i>	<i>9.77E-04</i>
<i>Reduced Chi-squared</i>	<i>7.94E-03</i>	<i>6.54E-03</i>	<i>2.48E-03</i>	<i>2.29E-04</i>
%improvement in fit statistics		18%	96%	9.5%

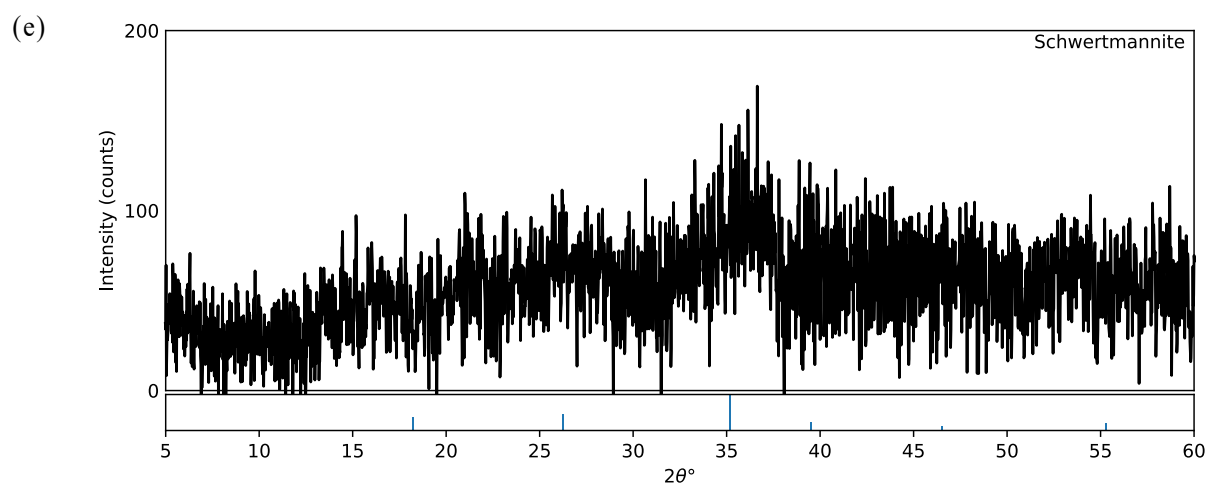
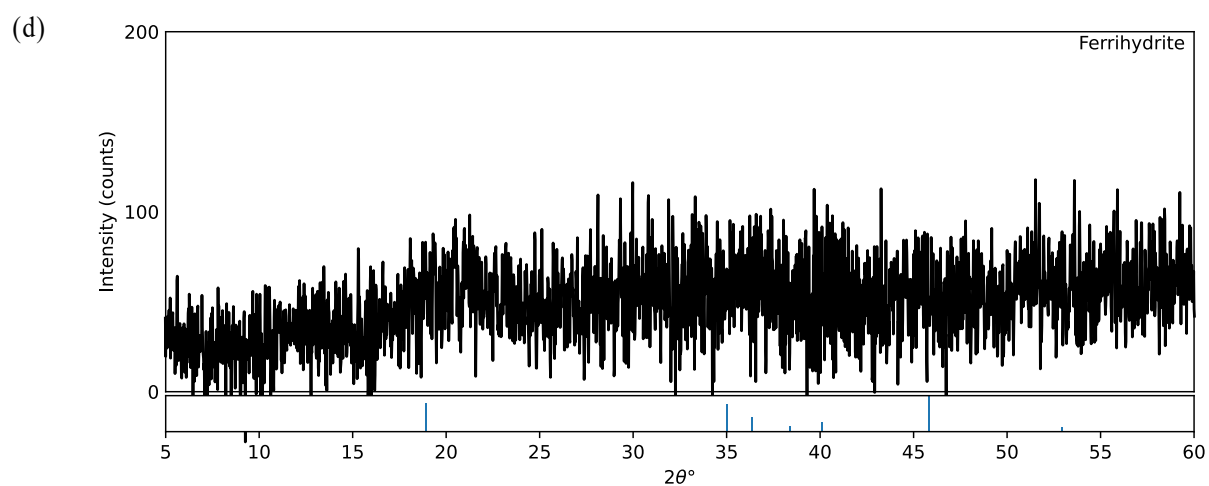
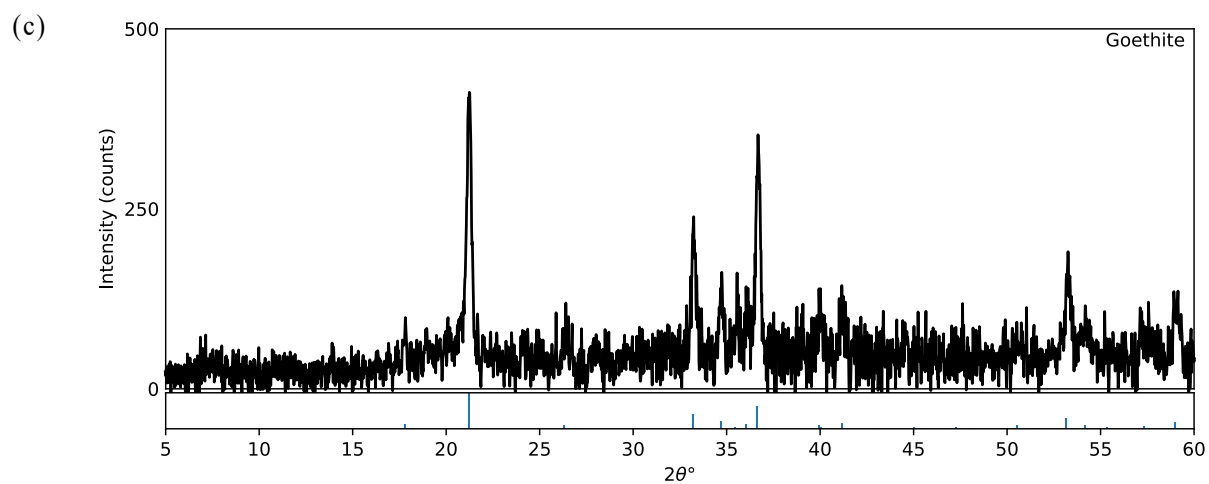
Appendix B

Supplementary Material for Chapter 3

Fe K-edge XANES across oxidizing pyrrhotite grains from natural samples of mining waste rock

Figures





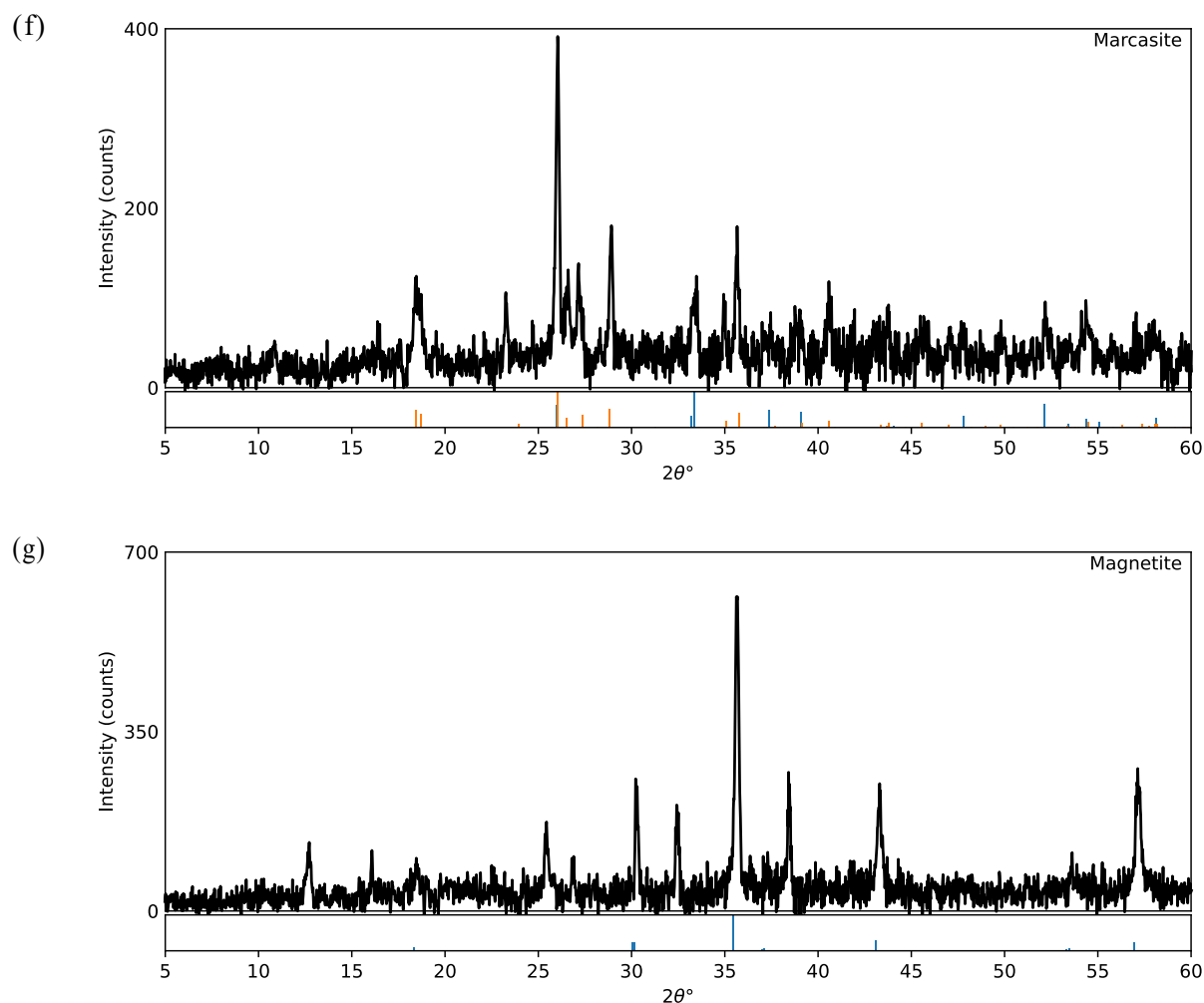


Figure B-1: Diffraction patterns from reference materials collected with a Rigaku MiniFlex II Desktop X-ray diffractometer. (a) jarosite, (b) hematite, (c) goethite, (d) ferrihydrite, (e) schwertmannite, (f) marcasite, (g) magnetite. Data was collected over 3 – 80 $2\theta^\circ$ with a step size of 0.05° and scan speed of $4.00^\circ \text{ min}^{-1}$. A copper anode tube X-ray source was used with a voltage of 30 kV and current of 15 mA. All materials were positively identified using the PDF4+ database and JADE Pro software (Materials Data, Inc., USA)

Diffraction patterns from ferrihydrite and schwertmannite samples showed no evidence of crystalline transformation products and contained broad peaks aligned with PDF4+ database patterns 01-072-7673 and 00-047-1775, respectively. The marcasite sample was identified to contain a mixture of szomolnokite [$\text{FeSO}_4 \cdot \text{H}_2\text{O}$; 04-008-9680] and marcasite [04-008-8452]. Jarosite [04-015-8168], hematite [01-087-1166], goethite [04-015-2899], and magnetite [04-012-7038] were positively identified. The diffraction pattern from magnetite contained seven unidentified peaks at d-spacings of 6.96, 5.51, 3.50, 2.76, and 2.34 Å.

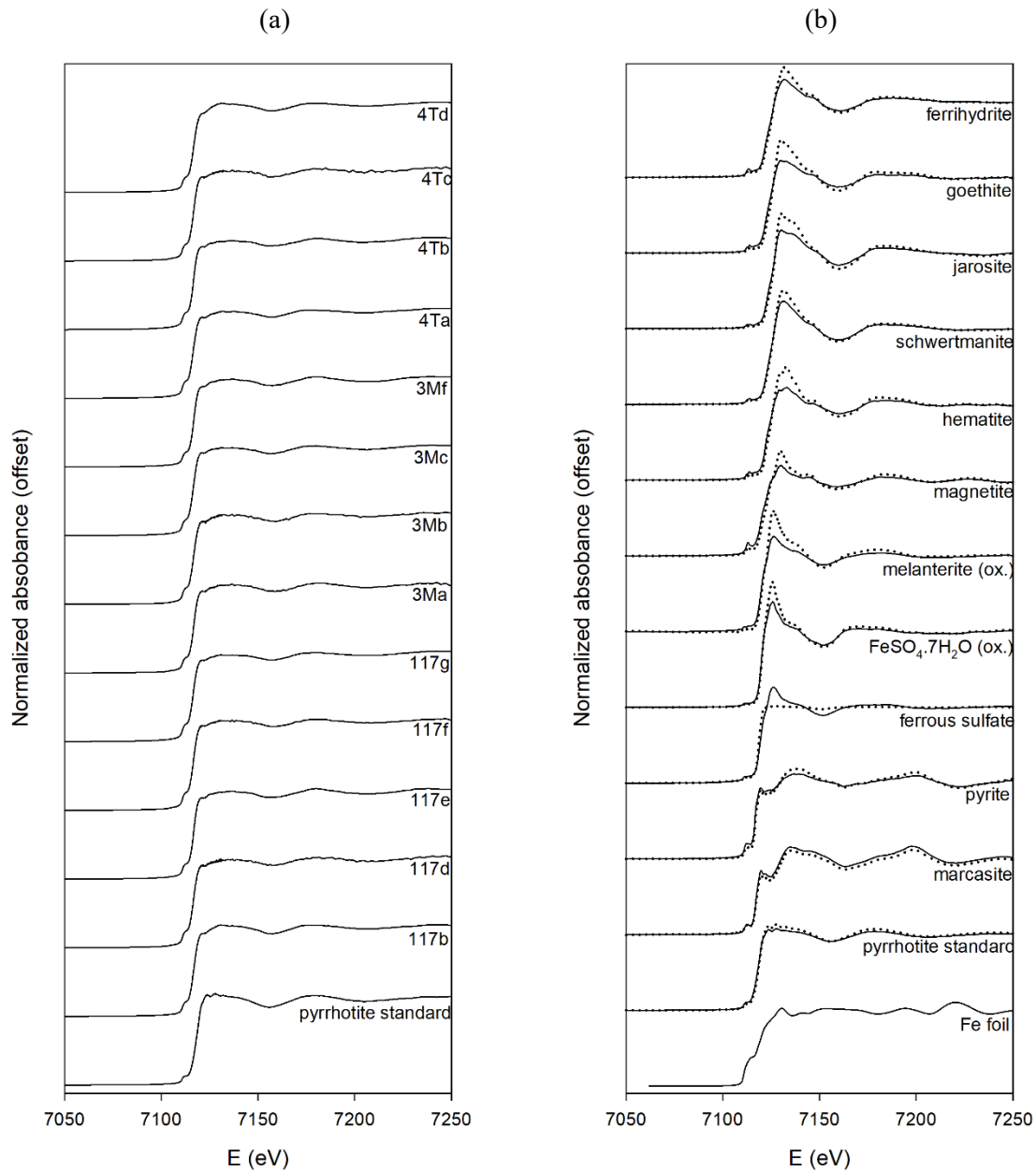


Figure B-2: Normalized standard spectra for (a) pyrrhotite standard (dark line) and sample spots from sample 117, 3M and 4T used as sample-specific standards in linear combination fitting; labels denote sample (117, 3M, 4T) and separate grains in each sample (a – g); and (b) standard spectra. Dotted line in (b) indicates standard spectra collected in transmission mode, demonstrating over-absorption occurred for spectra collected in fluorescence mode, with the exception of $\text{FeSO}_4 \cdot 7\text{H}_2\text{O}$.

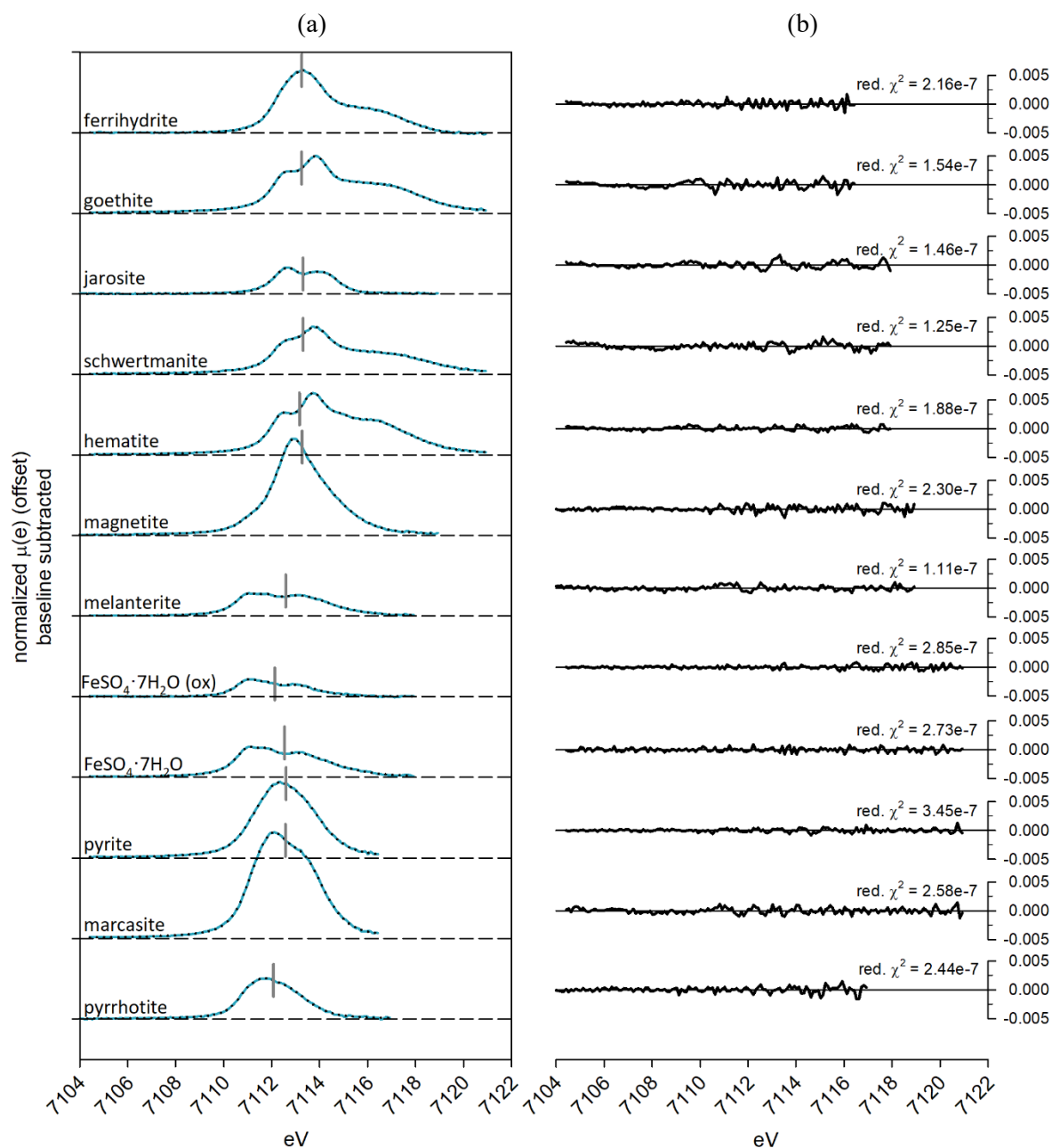


Figure B-3: (a) Baseline-subtracted pre-edge spectra (blue line), with deconvolution fit (dotted black line) for standard spectra collected in fluorescence mode. Vertical grey lines denote centroid energy of full pre-edge feature. Horizontal dashed lines represent the baseline. (b) Residual and fit parameters for pre-edge deconvolution using a baseline spline function and pseudo-Voigt components with a fixed 0.4 Gaussian fraction.

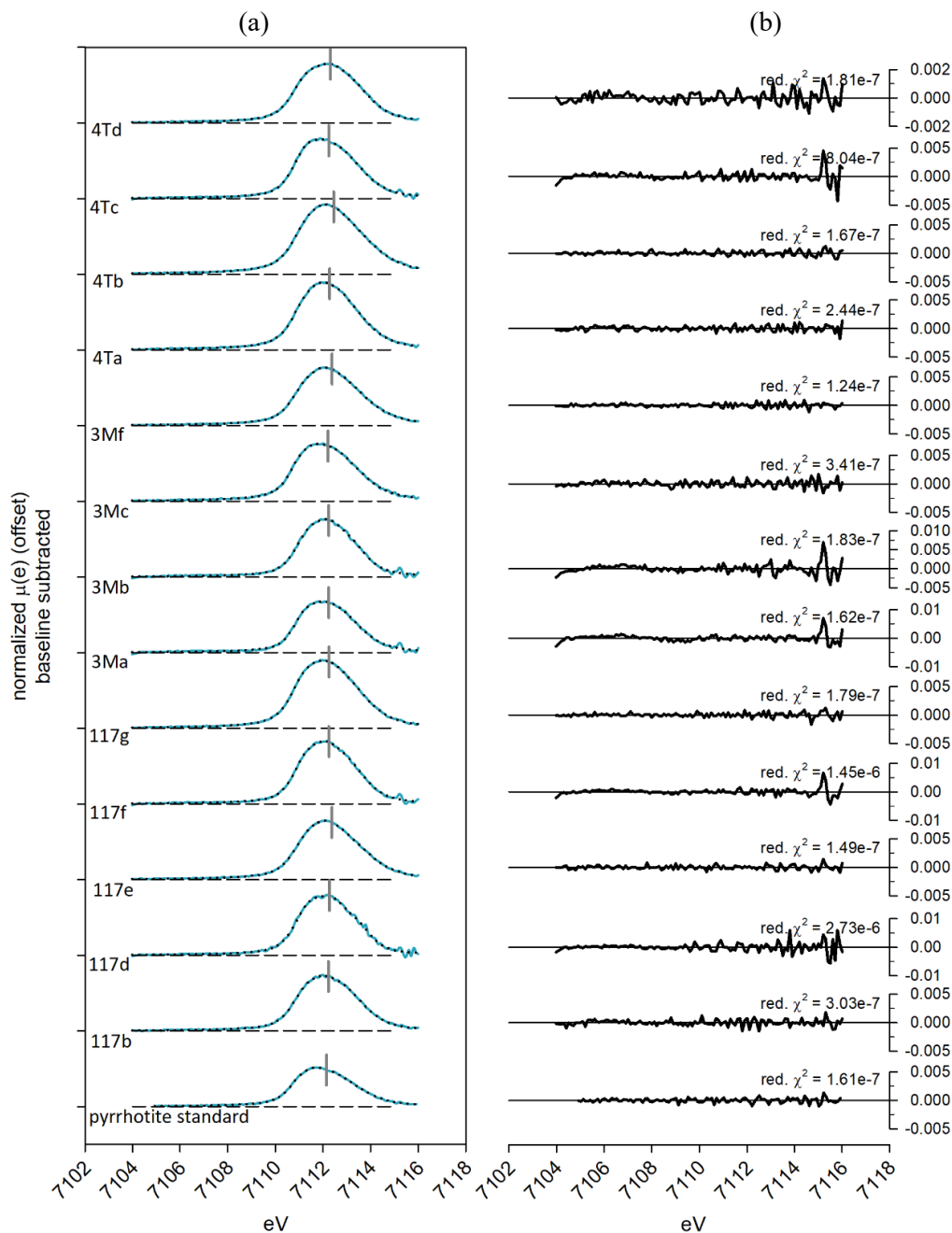


Figure B-4: (a) Baseline-subtracted pre-edge spectra (blue line), with deconvolution fit (dotted black line) for pyrrhotite spectra collected in fluorescence mode. Vertical grey lines denote centroid energy of full pre-edge feature. Horizontal dashed lines represent the baseline. (b) Residual and fit parameters for pre-edge deconvolution using a baseline spline function and pseudo-Voigt components with a fixed 0.4 Gaussian fraction.

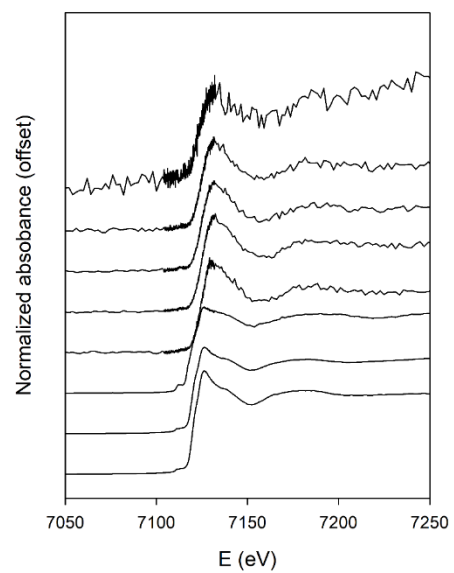


Figure B-5: Successive melanterite spectra illustrating oxidation and dehydration during data collection

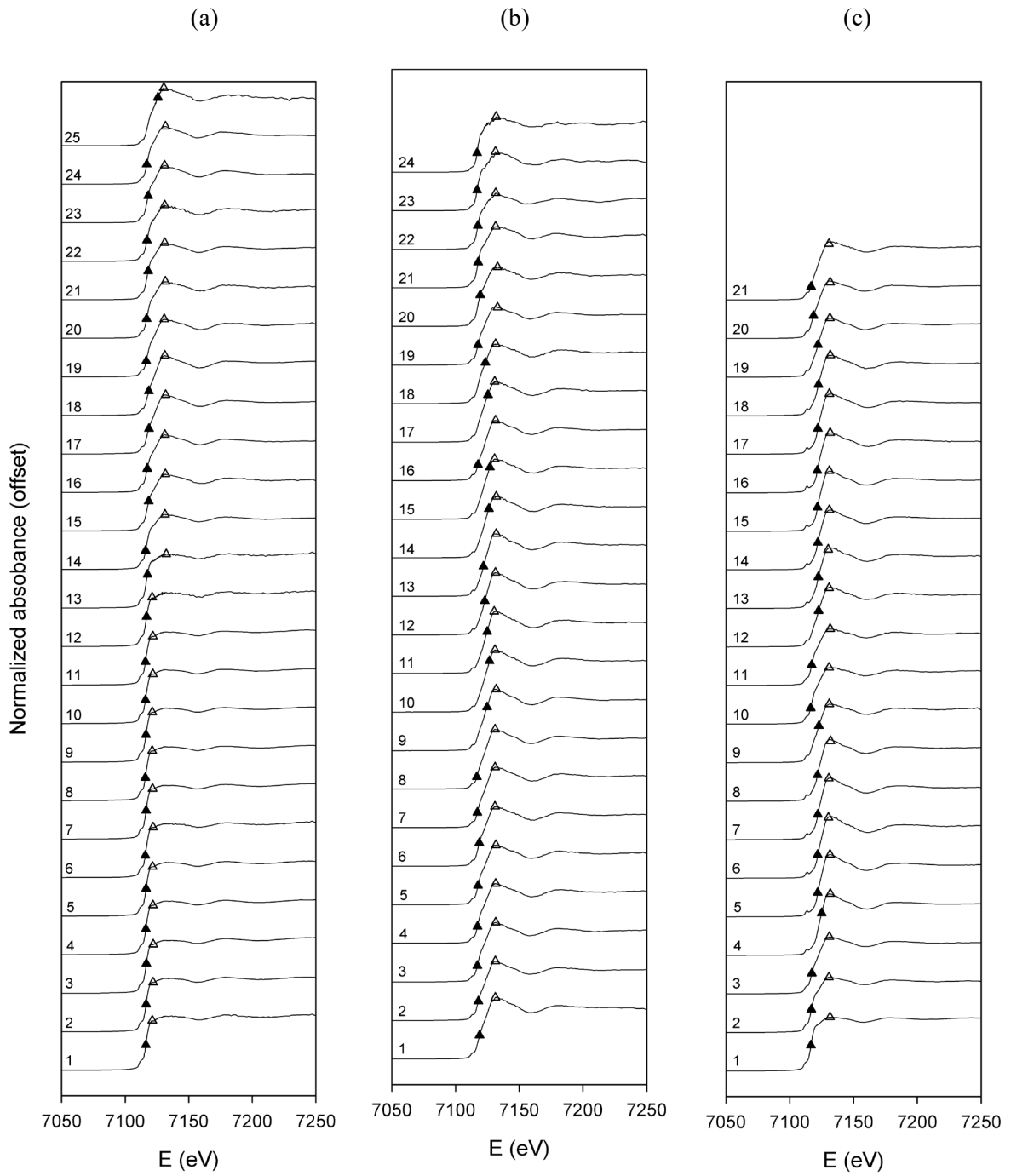


Figure B-6: Transects across pyrrhotite grains (a) 117, (b) 3M and (c) 4T. E0 energy values denoted by filled triangle symbols, white line energy values denoted by open triangles. Numbers indicate transect spot number.

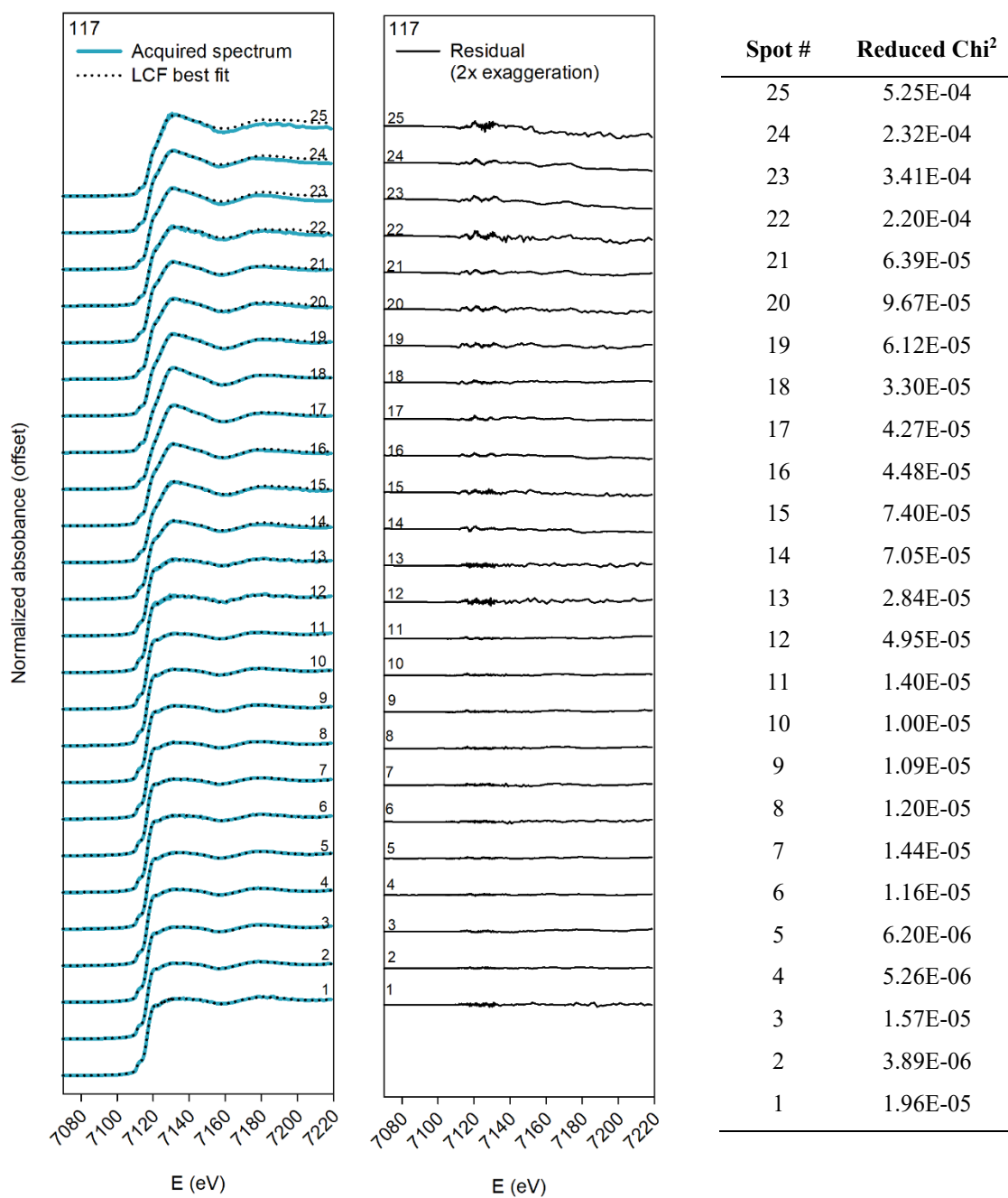


Figure B-7: Linear combination fitting results for transect spots across grain 117. Energy range of fit 7070 – 7220 eV.

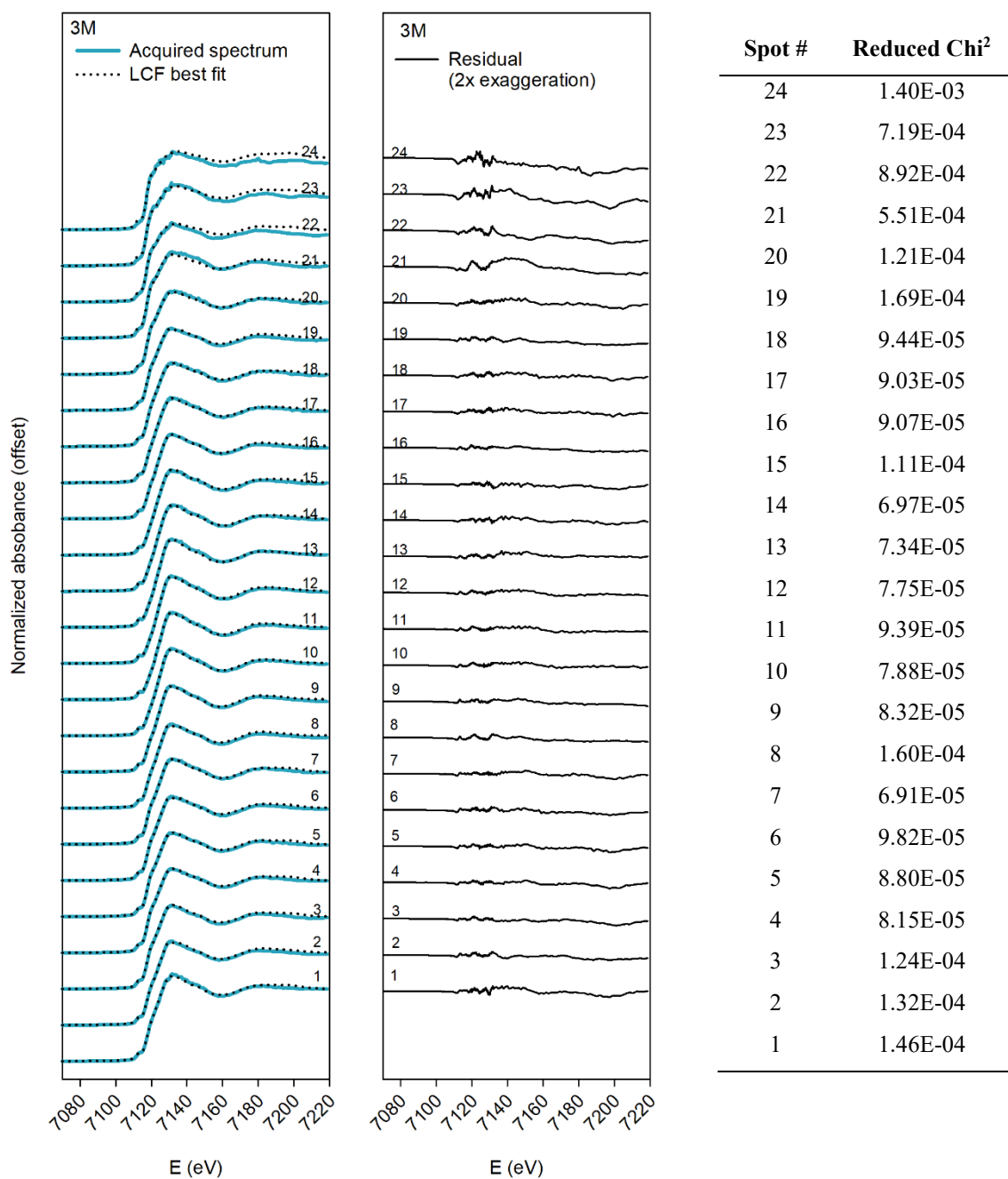


Figure B-8: Linear combination fitting results for transect spots across grain 3M. Energy range of fit 7070 – 7220 eV.

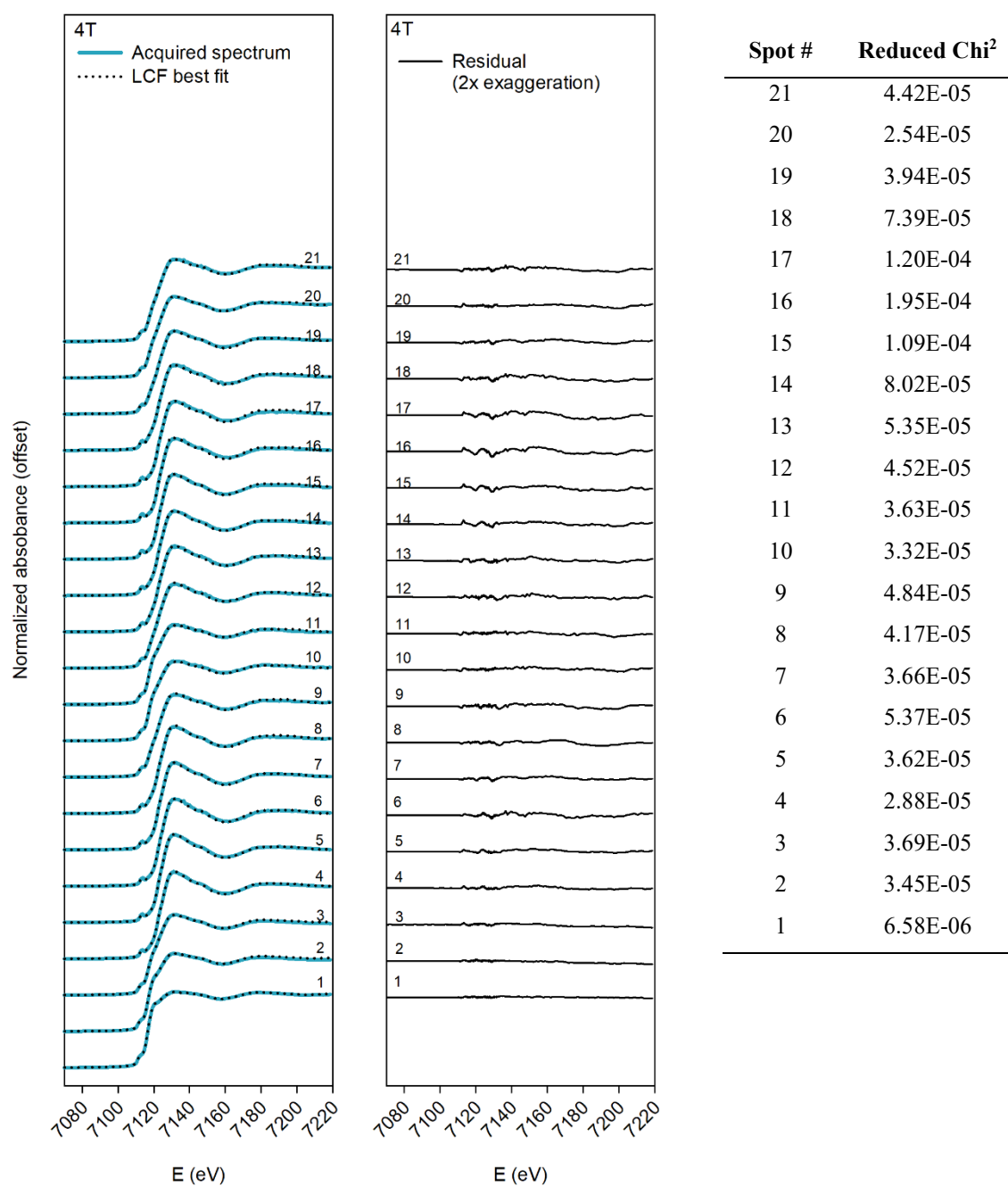


Figure B-9: Linear combination fitting results for transect spots across grain 4T. Energy range of fit 7070 – 7220 eV.

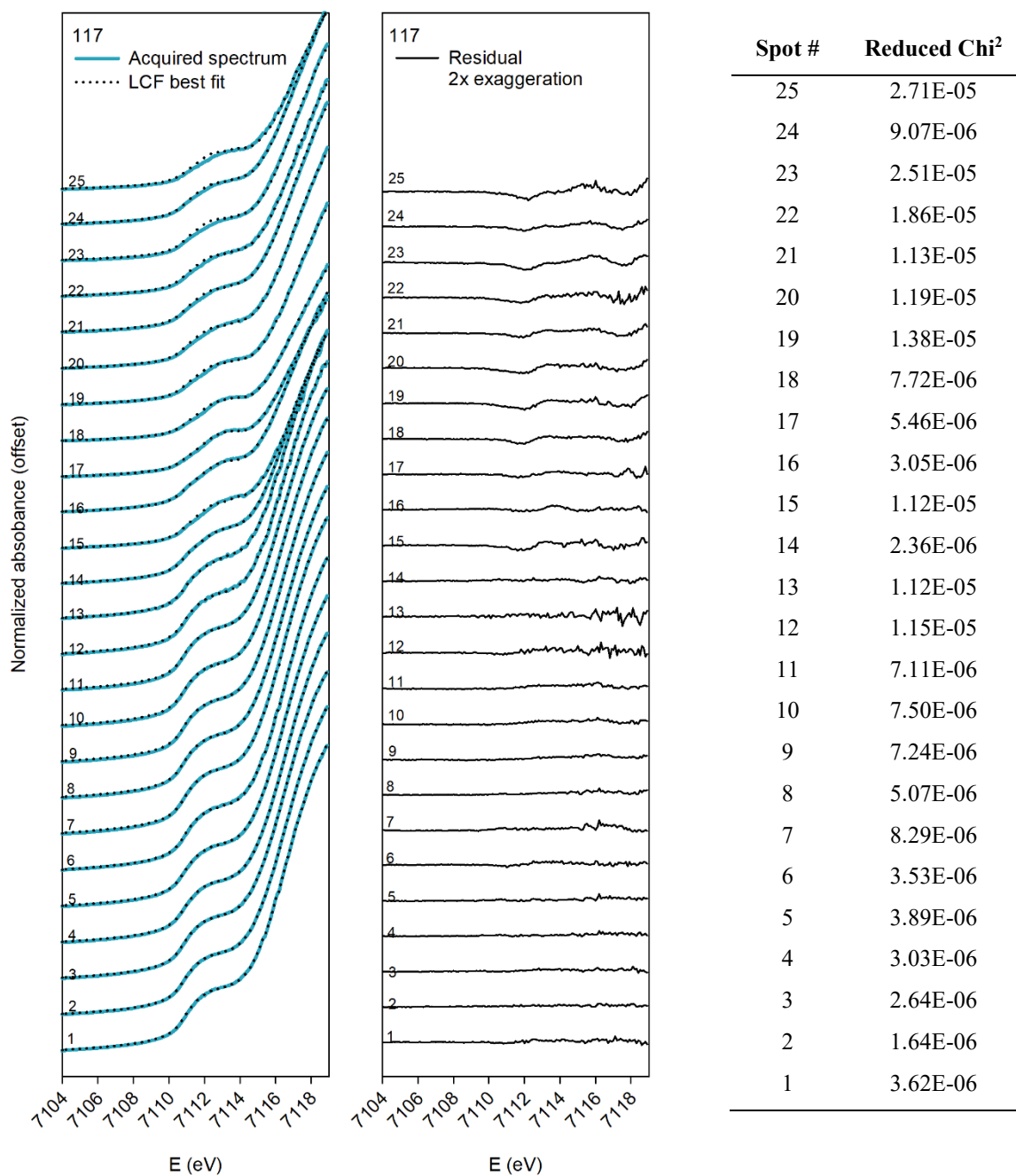


Figure B-10: Linear combination fitting results of the pre-edge region for transect spots across grain 117. Energy range of fit 7104 – 7119 eV.

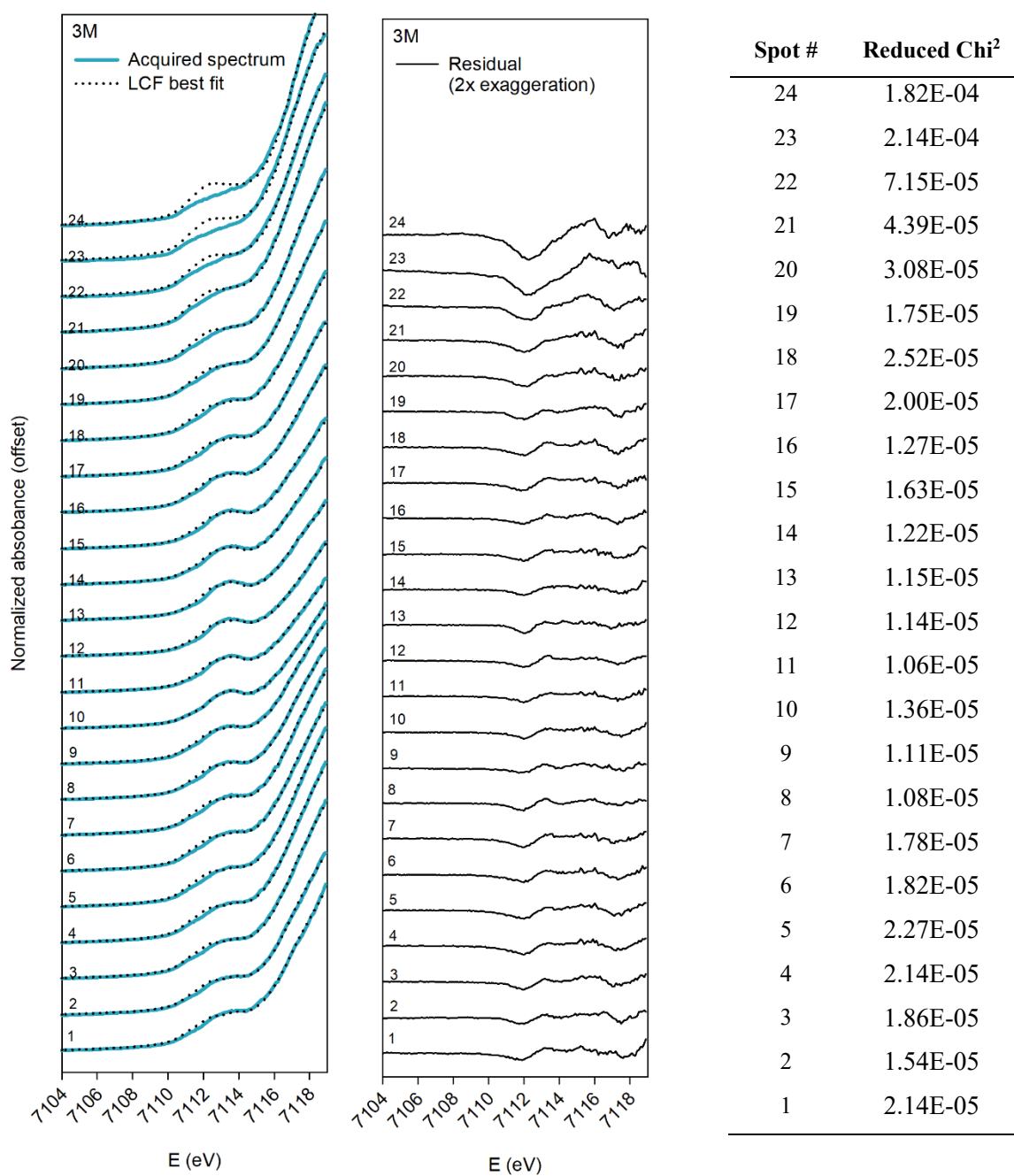


Figure B-11: Linear combination fitting results of the pre-edge region for transect spots across grain 3M. Energy range of fit 7104 – 7119 eV.

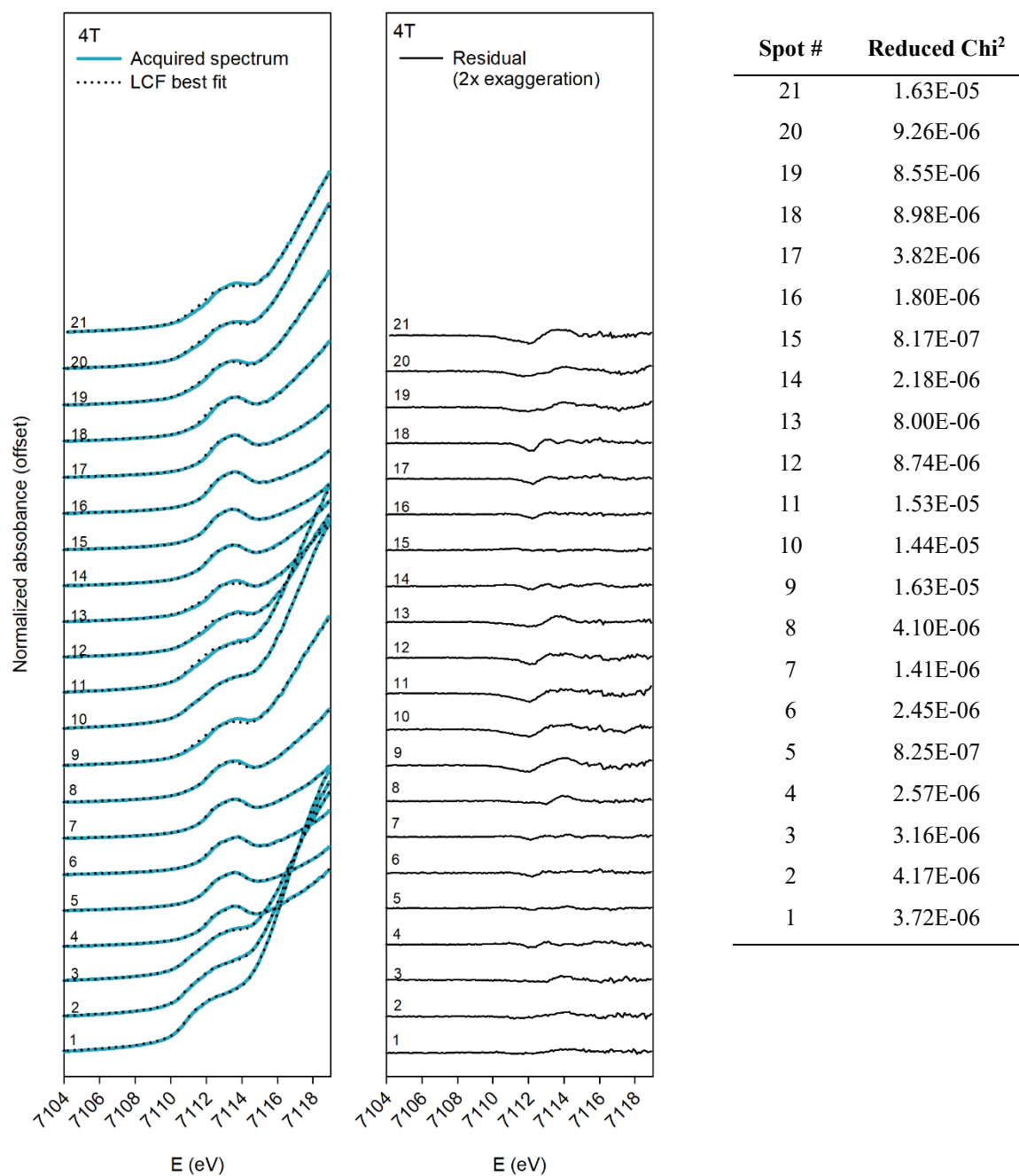


Figure B-12: Linear combination fitting results of the pre-edge region for transect spots across grain 4T. Energy range of fit 7104 – 7119 eV.

Tables

Table B-1: Pre-edge centroid energies and intensities for standard spectra collected in fluorescence mode and transmission mode.

	Fluorescence mode		Transmission mode	
	Pre-edge centroid energy (eV)	Pre-edge centroid intensity	Pre-edge centroid energy (eV)	Pre-edge centroid intensity
Pyrrhotite	7112.08	0.170	7112.15	0.184
Pyrite	7112.58	0.485	7112.59	0.354
Marcasite	7112.60	0.337	7112.55	0.300
FeSO ₄ ·7H ₂ O	7112.53	0.185	7112.17	0.149
FeSO ₄ ·7H ₂ O (oxidized)	7112.13	0.077	7112.19	0.069
Melanterite (oxidized ± dehydrated)	7112.59	0.144	7112.18	0.227
Magnetite	7113.27	0.386	7113.29	0.277
Hematite	7113.16	0.155	7113.25	0.121
Schwertmannite	7113.31	0.102	7113.45	0.062
Jarosite	7113.31	0.100	7113.33	0.072
Goethite	7113.25	0.118	7113.25	0.121
Ferrihydrite	7113.26	0.221	7113.17	0.143

Table B-2: References for data used to calculate standard deviation of Fe-S/O bond distances

Mineral	System	n Fe sites	Average Fe-S/O	Standard Deviation	Reference	Fe site	1	2	3	4	5	6	7	8	9	10
Pyrrhotite (Fe ₇ S ₈)	Trigonal	7	2.4534	0.1475	Fleet, 1971	ave	2.4481	2.4270	2.4270	2.4270	2.4694	2.4694	2.5057			
						stdv	0.0848	0.1054	0.1051	0.1054	0.0963	0.0963	0.3362			
Pyrrhotite (Fe ₇ S ₈)	Monoclinic	4	2.4485	0.0844	Tokonami et al., 1972	ave	2.4465	2.4481	2.4559	2.4435						
						stdv	0.1150	0.0861	0.0948	0.0550						
Marcasite	Orthorhombic	1	2.2439	0.0104	Buerger, 1937	ave	2.2439									
						stdv	0.0104									
Hematite	Trigonal	1	2.0309	0.0934	Finger and Hazen, 1980	ave	2.0309									
						stdv	0.0934									
Ferrihydrite	Trigonal	1	2.0830	0.1452	Drits et al., 1993	ave	2.0830									
						stdv	0.1452									
Goethite	Orthorhombic	1	2.0218	0.0750	Szytuła et al., 1968	ave	2.0218									
						stdv	0.0750									
Jarosite	Trigonal	1	1.9995	0.0361	Kato and Miura, 1977	ave	1.9995									
						stdv	0.0361									
Melanterite	Monoclinic	2	2.1228	0.0415	Peterson, 2003	ave	2.1157	2.1298								
						stdv	0.0426	0.0431								
Schwertmannite	Triclinic	10	2.0326	0.0815	Fernandez-Martinez et al., 2010	ave	2.0201	2.0558	2.0117	2.0244	2.0459	2.0120	2.0116	2.0240	2.0608	2.0602
						stdv	0.1063	0.0447	0.0340	0.1022	0.1416	0.0417	0.0277	0.0936	0.0720	0.1108

Appendix C

Supplementary Material for Chapter 4

Major ion chemistry and calcium isotopic composition of waste rock and porewater in calcite-dominant and calcite-depleted systems

Plagioclase composition

Plagioclase grains were analyzed by electron-probe microanalysis (EPMA) at the University of Ottawa (Ottawa, Canada) for potassium [K], calcium [Ca], sodium [Na], aluminum [Al], manganese [Mn], iron [Fe], titanium [Ti], barium [Ba], magnesium [Mg], and silicon [Si]. Standards included sanidine [KAlSi_3O_8], diopside [$\text{CaMgSi}_2\text{O}_6$], albite [$\text{NaAlSi}_3\text{O}_8$], tephroite [Mn_2SiO_4], hematite [Fe_2O_3], rutile [TiO_2], and sanbornite [$\text{Ba}_2\text{Si}_4\text{O}_{10}$].

Plagioclase and alkali feldspar grains were measured by EPMA in one freshly blasted and two historical samples to determine the Ca and Na components in the plagioclase solid solution series {end members albite [$\text{Na}(\text{AlSi}_3\text{O}_8)$] and anorthite [$\text{Ca}(\text{Al}_2\text{Si}_2\text{O}_8)$]}, and the K-Na components in the alkali feldspar solid solution series {end members orthoclase [KAlSi_3O_8] and albite}. The majority of the grains measured by EPMA had intermediate plagioclase compositions, with median mineral formulae in the historical and freshly blasted samples of [$\text{Na}_{0.74}\text{Ca}_{0.23}\text{Al}_{1.23}\text{Si}_{2.8}\text{O}_8$] (n=24), and [$\text{Na}_{0.77}\text{Ca}_{0.21}\text{Al}_{1.21}\text{Si}_{2.8}\text{O}_8$] (n=37), respectively. Approximately one third of the measured plagioclase grains in each sample had an albite composition with median mineral formulae for grains with $\text{Na} > 0.9$ of [$\text{Na}_{0.91}\text{Ca}_{0.04}\text{Al}_{1.1}\text{Si}_3\text{O}_8$] (n=12), and [$\text{Na}_{0.91}\text{Ca}_{0.02}\text{Al}_{1.1}\text{Si}_3\text{O}_8$] (n=20) for historical, and freshly blasted waste-rock samples, respectively. This ratio of albite:plagioclase is similar to the MLA-calculated modal mineralogy for the historical samples but is slightly higher than for the freshly blasted sample. Potassium [K] in feldspar was also investigated. The feldspar grains measured by EPMA (n= 56 for historical samples, none in freshly blasted sample) had a median composition of [$\text{K}_{0.93}\text{Na}_{0.04}\text{AlSi}_3\text{O}_8$], with most grains (n=31) having $\text{K} > 0.9$.

Figures

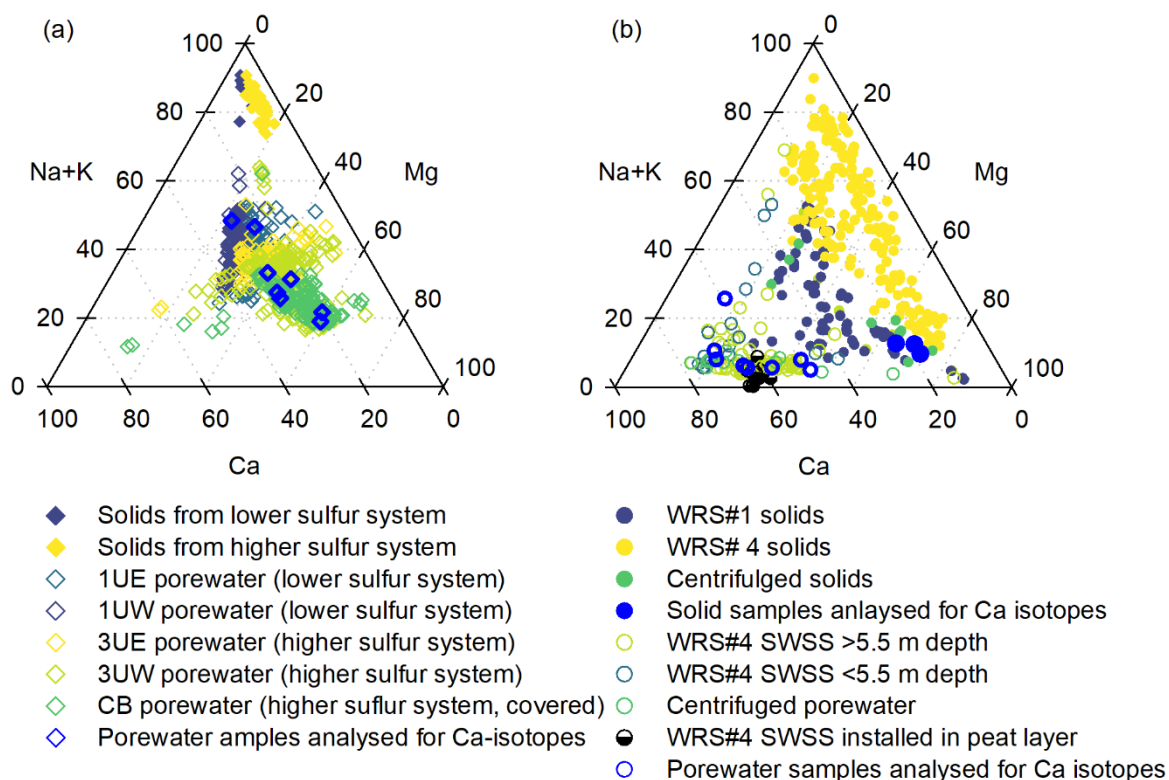


Figure C-1: Ternary diagrams by waste-rock system for (a) Diavik waste rock and porewater and (b) Detour waste rock and porewater. Higher metasediment systems in the Diavik waste rock contain higher sulfur concentrations.

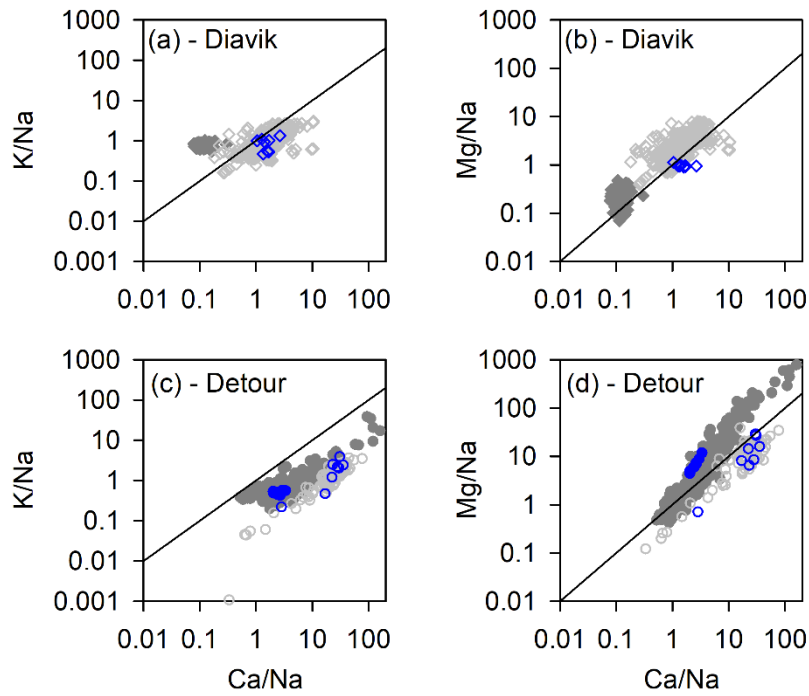


Figure C-2: Ratios of K/Na and Mg/Na vs. Ca/Na for Diavik and Detour datasets. Open light-grey symbols indicate porewater samples, solid dark grey symbols indicate solid samples, blue open symbols indicate porewater samples analyzed for Ca-isotope values and solid blue symbols indicate solid samples analyzed for Ca-isotope values. Lines plotted at 1:1. Diavik solid samples were not exposed to ambient conditions prior to analysis and have no observable trend. Detour solid samples were recovered from *in situ* waste-rock pile and the distributions indicate increasing K/Na and Mg/Na ratios with increasing Ca/Na ratios, suggesting ongoing weathering.

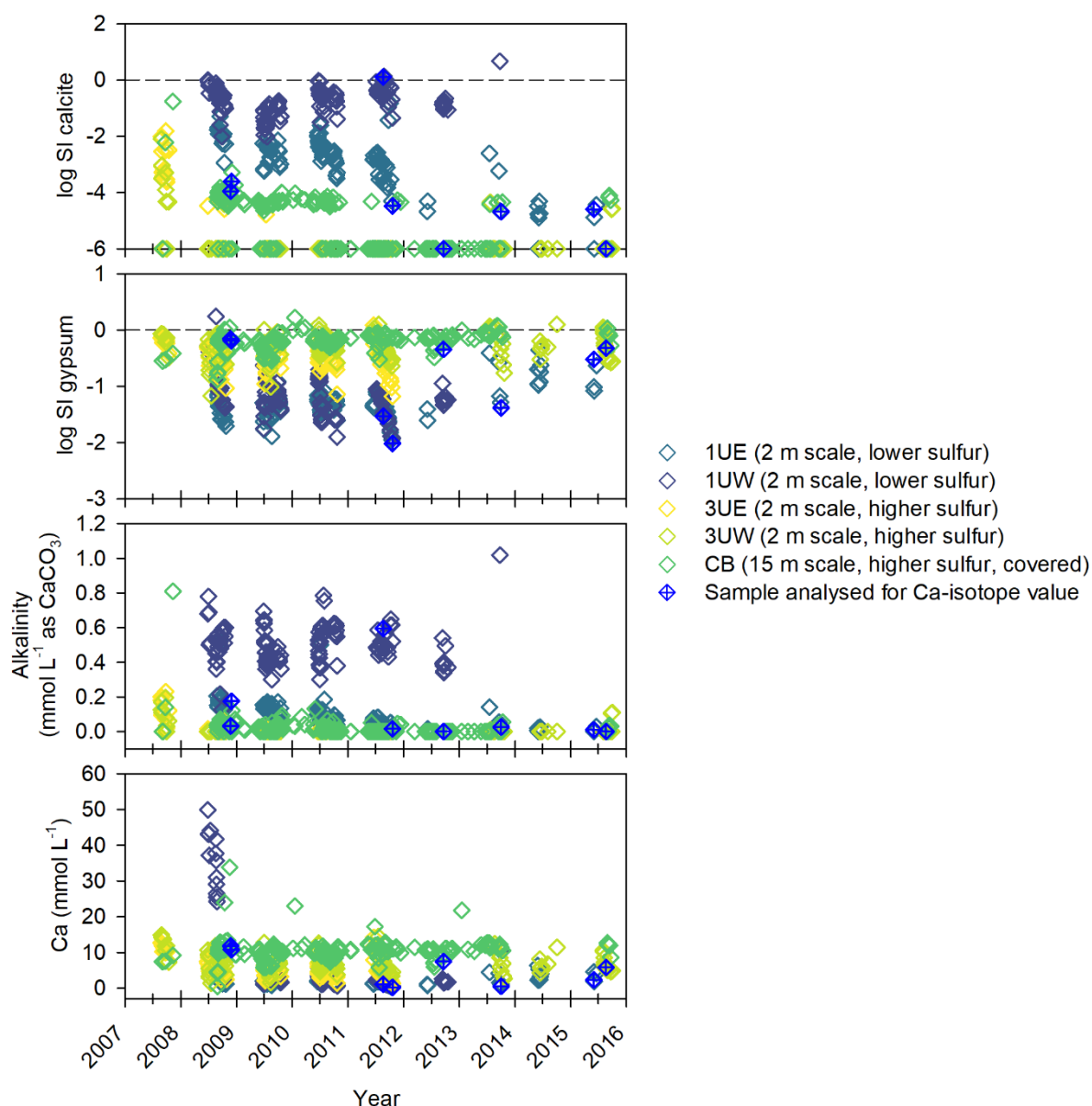


Figure C-3: Time series for Diavik porewater samples collected from 2 m scale experiments and a 15 m scale experiment. Alkalinity and calcium (Ca) concentrations from experiments from 2007 to 2011 previously reported by Bailey (2013), Bailey et al. (2016) and Hannam (2012). Calculated saturation indices from 2007 – 2011 also reported but re-calculated for this study; re-calculated saturation indices (as log SI calcite and log SI gypsum) presented here. All data from 2012 to 2016 inclusive have not been previously published. Calcite saturation indices for samples with alkalinity = 0 mmol L⁻¹ as CaCO₃ are plotted at log SI calcite = -6.

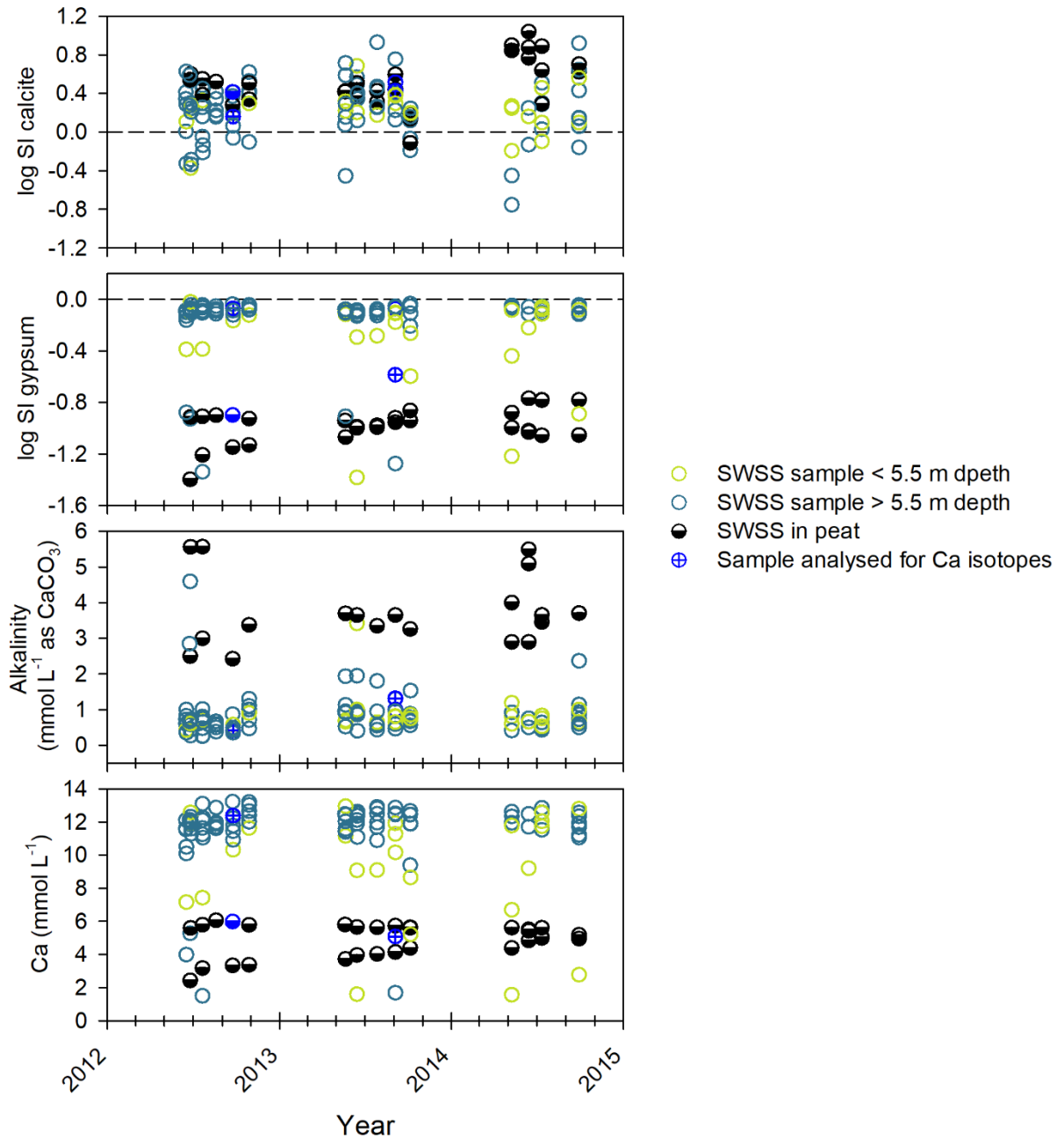


Figure C-4: Time series for Detour porewater samples collected from soil-water soliton samplers (SWSS) installed in WRS#4. Data previously reported by McNeill (2016). Concentrations of alkalinity and calcium (Ca) converted to mmol L⁻¹ for this study. Saturation indices of calcite and gypsum calculated for this study.

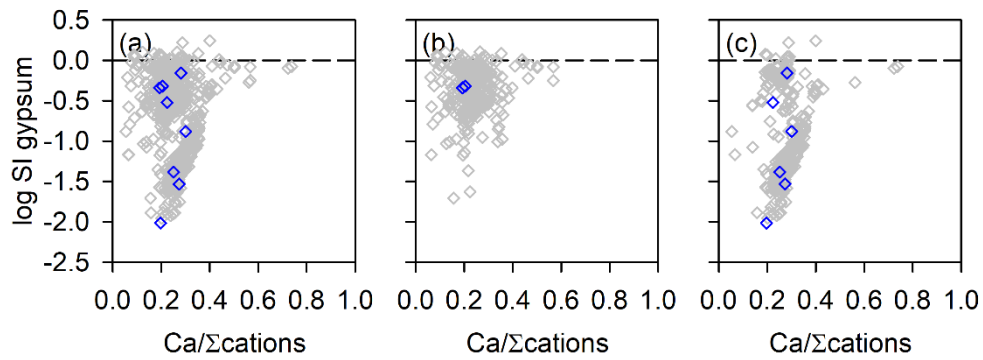


Figure C-5: Calculated saturation indices of gypsum for (a) full Diavik porewater dataset (b) Diavik porewater samples with no measurable alkalinity; (c) Diavik porewater samples with measurable alkalinity. Samples with no measurable alkalinity had slightly higher proportion of samples calculated to be saturated with respect to gypsum (n = 18 of 401 samples), compared to samples with measurable alkalinity (n = 9 of 392 samples)

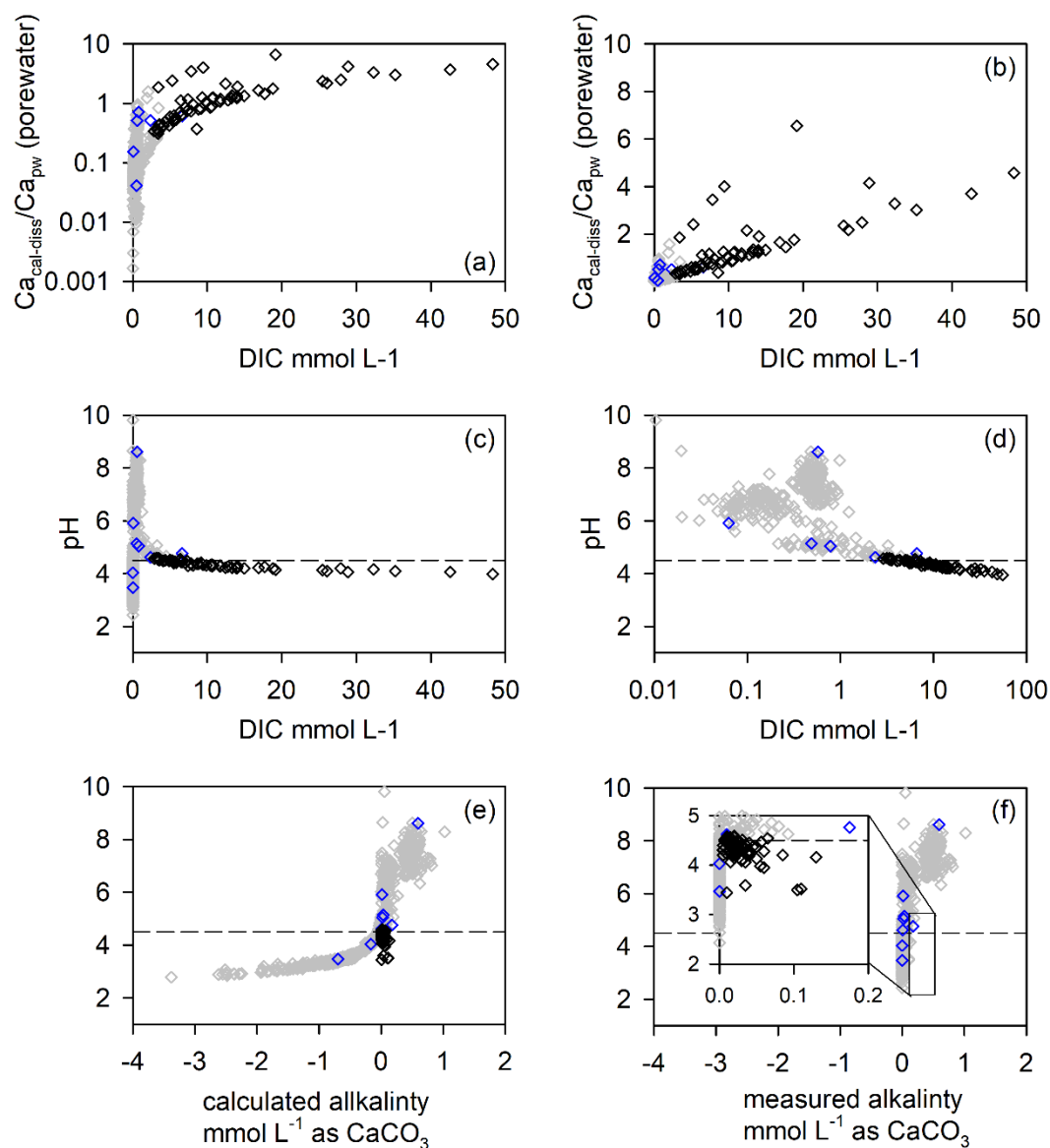


Figure C-6: Diavik porewater datasets illustrating relationships between (a) and (b) calculated carbonate contributions and calculated dissolved inorganic carbon (DIC) (log scale for y-axis in (a), linear scale in (b)); pH and calculated DIC (log scale for x-axis in (c), linear scale in (d)); (e) pH and PHREEQC-calculated alkalinity; (f) pH and measured alkalinity, with inset illustrating samples with low measured alkalinity concentrations and pH > 5. Open grey symbols indicate porewater samples, open blue symbols indicate porewater samples analyzed for Ca-isotopes; open black symbols indicate porewater samples with pH < 4.5, but with measured alkalinity concentrations.

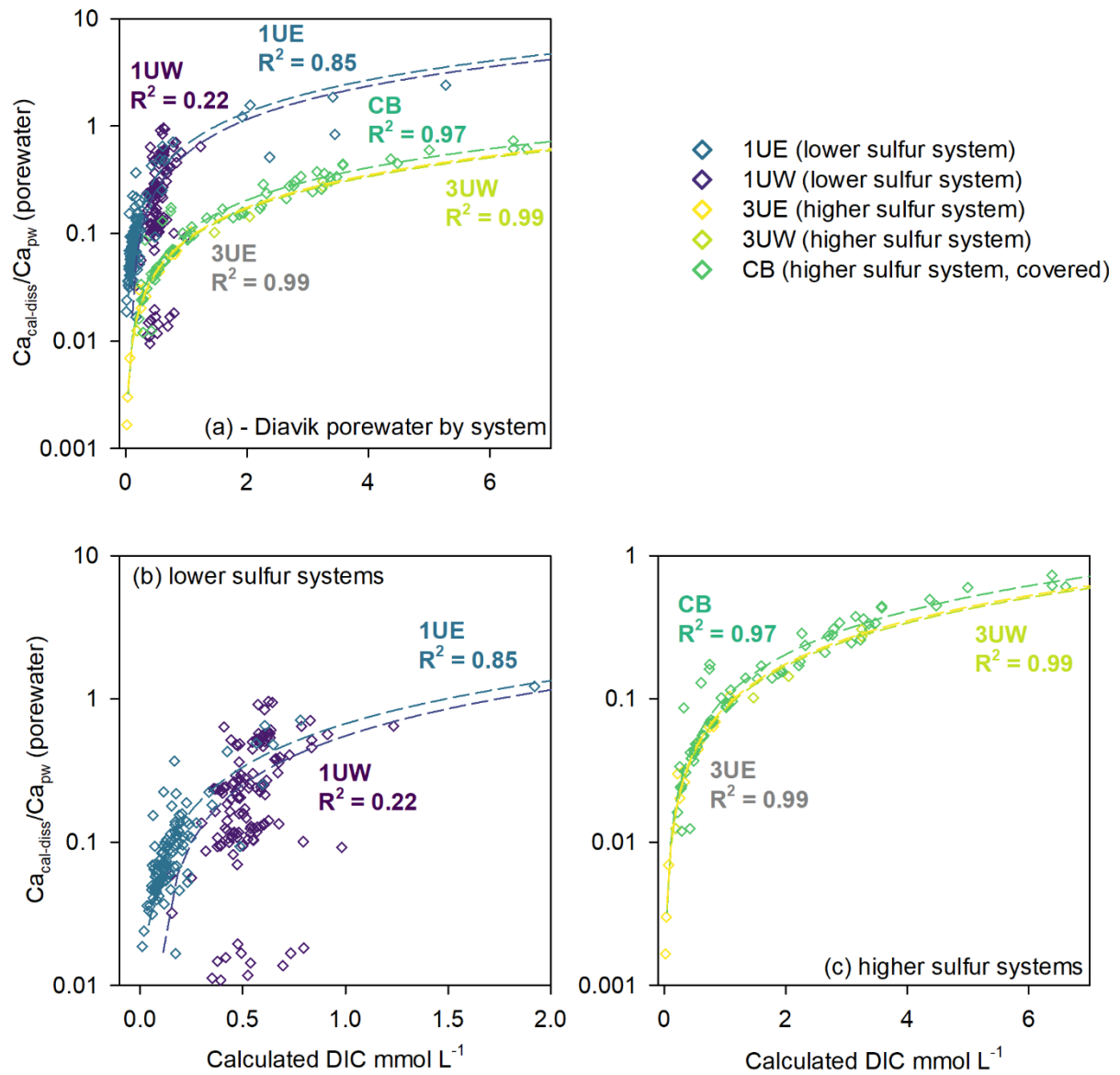


Figure C-7: Calculated regression curves for each of the five Diavik systems that comprise the full Diavik porewater dataset. (a) all five systems; (b) Systems 1UE and 1UW with lower sulfur component (note the change in scale from (a)); and (c) Systems 3UE , 3UW and CB with higher sulfur component (note the change in scale from (a)). Yellow series 3UE with grey label in (a) and (c) for clarity.

Tables

Table C-1: Electron probe microanalysis (EPMA) results for carbonate grains in weathered and fresh waste-rock samples from Detour Lake Mine. Reported as atomic proportion based on three oxygen molecules.

Sample ID	Sample type	Mineral	Ca	Sr	Fe	Mn	Mg	C	Total
2M	Weathered	Calcite	0.329	0	0	0.0003	0.0040	0.333	0.6663
2M	Weathered	Calcite	0.331	0	0.0001	0.0021	0.0005	0.333	0.6668
2M	Weathered	Calcite	0.333	0	0.0001	0.0003	0	0.333	0.6664
2M	Weathered	Calcite	0.33	0	0.001	0.0015	0.0014	0.333	0.667
2M	Weathered	Calcite	0.329	0	0.0001	0.0003	0.0043	0.333	0.6668
2M	Weathered	Calcite	0.33	0	0.0009	0.0014	0.0012	0.333	0.6665
2M	Weathered	Calcite	0.333	0	0.0002	0	0	0.333	0.6663
2M	Weathered	Calcite	0.232	0	0.0013	0.0002	0.1	0.333	0.6665
2M	Weathered	Calcite	0.333	0	0.0003	0.0001	0	0.333	0.6664
2M	Weathered	Calcite	0.326	0	0.0004	0.0001	0.0065	0.333	0.6661
3B	Weathered	Calcite	0.332	0	0.0002	0.0006	0.0006	0.333	0.6665
3B	Weathered	Calcite	0.332	0	0.0003	0.0001	0.0007	0.333	0.6661
3B	Weathered	Calcite	0.332	0	0.0001	0.0001	0.0012	0.333	0.6664
25/26	Fresh	Calcite	0.327	0	0.0021	0.0018	0.0028	0.333	0.6668
25/27	Fresh	Calcite	0.333	0	0.0001	0.0006	0.0001	0.333	0.6669
25/28	Fresh	Calcite	0.33	0	0.001	0.0002	0.0021	0.333	0.6663
25/29	Fresh	Calcite	0.327	0	0.0003	0.0001	0.0056	0.333	0.6661
090	Fresh	Dolomite	0.174	0	0.0033	0.0003	0.155	0.333	0.6657
090	Fresh	Dolomite	0.17	0	0.0002	0.0001	0.163	0.333	0.6663
090	Fresh	Dolomite	0.172	0	0.0019	0.0002	0.159	0.333	0.6662
090	Fresh	Dolomite	0.176	0	0.0022	0.0003	0.154	0.333	0.6656
090	Fresh	Dolomite	0.159	0	0.0003	0.0002	0.174	0.333	0.6665
090	Fresh	Dolomite	0.172	0	0.0007	0	0.161	0.333	0.6668
090	Fresh	Dolomite	0.169	0	0.0012	0	0.163	0.333	0.6663
090	Fresh	Calcite	0.247	0	0.0464	0.0143	0.026	0.3333	0.6666
090	Fresh	Dolomite	0.172	0	0.0002	0.0002	0.16	0.333	0.6655
090	Fresh	Dolomite	0.17	0	0.0006	0.0001	0.162	0.333	0.6658
090	Fresh	Calcite	0.333	0	0.0001	0	0	0.333	0.6662
090	Fresh	Dolomite	0.173	0	0.0003	0	0.16	0.333	0.6663
090	Fresh	Dolomite	0.172	0	0.006	0.0004	0.155	0.333	0.6665
090	Fresh	Dolomite	0.166	0	0.0017	0.0003	0.166	0.333	0.667
090	Fresh	Calcite	0.329	0	0.0012	0.0023	0.0006	0.333	0.6662
090	Fresh	Dolomite	0.177	0	0.0038	0.0002	0.152	0.333	0.6661
090	Fresh	Dolomite	0.166	0	0.0009	0	0.167	0.333	0.6669
090	Fresh	Calcite	0.319	0	0.0054	0.0054	0.0035	0.333	0.6664
090	Fresh	Calcite	0.329	0	0.0005	0.0002	0.0037	0.333	0.6664
090	Fresh	Dolomite	0.174	0	0.002	0.0002	0.157	0.333	0.6663
090	Fresh	Dolomite	0.17	0	0.0046	0.0006	0.158	0.333	0.6663
090	Fresh	Dolomite	0.169	0	0.0047	0.0006	0.16	0.333	0.6673
090	Fresh	Calcite	0.33	0	0.0004	0.0001	0.0025	0.333	0.6661
090	Fresh	Dolomite	0.17	0	0.0012	0.0003	0.162	0.333	0.6666
090	Fresh	Dolomite	0.172	0	0.0003	0.0001	0.161	0.333	0.6665

Table C-2: Linear regressions for the calculated minimum proportion of calcium derived from calcite and dolomite dissolution ($\text{Ca}_{\text{cal-diss}}/\text{Ca}_{\text{pw}}$ or $\text{Ca}_{\text{dol-diss}}/\text{Ca}_{\text{pw}}$, respectively) to the calculated dissolved inorganic carbon (DIC) concentrations for each of the Diavik waste-rock systems, and the Detour waste rock systems.

System	Linear regression	R ²	n	n > DIC = 0
1UE	$\text{Ca}_{\text{cal-diss}}/\text{Ca}_{\text{pw}} = 0.036 + (441 \times \text{DIC})$	0.85	120	114
1UW	$\text{Ca}_{\text{cal-diss}}/\text{Ca}_{\text{pw}} = -0.051 + (602 \times \text{DIC})$	0.22	138	134
3UE	$\text{Ca}_{\text{cal-diss}}/\text{Ca}_{\text{pw}} = 0.00002 + (87.6 \times \text{DIC})$	0.99	132	13
3UW	$\text{Ca}_{\text{cal-diss}}/\text{Ca}_{\text{pw}} = -0.0002 + (84.7 \times \text{DIC})$	0.99	166	5
CB	$\text{Ca}_{\text{cal-diss}}/\text{Ca}_{\text{pw}} = -0.0011 + (103 \times \text{DIC})$	0.97	183	72
Detour	$(\text{Ca}_{\text{cal-diss}} = -0.0052 + (90.3 \times \text{Ca}_{\text{cal-diss}}))$	0.95	135	135
Detour	$\text{Ca}_{\text{dol-diss}}/\text{Ca}_{\text{pw}} = -0.0026 + (90.2 \times \text{Ca}_{\text{dol-diss}})$	0.95	135	135

Appendix D
Supplementary Material for Chapter 5

**Secondary minerals and trace element reservoirs in weathered waste rock:
Integration of quantitative mineralogy and conventional mineralogical
techniques**

Figures

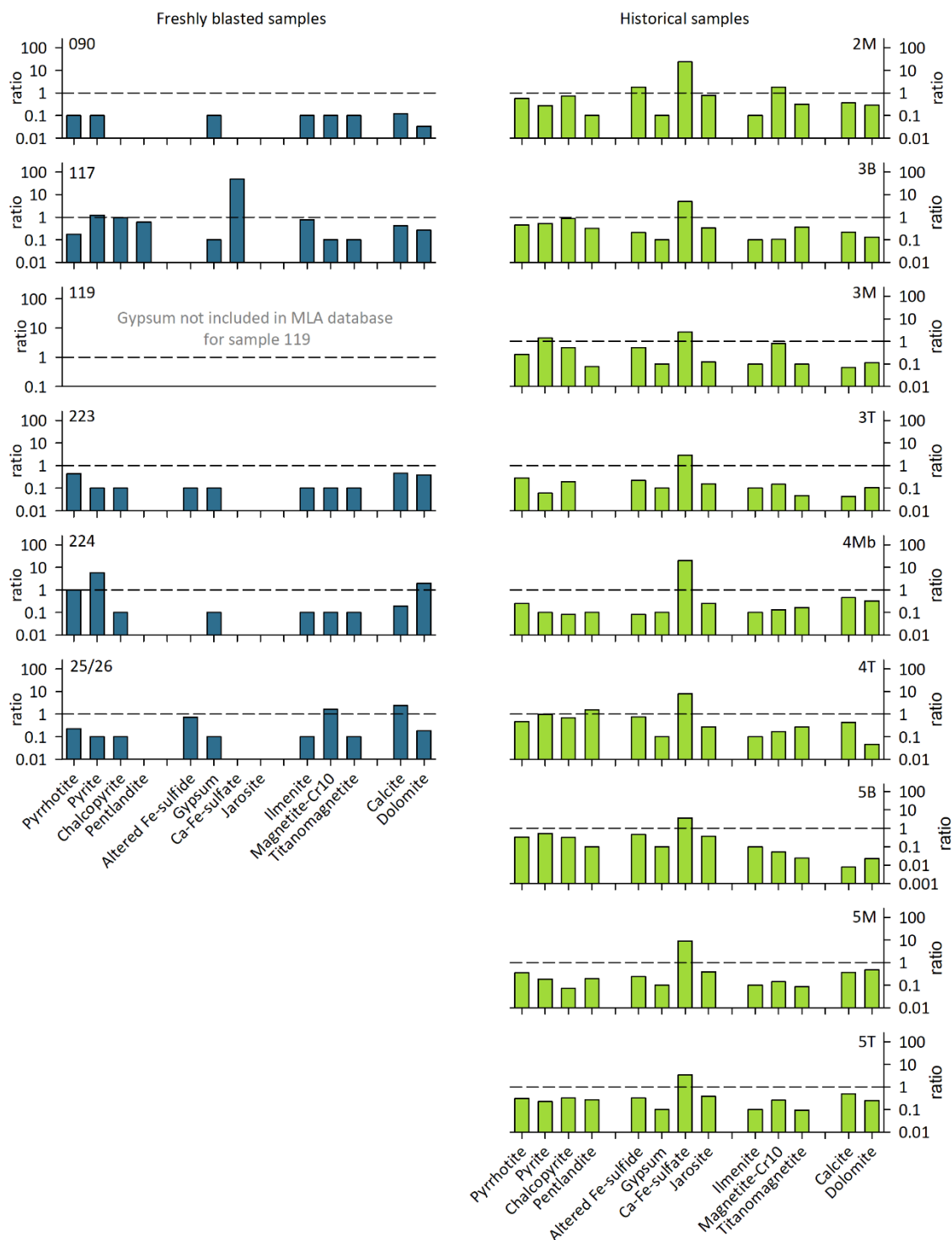


Figure D-1: Mineral associations with gypsum. Minerals with < 0.01 wt% modal abundances not included in association calculations. Y-axes scale (calculated association ratio) to 250.

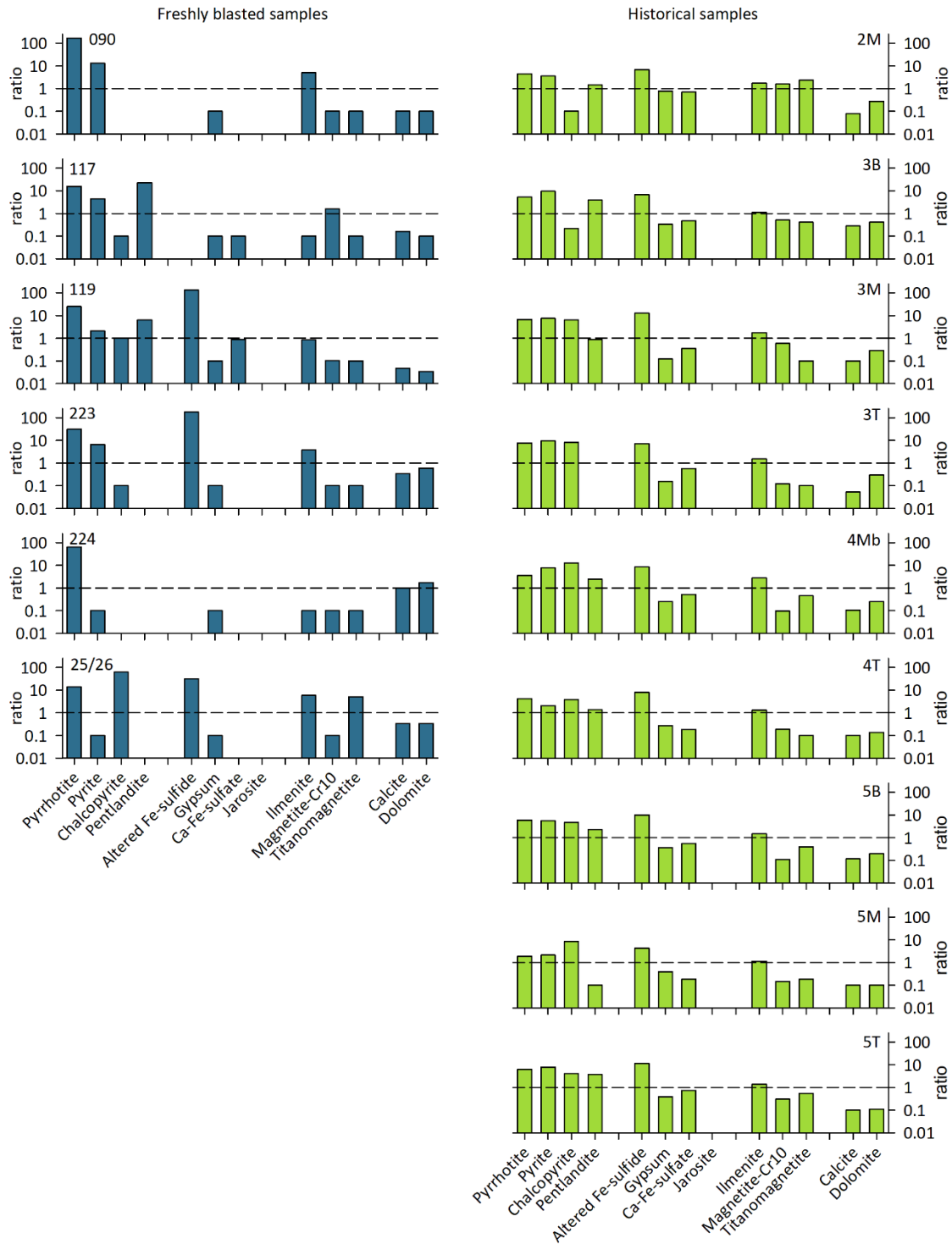
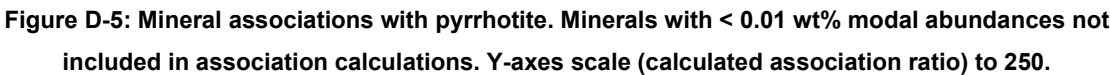


Figure D-3: Mineral associations with jarosite. Minerals with < 0.01 wt% modal abundances not included in association calculations. Y-axes scale (calculated association ratio) to 250.



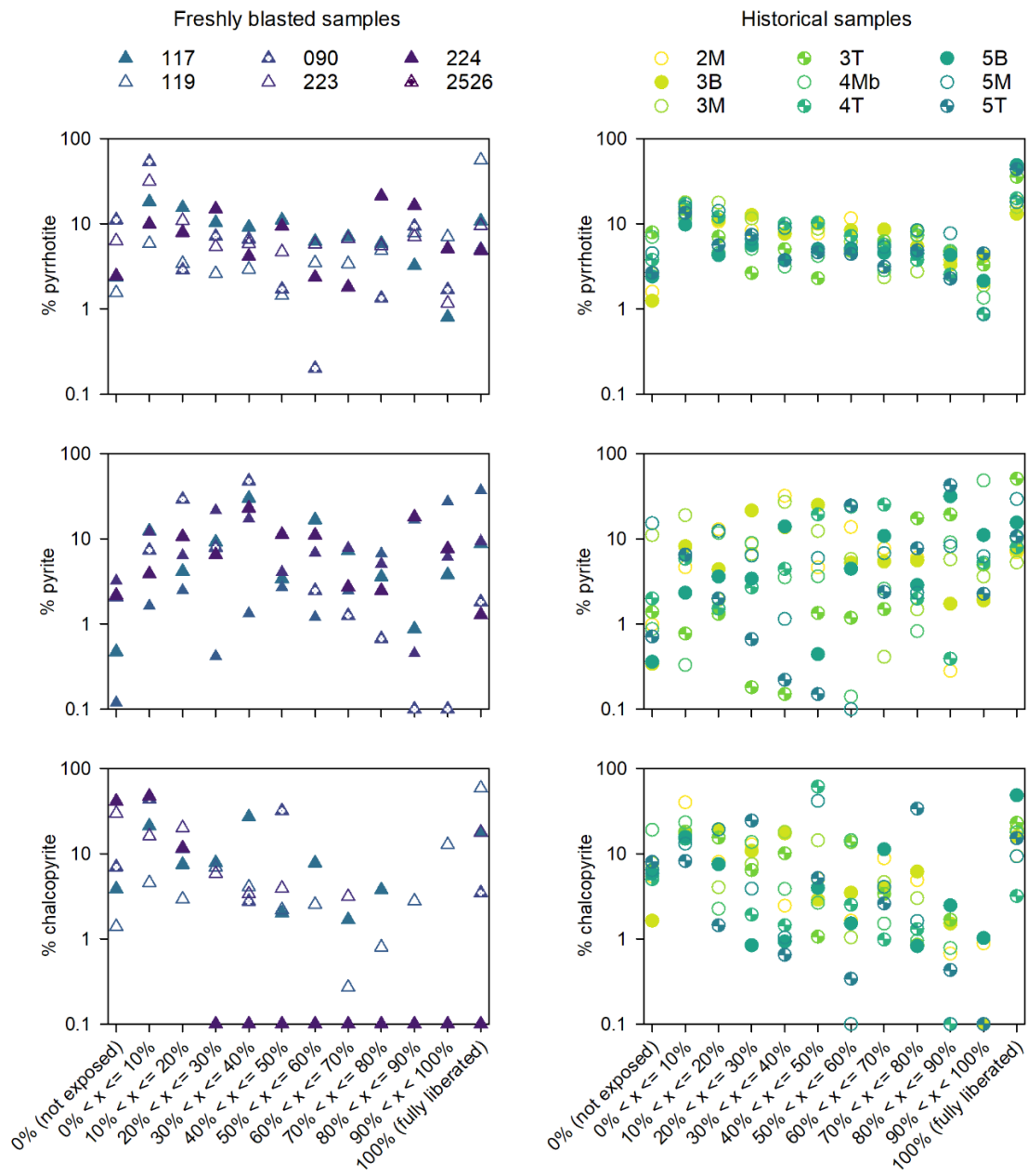


Figure D-6: Sulfide mineral liberation calculated by mineral liberation analysis (MLA).

Table D-1: Trace sulfide modal mineralogies calculated from four-acid digestion concentrations. Calculation verifications using MLA-provided pyrrhotite, pyrite, gypsum and jarosite modal mineralogies compared to sulfur [S] concentrations measured by induction furnace [IF]. All concentrations in wt%. Modal mineralogies <0.01 wt %, presented in italics, are considered estimates but were maintained at MLA-reported values for calculations. Jarosite* indicates modal mineralogies taken from the yavapaiite modal mineralogies, with the jarosite mineral formula applied. “n.a.” denotes “not analyzed”.

Mineral	MLA database formula or element	117	119	090	223	224	25-26	2M	3B	3M	3T	4MB	4T	5B	5M	5T
Mineral abundance calculated by MLA; MLA database formulae provided																
Pentlandite	$\text{Fe}^{(2+)}_{4.5}\text{Ni}_{4.5}\text{S}_8$	0.08	0.11	0.0001	0.0001	0.0009	0.0003	0.03	0.03	0.03	0.01	0.013	0.03	0.04	0.013	0.03
Chalcopyrite	$\text{CuFe}^{(2+)}\text{S}_2$	0.11	0.33	<i>0.008</i>	0.02	<i>0.007</i>	0.012	0.14	0.27	0.16	0.11	0.09	0.23	0.27	0.17	0.18
Sphalerite	ZnS	<i>0.009</i>	<i>0.009</i>	<i>0.002</i>	<i>0.005</i>	<i>0.002</i>	<i>0.0003</i>	<i>0.0010</i>	<i>0.0002</i>	<i>0.005</i>	<i>0</i>	<i>0.0005</i>	<i>0.00006</i>	<i>0.001</i>	<i>0.00005</i>	<i>0.001</i>
Pyrite	$\text{Fe}^{(2+)}\text{S}_2$	0.71	0.59	0.28	0.42	0.44	0.04	0.88	0.56	0.15	0.36	0.53	0.42	0.91	0.04	0.46
Pyrrhotite	$\text{Fe}^{(2+)}_{0.95}\text{S}$	2.04	3.74	0.08	0.45	0.34	0.13	2.58	1.94	1.00	0.24	0.33	0.98	1.08	0.63	1.05
Gypsum	$\text{CaSO}_4 \cdot 2\text{H}_2\text{O}$	0.12	n.a.	0.03	0.05	0.08	0.06	0.24	0.17	2.87	6.65	1.15	3.36	3.10	4.21	2.65
Jarosite*	$\text{KFe}^{(3+)}_3(\text{SO}_4)_2(\text{OH})_6$	<i>0.007</i>	0.06	<i>0.002</i>	<i>0.005</i>	<i>0.001</i>	<i>0.005</i>	0.16	0.15	0.15	0.20	0.37	0.27	0.13	0.58	0.20
Trace element concentrations measured by four-acid digestion																
	Ni	642	n.a.	33	50	n.a.	44.9	448.3	644.2	699.9	n.a.	n.a.	1486.0	n.a.	1634.9	563.7
	Cu	429	n.a.	62	138	n.a.	112	765	1806	740	n.a.	n.a.	925	n.a.	1052	774
	Zn	196	n.a.	38.3	67.0	n.a.	38.7	112	123	106	n.a.	n.a.	158	n.a.	185	105
Total sulfur measured by induction furnace																
	S	1.29	1.45	0.12	0.55	n.a.	0.12	1.52	1.88	1.32	n.a.	n.a.	1.72	n.a.	2.00	1.38
Maximum trace sulfide abundance calculated from four-acid digestion concentrations																
Pentlandite	$\text{Fe}^{(2+)}_{4.5}\text{Ni}_{4.5}\text{S}_8$	0.20	n.a.	0.010	0.016	n.a.	0.014	0.14	0.20	0.22	n.a.	n.a.	0.46	n.a.	0.51	0.18
Chalcopyrite	$\text{CuFe}^{(2+)}\text{S}_2$	0.12	n.a.	0.018	0.040	n.a.	0.032	0.22	0.52	0.21	n.a.	n.a.	0.27	n.a.	0.30	0.22
Sphalerite	ZnS	0.029	n.a.	0.006	0.010	n.a.	0.006	0.017	0.018	0.016	n.a.	n.a.	0.024	n.a.	0.027	0.016
Sulfur concentrations attributed to calculated trace sulfides																
Pentlandite	S	0.07	n.a.	0.003	0.005	n.a.	0.005	0.05	0.07	0.07	n.a.	n.a.	0.15	n.a.	0.17	0.06
Chalcopyrite	S	0.04	n.a.	0.006	0.014	n.a.	0.011	0.08	0.18	0.07	n.a.	n.a.	0.09	n.a.	0.11	0.08
Sphalerite	S	0.010	n.a.	0.002	0.003	n.a.	0.002	0.005	0.006	0.005	n.a.	n.a.	0.008	n.a.	0.009	0.005

Cont'd																
Mineral	MLA database formula or element	117	119	090	223	224	25-26	2M	3B	3M	3T	4MB	4T	5B	5M	5T
Sulfur concentrations attributed to MLA-provided modal mineralogies																
Pyrrhotite	S	0.77	n.a.	0.031	0.171	n.a.	0.049	0.97	0.73	0.38	n.a.	n.a.	0.37	n.a.	0.24	0.40
Pyrite	S	0.38	n.a.	0.150	0.224	n.a.	0.022	0.47	0.30	0.08	n.a.	n.a.	0.22	n.a.	0.02	0.25
Gypsum	S	0.02	n.a.	0.005	0.009	n.a.	0.011	0.05	0.46	0.54	n.a.	n.a.	0.63	n.a.	0.78	0.49
Jarosite*	S	0.0009	n.a.	0.0002	0.0006	n.a.	0.0006	0.021	0.020	0.019	n.a.	n.a.	0.034	n.a.	0.074	0.026
Mass balance check																
Total attributed S from calculations		1.29	n.a.	0.20	0.43	n.a.	0.10	1.64	1.76	1.16	n.a.	n.a.	1.51	n.a.	1.41	1.30
Residual ([S from IF] - [S from calculations])		-0.004	n.a.	-0.080	0.13	n.a.	0.023	-0.12	0.12	0.16	n.a.	n.a.	0.21	n.a.	0.59	0.08

Bulk chemical composition

Whole rock analysis (WRA) by lithium metaborate fusion with ICP-MS finish, and total sulfur [S] and total carbon [C] analyses by induction furnace were conducted by SGS Canada (Burnaby, Canada).

Concentrations of major elements calculated by MLA were typically within a factor of two measured by WRA (converted from oxide to elemental concentrations; Table D-1; Table D-2). There were no systematic positive or negative biases between MLA results and WRA, or between the freshly blasted samples and the historical waste rock samples. However, some individual elements were either over- or under-predicted by MLA-calculations. Differences in MLA-calculated and measured concentrations may be an artefact of subsampling, and therefore different mineral distributions analyses by each method, though care was taken to apply accepted sub-sampling methods (coning and quartering). The concentrations of silicon [Si] are consistent. The differences in the remaining major cations appear to be an artefact of MLA-assigned mineral formulae, particularly for minerals with solid solution series. In these samples, key mineral phases with solid solution series with major elements include feldspars (plagioclase and alkali), amphiboles, micas, pyroxenes and chlorite.

Table D-1: MLA-calculated assay for carbon [C], sulfur [S], and the major cations associated with silicate minerals in the samples in this study: calcium [Ca], sodium [Na], potassium [K], iron [Fe], magnesium [Mg], silicon [Si], and aluminum [Al].

	MLA Ca (wt%)	MLA Na (wt%)	MLA K (wt%)	MLA Fe (wt%)	MLA Mg (wt%)	MLA Si (wt%)	MLA Al (wt%)
<i>Freshly blasted</i>							
090	6.76	0.98	1.40	2.11	2.81	29.5	6.39
117	6.25	0.33	0.67	10.2	8.17	20.3	5.21
119	5.25	0.46	0.60	10.5	7.40	21.1	5.52
223	8.50	0.91	1.30	3.31	2.48	27.1	6.32
224	6.32	0.98	1.48	4.05	2.78	28.5	6.80
25-26	5.74	1.04	1.45	2.41	1.93	31.0	6.45
<i>Historical</i>							
2M	6.27	0.52	0.76	11.6	5.67	21.8	5.61
3B	5.83	0.45	0.75	12.2	5.06	21.9	5.62
3M	5.87	0.51	0.78	11.2	5.42	22.5	5.42
3T	6.36	0.55	0.98	8.79	4.80	23.0	5.43
4Mb	5.41	0.59	1.32	8.79	5.45	24.2	5.91
4T	5.82	0.36	0.96	13.4	6.86	19.5	5.36
5B	5.20	0.51	0.89	9.42	5.61	23.4	5.53
5M	5.29	0.43	0.87	12.3	6.24	20.9	5.14
5T	5.40	0.55	1.00	9.16	5.61	23.4	5.79

Table D-2: Whole rock analysis [WRA] of the major cations associated with silicate minerals in the samples in this study: calcium [Ca], sodium [Na], potassium [K], iron [Fe], magnesium [Mg], silicon [Si], and aluminum [Al]. WRA results converted from reported as oxides (wt%) to elemental concentrations for direct comparison to MLA-calculated assay. “n.a.” denotes not analyzed.

	WRA Ca (wt%)	WRA Na (wt%)	WRA K (wt%)	WRA Fe (wt%)	WRA Mg (wt%)	WRA Si (wt%)	WRA Al (wt%)
<i>Freshly blasted</i>							
090	5.52	2.05	1.83	2.18	2.26	30.4	5.82
117	4.90	0.57	0.56	8.32	9.29	16.4	4.38
119	3.05	0.95	0.53	7.41	9.41	22.9	4.23
223	6.85	1.77	1.38	3.97	2.23	28.2	5.82
224	n.a.	n.a.	n.a.	n.a.	n.a.	n.a.	n.a.
25-26	4.07	2.03	1.58	2.63	1.92	31.3	5.72
<i>Historical</i>							
2M	4.20	0.92	0.71	9.16	7.18	17.6	5.35
3B	3.94	0.91	0.65	9.86	6.75	24.1	5.45
3M	n.a.	n.a.	n.a.	n.a.	n.a.	n.a.	n.a.
3T	4.31	1.19	0.98	7.76	5.55	22.9	4.84
4Mb	3.26	1.20	1.09	7.20	6.15	24.6	5.25
4T	3.74	0.73	0.69	9.79	8.99	16.9	5.10
5B	3.34	1.02	0.77	7.90	6.33	23.5	4.89
5M	3.29	0.82	0.79	9.37	7.54	21.3	4.67
5T	3.18	1.00	0.87	7.48	6.27	23.1	4.91

Table D-3: Results of whole rock analysis by lithium metaborate fusion with ICP-finish. Conducted by SGS (Burnaby, Canada), method code ICP95A.

	Al ₂ O ₃ %	Ba %	CaO %	Cr ₂ O ₃ %	Fe ₂ O ₃ %	K ₂ O %	MgO %	MnO %	Na ₂ O %	Nb %	P ₂ O ₅ %	SiO ₂ %	Sr %	TiO ₂ %	Y %	Zn ppm	Zr %	LOI %
LOD	0.01	0.001	0.01	0.01	0.01	0.01	0.01	0.01	0.01	0.001	0.01	0.01	0.001	0.01	0.001	5	0.001	-10
<i>Freshly blasted</i>																		
090	11.0	0.047	7.72	0.02	3.12	2.2	3.75	0.05	2.76	<0.001	0.10	65.0	0.025	0.35	0.001	36	0.018	7.14
117	8.00	0.009	6.85	0.37	11.9	0.67	15.4	0.16	0.77	0.001	0.05	35.0	0.007	0.46	<0.001	178	0.004	6.69
119	8.0	0.015	4.27	0.39	10.6	0.64	15.6	0.14	1.28	0.002	0.04	49.0	0.010	0.34	0.001	183	0.007	6.01
223	11.0	0.032	9.58	0.02	5.67	1.66	3.70	0.10	2.38	0.001	0.08	60.3	0.020	0.41	0.001	54	0.011	6.53
25-26	10.8	0.039	5.70	0.02	3.76	1.9	3.18	0.06	2.74	<0.001	0.07	66.9	0.021	0.31	<0.001	32	0.014	4.18
<i>Historical</i>																		
2M	10.1	0.017	5.87	0.22	13.1	0.85	11.9	0.14	1.24	0.002	0.08	37.7	0.010	0.47	0.001	115	0.008	5.22
3B	10.3	0.017	5.51	0.22	14.1	0.78	11.2	0.14	1.22	0.001	0.07	51.6	0.010	0.44	0.001	121	0.007	6.26
3T	9.14	0.023	6.03	0.21	11.1	1.18	9.21	0.09	1.60	0.001	0.09	49.0	0.015	0.35	<0.001	86	0.010	7.37
4Mb	9.92	0.025	4.56	0.23	10.3	1.31	10.2	0.12	1.62	0.002	0.09	52.7	0.017	0.46	<0.001	78	0.010	6.11
4T	9.63	0.015	5.24	0.32	14	0.83	14.9	0.18	0.98	0.001	0.10	36.1	0.011	0.52	0.001	159	0.007	7.74
5B	9.24	0.019	4.68	0.24	11.3	0.93	10.5	0.12	1.37	0.002	0.07	50.3	0.013	0.43	0.001	106	0.008	6.63
5M	8.83	0.019	4.60	0.28	13.4	0.95	12.5	0.15	1.10	0.001	0.08	45.6	0.009	0.37	0.001	175	0.006	8.90
5T	9.28	0.021	4.45	0.26	10.7	1.05	10.4	0.1	1.35	0.001	0.09	49.5	0.016	0.36	0.001	98	0.008	6.60
Duplicates																		
2M																		5.34
4T	9.92	0.015	5.11	0.32	13.9	0.83	15.1	0.17	0.96	0.001	0.10	38.4	0.008	0.5	0.001	150	0.006	-
119																		6.04
3T	9.24	0.025	6.06	0.20	11.5	1.17	9.27	0.09	1.47	0.002	0.10	49.4	0.014	0.35	0.001	75	0.010	-
QC																		
SY-4	20.2	0.034	7.84	<0.01	6.09	1.64	0.54	0.11	6.94	0.001	0.13	50.1	0.115	0.28	0.012	93	0.056	-
OREAS 70B																		6.87
SY-4	20.1	0.033	7.78	<0.01	6.09	1.65	0.51	0.1	7.02	0.002	0.13	49.5	0.119	0.28	0.011	100	0.055	-
OREAS 70B																		6.29
Recommended values	20.69	0.034	8.05	<0.01	6.21	1.66	0.54	0.108	7.1	0.001	0.131	49.9	0.119	0.287	0.012	93	0.052	6.69

Table D-4: Results of four-acid digestion conducted at AGAT Laboratories (Mississauga, ON), with analysis by ICP-MS and ICP-OES at the University of Waterloo.

	Al wt%	Ca wt%	Fe wt%	K wt%	Mg wt%	Na wt%	S wt%	Ti wt%	Fe wt%	Li mg kg ⁻¹	Be mg kg ⁻¹	B mg kg ⁻¹	Si mg kg ⁻¹	P mg kg ⁻¹	V mg kg ⁻¹	Cr mg kg ⁻¹	Mn mg kg ⁻¹
<i>Freshly blasted</i>																	
090	5.12	5.17	2.07	1.62	2.08	1.91	0.22	0.19	2.07	15	0.9	<1.6	44	401	51	43	392
117	3.97	4.91	8.07	0.53	9.42	0.57	1.01	0.25	8.07	17	0.3	<0.5	78	199	68	1860	1160
223	5.13	6.33	3.91	1.30	2.11	1.66	0.58	0.23	3.91	19	0.7	<0.5	48	372	93	78	762
25/26	5.03	3.84	2.52	1.50	1.75	1.81	0.20	0.16	2.52	12	0.8	<1.6	65	307	53	79	404
<i>Historical</i>																	
2M	4.59	3.82	8.48	0.63	6.50	0.88	1.22	0.25	8.48	23	0.4	<0.5	73	324	86	1100	103
3B	4.66	3.78	9.00	0.59	6.01	0.85	1.62	0.23	9.00	22	0.5	<0.5	88	273	78	1160	985
3M	4.43	3.31	8.21	0.74	6.45	0.91	1.20	0.22	8.21	19	0.5	<0.5	84	304	50	1370	877
4B	4.56	2.98	5.32	1.08	5.02	1.38	0.61	0.17	5.32	16	0.7	<1.6	104	314	22	1020	694
4T	4.48	3.51	9.46	0.66	8.41	0.69	1.43	0.27	9.46	30	0.4	<1.6	165	430	59	1650	1260
5M	4.22	2.96	9.20	0.73	7.08	0.76	1.59	0.21	9.20	22	0.5	<0.5	76	341	31	1490	1180
5T	4.48	3.21	7.63	0.78	6.73	0.98	1.19	0.20	7.63	18	0.5	<0.5	87	298	41	1310	764
6T	4.85	3.55	7.16	1.06	2.12	1.49	1.39	0.21	7.16	16	0.6	<1.6	69	302	90	174	568
cont'd	Co mg kg ⁻¹	Ni mg kg ⁻¹	Cu mg kg ⁻¹	Zn mg kg ⁻¹	As mg kg ⁻¹	Se mg kg ⁻¹	Sr mg kg ⁻¹	Mo mg kg ⁻¹	Ag mg kg ⁻¹	Cd mg kg ⁻¹	Sn mg kg ⁻¹	Sb mg kg ⁻¹	Cs mg kg ⁻¹	Ba mg kg ⁻¹	Tl mg kg ⁻¹	Pb mg kg ⁻¹	U mg kg ⁻¹
<i>Freshly blasted</i>																	
90	10	33	62	38	1.6	<2.2	293	0.6	0.2	0.1	3.1	0.2	1.3	453	0.3	13	0.9
117	86	642	429	196	6.7	<2.2	92	2.4	0.9	1.0	2.6	0.2	1.2	88	0.2	8.7	0.2
223	25	50	138	67	18	<2.2	243	1.5	0.3	0.2	2.4	0.2	1.0	319	0.3	14	0.6
25/26	15	45	112	39	2.2	<2.2	249	0.6	0.2	0.1	2.5	0.7	0.9	396	0.3	14	0.6
<i>Historical</i>																	
2M	92	448	765	112	6.6	2.3	119	0.8	0.9	0.3	2.9	0.4	1.3	155	0.2	9.6	0.4
3B	108	644	1800	123	6.3	2.7	126	1.1	1.9	0.5	2.7	0.6	1.2	169	0.2	8.0	0.5
3M	90	700	740	106	5.0	2.4	123	0.9	1.0	0.3	2.7	0.4	1.3	204	0.2	12	0.5
4B	59	371	404	73	6.8	<2.2	194	0.7	0.5	0.3	2.1	0.5	1.4	297	0.2	9.3	0.5
4T	205	1490	925	158	7.9	2.7	102	1.0	0.8	0.6	2.4	1.5	3.8	148	0.2	5.7	0.5
5M	201	1640	1050	185	5.9	2.8	133	0.8	1.3	0.7	3.6	0.4	2.8	179	0.2	7.6	0.5
5T	74	564	774	105	5.0	<2.2	136	1.1	0.7	0.3	2.3	0.4	1.7	223	0.2	8.6	0.6
6T	33	80	778	56	5.5	2.3	192	0.8	1.0	0.1	7.2	0.3	1.1	287	0.2	9.3	0.4

Table D-5: Trace-element concentrations in MLA mineral formulae, and calculated trace element concentrations from EPMA measurements (as median values) applied to MLA mineral abundance. Median EPMA concentrations from sample 117 was applied to MLA samples 117 and 119; EPMA concentrations from 090 was applied to 090, 223, 224 and 25-26; and the median EPMA concentrations from all historical samples analyzed by EPMA (2M, 3B, 4T, 5M) were applied to the historical samples 2M, 3B, 3M, 3T, 4Mb, 4T, 5B, 5M and 5T analyzed by MLA. All concentrations in ppm of waste-rock fraction < 425 µm– i.e., [mg trace element] [kg < 425 µm fraction of waste rock]⁻¹. Sphalerite concentrations are considered estimates because sphalerite modal abundances were < 0.01 wt% in all samples. Cells with “-” indicate measurements were non-detect. * denotes sphalerite abundances considered estimates.

Mineral	MLA database formula or element	117	119	090	223	224	25-26	2M	3B	3M	3T	4MB	4T	5B	5M	5T
Mineral abundance calculated by MLA; MLA database formulae provided																
Sphalerite*	ZnS	94	87	15	53	18	3	10	2	53	0	5	1	12	1	10
Pyrite	Fe ²⁺ S ₂	7150	5910	2800	4190	4380	412	8840	5600	1490	3620	5260	4210	9120	438	4630
Pyrrhotite	Fe ²⁺ _{0.95} S	20400	37400	829	4540	3440	1300	25800	19400	9970	2410	3320	9760	10800	6350	10500
Chalcopyrite	CuFe ²⁺ S ₂	1110	3280	83	228	71	118	1410	2750	1600	1100	915	2310	2670	1700	1800
Altered Fe-sulfide	FeO(OH)·nH ₂ O)(Fe ²⁺ S ₂)	94	494	58	163	15	944	13400	10800	9300	11700	5880	8670	11500	15400	10500
Pentlandite	Fe ²⁺ _{4.5} Ni _{4.5} S ₈	849	1135	1	1	9	3	261	257	281	97	134	267	440	126	307
Trace element concentrations in samples calculated by MLA [mg element] [kg <425 µm waste rock] ⁻¹																
	Zn	63	59	10	35	12	1.8	7.0	1.2	35.6	0	3.5	0.4	7.8	0.3	6.5
	Se	-	-	-	-	-	-	-	-	-	-	-	-	-	-	-
	Cu	384	1140	29	79	25	41	489	951	554	378	317	801	925	588	622
	Co	-	-	-	-	-	-	-	-	-	-	-	-	-	-	-
	Ni	291	388	0.5	0.2	3.1	1.0	89	88	96	33	46	91	151	43	105
	As	-	-	-	-	-	-	-	-	-	-	-	-	-	-	-

Cont'd																
Mineral	MLA database formula or element	117	119	090	223	224	25-26	2M	3B	3M	3T	4MB	4T	5B	5M	5T
Calculated trace elements associated with pyrite [mg element] [kg <425 µm waste rock] ⁻¹																
	Zn	0	0	0.04	0.06	0.06	0.01	0	0	0	0	0	0	0	0	0
	Se	0.3	0.2	0.03	0.05	0.05	0.005	0.3	0.2	0.1	0.1	0.2	0.2	0.3	0.02	0.2
	Cu	0	0	0	0	0	0	0	0	0	0	0	0	0	0	0
	Co	1.0	0.9	0.1	0.2	0.2	0.02	3.7	2.3	0.6	1.5	2.2	1.8	3.8	0.2	1.9
	Ni	3.1	2.6	0.3	0.5	0.5	0.05	4.9	3.1	0.8	2.0	2.9	2.3	5.1	0.2	2.6
	As	0.9	0.7	0.4	0.6	0.6	0.06	2.7	1.7	0.5	1.1	1.6	1.3	2.8	0.1	1.4
Calculated trace elements associated with pyrrhotite [mg element] [kg <425 µm waste rock] ⁻¹																
	Zn	0	0	0.02	0.1	0.09	0.03	0	0	0	0	0	0	0	0	0
	Se	0.6	1.1	0.03	0.2	0.1	0.05	1.3	1.0	0.5	0.1	0.2	0.5	0.6	0.3	0.5
	Cu	0	0	0	0	0	0	0.6	0.5	0.2	0.06	0.08	0.2	0.3	0.2	0.3
	Co	0.4	0.8	0.4	2.2	1.7	0.63	5.8	4.4	2.2	0.5	0.7	2.2	2.4	1.4	2.4
	Ni	66	121	1.6	8.9	6.7	2.5	71	53	27	6.6	9.1	27	30	17	29
	As	4.1	7.5	0.2	0.9	0.7	0.27	4.8	3.6	1.9	0.4	0.6	1.8	2.0	1.2	2.0
Calculated Trace elements associated with chalcopyrite [mg element] [kg <425 µm waste rock] ⁻¹																
	Zn	0	0	0.03	0.08	0.02	0.04	0.06	0.1	0.06	0.04	0.04	0.09	0.1	0.07	0.07
	Se	0.3	0.8	0.004	0.01	0.003	0.006	0	0	0	0	0	0	0	0	0
	Cu	-	-	-	-	-	-	-	-	-	-	-	-	-	-	-
	Co	0.03	0.1	0.002	0.006	0.002	0.003	0	0	0	0	0	0	0	0	0
	Ni	0	0	0.0001	0.0002	0.0001	0.0001	0.01	0.02	0.01	0.007	0.005	0.01	0.02	0.01	0.01
	As	0	0	0	0	0	0	0	0	0	0	0	0	0	0	0
Calculated trace elements associated with pentlandite [mg element] [kg <425 µm waste rock] ⁻¹																
	Zn	0.1	0.2	0.0002	0.0001	0.001	0.0004	0	0	0	0	0	0	0	0	0
	Se	0.1	0.1	0.0002	0.0001	0.001	0.0004	0.06	0.05	0.06	0.02	0.03	0.06	0.09	0.03	0.07
	Cu	0	0	0	0	0	0	0	0	0	0	0	0	0	0	0
	Co	15	20	0.02	0.01	0.16	0.05	10	9	10	3.6	5.0	10	16	4.7	11
	Ni	-	-	-	-	-	-	-	-	-	-	-	-	-	-	-
	As	0.13	0.17	0.0002	0.0001	0.001	0.0005	0.03	0.03	0.03	0.01	0.01	0.03	0.05	0.01	0.03

Cont'd																
Mineral	MLA database formula or element	117	119	090	223	224	25-26	2M	3B	3M	3T	4MB	4T	5B	5M	5T
Calculated trace elements associated with altered Fe-sulfides [mg element] [kg <425 µm waste rock] ⁻¹																
	Zn	0.005	0.03	0.01	0.03	0.003	0.2	3.9	3.2	2.7	3.4	1.7	2.5	3.4	4.5	3.1
	Se	0	0	0.006	0.02	0.002	0.1	0	0	0	0	0	0	0	0	0
	Cu	0	0	0.04	0.1	0.01	0.6	23	18	16	20	10	15	20	26	18
	Co	0.001	0.004	0.003	0.01	0.001	0.0	1.4	1.1	1.0	1.2	0.6	0.9	1.2	1.6	1.1
	Ni	0.2	1.1	0.05	0.1	0.01	0.8	13	10	9	11	6	8	11	15	10
	As	0.03	0.2	0.02	0.05	0.004	0.3	4.5	3.7	3.1	4.0	2.0	2.9	3.9	5.2	3.5
Total trace elements in sulfides and altered Fe-sulfides not accounted for by MLA formulae [mg element] [kg <425 µm waste rock] ⁻¹																
	Zn	0.1	0.2	0.1	0.3	0.2	0.3	4.0	3.3	2.8	3.5	1.8	2.6	3.5	4.6	3.1
	Se	1.3	2.3	0.1	0.3	0.2	0.2	1.7	1.3	0.6	0.3	0.4	0.7	1.0	0.4	0.8
	Cu	0	0	0.04	0.1	0.01	0.6	23	19	16	20	10	15	20	26	18
	Co	17	22	0.6	2.4	2.1	0.8	21	17	14	7	9	15	24	8	17
	Ni	69	124	2.0	9.5	7.2	3.4	89	67	37	20	18	37	46	32	41
	As	5.2	8.6	0.6	1.6	1.3	0.6	12	9.0	5.5	5.5	4.2	6.1	8.7	6.5	6.9